MULTI-SCALE MULTI-PHYSICS MODEL AND HYBRID COMPUTATIONAL FRAMEWORK FOR PREDICTING DYNAMICS OF HYDRAULIC ROD SEALS

A Dissertation
Presented to
The Academic Faculty

by

Azam Thatte

In Partial Fulfillment
of the Requirements for the Degree
Doctor of Philosophy in Mechanical Engineering

Georgia Institute of Technology
December, 2010

MULTI-SCALE MULTI-PHYSICS MODEL AND HYBRID COMPUTATIONAL FRAMEWORK FOR PREDICTING DYNAMICS OF HYDRAULIC ROD SEALS

Approved by:

Dr. Richard F. Salant, Advisor
School of Mechanical Engineering
Georgia Institute of Technology

Dr. Robert Braun
School of Aerospace Engineering
Georgia Institute of Technology

Dr. Jeffrey L. Streator
School of Mechanical Engineering
Georgia Institute of Technology

Dr. Emily Nelson
NASA Glenn Research Center

Dr. Suresh K. Sitaraman
School of Mechanical Engineering
Georgia Institute of Technology

Date Approved: October 6th , 2010

I dedicate this work to my parents Manisha Thatte and Mihir Thatte
and to my wife Anna Duraj-Thatte without the endless support and love of whom this work would not have been possible.

ACKNOWLEDGEMENTS

I sincerely thank Prof. Richard Salant for guiding me through the journey of doctoral research. I also wish to thank Prof. Jeffrey Streator for his continual guidance and philosophical discussions. Special thanks are due to Dr. Bo Yang for his invaluable help in my research and to Prof. Levent Degertekin , Ms. Zehra Parlak and Prof. Todd Sulchek for their help with atomic force microscopy. I also wish to thank Dr. Jack Moon and Mr. Liang Qizhen for their assistance with dynamic mechanical analysis. I wish to specially thank my friends Dr. Dinesh Bansal, Kory Swope, Dr. Lei Wang, Shankar Narayanan, Sahil Girotra, Vrinda Vasudeva, Sonali Tare, Karan Singhal, Nilesh Ostwal, Bhargavi Chavali, Aniket Patil, Namrata Patil, Dr. Satish Nargundkar and Marla Nargundkar who, through their friendship, have made my Ph.D journey, the one to cherish. I express my deepest gratitude towards my grandparents Madhumalati Borate and Chandrakant Borate, my uncle Gaganvihari Borate and my aunty Archana Raskar who have played a large role in helping me achieve my dream of higher education. I am extremely grateful to Dr. G.P. Patil, Dr. Lalita Patil and Dr. Anil Kulkarni at Penn State University who have played a major role in my journey towards doctorate education.

Finally, thanks is too short of a word to express my feelings towards my parents Manisha Thatte and Mihir Thatte and my wife Anna Duraj-Thatte who have lifted me up through all the peaks and valleys of my life and without the continuous love, support and guidance of whom I would not have seen this day.

TABLE OF CONTENTS

Page

LIST OF TABLES

Page

LIST OF FIGURES

Page

NOMENCLATURE

a_T	shift factor for time-temperature superposition
C_{ijkl}	effective modulus defined by Eq. (3.3)
c	convective velocity in ALE method
cA_i	approximation coefficients vector in wavelet algorithm
cD_i^H	horizontal details coefficient vector in wavelet algorithm
cD_i^V	vertical details coefficient vector in wavelet algorithm
cD_i^D	diagonal details coefficient vector in wavelet algorithm
D	rod diameter
E	elastic modulus
$E(t)$	relaxation modulus
E_∞, E_i	elastic moduli in the Prony series
$E^{'}$	storage modulus
$E^{''}$	loss modulus
F	cavitation index, 1 when $\phi \geq 0$, 0 when $\phi < 0$
$F_{k\ Elastic}$	load due to k^{th} asperity of an elastic material
$F_{k\ Viscoelastic}$	load due to k^{th} asperity of a viscoelastic material
F_i^a	global load vector
F_{bi}	body force vector
f	friction coefficient

g	gap distance defined for macro-contact
$G(t)$	shear relaxation modulus
$g(n)$	high pass filter for wavelet algorithm
H	dimensionless average film thickness, h/σ
H_d	dry film thickness, h_d/σ
H_{def}	normal deformation of sealing surface
H_T	dimensionless average truncated film thickness, h_T/σ
$\tilde{\mathrm{H}}$	Heaviside function
$h(n)$	low pass filter for wavelet algorithm
$J(t)$	creep compliance of the viscoelastic material
K	bulk modulus
K_{aibk}	global stiffness matrix
L	length of solution domain in x-direction
L_s	stroke length
$N^a(\mathbf{x})$	shape functions
P	dimensionless fluid pressure, p/p_a
p_a	ambient pressure
$P_{dc,p}$	penalized dry contact pressure
p_n	normal penalty factor defined for macro-contact
P_c	dimensionless contact pressure for linear elastic material used for deformation analysis, p_c/E
p_{cav}	cavitation pressure

$P_{c\,Viscoelastic}$	dimensionless contact pressure for viscoelastic material
P_{dc}	dimensionless dry contact pressure for deformation analysis, p_{dc} / E
$P_{dc,p}$	dimensionless penalized dry contact pressure $p_{dc,p} / E$
P_t	dimensionless total pressure, $P\, p_a / E + P_c$
P_{sealed}	dimensionless sealed pressured, p_{sealed}/p_a
$\hat{q}$	dimensionless flow rate per unit circumferential length, $12\mu_0 qL/p_a\sigma^3$
Q_{net}	leakage per cycle
R	asperity radius
R_S	risk function in wavelet algorithm
S	deviatoric stress tensor
$\hat{t}$	dimensionless time, $t/t_{reference}$
T	temperature or threshold value in wavelet algorithm (as per the context)
$T_{f,p}$	penalized friction traction
T_j^*	normal pressure on seal boundary
u	displacement vector
U	surface speed of rod
v	particle velocity in ALE method
$\hat{v}$	mesh velocity in ALE method
w	particle velocity in referential domain of ALE method
$\hat{x}$	dimensionless axial coordinate, x/L
z	asperity height
$\hat{\alpha}$	dimensionless pressure-viscosity coefficient, $\alpha\, p_a$

δ	normal deformation of the asperity or Kronecker delta (as per the context)
$\delta(\omega)$	phase difference for viscoelastic materials
ε	strain tensor
$\tilde{\varepsilon}$	$\mu_0 L^2 / \left(\sigma^2 p_a t_{reference}\right)$
Φ	fluid pressure/density function, P when $F = 1$, $\hat{\rho}$ -1 when $F = 0$
	or a mapping operator in ALE method (as per the context)
ϕ	scaling function of wavelet algorithm
$\phi_f, \phi_{fss}, \phi_{fpp}$	shear stress factors
$\phi_{s.c.x}$	shear flow factor
ϕ_{xx}	pressure flow factor
λ_N	Lagrange multiplier
μ	viscosity
μ_0	viscosity at atmospheric pressure
ν	Poisson's ratio
$\hat{\rho}$	dimensionless density, ρ / ρ_l
ρ_l	density of the liquid
ρ_s	density of the solid
ρ_0	density of the material in reference state
$\hat{\sigma}$	dimensionless rms roughness of sealing element surface, $\sigma R^{1/3} \eta^{2/3}$
σ	stress tensor or rms roughness (as per the context)
$\hat{\tau}_f$	average dimensionless viscous shear stress in the x-direction, τ_f / E

$\hat{\tau}_c$	dimensionless shear stress due to contacting asperities, τ_c / E
τ_i	i^{th} relaxation time constant
υ	Poisson's ratio
ω	excitation frequency
ξ	$R^{1/3}\eta^{2/3}EL / p_a$
ξ_1, ξ_2	normalized coordinate system for finite elements
ζ	dimensionless rod speed, $\mu_0 UL / p_a\sigma^2$
η	asperity density
η_T	output of soft thresholding scheme in wavelet algorithm
ψ	probability density function of asperity heights or wavelet function (as per the context)
$\tilde{\psi}$	probability density function of normalized asperity heights
Ψ	mapping operator in ALE method
φ	mapping operator in ALE method

SUMMARY

Hydraulic actuators are extensively used in today's fluid powered industries. Leakage of hydraulic fluid past the reciprocating rod seals is a serious problem in such hydraulic systems. Fundamental physics of hydraulic seals is still poorly understood and the seal designers have virtually no analytical tools, beyond finite element structural analysis, with which to predict the behavior of potential seal designs or interpret test results.

In this research a multi-scale multi-physics (MSMP) seal model is developed. It solves macro-scale deformation mechanics, macro-scale contact, micro-scale contact of surface asperities, micro-scale fluid mechanics in the sealing zone and micro-scale deformation mechanics of the sealing edge in a strongly coupled manner. The model takes into account the surface roughness, mixed lubrication, cavitation and two phase flow, transient squeeze film effects, dynamic operation with temporally varying sealed pressure and rod velocity as well as the effect of macro/ micro/ nano scale viscoelasticity of the seal. A hybrid finite element-finite volume-statistical computational framework is developed to solve the highly coupled multi-physics interactions of the MSMP model efficiently.

To extract the surface parameters needed for MSMP model, surface characterization experiments are performed. These experiments revealed some new seal surface characteristics like directionality and helped in detecting micro-scale surface imperfections. To remove the high frequency noise without removing the high frequency

surface features, a wavelet transform based adaptive surface extraction method is implemented.

Dynamic mechanical analysis is performed to extract the macro-scale viscoelastic parameters of the seal. DMA experiments revealed the strong temperature and frequency dependence of storage and loss moduli of polyurethane and PTFE seals.

To investigate the micro/nano scale viscoelastic response of surface asperities, atomic force microscopy (AFM) experiments are conducted on polyurethane seal samples. The micro/nano scale elastic moduli for polyurethane produced a surprising finding showing several local moduli to be varying within 2 orders of magnitude (as high as 3000 MPa) higher than the bulk of the polymer (43 MPa). The phase plots of these micro-scale regions showed significant differences in local stiffness and adhesion. To extract the viscoelastic response of the individual asperities, time resolved interaction force measurements were performed. Significant differences in both, the magnitude of the moduli and the relaxation time scales, of individual asperities were observed. Understanding the nano-scale viscoelastic properties of the seal asperities is believed to be a valuable addition to the fundamental understanding of multi-scale sealing dynamics.

With the comprehensive MSMP model developed, key seal performance characteristics were analyzed. The results confirmed the mixed lubrication in the sealing zone, and that seal roughness plays an important role in determining seal behavior. Critical seal roughness, above which the seal leaks, was found for the transient operation. During instroke, fluid films were found to be thicker than those during the outstroke, which promotes non-leaking. Cavitation was shown to take place during outstroke which also helps in reducing leakage. It was found that the shear stress on the rod is primarily

due to contacting asperities. With time changing sealed pressure, it was seen that the time variations in fluid pressure distributions are governed by a complex dual dependence on changes due to time varying sealed pressure boundary condition and those due to hydrodynamic effects produced by time varying rod velocity.

Viscoelasticity is seen to critically affect the leakage and friction characteristics through its effects on the fluid pressure and contact pressure distributions. It produces thicker fluid films during both, the outstroke and the instroke, and produces a significant increase in the Poiseuille component of the flow during the instroke. It is found that ignoring viscoelasticity leads to under prediction of the time required to reach the zero leakage state during a cycle.

Comprehensive viscoelastic MSMP model was also used to analyze high pressure - high frequency sealing applications. A new phenomenon of "secondary" contact was observed in the rod seals. A surprising finding of increase in the dry contact pressures in the secondary contact with time at a constant operating pressure is attributed to the viscoelastic creep induced pressures surrounding the sealing edge. Sealing characteristics in such applications are found to be significantly different than those observed previously. Viscoelasticity induces significant differences in Poiseuille flow and friction force from one cycle to the next. It is also found that with reduction in cycle frequency, the differences in fluid flow and contact variables from cycle to cycle are reduced. This is because, the viscoelastic seal gets more time to relax and come to internal equilibrium before its next cycle. Leakage characteristics were found to be very different for the same seal if it is operated in an application with different cycle frequency. This shows that the

seals need to be designed by taking the relaxation time scales of the seal's polymer and cycle frequencies of application into consideration.

The study also showed that reducing temperature or increasing the relaxation time constant of the polymer, would reduce the tendency of secondary contact for a given frequency of operation. It revealed that for a given frequency, there is a "critical temperature" above which secondary contact will occur and the consecutive cycles may not be considered repetitive. Similarly, for a given operating temperature, there exists a "critical frequency" of operation below which the seal will exhibit secondary contact and the contact pressure distributions will change significantly. These findings show that the seals performance can be manipulated by controlling its temperature or relaxation time constants. With this, the new seal designs where local temperature control is achieved by embedding resistive heating circuits can then be envisioned for controlling the seal response.

The comprehensive MSMP framework developed here can be used as an effective seal analysis and design tool. Due to object-oriented nature of the MSMP framework, a variety of multi-physics phenomena can be added to the existing framework and new seal designs like, seals with embedded shape memory alloys, seals with micro/nano surface pattern or the seals with piezoelectric elements to micro-control the sealing edge deformations, can be proposed and analyzed. With this in mind, the MSMP computational framework developed here has a great potential to be used as a stand-alone seal design and analysis software in academic and industrial research.

CHAPTER 1. INTRODUCTION

1.1 Problem Description

Hydraulic actuators are extensively used in today's fluid powered industries including but not limited to aviation, mining, automation, biomedical, excavation, heavy lifting and space exploration. A serious problem that exists in such hydraulic systems is the leakage of hydraulic fluid past the reciprocating rod seals. Not only does this leakage affect the system performance but, more importantly, it can lead to serious consequences. NASA's space shuttle Challenger's explosion in 1986 is a vivid example of what happens when the sealing ability of the system is lost. Dr. Richard Feynman in his famous report demonstrated that the loss of sealing and hence the explosion was due to malfunction of a static elastomeric O-ring at the low ambient temperatures that existed the night before the shuttle's launch. Besides more serious effects like this, environmental pollution is another consequence of unsatisfactory performance of hydraulic rod seals, since operating fluid leaking past the seal directly enters its surroundings. Frictional losses and hence energy inefficiencies are also important factors that are attributed to the poor design of rod seals. Considering this, the rod seals are one of the most critical components in today's hydraulic systems.

At the present time, although much has been learned about such seals from experimental studies, their basic behavior is still poorly understood. Consequently, the seal designers have virtually no analytical tools, beyond finite element structural analysis [1-4], with which to predict the behavior of potential seal designs or interpret test results.

Neither do they have a physics based framework upon which to base a design. Thus, current seal design is almost completely an empirical process.

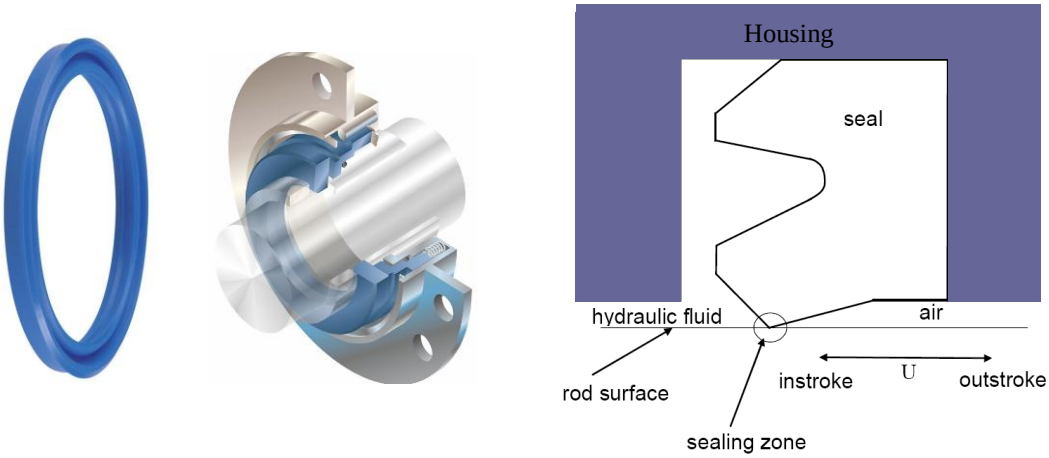

Figure 1.1: (a) Typical hydraulic rod seal (b) seal mounted between rod and cylinder housing (c) schematic of a mounted seal.

Figure 1.1 shows a typical hydraulic rod seal mounted between the piston rod and the cylinder housing. The region where the seal lip appears to meet the rod is termed the sealing zone; it is where all the sealing action takes place. Multi-scale elastohydrodynamics governs the operation of such seals. Following is the list (not complete) of phenomena that govern the sealing physics:

1) The seal is deformed under the action of interference fit and sealed pressure. This creates the sealing zone and gives rise to macro-scale contact pressure.

2) The surface of the seal is rough and consists of micro-scale asperities which are deformed and further generate contact pressures.

3) Fluid is trapped in the micro-channels between asperities and gives rise to fluid pressure distribution in the sealing zone.

4) The sealing edge deforms under the action of fluid pressure and macro-scale and asperity contact pressures, which in turn affects the fluid film thickness.

5) The film thickness and fluid viscosity in turn determines the fluid pressure distribution.

6) Fluid viscosity is a function of fluid pressure and temperature.

7) During sealing, the fluid film thickness may fall below a critical value allowing for significant asperity contact between the seal and the rod, a condition known as "mixed lubrication". The fluid mechanics is critically altered in the presence of such mixed lubrication effects.

8) If the fluid pressure falls below the cavitation pressure, the fluid forms striations or two-phase regions where both the liquid and air phases are simultaneously present. In writing the equations governing the micro-scale fluid mechanics in the sealing zone such surface roughness and cavitation effects need to be taken into account.

9) The macro-deformation of the entire seal and micro-deformations of the sealing edge depend on the type of seal material and are governed by linear / nonlinear elasticity and viscoelasticity.

10) Viscoelastic response of a polymeric seal is highly temperature dependent. Hence the operating temperature and thermal transport plays a crucial role in overall sealing dynamics.

11) Thermal transport produced by frictional forces can also play a role in overall seal performance.

12) The shear stress generated by contacting asperities and the fluid viscous shear can also cause deformations of the sealing edge and hence affects the entire sealing dynamics.

13) Micro-nano scale viscoelastic response of surface asperities affect the micro-scale viscoelastic contact pressure distributions in the sealing zone.

14) Directionality and statistical nature of surface roughness plays an important role in governing fluid flow through asperities and the asperity contact pressures.

15) Transient effects from time varying rod velocity produce significant changes in hydrodynamics while the transient sealed pressure creates a time varying sealing zone. Since micro-scale fluid, contact and deformation mechanics now needs to be solved in the time varying sealing zone, the whole computational domain changes with time.

It can be seen that all of the above physical phenomena are inter-dependent and the equations governing them need to be solved in a highly coupled manner in order to accurately model the sealing dynamics. Also this coupled physics spans across several length and time scales, ranging from nano-meter to millimeter and millisecond to hundreds of seconds. Hence this kind of sealing analysis is a multi-scale, multi-physics problem.

1.2 Research Objectives

This research aims at developing a comprehensive multi-scale multi-physics (MSMP) model of generalized reciprocating hydraulic rod seals that will solve the above mentioned physical phenomena in a strongly coupled manner. An efficient computational framework to solve these multi-physics equations will be developed. Such a model would

be capable of predicting the key seal performance characteristics, such as fluid film thickness, contact pressures, fluid pressures, leakage and friction. Once developed and tested, this computational model could be used as a stand-alone seal design and analysis software. The software will allow evaluation of existing seal designs before manufacturing. The analysis tool developed will save the time and costs of experimental seal analysis test-beds, as it will allow screening potential seal designs and selecting only the most promising ones to be prototyped and tested. The software could then be used to suggest design modifications.

In addition, such a multi-scale multi-physics seal model would stimulate the development of innovative seal concepts by modifying seal geometries at macro-scale as well as at micro/nano scale. For example, producing piezo-electric polymer composite seals, temperature controlled seals with embedded shape memory alloys or engineering micro patterned seal surfaces. Computational tool's capability to model multi-scale time dependent material response will allow us to understand macro-scale as well as nano-scale viscoelastic response of the seal and use it in designing seals with controlled performance variables.

Since surface properties of seals play a critical role in sealing dynamics, surface characterization experiments will be performed to better model sealing physics. Time dependence of material properties is expected to play a vital role in transient sealing dynamics. To extract accurate parameters for the numerical model, macro-scale as well as micro/nano scale material characterization experiments will be performed to evaluate the role of viscoelasticity over a broad range of length and time scales. Some fundamentally

new findings that were revealed through nano-scale material characterization will be discussed.

Finally, using the MSMP model and hybrid computational framework developed, a variety of sealing applications will be analyzed and their performance will be evaluated. Some of these applications will include high pressure, high frequency sealing cycles. In such applications, the effect of operating pressure on phenomena like secondary contact, effect of cycle frequencies, effect of viscoelastic relaxation time scales and effect of temperature on the cycle performance will be quantified. Some new phenomena that were observed through these simulations will also be discussed.

1.3 Organization of the Dissertation

Chapter 1 gives a brief description of the research problem and elaborates on the objectives of this research.

Chapter 2 provides the research background. The experimental and theoretical studies performed in the field of seal analysis and design are described. Some of the material models that can be used to capture the viscoelastic response of thermoset and thermoplastic polymers are discussed. Past numerical models developed, important findings from these models and their deficiencies are discussed. A brief overview of the existing mathematical methods and high performance computational algorithms needed to solve the multi-physics problem at hand is also presented in this chapter. A short literature review discussing the reasons for implementing wavelet based algorithm for surface characterization is presented. Review of the literature on atomic force microscopy

(used in this work for characterizing micro/nano scale viscoelastic response of the seal) is also presented in chapter 2.

Chapter 3 discusses the development of multi-scale multi-physics hybrid computational framework which forms the backbone of this work. Individual modules that solve various governing equations and the coupling scheme used is described. The mathematical solution methods and computational algorithms used are also discussed in detail. The results obtained from using the computational model to solve a sealing problem with time varying rod velocity are presented. Important new findings from this study are discussed.

Chapter 4 describes the experimental methods used for surface characterization. Using recent advances in optical, laser and micro-sensor based measurement techniques like optical profilometry, scanning electron microscopy and atomic force microscopy; surface parameters like RMS roughness, asperity density, asperity radius and auto-correlation lengths of seal surfaces are measured. A wavelet transform based adaptive signal extraction algorithm is developed to separate the high frequency surface features from high frequency noise induced by optical interference. Experimental results obtained for several different polyurethane and PTFE seal surfaces are presented. Differences in surface characteristics of new and used seals, seals produced by different manufacturing processes etc. are discussed. Use of these advanced techniques in detecting micro-scale surface defects that eventually lead to failure of sealing ability is demonstrated. The surface parameters extracted are then used in the computational model to model the seal performance more realistically.

Chapter 5 discusses the improvement in the MSMP model to handle transient operating pressures. The modifications in the mathematical algorithm needed to solve such a "moving mesh" problem and corresponding "Arbitrary-Lagrangian-Eulerian" framework and "Dynamic Domain Mapping" method developed is described in detail. The results obtained by applying this improved MSMP computational framework for solving a fully transient injection molding sealing application are presented.

Chapter 6 develops a comprehensive MSMP model by incorporating multi-scale viscoelasticity of the seal. First, the dynamic response of general viscoelastic solids is analyzed. Some preliminary macro- deformation finite element studies are performed on the seal that show the effect of polymer's relaxation spectrum on seal's performance.

Effect of excitation frequency, relaxation time constants and instantaneous elastic moduli on seal's hysteresis, sealing zone length, internal stresses and strains and contact pressures are discussed through analytical and finite element solutions.

A new analytical model for viscoelastic contact of rough surfaces is developed and is incorporated in the comprehensive MSMP framework.

The comprehensive MSMP framework developed is used for analyzing the performance of a seal used in an injection molding application. The key differences in the performance of purely elastic and viscoelastic seal materials are discussed.

Chapter 7 discusses the macro-scale characterization of polyurethane and PTFE viscoelasticity using dynamic mechanical analysis. A multi-variate constrained optimization algorithm is developed to extract Prony coefficients from the frequency dependent dynamic storage and loss moduli. Atomic force microscopy is performed on polyurethane seal surfaces and time resolved interaction force measurements are obtained

to characterize the nano-scale viscoelastic response of surface asperities. Surprising findings regarding local nano-scale elastic moduli of polyurethane seals and their viscoelastic behavior are presented.

Chapter 8 describes the use of comprehensive MSMP model in predicting the effect of multi-scale viscoelasticity on the performance of seals used in high pressure, high frequency sealing applications. Critical differences in visco-elastohydrodynamic characteristics are observed for such seals. The effects of cycle frequency on fluid pressures, contact pressures, Poiseuille flows, sealing zone lengths , friction and leakage are quantified. The effect of relaxation time scales of seal's polymer and its temperature on sealing performance is discussed and suggestions of appropriate materials for particular sealing applications are made.

Chapter 9 discusses the main conclusions achieved from this research and how it can be used in the future work.

CHAPTER 2. LITERATURE REVIEW

A significant amount of experimental and theoretical research on hydraulic seals, has been performed since 1960's. Unfortunately, these studies did not have a significant impact on the seal design process. The seal designers had no analytical tools beyond structural analysis. It is only recently that numerical modeling has revealed some of the significant fundamental physical phenomena that govern the behavior of such seals. In the following discussion a brief review of some of these studies is presented.

2.1 Experimental Investigations

Experimental research on hydraulic seals has made steady progress over the years due to advances in optical measurements techniques and micro-machined sensors. Measurements of leakage rate, friction, fluid film thickness and contact pressure distributions have been the main characteristics of most of these studies. The foundation of present understanding of the behavior of reciprocating elastomeric rod seals was laid by White and Denny[5]. In their studies they measured the variation in tensile strain and contact stress along the sealing interface of a rectangular seal. They also identified the dependence of seal friction on the nominal contact area and experimentally evaluated the effects of pressure, hardness and the groove shape on the O-ring contacts.

Several experimental studies have measured the frictional force exerted on the rod by the reciprocating seals using force transducers [6-8]. However these measurement techniques are affected by two problems. First, the suspension of housing or rod introduces a contributions to the total friction. Secondly, the separation of friction

measurements during outstroke from that of instroke. A technique with rod and a closed housing was developed by Lawrie and O'Donoghue [9] while a method where two rods are connected by a force transducer, was used by [10]. Cnops [11] devised a spring-loaded piston containing brake fluid of harmonically varying volume and observed the mechanism of oil film formation at the sealing contact, the thickness of which varied from partially collapsed at low speeds to relatively thick at higher speeds. He also observed the effects of stiction and elastomer relaxation and creep, which characterize the viscoelastic nature of rubber like materials. Development of a fluid film at a sealing contact and the transition from boundary lubrication to full film lubrication was the focus of Müller's experimental work [12]. Aston et al.[13] worked on rubber seal friction at temperatures up to 200^{o} C and found the relation between temperature and rubber dimensions. They also investigated the relaxation and recovery rate of rubber which caused a reduction of the frictional force in time. Such viscoelastic phenomena are crucial in sealing performance in the aerospace sector.

The techniques for measuring static contact pressure distributions include strain gauge, piezoelectric force transducer, photo elastic methods, as well as the inductive transducers. Most of these methods were developed in 1970s and 1980s by Molari, Austin, Kawahara and others [14-17]. Dowson and Swales [18] devised a rotating disc machine to emulate reciprocating seals during long strokes. Their experiments demonstrated increase of film thickness with speed and decrease with contact pressure.

In the leakage studies of recent years, precise and real-time techniques like electrical capacitance measurement of leaked oil layers have been used by researchers [19]. White and Denny [5] found a progressive increase in the leak rate due to growth of

fine axial scores on the sealing face. These scores were shown to be due to fluid's cutting action. They ran experiments with various lubricants with a broad range of viscosity and speeds. Only with the most viscous fluid, and seals with beveled edges, the expected form of friction - speed curve demonstrating a transition from mixed-film to full-film lubrication was obtained. Having demonstrated the possibility of hydrodynamic lubrication, they went on to apply the Reynolds equation to predict the minimum film thickness and hydrodynamic friction of a rectangular seal.

Optical interferometry has been a method of choice for measuring the film thickness in the sealing zone. These methods were mainly troubled by the poor reflectivity of polymer surfaces. Rana [20] developed a gold coating method which minimized the influence on seal roughness. Kawahara *et. al*. [17] and Rana *et. al.* [21] have designed various test rigs to record the sealing surfaces using high speed cameras. Some of these recent setups are capable of observing the cavitations arising from hydraulic fluid starvation and air bubbles formed at the edges of the sealing contacts, Field and Nau [15] have also used optical interferometry and electrical transducers to measure the sealing film thickness.

2.2 Theoretical Studies

2.2.1 Material Models

Seals made from both thermoset (e.g. Polyurethane, Nitrile Rubber) and thermoplastic (e.g. PTFE) polymers are widely used for hydraulic sealing. Thermoplastics have only secondary bonds between the chains, while thermosets have the primary bonds as well. Their thermal and processing characteristics are different due

to their basic structural difference. Thermoplastics like PTFE are widely used for rod seals due to their excellent mechanical and chemical properties like low friction and high resistance to thermal and chemical degradation. They have a very high resistance to ageing and is suitable for applications with temperatures in excess of 250^{o}C [22] which are not possible with elastomeric seals. On the other hand, thermoset polymers show better thermal stability and high strength. For strains exceeding a certain limit, such materials exhibit a non-linear stress–strain behavior as in hyperelasticity which make their material property modeling a complex task. Most popular phenomenological models describing hyperelasticity are Ogden model [23], Neo-Hookean model [24] and Mooney–Rivlin model [25-26]. In these models, the mechanical properties are represented in terms of elastic strain energy functions which in turn are the functions of principle stretch ratios.

Both these classes of polymers exhibit time dependent behavior and hence are viscoelastic in nature. Differences in stress relaxation and creep/creep recovery behavior between thermoplastic and thermoset polymers is demonstrated in Figure 2.1.

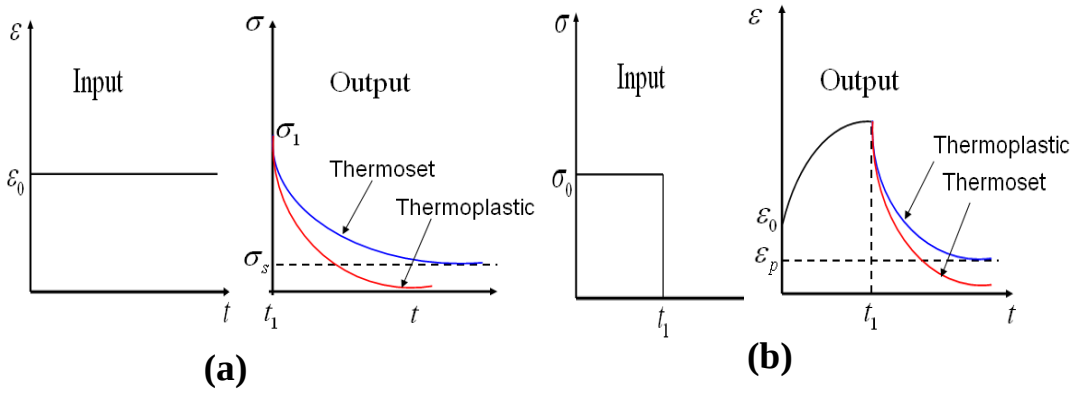

Figure 2.1: Difference in stress relaxation behavior (a) and difference in creep and creep recovery (b) for thermoplastic and thermoset polymers.

2.2.1.1 *Phenomenological Viscoelastic Models*

Before complex constitutive relations that govern viscoelastic behavior of seals are developed, it is useful to look at the development of some simple phenomenological models. “Maxwell Fluid” and “Kelvin Solid” are two such models and are shown in Figure 2.2. Brinson and Brinson [27] discuss several phenomenological models needed for capturing the viscoelastic response seen in common thermoplastic and thermoset polymers. They also develop the constitutive equations describing these models, some of which are shown below. The basic elements can further be combined into other variations to form more complex models like “Three Parameter Solid” or “Four Parameter Fluid”. Such models are useful in understanding the physical relation between stresses and strains that occur in polymers, e.g. under the application of a sudden constant stress, the models with a free spring will show an instantaneous increase in the strain and they will creep to a limiting constant strain. However, the model with a damper will not allow such an instantaneous increase in the strain. Also, in the relaxation process for models with a free damper, the stress will decay to zero, while in the models without a free damper, the stress will decay to a limiting value during the relaxation process.

We can obtain the constitutive relations for these models by using equilibrium and kinematic equations [28]. For Maxwell Fluid, assuming deformation to be quasi-static and neglecting inertia, the stress is same in both the elements and total strain is the sum of the strains in individual elements.

$$\sigma + \frac{\eta}{E}\frac{d\sigma}{dt} = \eta\frac{d\varepsilon}{dt} \tag{2.1}$$

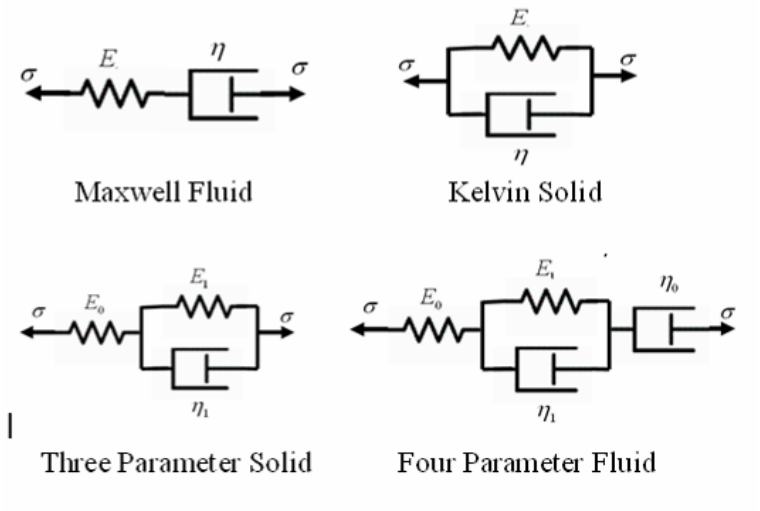

Figure 2.2: Various phenomenological viscoelastic models.

The solution of Eq.(2.1) for a step input of strain ($\varepsilon(t)=\varepsilon_0\tilde{\mathrm{H}}(t)$) is given by, $\sigma(t)=\varepsilon_0 E e^{-t/\tau}=\varepsilon_0 E(t)$. Here, $\tau=\frac{\eta}{E}$ is the "Relaxation Time Constant" and $E(t)=Ee^{-t/\tau}$ is the "Relaxation Modulus". The relaxation time indicates the time scale associated with the intrinsic viscosity of the polymer. The polymer actually possesses not a single relaxation time, but a spectrum of relaxation times.

A similar analysis for a Kelvin solid under creep loading gives $\varepsilon(t)=\frac{\sigma_0}{E}\left(1-e^{-t/\tau}\right)$ and is shown in Figure 2.3 (a). It can be seen that Kelvin solid model shows no initial elasticity and for a large enough time, a constant strain state ε_∞ is achieved. However, for a real polymer, the network of molecular chains shows a more complicated response and a wider spectrum of relaxation times [27]. With this in mind, we need to assemble multiple primary elements in order to better mimic polymer behavior by providing multiple relaxation times. For example, for the constant stress creep test of a four parameter fluid we get,

$$\varepsilon(t) = \sigma_0 \left[\frac{1}{E_0} + \frac{1}{E_1}\left(1 - e^{-t/\tau}\right) + \frac{t}{\eta_0} \right] \tag{2.2}$$

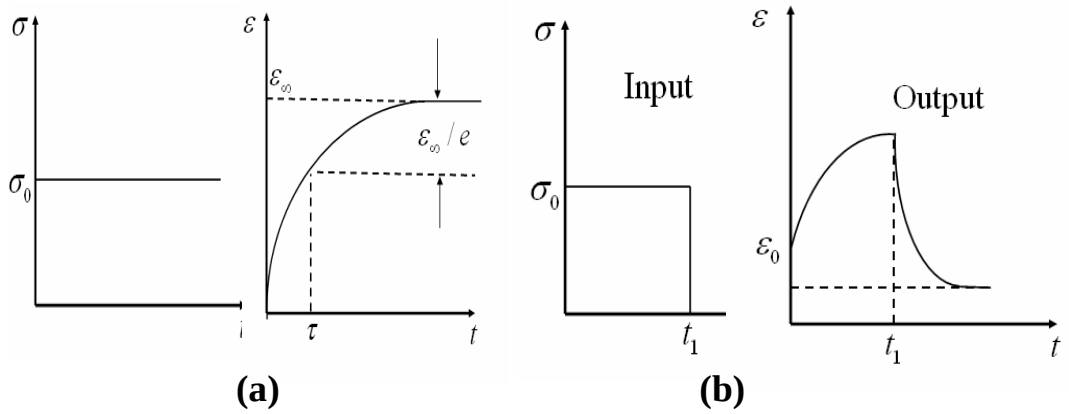

Figure 2.3: (a) Creep of a Kelvin solid. (b) Creep and creep recovery of a four parameter fluid.

The creep and creep recovery obtained using this formulation is plotted in Figure 2.3 (b) and illustrates a much closer representation to that demonstrated by thermoplastic polymers (Figure 2.1).

To capture a broader range of relaxation time scales associated with the polymer chains of varying lengths, sometimes it is required to connect several Maxwell elements in parallel. The resulting model is called "Generalized Maxwell Model" and is shown in Figure 2.4 (a). Differential equation for such a model is given by,

$$\sum_{j=0}^{n} p_j \frac{d^j \sigma}{dt^j} = \sum_{j=0}^{n} q_j \frac{d^j \varepsilon}{dt^j} \quad \left(\text{with } q_0 = 0\right) \tag{2.3}$$

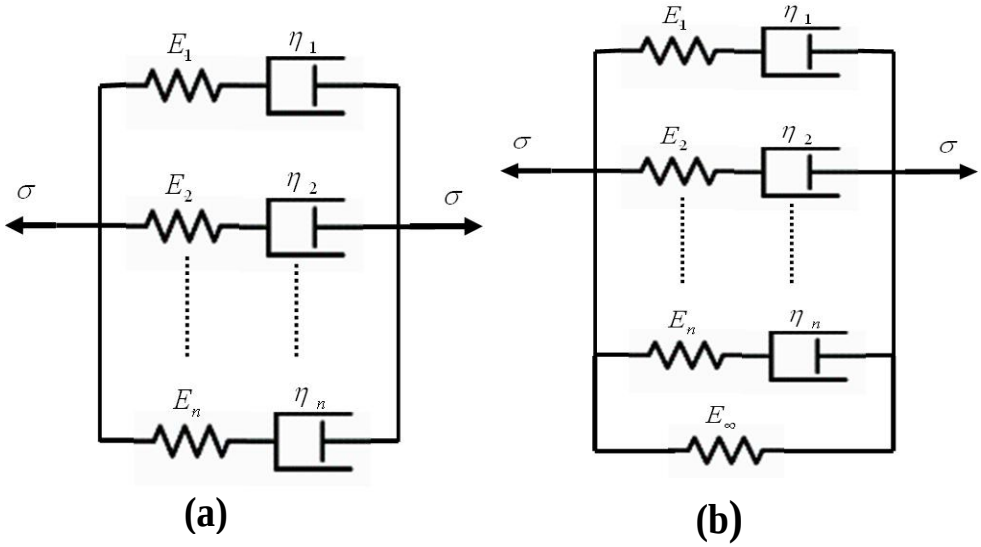

Figure 2.4: Different forms of Generalized Maxwell model.

The solution of this system of ODEs for a given strain input $\varepsilon(t)$ can be found by superposition of n first order differential equation solutions. A free spring can be added to the above model as shown in Figure 2.4 (b) to better represent the thermoset polymers. The solution for stress relaxation of this system can be found by superposition to be,

$$\sigma(t) = \varepsilon_0 \left[E_\infty + \sum_{i=1}^{n} E_i e^{-t/\tau_i} \right] \tag{2.4}$$

and the relaxation modulus is given by, $E(t) = \left[E_\infty + \sum_{i=1}^{n} E_i e^{-t/\tau_i} \right]$, where. E_∞ is the equilibrium modulus.

Without making any attributions to a specific model or process, the "general constitutive relation" for a viscoelastic solid can be written using Boltzmann superposition integral [29] as,

$$\sigma_{ij} = \int_{-\infty}^{t} \left\{ G\left(t-t'\right)\left[\dot{\gamma}_{ij} - \frac{1}{3}\sum \dot{\gamma}_{kk}\delta_{ij} \right] + \frac{3}{2} K\left(t-t'\right)\left[\frac{1}{3}\sum \dot{\gamma}_{kk}\delta_{ij} \right] \right\} dt' \qquad (2.5)$$

where, G is the shear relaxation modulus and K is the bulk relaxation modulus. This formulation takes into account the changes in volume of the material. Since in most experiments, initial conditions are known at the start of the deformation process, and hence the lower $-\infty$ limit of the integral is often replaced by 0 [27, 30].

2.2.2 Modeling the Physics of Sealing

Sealing problems fall in the category of soft elasto-hydrodynamics. Its multi-physics nature makes the theoretical analysis of hydraulic seals a complex task. Advanced phenomenological material models allow the analytical solutions for only the simplest geometries like rectangular cross section. In recent years, commercial finite-element softwares have been used to perform structural analysis with complex geometries but still many of these methods can not solve the problem in a fully-coupled manner.

A lubricating film of micrometer level thickness is present between the contacting surfaces, the fluid mechanics of the lubricating film is coupled with the elastic deformation mechanics of the sealing element. The fluid mechanics of the lubricating film is governed by the Reynolds equation (with hydrodynamic pressure, P, as the unknown), which contains the local film thickness, H, as a known variable. The macro and micro deformations of the seal are governed by the elasticity equations (for H), which in turn contain P. The coupling between these equations can be handled in one of two ways, the direct method or the inverse method. In the inverse method [31-32], the hydrodynamic pressure distribution is assumed to be known and equal to the static

contact pressure distribution (assuming the static interference is much larger than the additional deformations due to the hydrodynamic pressure). The Reynolds equation is then solved for the film thickness distribution, in closed form. However, the large deformations, high strain rates and incompressibility of the seals produce numerical instability problems in this method. To tackle this problem, Nikas [33] developed a modified version of the inverse hydrodynamic theory, which is used by several others [34-36]. Instead of solving the cubic algebraic equation, a first order, ordinary differential equation was solved. In the direct method, iterations are used. The film thickness distribution H is initially guessed, and the Reynolds equation is numerically solved for the pressure distribution P. The pressure is then inserted into the elasticity equations, which are solved for the deformation (using FEA) and, hence for H. The new values of H are inserted into the Reynolds equation, which is then re-solved for new pressure P. Iteration continued until the solution is converged. However, numerical instabilities and divergence problems are commonly encountered in these methods as well. Ruskell [37] and others worked on reducing these instability problems. However the issues of convergence have not been completely resolved.

Most of the previous analytical models make two key assumptions: 1) full film lubrication and 2) perfectly smooth sealing surfaces. However, it was found as early as 1973 that there are serious problems with the basic assumptions of all these models [38]. Experiments revealed that the assumption of full film lubrication is very questionable and that mixed lubrication occurs over a wide range of conditions [17]. Furthermore, it has been found experimentally that the surface roughness plays an important role in the lubrication of these seals [39]. Thus, it is not surprising that previous analytical models,

have not had a significant impact on practical seal design. A successful model must account for both mixed lubrication and the surface roughness effects. While most of the past theoretical models assumed smooth seal and rod surfaces and full film lubrication, some recent studies [40-42] take into account the surface roughness as well as mixed lubrication, but are limited to seals with a rectangular cross section. Models by Salant and his students [43-46] have successfully incorporated more complex geometries, surface roughness and mixed lubrication but are limited to steady-state operation. These steady-state models have shown numerically that the RMS roughness of the seal surface strongly influences the seal behavior, and there is significant asperity contact in the interface. Some other recent numerical studies by Ongun *et. al.* [47], Stupkiewicz *et. al* [48] and Schmidt *et. al.* [49] have also taken into account the elastohydrodynamics of more complex seal geometries. Nikas [50] has recently presented a comprehensive overview of the past experimental and theoretical work related to hydraulic reciprocating seals.

2.3 Contact of Rough Surfaces

All engineering surfaces exhibit roughness at different length scales from macro-scale (waviness) to roughness at micro and nano scales. The roughness pattern or surface texture can be described as random, isotropic or anisotropic, and Gaussian or non-Gaussian. Greenwood and Williamson [51] put forth one of the first statistical based model for frictionless contact between two rough surfaces. This (GW) model idealized the scenario as contact between a rough elastic surface and a rigid flat plane. They assumed that all the asperities have same the radius of curvature and they deform according to Hertzian contact theory [52] and their heights follow Gaussian distribution.

Using this GW model, the contact pressure can be estimated using the asperity density, RMS roughness and asperity radius. McCool [53] presented a good summary and numerical analysis of GW model [51], BGT model [54] and BGK model [55]. McCool recommended the use of GW model based on its simplicity and in comparison with asperity simulation model.

Some of the more advanced contact models include the recent work by Persson and coworkers [56] who used molecular dynamics simulations to model a multi-scale contact . Fractal based contact models [57] were found to be insensitive to the resolution of the surface scan. Jackson and Streator [58] have developed an advanced non-statistical multi-scale contact model based on the concept of "protuberance upon protuberance". This model computes the FFT of the surface scan and arranges the asperities of higher frequencies upon asperities of lower frequencies. One of the main advantages of this model is that its predictions are not sensitive to the sampling resolution of the measurement.

2.4 Fluid Flows between Rough Surfaces and Flows with Cavitation

Patir and Cheng [59-60] developed a study involving an average flow model for determining the effects of surface roughness on partial hydrodynamic lubrication. An average Reynolds equation was defined relative to pressure and shear flow factors, which are functions of the surface characteristics that are obtained from numerical simulations. Patir-Cheng flow factors are extensively used for modeling flow between rough surfaces and have been implemented in this work.

In the regions where Reynolds equation yields pressures below the cavitation pressure, P_{cav}, the fluid forms striations and both, liquid and air, are present at a uniform pressure of P_{cav} [61]. Such cavitation phenomenon is well described by Jakobsson-Floberg-Olsson (JFO) theory. Elrod [62] and Payvar-Salant [63] have developed algorithms in which all JFO conditions are met using a "universal Reynolds equation". Salant & Harp [64] developed an inter-asperity cavitation model [65] where the switch between global cavitation, full film flow and inter-asperity cavitation was achieved by including a cavitation index , F, in the universal, average Reynolds equation.

2.5 Wavelet Transform and Its Applications in Signal De-noising

In the current work, wavelet transform based signal de-noising is implemented for accurate seal surface characterization. Here, wavelets are used to remove the high frequency surface noise induced by optical interferometry without removing the high frequency real surface features.

In last ten years wavelets have gained popularity in wide variety of fields involving signal processing. Daubechies ten lectures on wavelets [66] have laid a great foundation for their use. Wavelets have found applications in the fields ranging from biomedical signal processing [67] to Astrophysics [68-69]. Fundamental work of Mallat [70-71] and Donoho & Johnstone [72-74] has produced significant advances in time-scale based signal extraction techniques. Detailed description on the theory of wavelet decomposition is presented in [75].

2.6 Atomic Force Microscopy and Its Applications for Micro / Nano Scale Material Characterization

In the current work, atomic force microscopy is used to measure the elastic properties of seal surface asperities and to characterize their viscoelastic response at micro/ nano scale. Since its invention, the atomic force microscope (AFM) [76] has been widely used in the field of micro/nano scale material characterization. Nano-indentation method has been utilized to measure the elastic and plastic response and hardness at small scales [77]. Butt et. al [78] provided a comprehensive discussion of techniques, interpretations and applications of AFM for nano-scale force measurements. Atomic force acoustic microscopy [79] and ultrasonic force microscopy [80] have been used to determine the contact stiffness by measuring the cantilever contact resonance frequencies. The pulsed-force mode of AFM [81] can measure the elastic and adhesive properties of the sample simultaneously with the topography, however the operating speeds are much slower due to the high quality factor of commercial cantilevers.

In ambient conditions, most samples develop a liquid meniscus layer and keeping the probe tip close enough to the sample for short-range forces to be detectable while preventing the tip from sticking to the surface becomes a major problem. Tapping mode of the AFM was developed to bypass this problem [82] , where the cantilever is driven to oscillate at or near its resonance frequency by a small piezoelectric element mounted in the AFM tip holder. Interactions due to van der Waals forces, electrostatic forces, dipole-dipole interaction etc. cause the amplitude of this oscillation to decrease as the tip gets closer to the sample. A tapping AFM image is then produced by tracking the force of the intermittent contacts of the tip with the sample surface.

To probe the properties like micro/nano scale viscoelasticity, ideally we need a probe that has high sensitivity for nondestructive characterization and high bandwidth for fast operation. Degertekin and his students [83] recently introduced the FIRAT (force sensing integrated readout and active tip) probe as an alternative to the AFM cantilever. A sharp tip fabricated on top of micro-machined sensor combines the electrostatic actuation capability and interferometric detection sensitivity. They also used the FIRAT probe to obtain time-resolved interaction forces between the probe tip and sample at high speeds needed for fast imaging of material properties. Parlak et. al [84] developed an active tip control method for controlling the interaction forces during individual tapping events of tapping mode AFM. This work has formed the basis for nano-scale viscoelastic characterization that is performed in the current study.

CHAPTER 3. MULTI-SCALE MULTI-PHYSICS HYBRID COMPUTATIONAL FRAMEWORK

This chapter discusses the development of a multi-scale multi-physics (MSMP) hybrid computational framework in view of solving a broad range of dynamic sealing problems. The model is multi-scale because it takes into account mechanics happening at length and time scales ranging several orders of magnitude. It is multi-physics because it takes into account several physical phenomena that are strongly coupled with each other. These include structural mechanics, fluid dynamics, thermal transport, viscoelasticity as well as piezo-electro-mechanical coupling. The framework is termed "hybrid" as it is composed of three different solution methods, namely: 1) finite element method 2) finite volume method and 3) statistical method coupled with Fourier analysis. The development of the MSMP framework starts by taking into consideration the direct application for mechanics of sealing with a time varying rod velocity. The MSMP framework developed in this chapter will be made progressively sophisticated in following chapters by adding ability to handle the phenomena like transience in sealed pressure, dynamic viscoelasticity, thermal transport and piezo-electro-mechanical coupling.

3.1 Overview of the MSMP Framework

Figure 3.1 shows the schematic of a reciprocating single lip U-cup hydraulic rod seal. The sealed fluid lies on one side of the seal while other side of the seal is exposed to atmosphere. The seal has to be "statically tight" and hence is mounted with an interference fit.

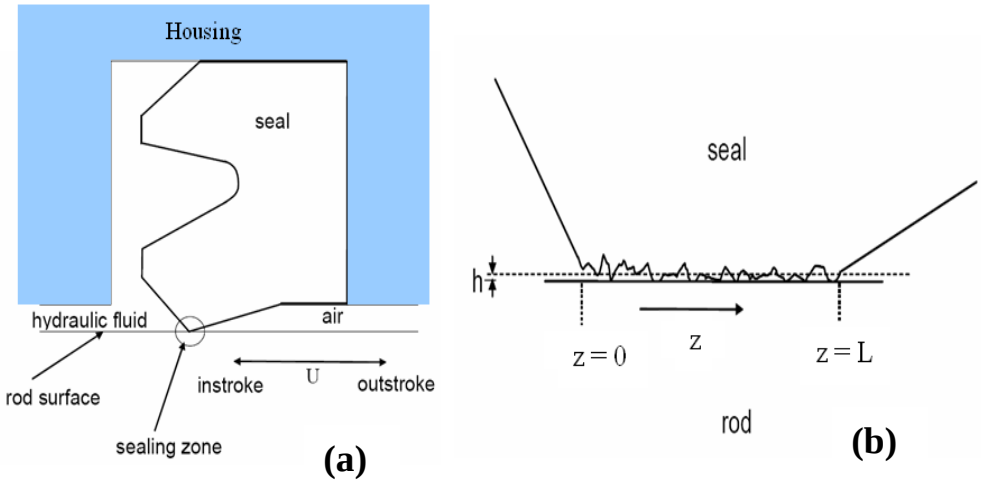

Figure 3.1: (a) Schematic of the mounted seal. (b) Magnified sealing zone.

The region where seal lip appears to meet the rod surface is termed the sealing zone and in encircled in the schematic. A magnified view of this sealing zone is shown in part (b). Since the rod is much smoother than the seal lip due to polishing during the run-in period, the rod is treated as perfectly smooth while the seal lip is treated as rough as shown in the figure. The film thickness 'h' indicated by dotted line varies along the axial direction due to the surface roughness and dynamic boundary deformation and hence needs to be computed dynamically. The RMS roughness of the seal is typically in the 0.5 to 5 μm range, the film thickness is generally in the 0.1-3 μm range while the seal dimensions are typically at the mm level. As discussed in chapter 1, the mechanics of sealing is very multi-physics and multi-scale in nature (see bullet # 1-15 in chapter 1) and the equations governing these effects are highly coupled with each other. In order to capture the detailed physics of dynamic operation of such a seal, we need to construct a MSMP algorithm that can solve all these governing equations in a strongly coupled manner. In an effort to construct such comprehensive MSMP framework, here we start

with a simpler model, get preliminary results and analyze and then add additional complex components to it. The MSMP framework developed is shown in Figure 3.2.

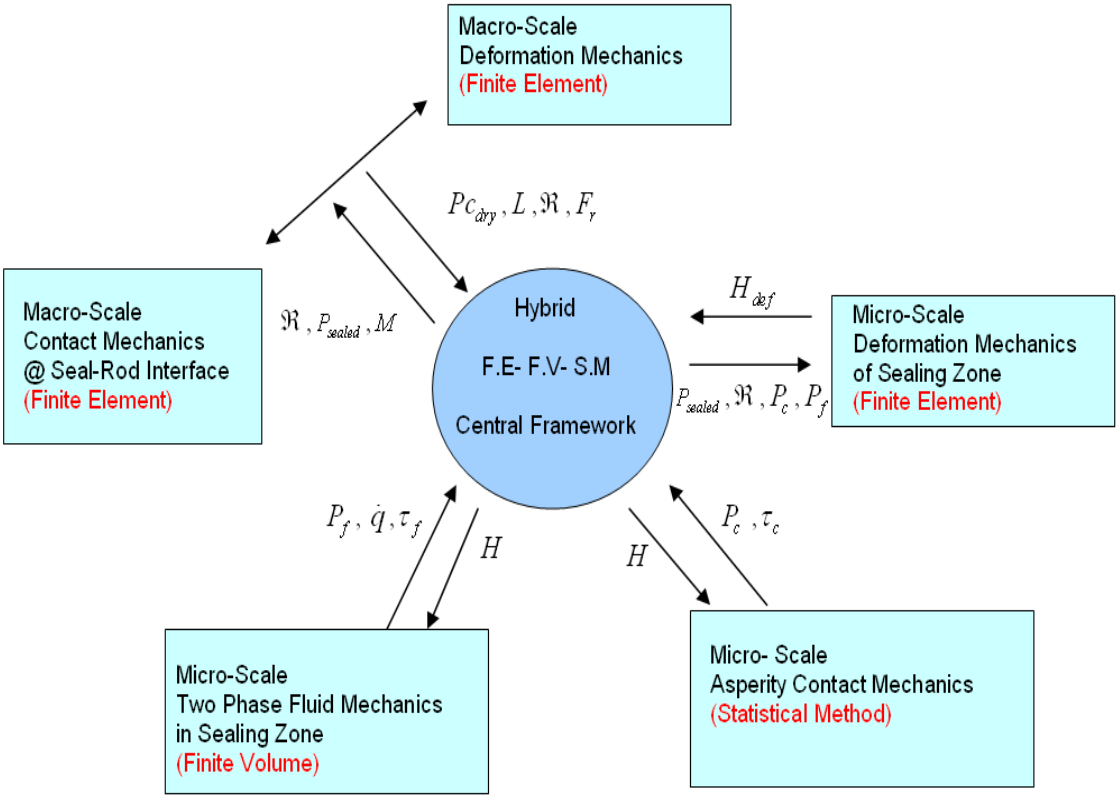

Figure 3.2: Hybrid MSMP computational framework.

The framework is termed "hybrid" because it implements three different types of solution algorithms, thus giving the flexibility to use the highly developed, robust and well-tested solvers for individual component of the framework. Coupling of the fluid and solid continua is achieved through the transfer of information at the fluid-solid interface and a moving mesh algorithm using Arbitrary-Lagrangian-Eulerian method (described in chapter 5) is implemented for handling fluid domain over large structural deformations.

MSMP Seal Model with Transient Rod Velocity

In a typical dynamic operation, both the rod velocity and sealed pressure vary with time. Here we start with only the transience in rod velocity, while keeping sealed pressure at a constant high value. The model consists of macro-scale deformation mechanics of the entire seal body under the action of mounting and application of sealed pressure, macro-scale contact mechanics at the seal-rod interface, micro-scale fluid mechanics of the fluid film in the sealing zone, a micro-scale contact mechanics between the asperities on the rough seal surface and the smooth rod surface, a micro-scale deformation analysis of the sealing edge and an iterative computational procedure coupling all of them together. Let's consider each of these components briefly.

3.2 Macro-Scale Deformation Mechanics

3.2.1 Governing Equations and Boundary Conditions

This module solves the quasi-steady, axisymmetric problem of a linear, perfectly elastic seal deforming under the action of applied load along with the equations defining the contact between the soft seal body and the rigid steel rod. Governing equations and boundary conditions used in this module are listed below.

Equilibrium Equations:

$$\frac{\partial \sigma_{ij}}{\partial x_i} = 0 \tag{3.1}$$

Constitutive Relations:

$$\sigma_{ij} = \frac{E}{1+\nu}\left\{\varepsilon_{ij} + \frac{\nu}{1-2\nu}\varepsilon_{kk}\delta_{ij}\right\} = C_{ijkl}\,\varepsilon_{kl} \tag{3.2}$$

where

$$C_{ijkl} = \frac{E}{2(1+\nu)}\left(\delta_{il}\delta_{jk} + \delta_{ik}\delta_{jl}\right) + \frac{E}{(1+\nu)(1-2\nu)}\delta_{ij}\delta_{kl} \tag{3.3}$$

and δ is the Kronecker delta.

Strain-Displacement relations:

$$\varepsilon_{ij} = \frac{1}{2}\left(\frac{\partial u_i}{\partial x_j} + \frac{\partial u_j}{\partial x_i}\right) \tag{3.4}$$

Boundary Conditions:

$$u_i = u_i^* \text{ on } \partial R_1 \quad \text{and } \sigma_{ij} n_i = T_j^* \text{ on } \partial R_2 \tag{3.5}$$

where u_i^* are the values of the kinematic constraints (mounting interference / constrained axial movement / free movement etc.) specified on the boundaries ∂R_1 respectively and T_j^* are the values of the normal pressure (sealed pressure / atmospheric pressure etc.) and traction specified on the boundaries ∂R_2 respectively.

By defining a kinematically admissible virtual displacement field $\delta u(x)$ and an associated virtual strain field $\delta\varepsilon_{ij} = \frac{1}{2}\left(\frac{\partial \delta u_i}{\partial x_j} + \frac{\partial \delta u_j}{\partial x_i}\right)$, the "weak" form of the governing equations for the displacement field is obtained:

$$\int_R C_{ijkl}\frac{\partial u_k}{\partial x_l}\frac{\partial \delta u_i}{\partial x_j} dV - \int_{\partial R_2} T_i^* \delta u_i dA = 0 \tag{3.6}$$

With this, we can find a displacement field satisfying Eq.(3.6), compute the strains in the seal body from Eq. (3.4) and compute the stress field using Eq. (3.2) and (3.3).

The significance of the "weak form" is that it replaces the derivatives in the partial differential equations of equilibrium with an equivalent integral, which is easier to handle numerically.

3.2.2 Finite Element Solution using Comsol Multiphysics

The integral form of the governing equations given above is solved using the finite element method. The displacement field is discretized using triangular elements. The displacement and virtual displacement field within an element is represented using shape functions $N^a(\mathbf{x})$ as,

$$\begin{aligned} u_i(\mathbf{x}) &= \sum_{a=1}^{n} N^a(\mathbf{x}) u_i{}^a \\ \delta u_i(\mathbf{x}) &= \sum_{a=1}^{n} N^a(\mathbf{x}) \delta u_i{}^a \end{aligned} \tag{3.7}$$

Substituting the interpolated field variables into the virtual work equation, we get

$$\int_R C_{ijkl} \frac{\partial N^b(\mathbf{x})}{\partial x_l} u_k{}^b \frac{\partial N^a(\mathbf{x})}{\partial x_j} \delta u_i{}^a dV - \int_{\partial R_2} T_i^* N^a(\mathbf{x}) \delta u_i{}^a dA = 0 \tag{3.8}$$

where summation on a and b as well as on i, j, k, l is implied.

Since the shape functions are known functions of position, we can write Eq. (3.8) in a matrix form as,

$$\left(K_{a\,ibk}\; u_k{}^b - F_i^a \right) \delta u_i{}^a = 0 \tag{3.9}$$

where

$$K_{aibk} = \text{global stiffness matrix} = \int_R C_{i\,jkl} \frac{\partial N^a(\mathbf{x})}{\partial x_j} \frac{\partial N^b(\mathbf{x})}{\partial x_l} dV$$

$$F_i^a = \text{global force vector} = \int_{\partial_2 R} T_i^* N^a(\mathbf{x})\, dA$$

$K_{a\,ibk}$ is a function of only the elastic properties of the seal, seal geometry, shape functions and nodal position vector. It is therefore a known matrix. Similarly F_i^a is a

function of only the known boundary forces, shape functions and nodal positions and is a known vector. Hence Eq.(3.9) is a system of N linear equations for N unknown nodal displacements.

Here C_{ijkl} and T_i^* are known as defined earlier while the shape functions N^a are defined using Lagrange polynomials. The Lagrange quadratic shape function N^a takes the form as shown in Figure 3.3 in a normalized coordinate system (ξ_1, ξ_2):

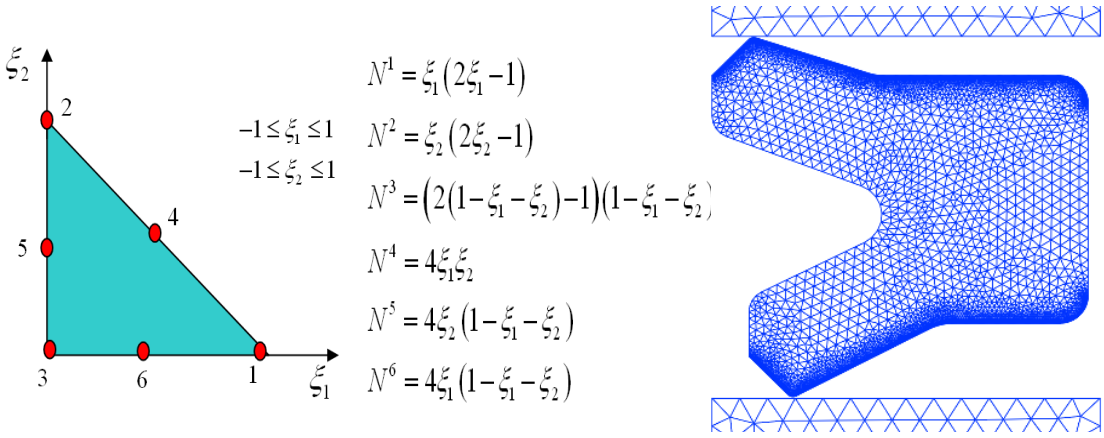

Figure 3.3: Six nodded triangular element (left) and Lagrange quadratic shape functions (center) used for discretizing the computational domain (right).

COMSOL Multiphysics is used to solve these finite element equations. The solution procedure progresses in the following manner:

1. Once the domain is discretized as above, the displacement field and position coordinate inside an element are computed using shape functions:

$$u_i = \sum_{a=1}^{N_e} N^a(\xi_j)\, u_i^a \; ; \qquad x_i = \sum_{a=1}^{N_e} N^a(\xi_j)\, x_i^a$$

2. The element stiffness matrix and load vector of each element m are calculated using

$$K^{m}{}_{aibk} = \int_{V_e^m} C_{ijkl} \frac{\partial N^a(\mathbf{x})}{\partial x_j} \frac{\partial N^b(\mathbf{x})}{\partial x_l} dV \quad ; \quad F_i^{a,m} = \int_{\partial V_e^m} T_i^* N^a(\mathbf{x})\, dA$$

where the shape function derivatives are evaluated as

$$\frac{\partial N^a}{\partial x_j} = \frac{\partial N^a}{\partial \xi_i} \frac{\partial \xi_i}{\partial x_j} \quad \text{and}$$

$$\frac{\partial \xi_j}{\partial x_i} = \left(\frac{\partial x}{\partial \xi} \right)^{-1}_{ji} \quad \text{where} \quad \frac{\partial x_i}{\partial \xi_j} = \frac{\partial}{\partial \xi_j} \left(\sum_{a=1}^{N_e} N^a(\xi) x_i{}^a \right) = \sum_{a=1}^{N_e} \frac{\partial N^a(\xi)}{\partial \xi_j} x_i{}^a$$

3. The volume integrals over each element are calculated using a quadrature formula,

$$\int_{V_e} f(\xi_i) dV_\xi = \sum_{I=1}^{N_I} W_I \, f(\xi_i^I) \quad \text{where } W_I \text{ is a set of integral weights.}$$

4. The "Global Stiffness Matrix" and "Global Load Vector" are then assembled from contributions of individual elements using,

$$K_{aibk} = \sum_{m=1}^{N_m} K^{m}{}_{aibk} \quad ; \quad F_i^a = \sum_{m=1}^{N_m} F_i^{a,m}$$

6. Global stiffness matrix is modified to enforce the prescribed displacement constraints.

7. The system of equations

$$K_{aibk}\, u_k{}^b = F_i^a \qquad \forall\, a,i : \mathrm{x}_k^a \text{ not on } \partial \mathrm{R}_1$$
$$u_i{}^a = u_i^*(\mathrm{x}_i^a) \qquad \forall\, a,i : \mathrm{x}_k^a \text{ on } \partial \mathrm{R}_1$$

is solved for unknown nodal displacements, u_k.

8. Strain and stress distribution as well as other post-processing variables are then calculated using solution for the displacements.

3.2.3 Modeling Near-Incompressible Behavior

The bulk modulus becomes infinite for a fully incompressible material, which leads to an infinite stiffness matrix if we use the standard FE formulation. This phenomenon causes the stiffness matrix for a nearly incompressible material to become ill-conditioned, such that even small round off errors during the computation result in large numerical errors in the solution. This problem can be bypassed if we include the hydrostatic stress distribution as an additional unknown variable. Hydrostatic stress must be computed at the same time as the displacement field. This allows the stiff terms to be removed from the system of FE equations.

To implement this method, a modified version of the principle of virtual work (for small strains) [85] is written as,

$$\int_R S_{ij}\,\delta\varepsilon_{ij}dV_0 + \int_R p\,\delta\varepsilon_{qq}dV_0 + \int_R \delta p\left(\frac{\sigma_{kk}}{3K_b} - \frac{p}{K_b}\right)dV_0 - \int_{\partial_2 R} T_i^*\,\delta u_i dA = 0 \qquad (3.10)$$

where, $S_{ij} = \sigma_{ij} - \dfrac{\sigma_{kk}\delta_{ij}}{3}$ is the deviatoric stress component determined from the displacement filed and $\dfrac{\sigma_{kk}}{3}$ is the hydrostatic stress component determined from the displacement field, which for isotropic, linear, elastic material respectively become:

$$S_{ij} = \mu\left(\delta_{il}\delta_{jk} + \delta_{ik}\delta_{jl} - \frac{2}{3}\delta_{ij}\delta_{kl}\right)\left(\frac{\partial u_k}{\partial x_l}\right); \qquad \frac{\sigma_{kk}}{3} = K_b\left(\frac{\partial u_k}{\partial x_k}\right) = \frac{E}{3(1-2\nu)}\left(\frac{\partial u_k}{\partial x_k}\right)$$

Also, p is the additional degree of freedom representing the unknown hydrostatic stress, δp is the arbitrary variation in the hydrostatic stress and $K_b = \dfrac{1}{3}\dfrac{\partial\sigma_{kk}}{\partial\varepsilon_{pp}}$ is the bulk modulus of the material.

Eq.(3.10) states that if the virtual work equation is satisfied for all kinematically admissible variations in displacement, in strain and in δp, then the pressure variable p will be equal to the hydrostatic stress in the solid. With this formulation the pressure being an independent variable, is also interpolated as : $p(\mathbf{x}) = \sum_{a=1}^{N_p} M^a(\mathbf{x}) p^a$, where M^a are a set of shape functions for the pressure. The Lagrange polynomial used for interpolating pressure field is an order of magnitude less than that used for the displacement. Following the methodology as described by [85], the linear elasticity equations and F.E. shape functions can now be substituted into the new virtual work principle. This leads to the following system of equations which needs to be solved for unknown displacement $u_k{}^b$ and pressure p^b,

$$\begin{aligned} &K_{aibk} u_k{}^b + Q_{aib} p^b = F_i^a \qquad \forall a,i : \mathrm{x}_k^a \text{ not on } \partial \mathrm{R}_1 \\ &Q_{akb} u_k{}^b - \tilde{P}_{ab} p^b = 0 \\ &u_i{}^a = u_i^* \left(x_i{}^a \right) \qquad \forall a,i : \mathrm{x}_k^a \text{ on } \partial \mathrm{R}_1 \end{aligned} \tag{3.11}$$

Here the global stiffness matrices $K, Q, \tilde{P}$ are obtained by summing the following element stiffness matrices,

$$K^m{}_{aibk} = \int_{V_e} C_{ijkl} \frac{\partial N^a(\mathbf{x})}{\partial x_j} \frac{\partial N^b(\mathbf{x})}{\partial x_l} - K_b \frac{\partial N^a(\mathbf{x})}{\partial x_i} \frac{\partial N^b(\mathbf{x})}{\partial x_k} dV$$

$$q^m{}_{aib} = \int_{V_e} \frac{\partial N^a(\mathbf{x})}{\partial x_i} M^b(\mathbf{x}) dV$$

$$\tilde{p}^m_{ab} = \int_{V_e} \frac{1}{K} M^a(\mathbf{x}) M^b(\mathbf{x}) \, dV$$

3.3 Macro-Scale Contact Mechanics

The contact mechanics at the seal-rod interface and the seal-housing interface are solved using augmented Lagrangian method of Comsol Multiphysics. Here, an augmentation component is introduced for the dry contact pressure P_{dc}. Displacements variables are solved separately from the contact pressure variable and the procedure is repeated until the convergence criterion is met. Comsol contact solver defines a contact map operator $\tilde{C}$ and a gap distance variable g and for each slave point of interest a corresponding master point is searched in the direction normal to the slave boundary as shown in . If $Expr$ is an expression evaluated on the slave boundary, then $\tilde{C}(Expr)$ will be the value of $Expr$ at a corresponding master point.

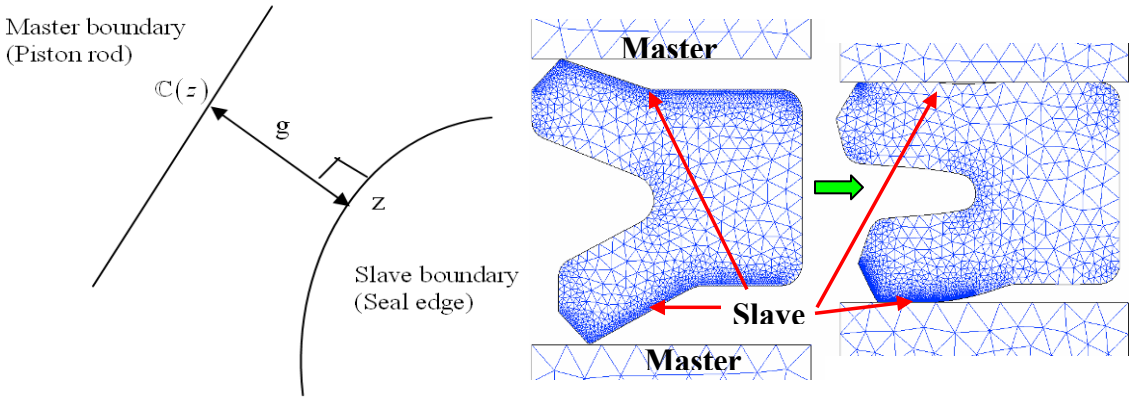

Figure 3.4: Contact mapping between the seal (slave) boundary and the rod (master) boundary.

As the boundaries approach each another, master point converges to the closest point as the gap distance goes to zero. The penalized contact pressure $P_{dc,p}$ is defined on the slave boundary as:

$$P_{dc,p} = \begin{cases} P_{dc} - p_n g & \text{if } g \le 0 \\ P_{dc}\, e^{-\frac{p_n g}{P_{dc}}} & \text{if } g > 0 \end{cases} \tag{3.12}$$

where p_n is the normal penalty factor for contact. Contact solver also defines the Penalized friction traction $T_{f,p}$ on the slave boundary [86] as,

$$T_{f,p} = \Theta\left(\frac{\mu P_{dc,p}}{\left| T_f - p_t \tilde{C}(\mathbf{F})\left(\tilde{C}(\mathbf{x}) - \tilde{C}(\mathbf{x})_{prev}\right)\right|}, 1 \right)\left(T_f - p_t \tilde{C}(\mathbf{F})\left(\tilde{C}(\mathbf{x}) - \tilde{C}(\mathbf{x})_{prev}\right)\right) \tag{3.13}$$

where, Θ = minimum operator, μ = friction coeff., p_t = traction penalty,

T_f = friction traction, $\tilde{C}(\mathbf{x})_{prev}$ = previous map of **x**, **F** = deformation gradient tensor

The contact interaction adds integral of the component $\left(P_{dc,p}\,\delta g + T_{f,p}\,\tilde{C}(\mathbf{F})\,\delta\tilde{C}(\mathbf{x})\right)$ to the weak form of the original governing equations described in previous section.

3.4 Micro-Scale Fluid Mechanics

3.4.1 Reynold's Equation

In this section, the equations governing the fluid mechanics in the micro-scale sealing zone are developed. The assumptions from lubrication theory that underlie the development of these equations are:

1) Body forces in the fluid column are neglected. 2) Since the fluid film thickness is typically of the order of micrometer and sealing zone length is typically of the order of millimeter, the pressure can be assumed to be constant throughout the thickness of the fluid film. 3) The curvature of the surfaces is large compared with film thickness.

4) There is no slip at the boundaries 5) Fluid is assumed to be Newtonian. 6) Since the characteristic dimension is very small and magnitudes of velocities are not high enough,

the flow can be assumed laminar. 7) Fluid inertia is neglected. 8) Fluid is assumed incompressible.

Now consider a column of fluid of dimensions $dx,\ dy$ and thickness h. Let the flow rates per unit width along x and y directions be q_x and q_y. If the floor of the fluid column moves upward with a velocity w_0 and roof moves upwards with a velocity w_h, then the continuity equation reduces to,

$$\frac{\partial \rho q_x}{\partial x} + \frac{\partial \rho q_y}{\partial y} + \frac{d\left(\rho h\right)}{dt} = 0 \tag{3.14}$$

Also, the force balance on the fluid column gives,

$$\begin{aligned} \frac{\partial p}{\partial x} &= \frac{\partial \tau_x}{\partial z} = \frac{\partial}{\partial z}\left(\mu \frac{\partial u}{\partial z}\right) \\ \frac{\partial p}{\partial y} &= \frac{\partial \tau_y}{\partial z} = \frac{\partial}{\partial z}\left(\mu \frac{\partial v}{\partial z}\right) \end{aligned} \tag{3.15}$$

where τ is the shear stress, μ is the fluid viscosity and u, v are local fluid velocities in x and y directions. Integrating above equations and applying boundary conditions of velocities U_1, U_2 at the surfaces, we can deduce the flow rate as,

$$\begin{aligned} q_x &= \int_0^h u\, dz = \frac{-h^3}{12\,\mu}\frac{\partial p}{\partial x} + \left(U_1 + U_2\right)\frac{h}{2} \\ q_y &= \int_0^h v\, dz = \frac{-h^3}{12\,\mu}\frac{\partial p}{\partial y} \end{aligned}$$

Substituting these equations into Eq. (3.14), writing U for $\left(U_1 + U_2\right)$ and neglecting density variation with time as per our assumptions, we get 2D Reynold's equation:

$$\frac{\partial}{\partial x}\left(\frac{\rho h^3}{\mu}\frac{\partial p}{\partial x}\right) + \frac{\partial}{\partial y}\left(\frac{\rho h^3}{\mu}\frac{\partial p}{\partial y}\right) = 6\left\{ U\frac{\partial \rho h}{\partial x} + 2\rho\frac{dh}{dt} \right\} \tag{3.16}$$

3.4.2 Taking Cavitation into Account

In the regions where Eq.(3.16) yields pressures below the cavitation pressure, p_{cav} , the fluid forms striations and both liquid and vapor are present at a uniform pressure of p_{cav} [61]. Figure 3.5 (left) shows the schematic of a fluid control volume with striated cavitation regions. Such cavitation phenomenon is well described by Jakobsson-Floberg-Olsson (JFO) theory [62]. In such cavitation regions, following boundary conditions must be satisfied [61]:

$$\frac{\partial p}{\partial n} = 0 \qquad \text{at the locus of film rupture}$$

and

$$\frac{h^3}{12\mu}\frac{\partial p}{\partial n} = \frac{V_n}{2}\left(1-\frac{\rho}{\rho_c}\right) \qquad \text{at the locus of film reformation}$$

Where V_n is the component of the velocity in the direction $\hat{n}$, normal to the cavitation boundary. Above equations express the conservation of mass at the two internal boundaries. In the liquid region, density ρ does not change appreciably and can be taken as constant at ρ_f, while in the cavitation region, ρ_e represents average density of two phase fluid. Mass must be conserved in the full film and cavitation regions as well as at the boundaries of the cavitation zones. Our objectives are to obtain the pressure distribution in the liquid region, to define the boundaries of the cavitation zone and to calculate the density distribution in the cavitation zone.

Elrod [62] and Payvar-Salant [63] have developed algorithms in which JFO conditions are met using a "universal Reynolds equation". Payvar-Salant introduced a variable Φ which has different definitions in liquid and cavitation regions and a cavitation index F such that,

$$\frac{p - p_{cav}}{P_{ref} - P_{cav}} = F\Phi \quad \text{and} \qquad \hat{\rho} = \frac{\rho_e}{\rho_f} = 1 + (1 - F)\Phi$$

In the full-film region this gives,

$$\hat{p} = \frac{p - p_{cav}}{P_{ref} - P_{cav}} = F\Phi \;\; ; \;\; F = 1 \;\; ; \;\; \hat{\rho} = \frac{\rho_e}{\rho_f} = 1 \tag{3.17}$$

and in the cavitation region,

$$\hat{p} = \frac{p - p_{cav}}{P_{ref} - P_{cav}} = 0 \;\; ; \;\; F = 0 \;\; ; \;\; \hat{\rho} = \frac{\rho_e}{\rho_f} = 1 + \Phi \tag{3.18}$$

Hence in the liquid region Φ represents dimensionless pressure while in the cavitation region Φ is related to the dimensionless equivalent density.

3.4.3 Taking Surface Roughness into Consideration

Local hydrodynamic pressure in a flow between rough surfaces is statistical in nature due to random nature of the film thickness arising from surface roughness distribution. Since most of the times, the mean pressure level is of interest , several past studies had concentrated on predicting such mean pressure without solving for random local pressure. While incorporating the experimentally observed random roughness pattern into the deterministic models would make them more realistic, their numerical solution becomes impractical due to intractable number of asperities. In this work, Patir-Cheng "flow-factor" method [59-60] is used to obtain the "average" Reynolds equation as part of a comprehensive micro-scale fluid flow model.

Figure 3.5 (right) shows the fluid film between 2 rough surfaces. The possibility of mixed lubrication is taken into account, i.e. $(h/\sigma) < 3$, where h is the nominal film thickness (distance between mean levels of the two surfaces). Also shown is the

truncated (local) film thickness $h_T = h + \delta_1 + \delta_2$, where δ_1, δ_2 are the random heights of the two surfaces defined from the mean levels of the surfaces. They are assumed to have Gaussian distribution of heights with zero mean and σ_1, σ_2 as the standard deviations. The combined roughness $\delta = \delta_1 + \delta_2$ has a variance $\sigma^2 = \sigma_1^{\,2} + \sigma_2^{\,2}$. The average truncated film thickness is defined as,

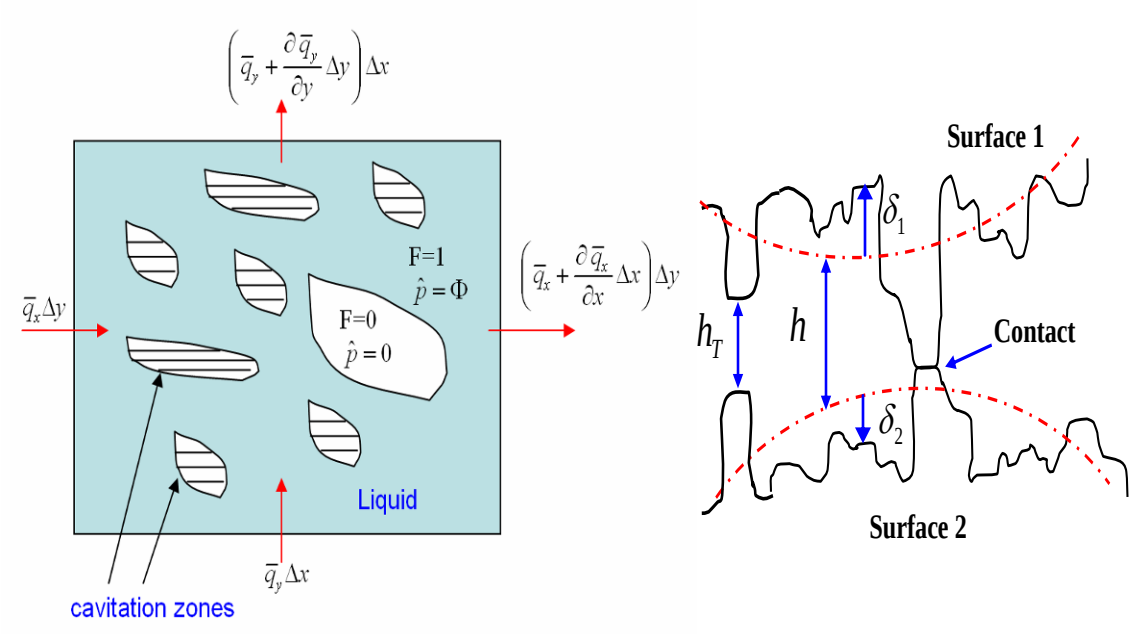

Figure 3.5: Micro-scale fluid flow model. Fluid control volume showing cavitation zones (left) and definition of local film thickness between rough surfaces (right).

$$\bar{h}_T = \int_{-h}^{\infty} (h + \delta)\, f(\delta)\, d\delta$$

where $f(\delta)$ is the probability density function of δ. With this statistical representation of surface roughness, now the mean (expected) unit flows entering the control volume of Figure 3.5 (left) are given by,

$$\bar{q}_x = \frac{1}{\Delta y}\int_{y}^{y+\Delta y} q_x\, dy \overset{Let}{=} -\phi_{xx}\left(\frac{h^3}{12\mu}\frac{\partial \bar{p}}{\partial x}\right) + \frac{U_1+U_2}{2}\bar{h}_T + \frac{U_1-U_2}{2}\sigma\phi_{scx}$$

$$\bar{q}_y = \frac{1}{\Delta x}\int_{x}^{x+\Delta x} q_y\, dx \overset{Let}{=} -\phi_{yy}\left(\frac{h^3}{12\mu}\frac{\partial \bar{p}}{\partial y}\right) \tag{3.19}$$

where $\bar{p}$ is the mean (expected) pressure. Here ϕ_{xx} and ϕ_{yy} are the pressure flow factors that when multiplied with, would give us same mean flow rate using a smooth surface model as that would be obtained with a deterministic solution of a rough surface flow model. These pressure flow factors reflect the impedance of flow due to roughness flow is driven by a macro-scale pressure gradient. The factor ϕ_{scx} accounts for the additional flow transport due to micro-scale pressure gradient developed by sliding between rough surfaces. With these modifications to the flow rate terms and assuming constant density, Eq. (3.16) for Reynolds equation becomes,

$$\frac{\partial}{\partial x}\left(\phi_{xx}\frac{h^3}{\mu}\frac{\partial \bar{p}}{\partial x}\right) + \frac{\partial}{\partial y}\left(\phi_{yy}\frac{h^3}{\mu}\frac{\partial \bar{p}}{\partial y}\right) = 6\left(U_1+U_2\right)\frac{\partial h_T}{\partial x} + 6\sigma\left(U_1-U_2\right)\frac{\partial \phi_{scx}}{\partial x} + 12\frac{dh_T}{dt} \tag{3.20}$$

Now, looking at Figure 3.1 of our current sealing application and noting that the seal is axisymmetric and the film thickness is much smaller than the seal radius (h/R is typically of the order of 10^{-5}), the flow in the micro-scale sealing zone can be approximated as one-dimensional in a Cartesian coordinate system. With this approximation the second term on left side of Eq. (3.20) drops out and it becomes,

$$\frac{\partial}{\partial x}\left(\phi_{xx}\frac{h^3}{\mu}\frac{\partial \bar{p}}{\partial x}\right) = 6\left(U_1+U_2\right)\frac{\partial h_T}{\partial x} + 6\sigma\left(U_1-U_2\right)\frac{\partial \phi_{scx}}{\partial x} + 12\frac{dh_T}{dt} \tag{3.21}$$

Eq. (3.21) is the form of Reynolds equation which takes surface roughness effects into account (but no cavitation). Modifications of Reynolds equation for accounting cavitation is already discusses earlier.

3.4.4 Comprehensive Reynolds Equation for MSMP

Substituting the cavitation modifications described in sections 3.4.2 into the roughness-accounted form of Reynolds equation, Eq. (3.21) and after using following non-dimensionalization of variables,

$$\hat{x} = \frac{x}{L},\ \ P = \frac{p}{p_a} = F\Phi,\ \ \hat{\rho} = \frac{\rho_e}{\rho_f} = 1 + (1-F)\Phi,\ \ H = \frac{h}{\sigma},\ \ \hat{t} = \frac{t}{t_{ref}}$$

we get,

$$\begin{aligned} \frac{\partial}{\partial \hat{x}}\left(\phi_{xx} H^3 e^{-\hat{\alpha} F\Phi} \frac{\partial}{\partial \hat{x}}(F\Phi) \right) = \ & 6\zeta \frac{\partial}{\partial \hat{x}}\left(\left\{ 1 + (1-F)\Phi \right\} \left\{ H_T + \phi_{s.c.x} \right\} \right) \\ & + 12\tilde{\varepsilon} \frac{\partial}{\partial \hat{t}}\left(\left\{ 1 + (1-F)\Phi \right\} H_T \right) \end{aligned} \tag{3.22}$$

where σ is the RMS roughness of the seal surface, $\zeta = \mu_0 UL / p_a \sigma^2$ is the dimensionless rod velocity, $\hat{\alpha} = \alpha p_a$ is the dimensionless pressure-viscosity coefficient, $\tilde{\varepsilon} = \mu_0 L^2 / \left(\sigma^2 p_a t_{ref} \right)$ is the dimensionless squeeze term coefficient and H_T is the average truncated film thickness (defined below). Eq. (3.22) is the final form of modified Reynolds equation that is used for modeling the micro-scale fluid mechanics of the current MSMP framework.

Now, in the liquid region,

$$\Phi \geq 0,\ \ F = 1 \text{ and } P = \Phi \tag{3.23}$$

and in the cavitated region,

$$\Phi < 0,\ F = 0,\ P = 0 \text{ and } \hat{\rho} = 1 + \Phi \tag{3.24}$$

The boundary conditions for the modified Reynolds equation are,

$$\begin{aligned} P &= P_{sealed} \text{ at } \hat{x} = 0 \\ P &= 1 \qquad \text{at } \hat{x} = 1 \end{aligned} \tag{3.25}$$

The average truncated film thickness is given by,

$$H_T = \int_{-H}^{\infty} (H + \delta) f(\delta) d\delta \tag{3.26}$$

In the model, a Gaussian distribution for surface heights is assumed, yielding,

$$H_T = \frac{H}{2} + \frac{H}{2} erf\left[\frac{H}{\sqrt{2}}\right] + \frac{1}{\sqrt{2\pi}} e^{-H^2/2} \tag{3.27}$$

Equations (3.22), (3.23), (3.24) along with boundary condition Eq.(3.25) are solved for Φ and F at each time step numerically with a finite volume formulation and the tri-diagonal matrix algorithm (TDMA) as described in section 3.7.2 . This yields the fluid pressure distribution and location of cavitation regions in the sealing zone at each time step.

Pressure Flow Factors:

Patir and Cheng [59-60] have developed a method to obtain the flow factors ϕ_{xx}, ϕ_{yy} using numerical simulation. They performed a series of numerical experiments in which the Reynolds equation containing the local film thickness was solved for a variety of randomly generated roughness patterns. They apply an arbitrary pressure gradient across boundaries of a rectangular fluid control volume of nominal film thickness “h” as the height. This control volume accommodates a large number of asperities of specific aspect ratios. They solve for pressure driven flow and compare this solution with that

obtained for fluid volume without any asperities. From this comparison and using Eq. (3.19), ϕ_{xx} and ϕ_{yy} are obtained as a function of h/σ. The values of flow factors obtained with different but statistically identical rough surfaces are used to get an ensemble average of flow factor for that particular h/σ.

For an isotropic surface roughness, there is no preferred orientation (i.e. statistical properties are same along any direction) and hence ϕ_{xx} and ϕ_{yy} are equal. It is observed that ϕ_{xx} is close to 1 for $h/\sigma > 6$ and average Reynolds equation for a rough surface becomes same as that for a smooth surface at these values of h/σ. However in "mixed lubrication" $h/\sigma < 3$ and asperities start interacting with each other and form barriers to flow resulting in sharp decrease in Poiseuille flow and hence in ϕ_{xx}. For such isotropic roughness, flow factor variation can be fitted using following equation:

$$\phi_{xx} = 1 - 0.9e^{-0.56H}$$

where $H = h/\sigma$.

Flow factors for surfaces with Directional Patterns:

Many seal surfaces show directional pattern resulting from different manufacturing processes or because of "running-in". These directional patterns are mostly in longitudinal or transverse directions. The aspect ratio for asperities in such directional rough surfaces can be described using parameter "γ" such that $\gamma > 1$ for asperities having larger correlation lengths in longitudinal asperities and $\gamma < 1$ for those in the transverse direction. Now, the flow field around the asperities with different $\gamma's$ will be different and it will generate difference in fluid pressure distributions and hence

flow rates. This in turn will produce variation in flow factors. This is elaborated using a numerical simulation of fluid flow around asperities of different aspect ratio. The velocity field obtained from this numerical solution is shown in Figure 3.6. Figure 3.7 shows the corresponding streamline plots of the velocity field around these asperities. In both these figures, (a) shows the longitudinal directionality of asperities ($\gamma > 1$); (b) shows isotropic surface ($\gamma = 1$) and (c) shows the transversely oriented asperities ($\gamma < 1$). The fluid has a density of 890 kg/m^3 and dynamic viscosity of 0.05 $Pa-s$ which similar to that of a typical fluid in a rod seal application. In all the plots, the incoming flow velocity has the same mean value of 0.5 m/s and hence same incoming "main" flow rate. Observing the magnitudes of velocities in the constriction regions for (a) through (c), it can be seen that the asperities with $\gamma > 1$ has the lowest increase in the side flow around asperities. Side flow progressively increases for $\gamma = 1$ and becomes highest for $\gamma < 1$. The increased side flow for $\gamma = 1$ and $\gamma < 1$ increases the resistance to the main flow. The variation of local flow pattern becomes clearer by looking at the streamlines as for $\gamma < 1$ even some vortices are formed between two asperities.

The sensitivity of ϕ_{xx} on γ in the mixed lubrication regime can be explained by considering that the asperity contact areas with $\gamma > 1$ offer little resistance to the pressure flow and hence permit only a small side flows. A decrease in γ results in smaller valley lengths and increases the side flow. This in turn decreases the main flow and hence reduces ϕ_{xx}. When the roughness is isotropic ($\gamma = 1$), the resistance to main flow increases, which in turn results in $\phi_{xx} < 1$. For roughness with $\gamma < 1$, the side flow and the resistance to the main flow is increased further.

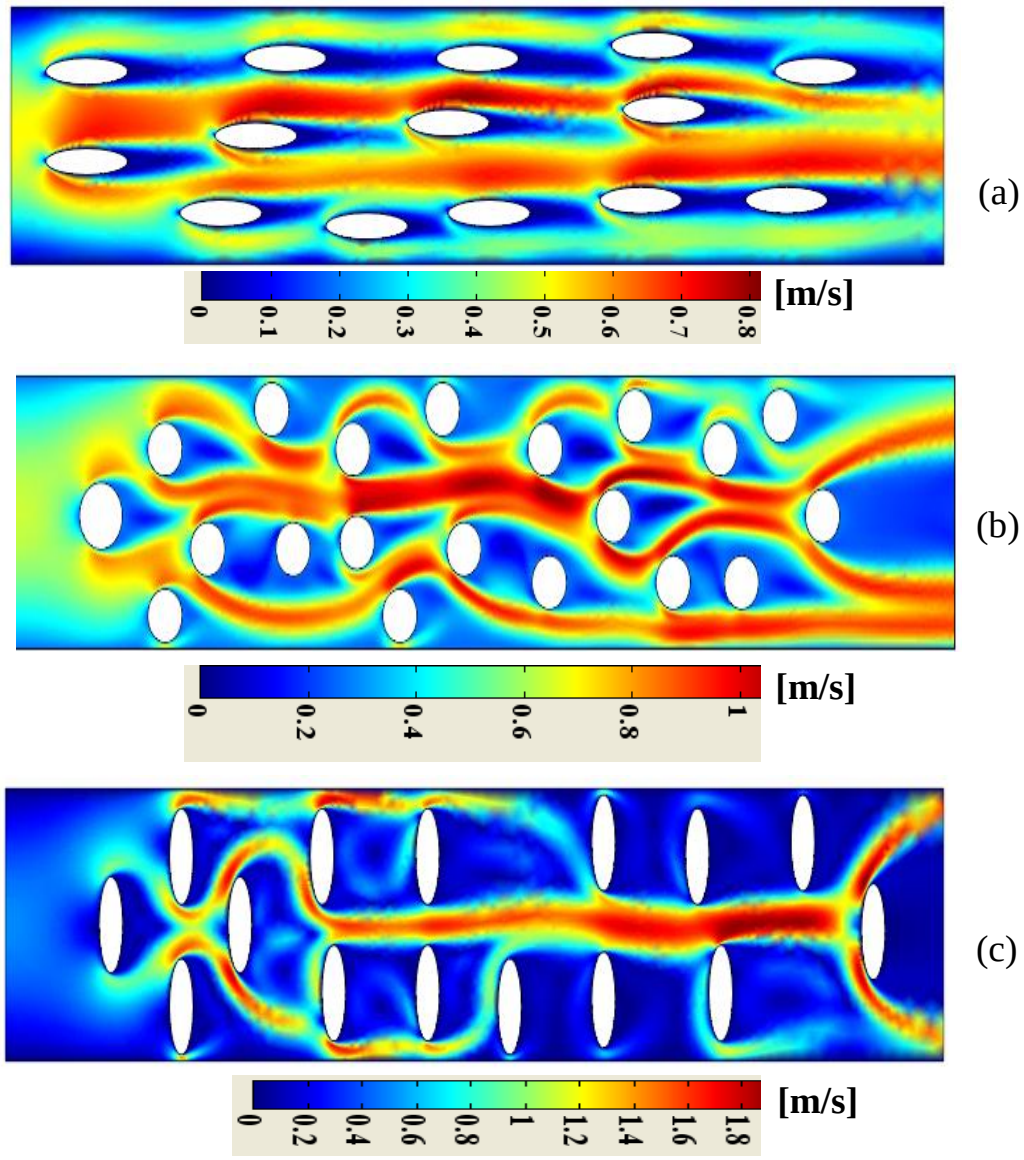

Figure 3.6: **Velocity field obtained from a numerical simulation of flow around asperities of different aspect ratios: (a) longitudinal $\gamma > 1$ (b) isotropic $\gamma = 1$ (c) Transverse $\gamma < 1$.**

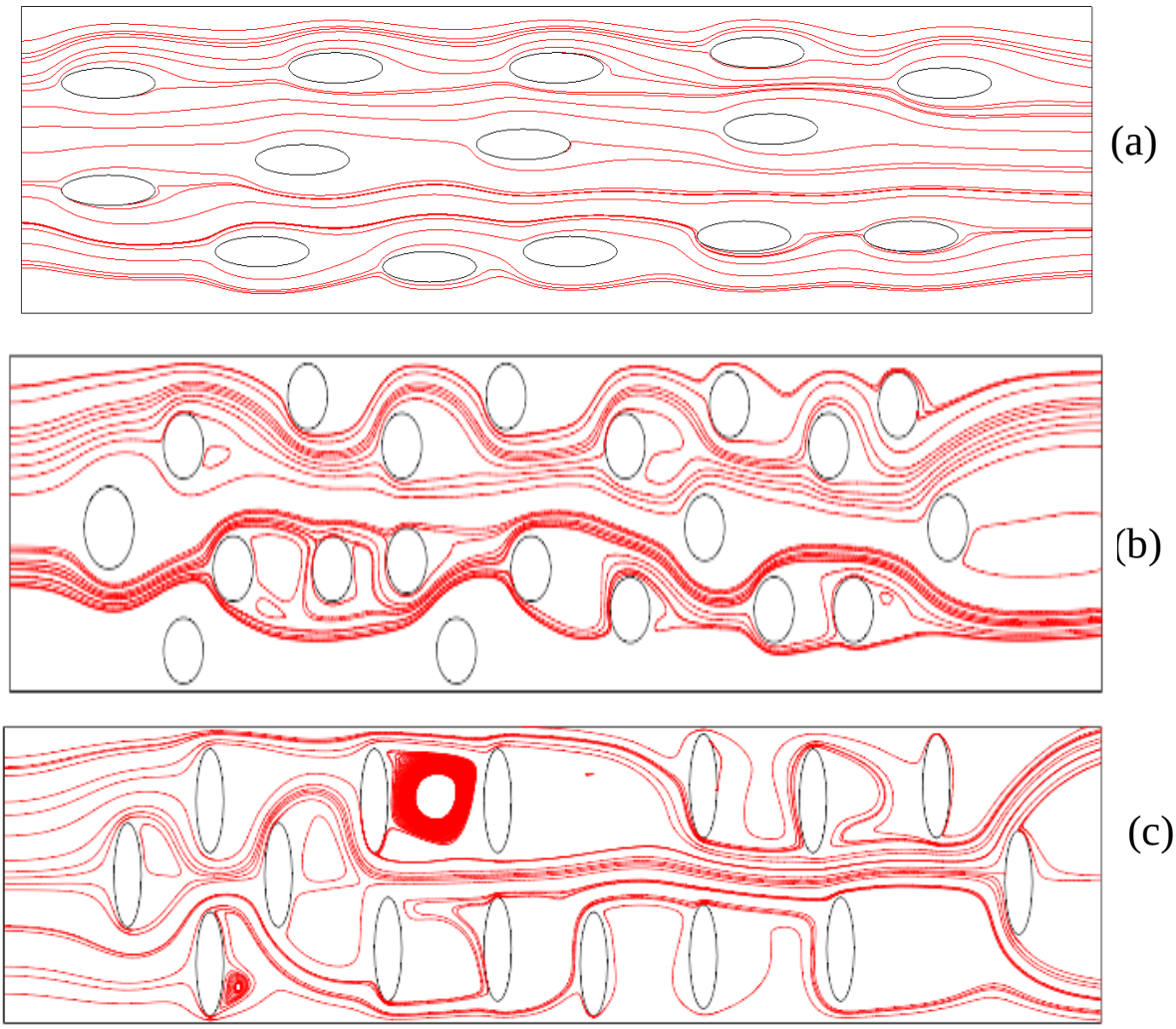

Figure 3.7: Streamlines showing velocity field obtained from the numerical simulation of flow around asperities of different aspect ratio: (a) longitudinal $\gamma > 1$ (b) isotropic $\gamma = 1$ (c) Transverse $\gamma < 1$.

Patir and Cheng [59-60] have conducted similar numerical simulations but for a large number of values of γ and h/σ. Based on their findings, the values for ϕ_{xx} to be used in the current MSMP fluid mechanics model are calculated using Eq.(3.28).

$$\phi_{xx} = \begin{cases} 1 - C\,e^{-RH} & \text{for } \gamma \le 1 \\ 1 + C\,H^{-R} & \text{for } \gamma > 1 \end{cases} \tag{3.28}$$

where constants C and R depend on γ and are given in Table 3.1.

Shear Flow Factors:

It was mentioned earlier that the shear flow factor takes into account additional fluid transport due to sliding of rough surfaces and hence can be given as,

$$\phi_{scx} = \frac{2}{U_s \sigma} \int_0^{L_y} \int_0^{L_x} \left(-\frac{h^3}{12\mu} \frac{\partial p}{\partial x} \right) dx\, dy \tag{3.29}$$

Similar to pressure flow factor, ϕ_{scx} is also a function of film thickness and roughness parameters. It also depends on the orientation parameter γ of the asperities. It should be noted that Eq. (3.29) gives the value of ϕ_{scx} for a given set of rough surfaces. In order to get an "expectancy" of ϕ_{scx} over possible roughness configurations, the same problem needs to be solved a number of times with different but statistically identical rough surfaces. Patir and Cheng [59-60] have conducted such numerical simulations and curves are fitted to extract analytical expressions for shear flow factors as functions of film thickness and aspect ratio. Eq. (3.30) gives the relations for calculating ϕ_{scx} based on instantaneous film thickness values that are used in the current micro-scale fluid mechanics model of the MSMP framework.

$$\phi_{scx} = \begin{cases} A_1 H^{\alpha_1} e^{-\alpha_2 H + \alpha_3 H^2} & \text{for } H \le 5 \\ A_2 e^{-0.25H} & \text{for } H > 5 \end{cases} \tag{3.30}$$

where the values of constants A_1, A_2, α_1, α_2 and α_3 also depend on the asperity orientation parameter γ and are tabulated in Table 3.1.

Table 3.1: Coefficients used for calculating pressure flow factors and shear flow factors

γ	C	R	A_1	A_2	α_1	α_2	α_3
1/9	1.480	0.42	2.046	1.856	1.12	0.78	0.03
1/6	1.380	0.42	1.962	1.754	1.08	0.77	0.03
1/3	1.180	0.42	1.858	1.561	1.01	0.76	0.03
1	0.900	0.56	1.899	1.126	0.98	0.92	0.05
3	0.225	1.5	1.560	0.556	0.85	1.13	0.08
6	0.520	1.5	1.290	0.388	0.62	1.09	0.08
9	0.870	1.5	1.011	0.295	0.54	1.07	0.08

3.5 Micro-Scale Contact Mechanics

In the mixed lubrication regime, significant contact between asperities of the rough seal surfaces and the rod surface can occur. This generates the contact pressures in these micro-scale contact zones which need to be added to the hydrodynamic pressures in the fluid film (calculated in the previous section) for computing the radial deformations of sealing edge and hence the film thickness. As discussed in chapter 2, several studies have been performed to characterize the contact between rough surfaces. For the current MSMP framework the Greenwood - Williamson model [51] is adapted which analyzes the contact of a rough surface with a plane.

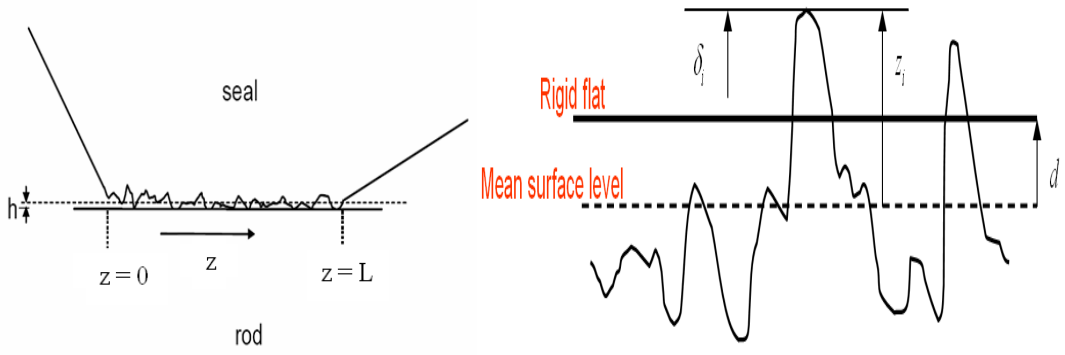

Figure 3.8: Contact of a rough seal surface with a flat rod surface.

Consider the contact between a relatively flat rod surface and a rough seal surface covered with a large number of asperities as shown in Figure 3.8. At least near their summits, the asperities are assumed spherical. It is also assumed that all asperity summits have the same radius R , and that their heights have follow a random distribution with a probability density function $\psi(z)$. Then the probability that a particular asperity has a height between $z \text{and} \, z+dz$ above some reference plane can be given by $\psi(z)\,dz$. From Hertzian theory, the contact area A_i, and load P_i can be expressed in terms of the compliance (the distance which points outside the deforming zone move together during the deformation) δ_i as

$$A_i = \pi R\delta \;\; ; \quad F_i = \frac{4}{3}\frac{E}{(1-\upsilon^2)} R^{1/2}\delta^{3/2}$$

If the two surfaces come together until their reference planes are separated by a distance d, then there will be contact at any asperity for which $z > d$. Thus, the probability of making contact at any given asperity, of height z , is

$$\text{Prob}(z > d(t)) = \int_d^\infty \psi(z)dz$$

with this, the total area of contact for N asperities can be given by,

$$A = \pi NR\int_d^\infty (z-d)\cdot\psi(z)dz = \pi\eta AR\int_d^\infty (z-d)\cdot\psi(z)dz \qquad (3.31)$$

where η is the asperity density (number of asperities per unit area). Similarly, expected total load for all N asperities is,

$$F = \frac{4}{3}\eta A \frac{E}{(1-\upsilon^2)} R^{1/2} \int_d^\infty (z-d)^{3/2} \cdot \psi(z)\, dz \tag{3.32}$$

From the above equations, after normalizing the separation between reference planes with respect to the standard deviation of the asperity heights ($H(\tau) = d(\tau)/\sigma$) and replacing $\psi(z)$ by standardized height distribution $\tilde{\psi}(s)$ such that $\tilde{\psi}(s)$ has standard deviation of unity ($\tilde{\sigma} = 1$), we get micro-scale contact pressure as,

$$p_c = \eta \frac{4}{3} \frac{E}{(1-\upsilon^2)} R^{1/2} \sigma^{3/2} \int_{H(t)}^\infty (s-H)^{3/2}\ \tilde{\psi}(s)\, ds \tag{3.33}$$

Assuming Gaussian distribution of asperity heights with zero mean,

$$\tilde{\psi}(s) = \frac{1}{\tilde{\sigma}\sqrt{2\pi}} e^{-\frac{s^2}{2\tilde{\sigma}^2}} = \frac{1}{\sqrt{2\pi}} e^{-\frac{s^2}{2}} \quad (\text{since } \tilde{\sigma} = 1 \text{ as shown earlier})$$

we get,

$$p_c = \eta \frac{4}{3} \frac{E}{(1-\upsilon^2)} R^{1/2} \sigma^{3/2} \frac{1}{\sqrt{2\pi}} \int_H^\infty (s-H)^{3/2}\ e^{-s^2/2}\, ds$$

Now using normalizations: $P_c = \frac{p_c}{E}$; $\hat{\sigma} = \sigma R^{1/3} \eta^{2/3}$, we get the following dimensionless form of micro-scale contact pressure:

$$P_c = \frac{4}{3} \frac{1}{(1-\nu^2)} \hat{\sigma}^{3/2} \frac{1}{\sqrt{2\pi}} \int_H^\infty (z-H)^{3/2}\, e^{-z^2/2} dz \tag{3.34}$$

Eq. (3.34) is used in the micro-scale contact mechanics module of the MSMP algorithm. The integral in Eq.(3.34) is evaluated numerically using the Adaptive Gauss-Kronrod quadrature.

3.6 Micro-Scale Deformation Mechanics

To compute the film thickness distribution, it is necessary to compute the radial deformation of the sealing element. In discretized form with *n* axial nodes across the sealing zone, the film thickness at the i^{th} node can be expressed as,

$$H_i = H_d + \left(H_{def}\right)_i \tag{3.35}$$

where $\left(H_{def}\right)_i$ is the deformation of the seal edge under the combined action of the sealed pressure, fluid pressure and contact pressure. The procedure for calculating this deformation is described below.

The dry film thickness, H_d, is the gap height under dry contact conditions (in the absence of fluid pressure in the sealing zone). It is computed by equating the dry contact pressure obtained from the macro-scale deformation & contact analysis (described in sections 3.2 & 3.3) of the smooth seal surface under pressurized conditions, P_{dc}, with the contact pressure distribution computed from Eq.(3.34) under dry conditions. Using regression to invert Eq. (3.34) yields,

$$H_d = \mathrm{a} + \mathrm{b}\cdot\log(\mathrm{z}) + \mathrm{c}\cdot(\log(\mathrm{z}))^2 + \mathrm{d}\cdot(\log(\mathrm{z}))^3 + \mathrm{e}\cdot(\log(\mathrm{z}))^4 + \mathrm{f}\cdot(\log(\mathrm{z}))^5 \tag{3.36}$$

where $\mathrm{z} = -\log_{10}\left|\,\mathrm{I}\,\right|$, $\mathrm{I} = \dfrac{\mathrm{P_{dc}}}{\dfrac{4}{3}\dfrac{1}{\left(1-\nu^2\right)}\hat{\sigma}^{3/2}}$ and

a = 0.86197, b = 1.16979, c = 0.34673, d = 3.57134, e = 1.07985, f = 1.68629

To compute the film thickness distribution at each time step, it is necessary to calculate the radial deformation of the sealing element under the combined action of the sealed pressure, the fluid pressure in the sealing zone and the contact pressure at the

given time step. Having obtained the fluid pressure distribution from the solution of Eq. (3.22) and the micro-scale contact pressure distribution from (3.34), a net pressure load of $\left(P_{fluid} + P_c - P_{dc}\right)$ is applied over the sealing edge obtained from the macro-scale deformation & contact analyses earlier. Corresponding radial deformations H_{def} of the sealing edge are then obtained from the finite element calculations in a similar manner as the macro-deformation analysis of section 3.2.

3.7 Computational Algorithm

3.7.1 Macro-Scale Deformation and Contact Mechanics Algorithm

Set of equations (3.11) coupled with Eq. (3.2)-(3.4) and Eq. (3.12)-(3.13) is solved using Comsol Multiphysics. An affine invariant form of the damped Newton method and an Augmented Lagrangian algorithm is implemented. The finite element mesh consists of 10710 2nd order Lagrange elements (based on a mesh refinement study).

Typically, the penalty method, the Lagrange multiplier method and the augmented Lagrangian multiplier method have been used to solve the variational equalities describing a contact problem. In the penalty method, the accuracy of the solution depends on the choice of the penalty parameter. Too small a penalty parameter may cause unacceptable error in the solution. Also, it is well-known that the penalty method suffers from ill conditioning as the penalty parameter becomes larger. The Lagrange multiplier method introduces new unknowns for each constraint. Therefore, it always increases the dimension of the system of equations to be solved. This increases the CPU time to solve the problem. The advantages and disadvantages of penalty and Lagrange multiplier techniques are discussed by Kikuchi and Oden [87], and Simo and Laursen [88].

Considering this, for many contact problems it is desirable to implement the "Augmented Lagrange Multiplier" method. The main advantage of this method is that the exact solution of the original problem can be obtained. Also, for large-scale problems considerable savings in the CPU-time can be realized. It provides an optimal convergence for Newton-Raphson method. This method is a combination of penalty and Lagrange multiplier methods [89] and is used by the Comsol solver. It solves the system iteratively using the calculated displacement field. Displacements caused by incremental loading, are stored and used to deform the structure to its current geometrical configuration. If the gap variable between master and slave boundaries at a given iteration becomes negative, (penetration), the user defined normal penalty factor p_n is augmented with Lagrange multipliers for contact pressure P_{dc}.

Consider $\Phi(u,\delta u)$ as all the terms on left side of the "weak form" given by Eq. (3.10), then the Lagrange multiplier formulation of this variational equation is given as,

$$\begin{aligned} &\Phi(u,\delta u)+\int_A \lambda_N\, \delta u\cdot \hat{n}\big(u(\mathrm{X})\big)\, dA = 0 \\ &\int_A \delta\lambda_N\, h\big(u(\mathrm{X})\big)\, dA = 0 \end{aligned} \tag{3.37}$$

where λ_N is the Lagrange multiplier, which is introduced as an additional variable of the system. $\delta\lambda_N$ is the variation of λ_N and h is the scalar valued gauge function define on the spatial domain. Now, in Augmented Lagrangian formulation, a penalty regularization is appended to the Lagrange multiplier of Eq.(3.37), which results in

$$\Phi(u,\delta u)+\int_A \big(\lambda_N + p_n g\left(u(\mathrm{X})\right)\big)\delta u\cdot \hat{n}\,(u(\mathrm{X}))\, dA = 0 \tag{3.38}$$

Eq. (3.38) is the penalization of the Lagrange Multiplier problem, which is exact if the multipliers are the correct ones. The main idea in the method of augmented Lagrangians is to regard λ_N as a fixed current estimate of the correct Lagrange multiplier and solve the problem

$$\Phi\left(u_{n+1}^{(k)}, \delta u\right) + \int_A \left(\lambda_N^{(k)} + p_n g\left(u_{n+1}^{(k)}(\mathrm{X})\right)\right) \delta u \cdot \hat{n}(u(\mathrm{X}))\ dA = 0 \qquad (3.39)$$

The superscript (k) denotes the fact that the search for correct λ_N is an iterative process and penalizing it using $\left(\lambda_N^{(k)} + p_n g\right)$ provides the update formula for next iteration $(k+1)$ in pursuit of the correct multiplier. Hence the augmented Lagrange solver algorithm takes the following form [88] for the contact problem at hand:

1) Initialization : Set $\lambda_N^{(0)} = \lambda_N + p_n g$ from previous time step.

2) Solve for $u_{n+1}^{(k)}$ using Eq. (3.39)

3) Check for constraint satisfaction:

If $g\left(u_{n+1}^{(k)}\right) \le Tol$ *for all* $x \in \partial R$ *then*
Converge
Else
Augment : $\lambda_N^{(k+1)} = \lambda_N^{(k)} + p_n g\left(u_{n+1}^{(k)}\right)$
$k = k+1$
Goto Step 2
End

It should be noted that in the augmented Lagrangian method, the value of the penalty factor does not affect the accuracy of the final solution. However, if the penalty factor is too high, the iteration process fails in some of the first augmented iterations. If the penalty factor is too low, the model seems to converge but very slowly. Increasing the

penalty factor extensively can lead to an ill-conditioned Jacobian matrix and causes convergence problems in the Newton iterations. In such cases the damping factor becomes less than 1 for many Newton iterations. In the advanced seal material model (discussed in chapter 6), if there is a significant decrease in material stiffness, it gives rise to convergence problems for the nonlinear solver because the penalty factor becomes too large. Hence the convergence of the coupled macro-deformation / macro-contact problem is sensitive to the value of the penalty factors. For successful convergence, their value needs to be approximately of the same order as the stiffness of the boundary divided by a typical length scale, that is, the mesh size. To resolve these problems of convergence, the values for the normal penalty factor are not hard set, but are decided during the calculation process according to

$$p_n = \frac{E}{(\Delta X)_{\min}} \min\left[4^{augiter}/10^n, 1\right]$$

where, E is the elastic modulus on the slave side and $(\Delta X)_{\min}$, the smallest mesh size on the slave boundary, is included in order to get a typical length scale. Variable *augiter* is the iteration number in the augmented Lagrange solver. It is used to make the penalty factor much softer at the beginning to help the solver get started. Using the expression in the bracket, the penalty factor is then gradually made stiffer to speed up the convergence. Also, the mesh size is made much finer for the seal boundaries which are expected to come in contact with the rod / housing surface.

To be lean on the memory requirements, GMRES iterative solver with an incomplete LU factorization as a pre-conditioner is used to solve the system of equations. Consider the discrete form of the equations written as $f(U) = 0$ where U is the solution

vector and $f(U)$ is the residual. Given the initial guess U_0, a linearized model is created using a linearization point U_0. Then the algorithm solves the discretized form of the linearized model $f'(U_0)\delta U = -f(U_0)$ for the Newton step δU using a linear system solver [90]. New iteration is computed using $U_1 = U_0 + \lambda \delta U$ and the damping factor λ. Next, the modified Newton correction estimates the error ε for the new iteration by solving $f'(U_0)\varepsilon = -f(U_1)$. If the relative error corresponding to ε is larger than the relative error ε in the previous iteration, the code reduces the damping factor λ and re-computes U_1. Once a successful step for U_1 is taken, the algorithm proceeds with the next Newton iteration. It stops the iterations when the relative error computed from the Euclidean norm shown below becomes less than the relative tolerance.

$$error = \sqrt{\frac{1}{N}\sum_{i=1}^{N}\left(\frac{|\varepsilon_i|}{|U_i|}\right)^2}$$

where ε is the estimated error in the current approximation of the true solution vector, and N is the number of degrees of freedom.

Mesh Refinement and Grid Convergence:

In the mesh refinement study, we start with a coarse mesh (~ 2000 elements) and solve the deformation/macro-contact mechanics problem using finite elements. Critical variables to be mapped are then selected for studying the grid convergence and their solution values are stored. These variables are: radial and axial stresses in the seal body at key points in the seal body, radial and axial strains and most importantly the dry contact pressure along the sealing zone. The mesh is then refined, the problem is solved

again and the difference between the new and old solution values of these variables is calculated and is compared against the tolerance.

This process is repeated until following criterion is met:

$$\left(\mathrm{V}^{\mathrm{N}} - \mathrm{V}^{\mathrm{N}-1}\right) < \varepsilon$$

where

V^N: Value of the *var*iable at N^{th} level of mesh refinement

ε: tolerance

In the current calculations, going from 8430 element mesh to a 10710 element mesh results in a deviation of less than 0.1 % in the selected variables.

3.7.2 Micro-Scale Fluid Mechanics Solution Algorithm

A closed form solution of Eq.(3.22) can not be obtained; hence a numerical solution method is needed. Here a finite volume method is implemented. This equation needs to be solved for fluid pressure/density function, Φ, for given H and ϕ_{xx}, ϕ_{scx}. Depending on the calculated value of Φ, the value of F needs to be updated from which pressure field can be estimated. Once the pressure is known, rest of the pressure dependent variables are evaluated and film thickness is re-calculated from deformation mechanics module. Due to its memory efficiency, here we implement the tri-diagonal matrix algorithm (TDMA) to solve the finite volume discretized equations. This algorithm is described in detail by Patankar [91]. TDMA refers to a matrix form in which all of the nonzero entries are located along the three main diagonals of the matrix.

The idea of control volume formulation is that the calculation domain is divided into non-overlapping control volumes such that there is one control volume surrounding each grid point. The differential equation is then integrated over each control volume.

Piecewise profiles expressing the variation of the field variable between grid points are used to evaluate the required integrals. The result is the discretized equation which expresses the conservation principle for the field variable for the finite control volume, just as the differential equation expresses it for the infinitesimal control volume. The most attractive feature of this is that the resulting solution implies the integral conservation of quantities like mass, momentum and energy is exactly satisfied over any group of control volumes not just in the limiting case of large number of grid points. This means that even the coarse grid solution would exhibit the exact integral balance.

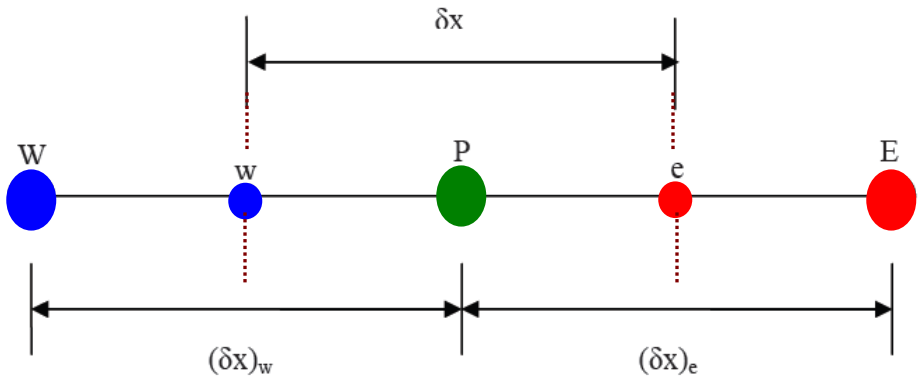

Figure 3.9: Finite volume discretization scheme employed for solving micro-scale fluid mechanics.

The finite volume scheme developed here uses a grid point cluster shown in Figure 3.9. P is the central grid point, E and W are East and West grid points respectively. The faces of the control volume are shown by dotted brown lines and are located at points "e" and "w", which are midway between the nodes W and P and E and P respectively, such that:

$$(\delta x)_w = x_P - x_W; \qquad (\delta x)_e = x_E - x_P; \qquad \delta x = \frac{(\delta x)_w + (\delta x)_e}{2}$$

Let's define: $K = \phi_{xx} H^3 e^{-\hat{\alpha} F \Phi}$

Eq.(3.22) then becomes

$$\frac{\partial}{\partial \hat{x}}\left(K \frac{\partial}{\partial \hat{x}}(F\Phi)\right) - 6\zeta \frac{\partial}{\partial \hat{x}}\left(\left\{1+(1-F)\Phi\right\} H_T\right) - 6\zeta F \frac{\partial \phi_{s.c.x}}{\partial \hat{x}} - 12\varepsilon \frac{\partial}{\partial \hat{t}}\left(\left\{1+(1-F)\Phi\right\} H_T\right) = 0 \tag{3.40}$$

Integrating Eq. (3.40) over the control volume from x_w to x_e yields,

$$\int_{x_w}^{x_e} \frac{\partial}{\partial \hat{x}}\left[K \frac{\partial}{\partial \hat{x}}(F\Phi)\right] d\hat{x} - 6\zeta \int_{x_w}^{x_e} \frac{\partial}{\partial \hat{x}}\left[\left\{1+(1-F)\Phi\right\} H_T\right] d\hat{x} - 6\zeta \int_{x_w}^{x_e} F \frac{\partial \phi_{s.c.x}}{\partial \hat{x}}\, d\hat{x} - 12\varepsilon \int_{x_w}^{x_e} \frac{\partial}{\partial \hat{t}}\left(\left\{1+(1-F)\Phi\right\} H_T\right) d\hat{x} = 0 \tag{3.41}$$

I) Consider the first term of Eq.(3.41),

$$\int_{x_w}^{x_e} \frac{\partial}{\partial \hat{x}}\left[K \frac{\partial}{\partial \hat{x}}(F\Phi)\right] d\hat{x} = \left[K \frac{\partial}{\partial \hat{x}}(F\Phi)\right]_e - \left[K \frac{\partial}{\partial \hat{x}}(F\Phi)\right]_w$$

Approximating the derivatives on RHS with finite differences gives,

$$\int_{x_w}^{x_e} \frac{\partial}{\partial \hat{x}}\left[K \frac{\partial}{\partial \hat{x}}(F\Phi)\right] d\hat{x} = K_e \frac{F_E \Phi_E - F_P \Phi_P}{\delta \hat{x}_e} - K_w \frac{F_P \Phi_P - F_W \Phi_W}{\delta \hat{x}_w} = Term_1 \ (say) \tag{3.42}$$

where K_e and K_w can be written in terms of harmonic means as,

$$K_e = \frac{2 K_E K_P}{(K_E + K_P)}; \qquad K_w = \frac{2 K_W K_P}{(K_W + K_P)}$$

II) The second term of Eq. (3.41) yields,

$$\int_{x_w}^{x_e} 6\zeta \frac{\partial}{\partial \hat{x}}\left[\left\{1+(1-F)\Phi\right\} H_T\right] d\hat{x} = 6\zeta \left(\left[\left\{1+(1-F)\Phi\right\} H_T\right]_e - \left[\left\{1+(1-F)\Phi\right\} H_T\right]_w\right) = Term_2 \ (say) \tag{3.43}$$

Now, an "upwind" scheme is applied to the above equation, where the scheme is dependent on the direction of flow [91]. Hence Eq.(3.43) reduces to,

$$\int_{x_w}^{x_e} 6\zeta \frac{\partial}{\partial \hat{x}}\left[\left\{1+(1-F)\Phi\right\}H_T\right] d\hat{x} \;=\; Term_{\,2} =$$

Flow in positive x direction: $6\zeta\left[\left\{1+(1-F_P)\Phi_P\right\}(H_T)_e-\left\{1+(1-F_W)\Phi_W\right\}(H_T)_w\right]$ (3.44)

Flow in negative x direction: $6\zeta\left[\left\{1+(1-F_E)\Phi_E\right\}(H_T)_e-\left\{1+(1-F_P)\Phi_P\right\}(H_T)_w\right]$

where $(H_T)_e$ and $(H_T)_w$ can be defined using arithmetic means as,

$$(H_T)_e=\frac{(H_T)_P+(H_T)_E}{2};\quad (H_T)_w=\frac{(H_T)_P+(H_T)_W}{2}$$

III) Third term of Eq.(3.41): grouping similar terms from the finite difference equations and applying a harmonic mean for the flow factors, we get

$$\begin{aligned} 6\zeta\int_{x_w}^{x_e} F\frac{\partial \phi_{s.c.x}}{\partial \hat{x}}\, d\hat{x} &= 6\zeta F_P\left[\frac{2(\phi_{s.c.x})_P(\phi_{s.c.x})_E}{(\phi_{s.c.x})_P+(\phi_{s.c.x})_E}-\frac{2(\phi_{s.c.x})_P(\phi_{s.c.x})_W}{(\phi_{s.c.x})_P+(\phi_{s.c.x})_W}\right] \\ &= Term_{\,3}\;\;(say) \end{aligned} \tag{3.45}$$

Now Eq. (3.41) is integrated with respect to time from t to $t+\Delta t$,

$$\begin{aligned} &\int_t^{t+\Delta t} Term_{\,1}\, dt-\int_t^{t+\Delta t} Term_{\,2}\, dt-\int_t^{t+\Delta t} Term_{\,3}\, dt \\ &\quad -12\varepsilon\int_t^{t+\Delta t}\int_{x_w}^{x_e}\frac{\partial}{\partial \hat{t}}\left(\left\{1+(1-F)\Phi\right\}H_T\right)d\hat{x}\,dt=0 \end{aligned} \tag{3.46}$$

It is at this point that we need an assumption about how field variables like $(H_T)_P$, Φ_P, F_P vary with time from t to $t+\Delta t$. It can be proposed that,

$$\int_t^{t+\Delta t}(H_T)_P\, dt=\left[\, f\,(H_T)_P^{\,1}+(1-f)(H_T)_P^{\,0}\right]\Delta t$$

where f is a weighting factor between 0 and 1. $f=0$ leads to an explicit scheme of time integration, $f=0.5$ gives Crank-Nicolson scheme and $f=1$ gives a fully implicit scheme. The superscript 1 denotes the value of the variable at the current time step, while superscript 0 denotes the value at previous time step. Hence the explicit scheme assumes that the old values of the variables prevail throughout the entire time step except at time $t+\Delta t$. In fully implicit scheme, the field variable value drops from $\left(H_T\right)_P^{\ 0}$ to $\left(H_T\right)_P^{\ 1}$ and stays there over the whole time step, while the Crank-Nicolson scheme assumes a linear variation of the variable from t to $t+\Delta t$.

Similarly we can write,

$$\int_t^{t+\Delta t}\left[\left\{1+\left(1-F\right)\Phi\right\}H_T\right]_P dt=$$

$$\left[f\left[\left\{1+\left(1-F\right)\Phi\right\}H_T\right]_P^{\ 1}+\left(1-f\right)\left[\left\{1+\left(1-F\right)\Phi\right\}H_T\right]_P^{\ 0}\right]\Delta t$$

Here a fully implicit scheme is implemented and hence $f=1$ is chosen. Hence various terms of Eq. (3.46) can be written as,

$$\int_t^{t+\Delta t} Term_1\, dt = 1\cdot\left(Term_1\right)^1\cdot\Delta t;$$

$$\int_t^{t+\Delta t} Term_2\, dt = 1\cdot\left(Term_2\right)^1\cdot\Delta t;$$

$$\int_t^{t+\Delta t} Term_3\, dt = 1\cdot\left(Term_3\right)^1\cdot\Delta t$$

and

$$
\begin{aligned}
&12\varepsilon \int_{t}^{t+\Delta t}\int_{x_w}^{x_e} \frac{\partial}{\partial \hat{t}}\left(\left\{1+\left(1-F\right)\Phi\right\}H_T\right)d\hat{x}\,dt \\
&=12\varepsilon \int_{x_w}^{x_e}\left[\int_{t}^{t+\Delta t} \frac{\partial}{\partial \hat{t}}\left(\left\{1+\left(1-F\right)\Phi\right\}H_T\right)dt\right]d\hat{x} \\
&=12\varepsilon \int_{x_w}^{x_e}\left[\left(\left[\left\{1+\left(1-F_P\right)\Phi_P\right\}\left(H_T\right)_P\right]^1-\left[\left\{1+\left(1-F_P\right)\Phi_P\right\}\left(H_T\right)_P\right]^0\right)\right]d\hat{x} \\
&=12\varepsilon\,\Delta x\left[\left(\left[\left\{1+\left(1-F_P\right)\Phi_P\right\}\left(H_T\right)_P\right]^1-\left[\left\{1+\left(1-F_P\right)\Phi_P\right\}\left(H_T\right)_P\right]^0\right)\right]
\end{aligned}
\tag{3.47}
$$

with this, Eq. (3.46) becomes,

$$
\begin{aligned}
&\left(Term_1\right)^1-\left(Term_2\right)^1-\left(Term_3\right)^1 \\
&\quad -12\varepsilon\,\frac{\Delta x}{\Delta t}\left(\left[\left\{1+\left(1-F_P\right)\Phi_P\right\}\left(H_T\right)_P\right]^1-\left[\left\{1+\left(1-F_P\right)\Phi_P\right\}\left(H_T\right)_P\right]^0\right)=0
\end{aligned}
$$

Re-arranging, we get the final form for numerical time integration of Eq. (3.41),

$$
\begin{aligned}
&\left(Term_1\right)^1-\left(Term_2\right)^1-\left(Term_3\right)^1-12\varepsilon\,\frac{\Delta x}{\Delta t}\left(1-F_P{}^1\right)\left(H_T\right)_P{}^1\Phi_P{}^1 \\
&\qquad -12\varepsilon\,\frac{\Delta x}{\Delta t}\left[\left(H_T\right)_P{}^1-\left\{1+\left(1-F_P{}^0\right)\Phi_P{}^0\right\}\left(H_T\right)_P{}^0\right]=0
\end{aligned}
\tag{3.48}
$$

where $Term_1, Term_2$ and $Term_3$ are given by Eq.(3.42), Eq.(3.44) and Eq.(3.45) respectively.

Eq. (3.48) can be written in the form of a system of algebraic equations,

$$
A_P\Phi_P = A_E\Phi_E + A_W\Phi_W + b \tag{3.49}
$$

where for a positive rod velocity,

$$
\begin{aligned}
A_P &= \left(\frac{K_e}{\delta x_e} + \frac{K_w}{\delta \hat{x}_w}\right) F_P + 6\zeta\left(1-F_P\right)\left(H_T\right)_E + 12\varepsilon\,\frac{\Delta x}{\Delta t}\left(1-F_P\right)\left(H_T\right)_P \\
A_E &= \frac{K_e}{\delta x_e} F_E \\
A_W &= \frac{K_w}{\delta x_w} F_W \\
b &= -6\zeta\left(H_T\right)_E + 6\zeta\left[\left\{1+\left(1-F_W\right)\Phi_W\right\}\left(H_T\right)_W\right] \\
&\quad - 6\zeta F_P\left[\frac{2\left(\phi_{s.c.x}\right)_P\left(\phi_{s.c.x}\right)_E}{\left(\phi_{s.c.x}\right)_P+\left(\phi_{s.c.x}\right)_E} - \frac{2\left(\phi_{s.c.x}\right)_P\left(\phi_{s.c.x}\right)_W}{\left(\phi_{s.c.x}\right)_P+\left(\phi_{s.c.x}\right)_W}\right] \\
&\quad - 12\varepsilon\,\frac{\Delta x}{\Delta t}\left[\left(H_T\right)_P - \left\{1+\left(1-F_P{}^0\right)\Phi_P{}^0\right\}\left(H_T\right)_P{}^0\right]
\end{aligned}
\tag{3.50}
$$

and for a negative rod velocity,

$$
\begin{aligned}
A_P &= \left(\frac{K_e}{\delta x_e} + \frac{K_w}{\delta \hat{x}_w}\right) F_P + 6\zeta\left(1-F_P\right)\left(H_T\right)_W + 12\varepsilon\,\frac{\Delta x}{\Delta t}\left(1-F_P\right)\left(H_T\right)_P \\
A_E &= \frac{K_e}{\delta x_e} F_E \\
A_W &= \frac{K_w}{\delta x_w} F_W \\
b &= 6\zeta\left(H_T\right)_W - 6\zeta\left[\left\{1+\left(1-F_E\right)\Phi_E\right\}\left(H_T\right)_E\right] \\
&\quad - 6\zeta F_P\left[\frac{2\left(\phi_{s.c.x}\right)_P\left(\phi_{s.c.x}\right)_E}{\left(\phi_{s.c.x}\right)_P+\left(\phi_{s.c.x}\right)_E} - \frac{2\left(\phi_{s.c.x}\right)_P\left(\phi_{s.c.x}\right)_W}{\left(\phi_{s.c.x}\right)_P+\left(\phi_{s.c.x}\right)_W}\right] \\
&\quad - 12\varepsilon\,\frac{\Delta x}{\Delta t}\left[\left(H_T\right)_P - \left\{1+\left(1-F_P{}^0\right)\Phi_P{}^0\right\}\left(H_T\right)_P{}^0\right]
\end{aligned}
\tag{3.51}
$$

Algebraic form required for TDMA:

In terms of node index, i, required for coding the system of equations in TDMA form,

$$A_i\Phi_i = B_i\Phi_{i+1} + C_i\Phi_{i-1} + D_i \tag{3.52}$$

For positive rod velocity:

$$A_i = \left(\frac{2\dfrac{K_{i+1}K_i}{K_{i+1}+K_i}}{\Delta x} + \frac{2\dfrac{K_{i-1}K_i}{K_{i-1}+K_i}}{\Delta x} \right) F_i + 6\zeta\left(1-F_i\right)\left(H_T\right)_{i+1} + 12\varepsilon\,\frac{\Delta x}{\Delta t}\left(1-F_i\right)\left(H_T\right)_i$$

$$B_i = \frac{2\dfrac{K_{i+1}K_i}{K_{i+1}+K_i}}{\Delta x} F_{i+1}$$

$$C_i = \frac{2\dfrac{K_{i-1}K_i}{K_{i-1}+K_i}}{\Delta x} F_{i-1}$$

$$\begin{aligned} D_i = & -6\zeta\left(H_T\right)_{i+1} + 6\zeta\left[\left\{1+\left(1-F_{i-1}\right)\Phi_{i-1}\right\}\left(H_T\right)_{i-1}\right] \\ & - 6\zeta F_P\left[\frac{2\left(\phi_{s.c.x}\right)_i\left(\phi_{s.c.x}\right)_{i+1}}{\left(\phi_{s.c.x}\right)_i+\left(\phi_{s.c.x}\right)_{i+1}} - \frac{2\left(\phi_{s.c.x}\right)_i\left(\phi_{s.c.x}\right)_{i-1}}{\left(\phi_{s.c.x}\right)_i+\left(\phi_{s.c.x}\right)_{i-1}}\right] \\ & - 12\varepsilon\,\frac{\Delta x}{\Delta t}\left[\left(H_T\right)_i - \left\{1+\left(1-F_i^{\,0}\right)\Phi_i^{\,0}\right\}\left(H_T\right)_i^{\,0}\right] \end{aligned} \tag{3.53}$$

For a negative rod velocity:

$$A_i = \left(\frac{2\dfrac{K_{i+1}K_i}{K_{i+1}+K_i}}{\Delta x} + \frac{2\dfrac{K_{i-1}K_i}{K_{i-1}+K_i}}{\Delta x} \right) F_i + 6\zeta\left(1-F_i\right)\left(H_T\right)_{i-1} + 12\varepsilon\,\frac{\Delta x}{\Delta t}\left(1-F_i\right)\left(H_T\right)_i$$

$$B_i = \frac{2\dfrac{K_{i+1}K_i}{K_{i+1}+K_i}}{\Delta x} F_{i+1}$$

$$C_i = \frac{2\dfrac{K_{i-1}K_i}{K_{i-1}+K_i}}{\Delta x} F_{i-1}$$

$$\begin{aligned} D_i = & \;6\zeta\left(H_T\right)_{i-1} - 6\zeta\left[\left\{1+\left(1-F_{i+1}\right)\Phi_{i+1}\right\}\left(H_T\right)_{i+1}\right] \\ & - 6\zeta F_i\left[\frac{2\left(\phi_{s.c.x}\right)_i\left(\phi_{s.c.x}\right)_{i+1}}{\left(\phi_{s.c.x}\right)_i+\left(\phi_{s.c.x}\right)_{i+1}} - \frac{2\left(\phi_{s.c.x}\right)_i\left(\phi_{s.c.x}\right)_{i-1}}{\left(\phi_{s.c.x}\right)_i+\left(\phi_{s.c.x}\right)_{i-1}}\right] \\ & - 12\varepsilon\,\frac{\Delta x}{\Delta t}\left[\left(H_T\right)_i - \left\{1+\left(1-F_i^{\,0}\right)\Phi_i^{\,0}\right\}\left(H_T\right)_i^{\,0}\right] \end{aligned} \tag{3.54}$$

3.7.3 Model Coupling and Post-Processing

The computational procedure is shown in Figure 3.10. An iterative algorithm is designed to solve the governing equations defined in sections 3.2 -3.6 in a strongly coupled manner. Initially, the seal and fluid properties and the operating conditions are input. Next, the deformed seal configuration, dry contact pressure and dry film thickness distributions are computed using macro-scale deformation and contact analyses, and initial guesses for the film thickness and asperity distributions are input. The micro-scale fluid mechanics analysis is then performed to compute the fluid pressure by computing F and Φ iteratively. Next the micro-scale contact mechanics analysis is performed to compute the asperity contact pressure. The fluid pressure and asperity contact pressure are then fed into the micro-scale finite element deformation analysis. The computed deformations are used in a second iteration loop to update the fluid film thickness and flow factors. Convergence criteria is set: the difference between successive iterations of film thickness and fluid pressure values at each node should be less than the tolerance (typically 0.01 %).

Ater all the computations are converged, these converged solutions are used to calculate the squeeze term for the next time step, and the entire process is repeated over the time interval of interest. After arriving at the solution for entire time period of interest, auxiliary calculations are performed for quantities such as fluid transport rate, total fluid transport and friction force on the rod.

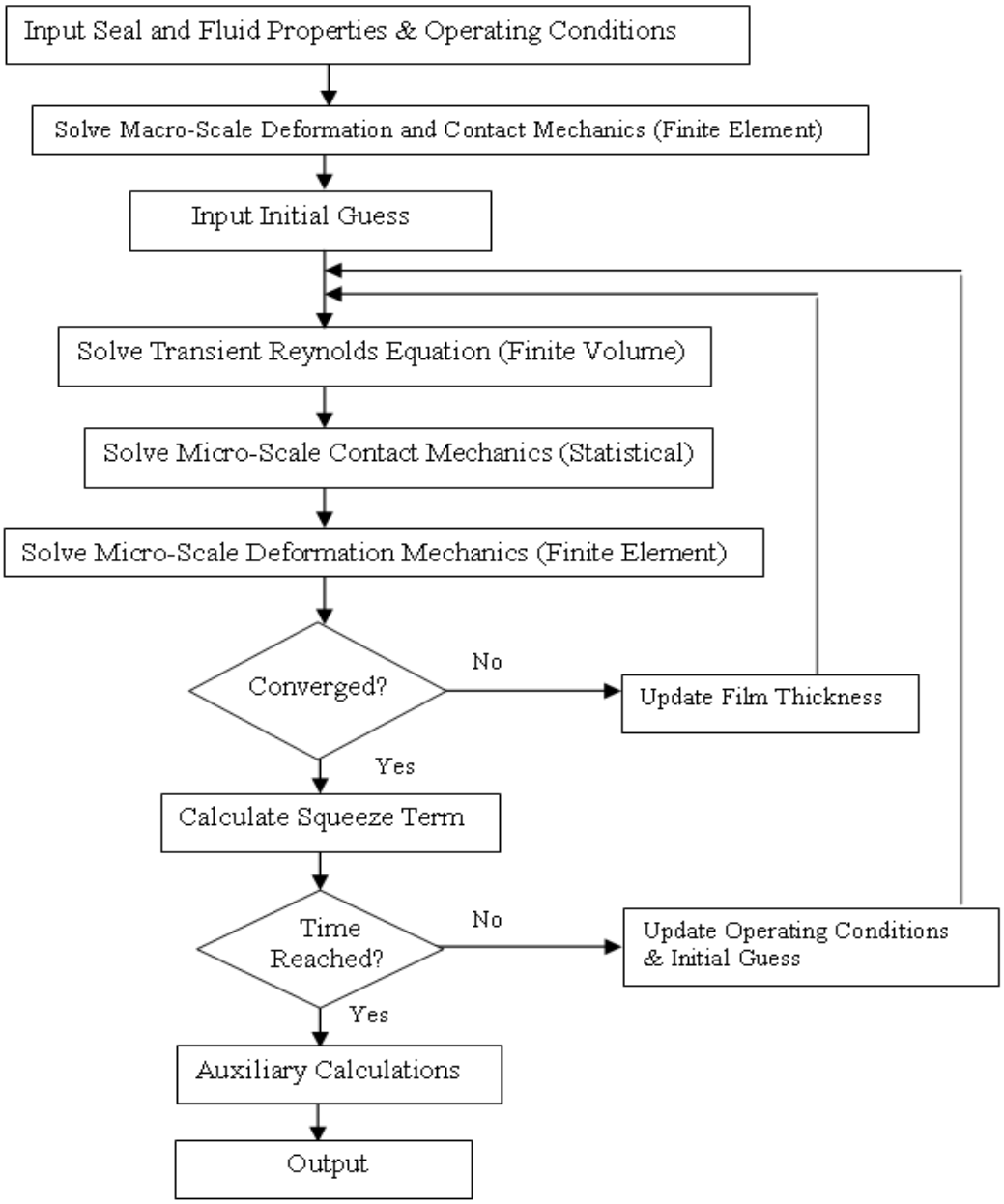

Figure 3.10: MSMP computational algorithm for the seal analysis in chapter 3.

I) Flow Rate and Fluid Transport:

Instantaneous transport rate (flow rate per unit circumferential length through the film) is normalized using

$$\hat{q} = \frac{q}{\left(p_a \sigma^3 / 12 \mu_0 L \right)}$$

In the dimensionless form it is written as,

$$\hat{q} = -\phi_{xx} H^3 e^{-\hat{\alpha} F \Phi} \frac{\partial \left(F \Phi \right)}{\partial \hat{x}} + 6\zeta \left(\left\{ 1 + \left(1 - F \right) \Phi \right\} \left\{ H_T + \phi_{s.c.x} \right\} \right) \tag{3.55}$$

The amount of transport (over elapsed time T_i) is then calculated from,

$$\hat{Q} = \int_0^{T_i} \hat{q} \, d\hat{t} \tag{3.56}$$

II) Fluid Shear Stress:

The average fluid shear stress on the rod (dimensionless) is given by,

$$\hat{\tau}_f = \frac{\tau_f}{E} = \frac{-\hat{\sigma}}{\xi} e^{\hat{\alpha} F \Phi} \frac{\zeta}{H} \left(\phi_f - \phi_{fss} \right) - \phi_{fpp} \frac{\hat{\sigma}}{\xi} \frac{H}{2} \frac{\partial \left(F \Phi \right)}{\partial \hat{x}} \tag{3.57}$$

Here ϕ_{fpp} is a correction factor for the mean pressure flow component of the shear stress, and it has been obtained by Patir and Cheng [60] using numerical simulations over a range of statistically identical rough surfaces. Results from their findings can be fitted into an empirical relation given by Eq. (3.58), where ϕ_{fpp} is only a function of the film thickness and the parameter γ describing asperity aspect ratio and orientation.

$$\phi_{fpp} = 1 - De^{-sH} \tag{3.58}$$

The coefficients in the above equation are listed in Table 3.2. ϕ_{fss} is another correction term which is a results of the combined effect of roughness and sliding, similar to the ϕ_{scx} term that was included for describing the mean flow. ϕ_{fss} can be calculated using empirical relation of Eq. (3.59).

$$\phi_{fss} = \begin{cases} A_3 H^{\alpha_4} e^{-\alpha_5 H + \alpha_6 H^2} & \text{for } 0.5 < H < 7 \\ 0 & \text{for } H > 7 \end{cases} \tag{3.59}$$

The coefficients in the above equation are listed in Table 3.2.

Table 3.2: Coefficients used in Eq.(3.58) and (3.59).

γ	D	s	A_3	α_4	α_5	α_6
1/9	1.51	0.52	14.1	2.45	2.30	0.10
1/6	1.51	0.54	13.4	2.42	2.30	0.10
1/3	1.47	0.58	12.3	2.32	2.30	0.10
1	1.40	0.66	11.1	2.31	2.38	0.11
3	0.98	0.79	9.8	2.25	2.80	0.18
6	0.97	0.91	10.1	2.25	2.90	0.18
9	0.73	0.91	8.7	2.15	2.97	0.18

ϕ_f term in Eq.(3.57) arises from averaging the sliding velocity component of the shear stress. It can be obtained through integration for any given frequency density of roughness heights. Using the numerical simulation results of Patir-Cheng [60] over rough surfaces, ϕ_f is obtained using the empirical relations given in Eq. (3.60), where $H = h/\sigma$; $z = H/3$; $\varepsilon^* = \varepsilon/3\sigma$ and ε is the value of film thickness below which the hydrodynamic shear stress is assumed not to exist.

for $H \le 3$:

$$\phi_f = \frac{35}{32} z \left\{ \begin{array}{l} \left(1-z^2\right)^3 \ln\left(\frac{z+1}{\varepsilon^*}\right) + \\ \frac{1}{60}\left[-55 + z\left(132 + z\left(345 + z\left(-160 + z\left(-405 + z\left(60 + 147z\right)\right)\right)\right)\right)\right] \end{array} \right\} \tag{3.60}$$

for $H > 3$

$$\phi_f = \frac{35}{32} z \left\{ \left(1-z^2\right)^3 \ln\left(\frac{z+1}{z-1}\right) + \frac{z}{15}\left[66 + z^2\left(30z^2 - 80\right)\right] \right\}$$

III) Contact Shear Stress:

There is also a component of shear stress acting on the rod due to contacting asperities. This can be computed using a friction coefficient *f*,

$$\hat{\tau}_c = \frac{\tau_c}{E} = -f\, P_c\left(\frac{\zeta}{|\zeta|}\right) \tag{3.61}$$

IV) Net Friction on Rod:

The net dimensional friction force on the rod is then calculated from,

$$F_r = \pi D \int_0^L \tau_t \, dx \tag{3.62}$$

where $\tau_t = \tau_f + \tau_c$ is the total dimensional shear stress obtained by combining the fluid viscous shear and the shear stress from contacting asperities.

3.8 Results

Computations have been performed for the typical polyurethane seal shown in Figure 3.1 with base parameters shown in Table 3.3 . The seal roughness is assumed to be isotropic. This seal is used in an injection molding application. It seals the actuator that moves the half-mold in and out of the injection molding machine. As described earlier, the rod is treated as perfectly smooth. The sealed pressure is held constant at P_{sealed} = 6.9 MPa (~1000 psi), and only the rod speed varies with time.

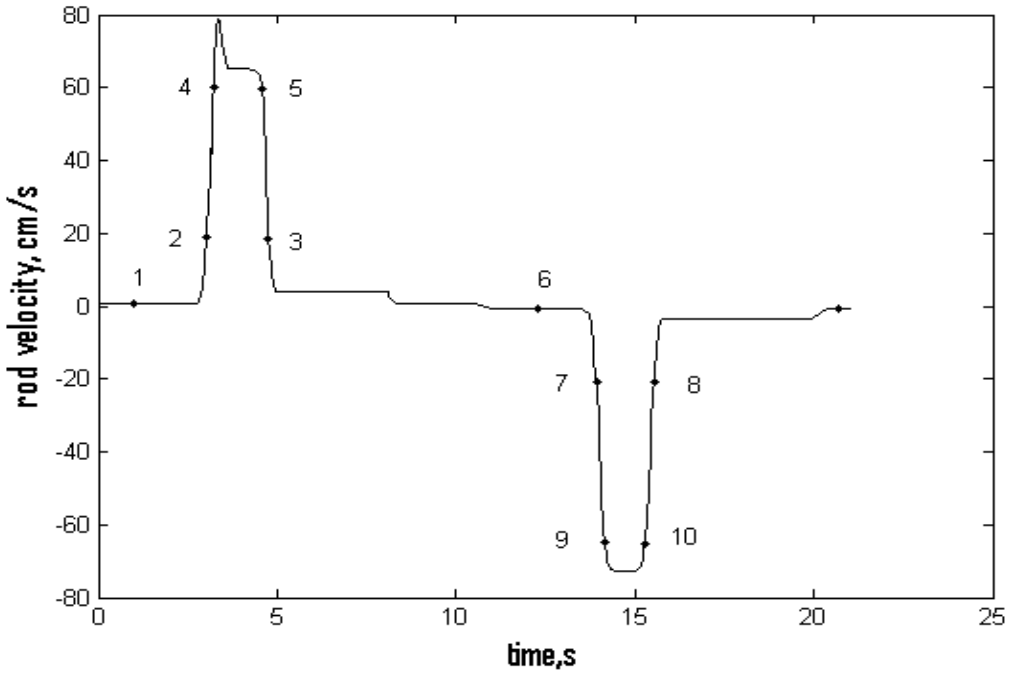

Figure 3.11: Rod velocity vs time.

Table 3.3: Base parameters for the seal model (left) and key points in time (right).

Elastic modulus, E	43 MPa
Poisson's ratio, υ	0.49
Rod diameter	88.9 mm
Stroke length	1.93 m
Seal width	6.8 mm
Reference viscosity, μ_0	0.043 $Pa \cdot s$
Pressure-viscosity coefficient, α	20×10^{-9} Pa^{-1}
RMS roughness , σ	variable
Asperity radius, R	1 μm
Asperity density, η	10^{12} m^{-2}
$t_{reference}$	1 s

point	time (sec)	rod velocity (cm/s)
1	1.0	0.5
2	3.02	19
3	4.76	19
4	3.22	60
5	4.59	60
6	12.3	-0.508
7	13.93	-20.7
8	15.53	-20.7
9	14.16	-65
10	15.26	-65

Figure 3.11 shows the specified rod velocity as a function of time, over one cycle. The outstroke occurs from t = 0 to t = 10.50 s, and the instroke from t = 10.51 s to t = 21.0 s. Also shown on Figure 3.11 are key times labeled 1 to 10. The times and rod velocities associated with these labels are given in Table 3.3.

Figure 3.12 shows the results from macro-deformation and contact mechanics modules. In part (a), the finite element mesh of the seal before mounting and after mounting and pressurization is shown. The sealing zone obtained from these calculations is circled red. Part (b) shows the displacement field in the seal body. Also shown in this figure (black contour) is the original un-deformed seal shape. Part (c) shows the contour plot of First Principal stress field showing area of stress concentration. Such a contour plot showing convergence of principal stress lines in the contact area is useful in understanding the contact pressure distribution in the sealing zone. Part (d) shows the dry contact pressure distribution over the sealing zone obtained from these calculations. The maximum slope in dry contact pressure occurs at the sealed end and a sealed pressure of 6.9 MPa gives a maximum dry contact pressure of about 17 MPa. Also the length of the sealing zone can be obtained from this dry contact pressure distribution, which is 2.4 mm. This sealing zone length and dry contact pressure distribution obtained from these calculations is used as input for micro-mechanics calculations as discussed earlier.

The resulting fluid transports per cycle for the instroke and outstroke are shown as a function of seal roughness in Figure 3.13. It is seen that both increase almost linearly with roughness. There is a critical roughness of 1.2 μm, below which the (potential) inflow transport exceeds the outflow transport and there is zero leakage. At roughness larger than the critical value, there is net leakage. This result is similar to that obtained

with a previous steady-state model [44], although the critical roughness is larger than the previous value due to a difference in the assumed asperity density.

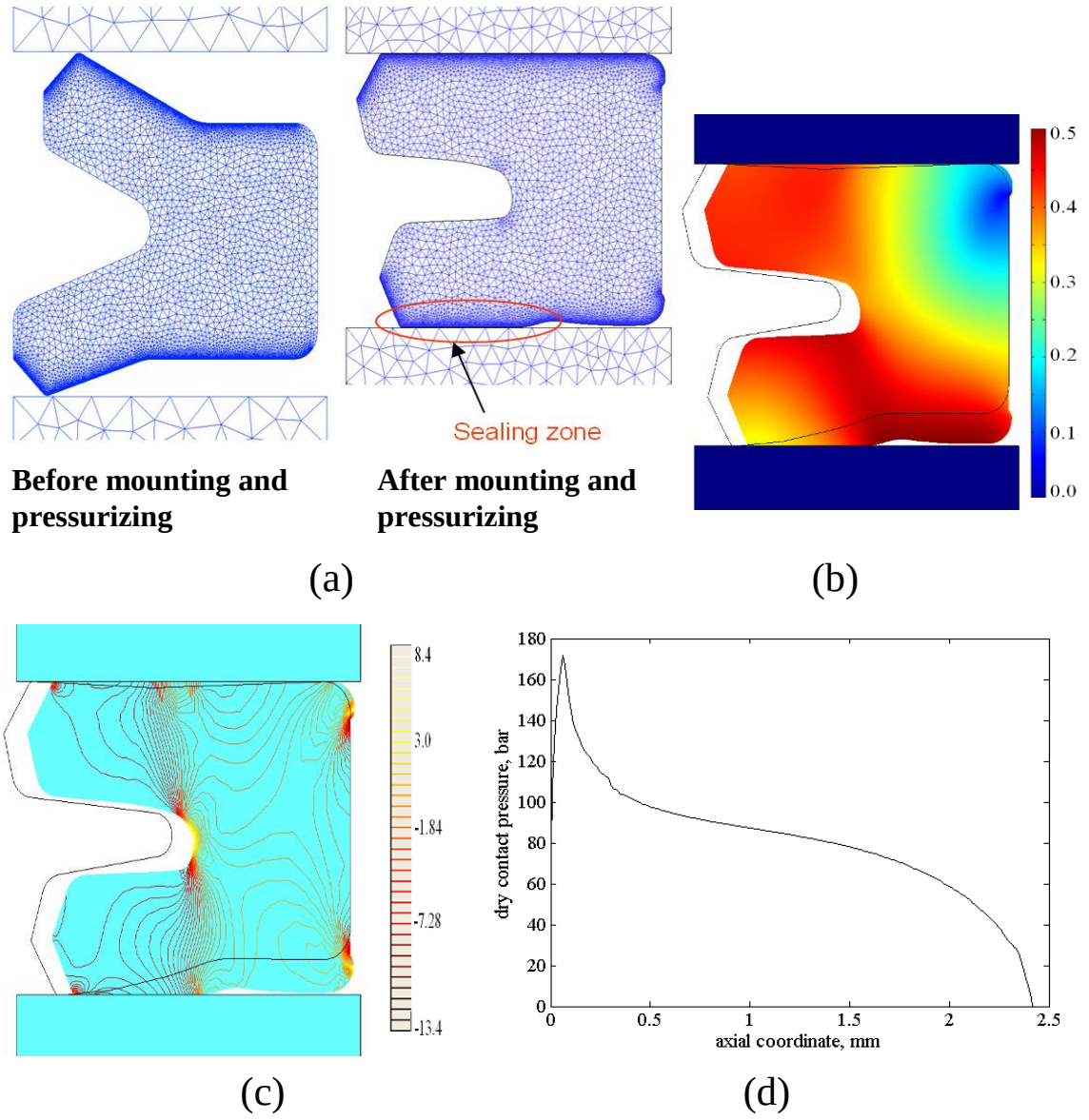

Figure 3.12: (a) Macro-deformation mechanics results showing seal before and after mounting and pressurizing. (b) Total displacement field in the seal body. (c) First Principal stress field in the seal body (d) Dry contact pressure along the sealing zone.

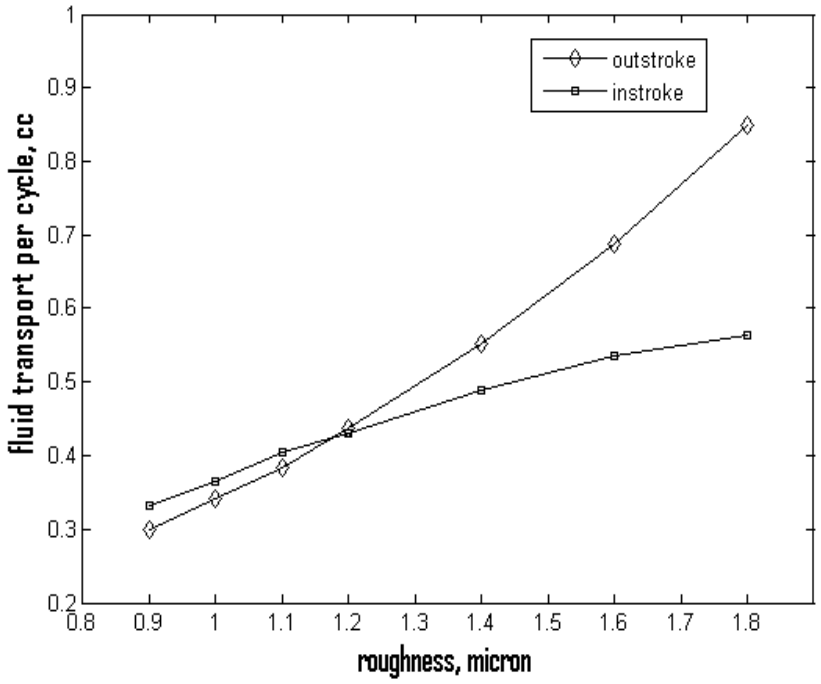

Figure 3.13: Fluid transport vs roughness.

All of the following results are for a seal roughness of 1.1 μm, which corresponds to a non-leaking seal according to Figure 3.13.

The instantaneous volumetric flow rate as a function of time is shown in Figure 3.14. The shape of the curve is almost identical to that of the rod velocity history. This indicates that the Poiseuille (pressure-driven) contribution to flow is very small compared to the Couette contribution. Figure 3.15 shows the net fluid transport (out of the cylinder) as a function of time. During the outstroke it increases and during the instroke it decreases. At the end of the cycle (t = 21.0 s) it has a negative value, indicating zero net leakage. Since the model assumes flooded conditions at the inlet to the sealing zone, model is no longer valid for the times after the net fluid transport goes negative.

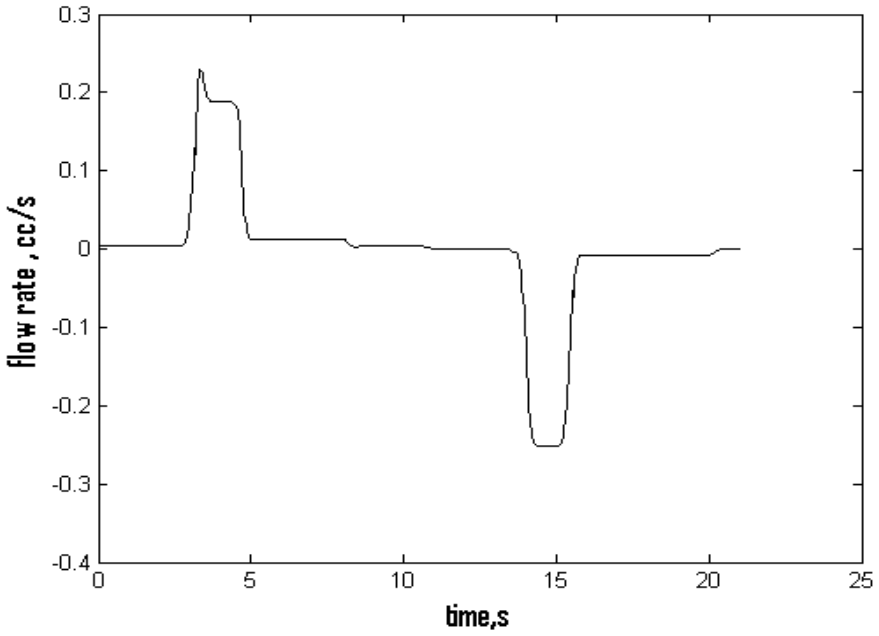

Figure 3.14: Flow rate vs time.

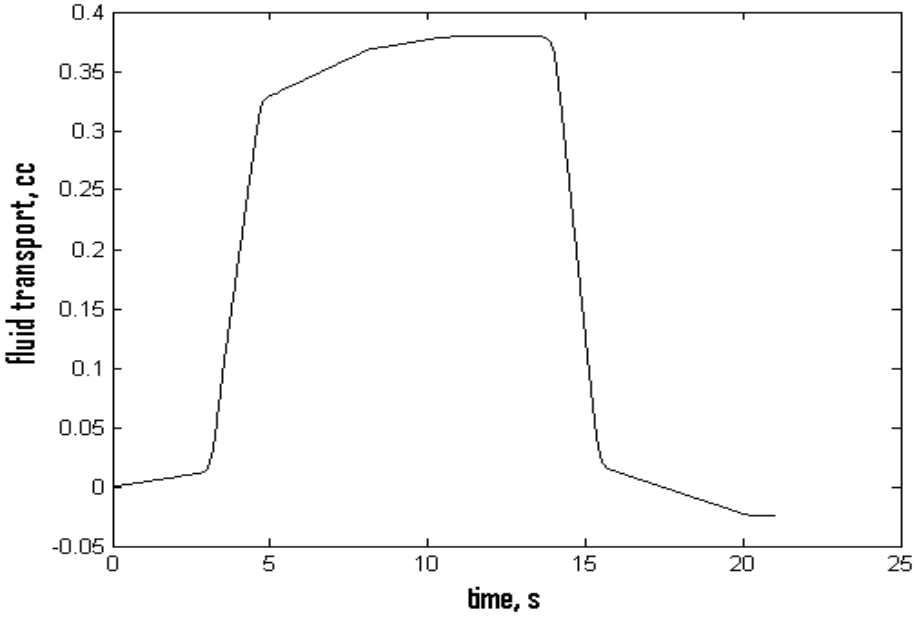

Figure 3.15: Net fluid transport vs time.

The friction force on the rod, as a function of time, is shown in Figure 3.16. During outstroke, its magnitude increases with rod speed, but during the instroke, it decreases with rod speed. This is because the friction force is primarily due to contacting asperities and, as will be shown below, the contact pressures increase with increasing rod speed during the outstroke, and decrease with increasing rod speed during the instroke.

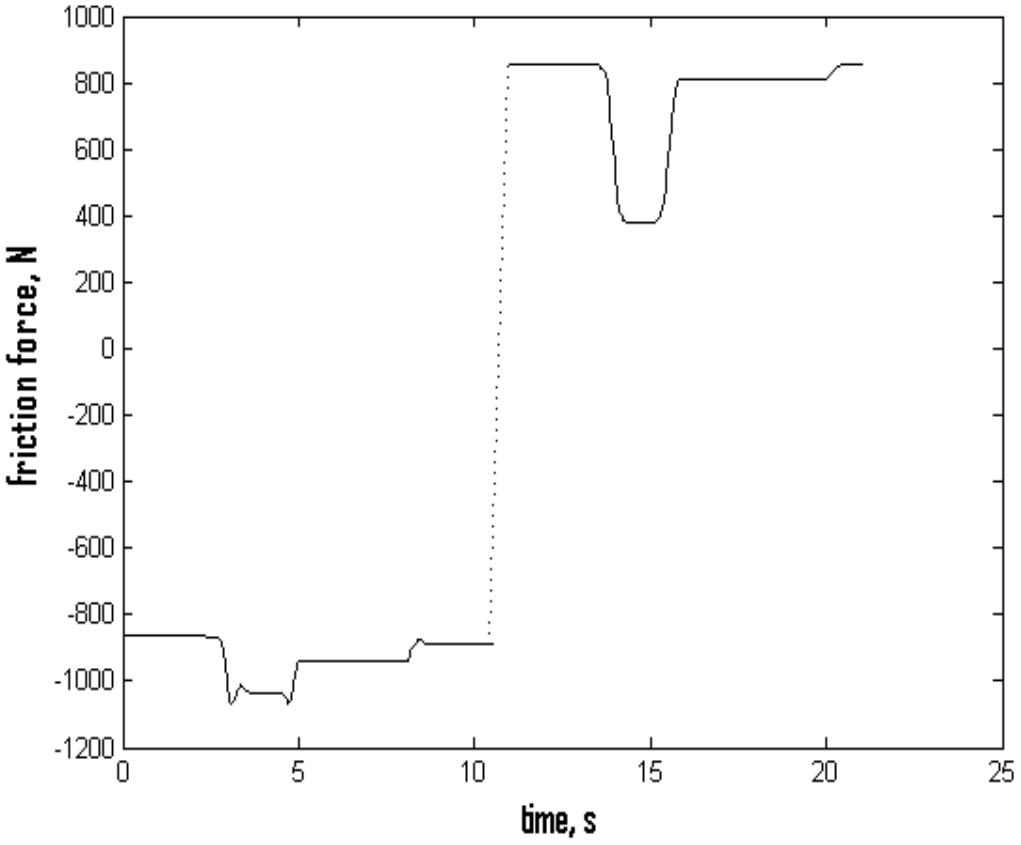

Figure 3.16: Friction force vs time.

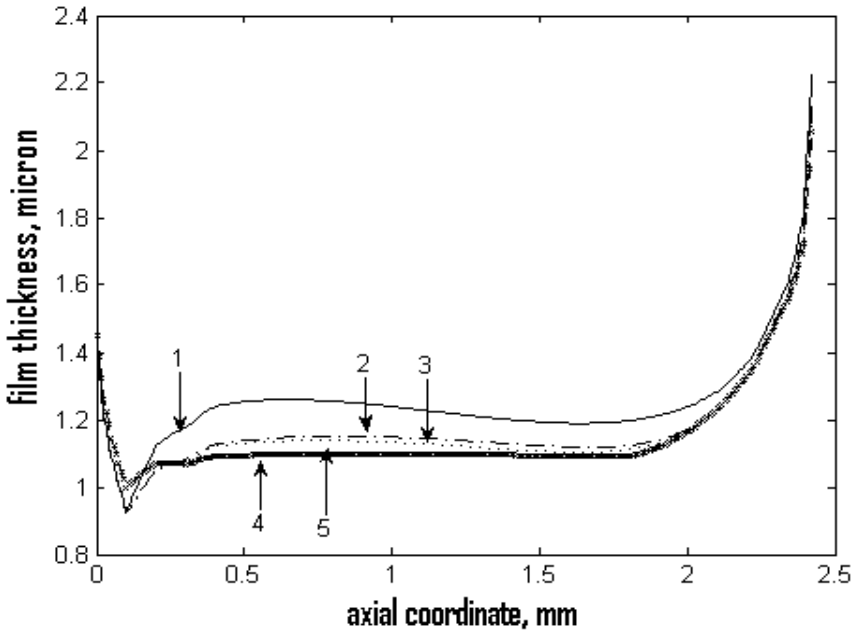

Figure 3.17: Film thickness distribution, outstroke.

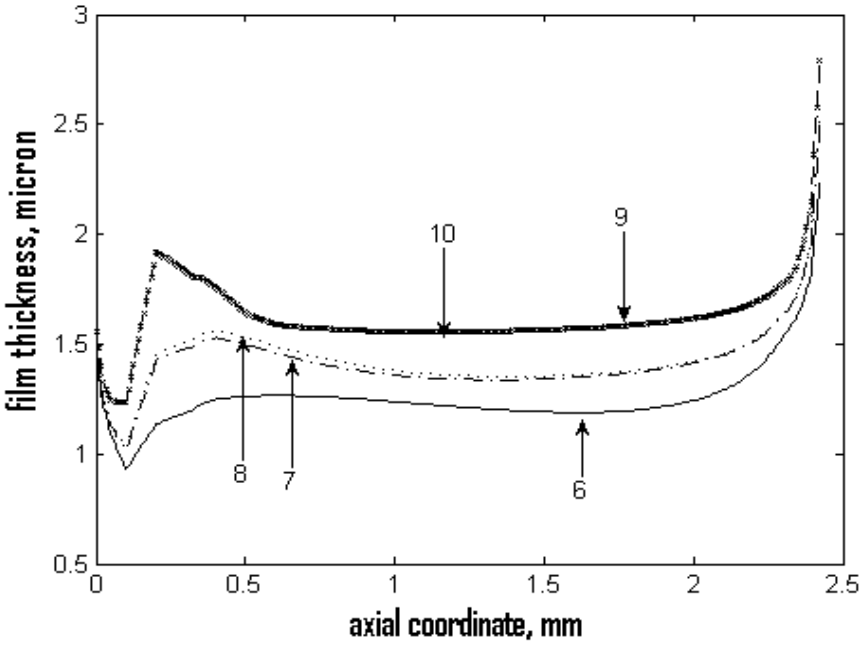

Figure 3.18: Film thickness distribution, instroke.

The film thickness, fluid pressure and contact pressure distributions during outstroke and instroke for the key points in time (Table 3.3) are shown in Figure 3.17 through Figure 3.22. From Figure 3.17 and Figure 3.18, it is seen that mixed lubrication occurs, since the film thickness is generally less than 3σ. During the outstroke, as the rod speed increases, the film thickness decreases; during the instroke the opposite occurs, as the rod speed increases, the film thickness increases. Thus the film is always thicker during the instroke than during the outstroke, which is favorable for preventing leakage.

Figure 3.19 and Figure 3.20 show that during the outstroke the fluid pressures decrease with increasing rod speed, while during the instroke they increase with increasing rod speed, explaining the film thickness behavior. This is because during the outstroke the flow is predominantly diverging, and during the instroke it is primarily converging. During the outstroke the fluid cavitates, which is again favorable for preventing leakage.

The contact pressure distributions in Figure 3.21 and Figure 3.22 show that the contact pressures increase with increasing rod speed during the outstroke, and decrease with increasing rod speed during the instroke. This is consistent with both the film thickness distributions and the fluid pressure distributions.

By comparing the profiles in Figure 3.17 through Figure 3.22 at time 2 with those at time 3 (at the same rod velocity) and at time 7 with those at time 8 (at the same rod velocity), the squeeze film effect can be seen. Although in this application it is small, it is nevertheless present.

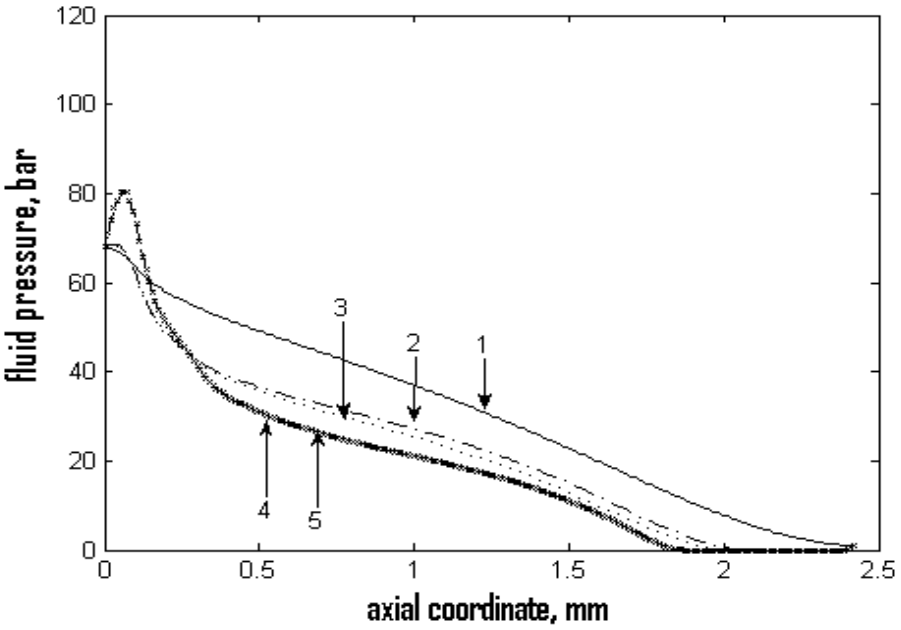

Figure 3.19: Fluid pressure distribution, outstroke.

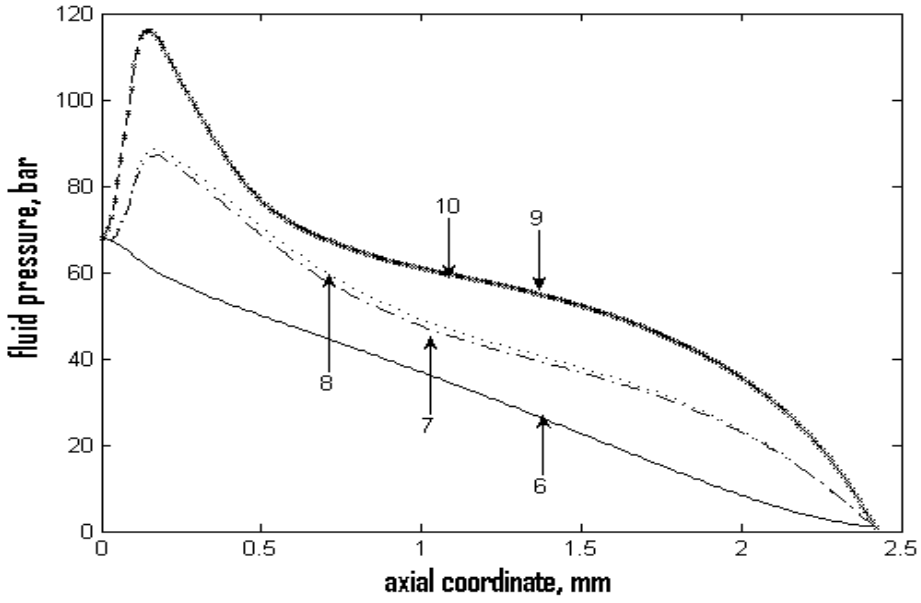

Figure 3.20: Fluid pressure distribution, instroke.

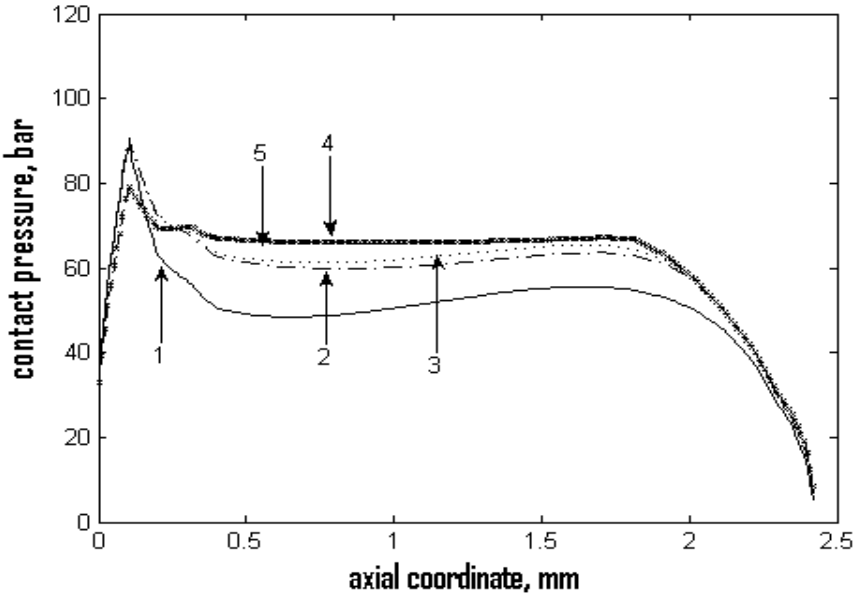

Figure 3.21: Contact pressure distribution, outstroke.

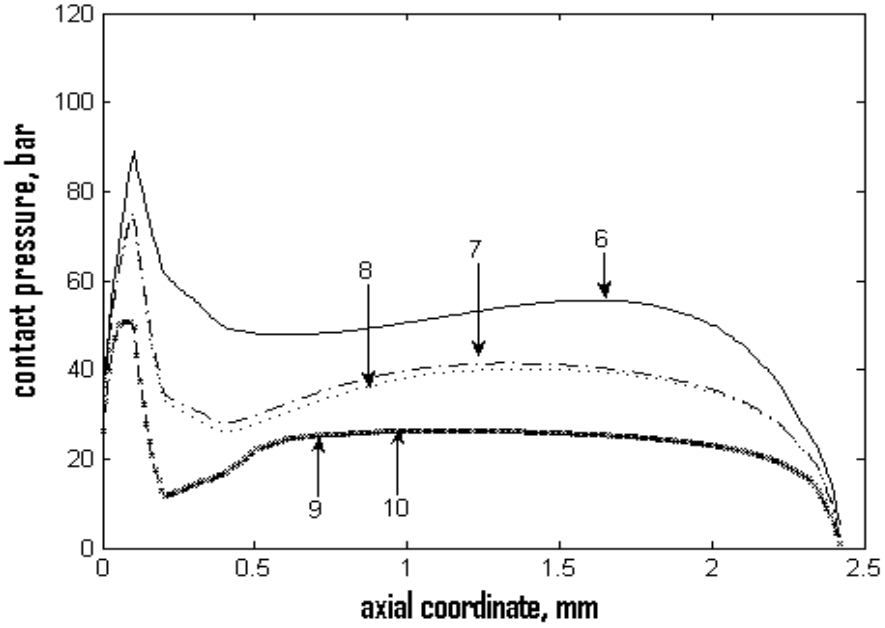

Figure 3.22: Contact pressure distribution, instroke

At time 2 during the outstroke, the film thickness is decreasing due to the increasing rod velocity, as discussed above. Therefore, one would expect the squeeze film effect to increase the fluid pressure above the quasi-steady value. Conversely, at time 3 the film thickness is increasing due to the decreasing rod speed, and the squeeze film effect would decrease the fluid pressure below the quasi-steady value. Thus, one would expect the fluid pressure profile at time 2 to be above the profile at time 3. This indeed occurs, as can be seen from Figure 3.19. The opposite behavior occurs during the instroke. At time 7 the film thickness is increasing due to the increasing magnitude of the velocity, and therefore the fluid pressure should be decreased, below the quasi-steady value. At time 8 the film thickness is decreasing, and the fluid pressure should be increased, above the quasi-steady value. Thus, the fluid pressure profile at time 7 should be below that at time 8. This is again seen from Figure 3.20. These differences in the pressure profiles are reflected in differences in the film thickness profiles, Figure 3.17 & Figure 3.18 and in the contact pressure profiles, Figure 3.21 & Figure 3.22.

3.9 Conclusions

A multi-scale multi-physics model and hybrid computational framework is developed. The framework allows solving macro-scale deformation and contact mechanics and micro-scale fluid / contact/ deformation mechanics equations in a strongly coupled manner.

Using this MSMP framework, a reciprocating hydraulic rod seal with time varying rod velocity is analyzed. Deformation mechanics calculations showed the stress concentration areas within the seal body and their effect on dry contact pressure

distribution in the sealing zone. The results from the analysis show that a transient EHL analysis can reveal the history of a reciprocating seal's behavior over a cycle. It has confirmed earlier conclusions of steady-state analyses regarding the importance of seal roughness, and that thinner films during the outstroke than during the instroke, and cavitation during the outstroke, are characteristics of non-leaking seals. It has also provided insight into why the fluid pressure, film thickness and frictional behaviors during outstroke and instroke differ significantly.

The MSMP framework developed in this chapter has showed the potential to serve as the backbone for more complex sealing dynamics that will be discussed in the next chapters.

CHAPTER 4. SURFACE CHARACTERIZATION

The micro-scale contact mechanics in the MSMP model is calculated using Greenwood-Williamson asperity contact mechanics theory which uses statistical parameters of a rough seal surface. These parameters include RMS surface roughness, asperity density (number of asperities per unit area) and average asperity radius. Since the wear of the soft surfaces can significantly alter its statistical properties, the quantities like average roughness and asperity density depend on the application in which the seal is used as well as the length of its usage. Hence we need to extract the surface roughness parameters for a seal which is actually being used in the application of interest. In an attempt to extract these parameters experimental methods like Optical Profilometry, Scanning Electron Microscopy and Atomic Force Microscopy are employed in this study.

In a method like optical profilometry, the surface profile produced by the optical interference fringes is observed to have several artificial peaks resulting from the noise associated with the interferometry. If not identified and removed, these noise peaks can seriously alter the values of the statistical roughness parameters discussed earlier. Hence, we need a method to filter out these features related to noise from rest of the data before making any statistical estimation of surface properties. Traditional Fourier transform based filtering methods do not serve this purpose well, as they can not distinguish between high frequency roughness features from the high frequency noise. To remedy this problem, a wavelet transform based adaptive surface extraction technique is employed in this work and will be discussed in following sections.

4.1 Statistical Parameters of the Surface

In order to adequately describe the surface profile, we need to rely on a combination of different parameters. Some of these parameters are Center Line Average (R_a), RMS roughness (σ), Autocorrelation Length (L_A), Peak to Valley Height (PV), Asperity Density (η)and Average Asperity Radius. The Autocorrelation function, $\rho(\tau)$ provides information about the spatial distribution of roughness. If the surface contains an inherent periodicity of spatial wavelength λ then $\rho(\tau)$ will display a characteristic sinusoidal shape having maxima whenever $\tau = n\lambda$. For random surfaces, the first zero crossing point of $\rho(\tau)$ indicates the distance along the surface at which the surface becomes uncorrelated. The Autocorrelation length (ACL) gives the distance where $\rho(\tau)$ first crosses zero. It can be thought of as the minimum distance along the profile where one point has no relation to the next.

Parameters η and R are highly scale dependent, while the autocorrelation length is relatively independent to the sampling interval. Hence one way of estimating asperity density, η, is using the autocorrelation length, ACL. Assuming the surface roughness to be isotropic, considering autocorrelation length to be the average distance between the two asperities, and taking asperity radius equal to autocorrelation length, η can be computed from the relation, $\eta = \frac{1}{(ACL/2)^2}$. Another way of estimating asperity density is directly from the optical profilometry data which computes the asperity density by measuring the number of peaks per unit scan area. However as mentioned, the asperity density obtained from this method is dependent on the scale of the scan. σ and ACL can

be measured directly from the optical profilometry data as well. It should be noted that the results of the MSMP model are sensitive to the values of asperity radius and asperity density through the dependence of contact pressure on the product $R^{1/2}\eta$ (as seen from Eq. 3.34). Although, the contact pressure (and hence film thickness and fluid pressure) distribution changes with variation in measured values of R and η, the results of MSMP model qualitatively follow the similar behavior as discussed in chapter 3.

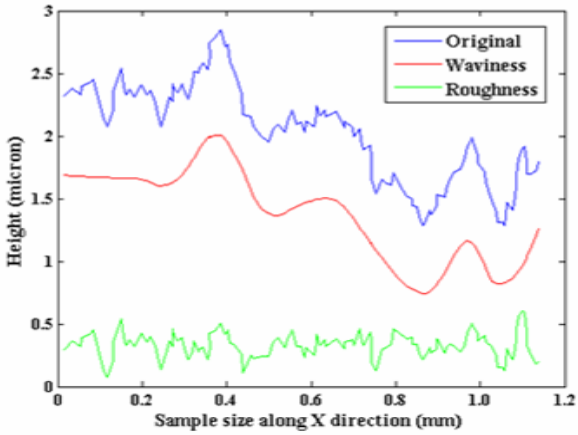

Figure 4.1: Decomposition of surface profile into waviness and roughness.

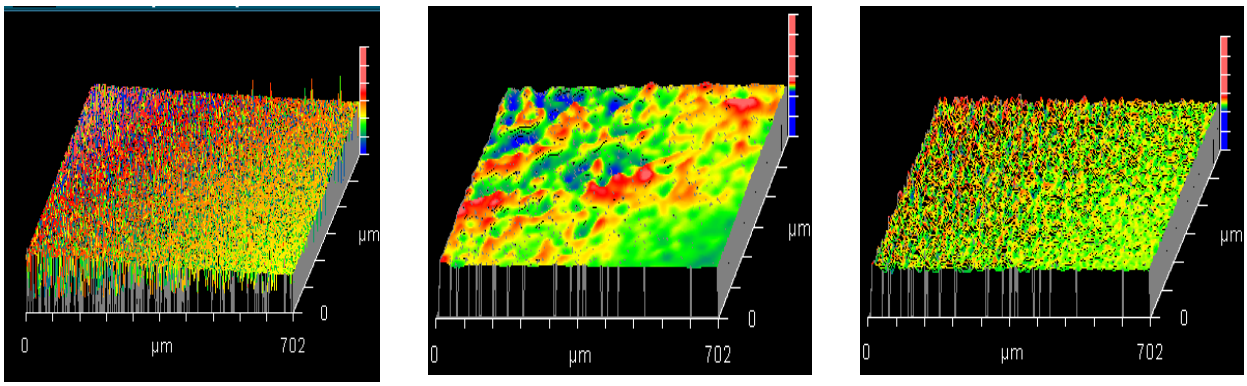

Original Profile **Waviness Component** **Roughness Component**

Figure 4.2: Decomposition of 3D optical profile of a PTFE seal surface into waviness and roughness components.

Figure 4.1 shows the 1D scan of a rough seal surface. The surface can be seen to possess two main features called “Waviness” and “Roughness”. Waviness is due to the undulations with relatively long wavelength which form underlying broader profile while roughness are the variations with much shorter wavelengths (high frequency) and lie on the top of the underlying profile. It is essential to decompose the surface profile into waviness and roughness components before we extract the statistical parameters pertaining to the roughness. We can achieve this decomposition using Fast Fourier Transform (FFT) based filtering algorithm. Results of such decomposition for a PTFE seal surface are shown in Figure 4.2.

4.2 Wavelet Transform based Adaptive Surface Extraction

One of the drawbacks of roughness measurement using optical Profilometer is the presence of artificial peaks in the surface profile that stem from the noise associated with acquisition of optical interference fringes. These spikes seriously affect the measured values of RMS roughness and asperity density. One way to get rid of these spikes is using Fourier domain low pass filtering. However, using such a low-pass filter also removes some of the high frequency components of “real” roughness features. This is certainly not recommended as the RMS roughness would be altered significantly if a large component of high-frequency roughness features lies in the spectral range above the cut-off frequency. As a result, removing the noise spikes without removing the high frequency surface features is a challenging problem to solve. Wavelet based de-noising techniques become useful in such problems and hence a wavelet transform based surface extraction

method is employed here to extract the real surface profile from that corrupted by noise spikes.

4.2.1 Mathematical Background for Wavelets

One of the disadvantages of the Fourier expansion is that it has only frequency resolution but no time (or spatial) resolution. Also, by definition, the sines and cosines that form basis functions in Fourier analysis are "non-local" and therefore do not do a very good job in approximating sharp spikes. On the other hand, the supports of wavelet functions are finite (compact) and hence wavelets are "localized". This makes wavelets suitable for applications where temporal location of the signal's frequency content is important and hence for approximating signals with sharp discontinuities. Wavelet basis is a set of functions generated by dilation and translation of a single "Mother" wavelet function, along with a scaling function. The fundamental idea behind wavelets is to analyze according to scale. Wavelet algorithms process data at different scales or resolutions. The function ϕ is defined as a "scaling function" and the set of functions $\{\phi(t-k): k \in \tilde{Z}\}$ forms the orthonormal basis of subspace V_j ($V_{j-1} \subset V_j \subset V_{j+1} \subset ...L^2$). A "wavelet" function ψ is also defined such that $\{\psi(t-k): k \in \tilde{Z}\}$ forms the basis for subspace W_j which is the orthogonal complement of subspace V_j [92] such that:

$$V_j \oplus W_j = V_{j+1} \tag{4.1}$$

Hence wavelet ψ lies in the orthogonal complement of subspace V_j. Eq.(4.1) allows that ψ captures the local fluctuations in the signal while ϕ captures the broader trend in the signal.

The main concept of wavelet decomposition is the representation of an arbitrary function as a combination of basis functions, generated as scaled and translated versions of an oscillatory "Mother" function. Temporal analysis is performed with a contracted, high-frequency version of the mother wavelet, while frequency analysis is performed with a dilated, low-frequency version of the same wavelet. This "Mother" wavelet is used to generate a set of "daughter" functions through the operations of scaling and translation as follows,

$$\psi_{j,k}(x) = 2^{j/2}\psi_{0,0}\left(2^{j}x - k\right) \tag{4.2}$$

Figure 4.3 shows various daughter wavelets obtained by scaling and translation of mother "S8 Symlet". First index in the parenthesis indicates the scale and second number indicates the location. It can be seen that the two red curves have the same scale (3) but different locations (2 and 5). Similarly the two green curves have same scale (6) but are shifted in location (30 and 50). It can also be noticed that as the scale reduces, the wavelets get spatially stretched. By using various scale and location indices we can capture the finer details of a signal effectively.

Another important concept in the wavelet's multi-resolution analysis is the "two-scale relationship" [70-71], which says that there exist real valued sequences $\left\{h(n) : n \in \tilde{Z}\right\}$ and $\left\{g(n) : n \in \tilde{Z}\right\}$ such that [92],

$$\begin{aligned} \phi(2^{j}x) &= \sum_{n} h_{j+1}(n)\, \phi(2^{j+1}x - n) \\ \psi(2^{j}x) &= \sum_{n} g_{j+1}(n)\, \phi(2^{j+1}x - n) \end{aligned} \tag{4.3}$$

Taking into consideration the orthonormality of basis functions $\{\phi\}$ and $\{\psi\}$ and orthogonality of functional subspaces V_0 and W_0, it can be shown that,

$$g(n) = (-1)^n h(1+2k-n) \tag{4.4}$$

where k is a pre-determined integer. Eq. (4.4) is the expression for "quadratic mirror filter" which is used in the wavelet decomposition used for calculating the discrete wavelet transform coefficients in this study. Sequence $h(n)$ acts as a low pass filter and sequence $g(n)$ acts as a high pass filter.

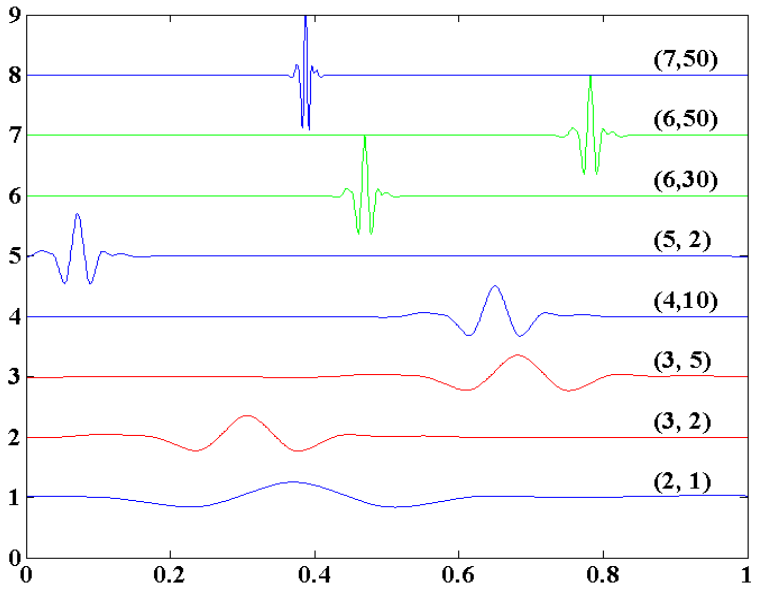

Figure 4.3: Daughter wavelets obtained by scaling and translation of a mother "S8 Symlet". First index in parenthesis indicates the scale and second index shows the location.

Discrete Wavelet Transform (DWT) and Wavelet Decomposition

Consider α_k^j as a coefficient of a wavelet transform of a signal $f(x)$ and corresponds to the k^{th} scaling function at the j^{th} scale and $\beta_{k'}^j$ as a coefficient of a transform of $f(x)$ and corresponds to the k'^{th} scaling function at the j^{th} scale, then

$$\alpha_k^j = \int f(x)\,\phi(2^j x - k)\,dt$$
$$\beta_{k'}^j = \int f(x)\,\psi(2^j x - k')\,dt \tag{4.5}$$

Using Eq. (4.3),

$$\alpha_k^j = \sum_n h(n)\,\alpha_{n+2k}^{j+1}$$
$$\beta_{k'}^j = \sum_n g(n)\,\alpha_{n+2k}^{j+1} \tag{4.6}$$

Eq. (4.6) determines the wavelet transform coefficients (two-scale relationship) in the discrete algorithm. It states that the wavelet and scaling function coefficients on a certain scale can be found by convolving low pass filter ($h(n)$) and high pass filter ($g(n)$) with the scaling function coefficients from the previous scale. Also, Eq. (4.6) states that the sequence α^{j-1} is a downsampled version of a convolution of two sequences α^j and h and β^{j-1} is a downsampled version of a convolution of sequences α^j and g. Starting with α^j in subspace V_j, we get sequences α^{j-1} and β^{j-1} (using Eq. (4.6)) corresponding to decompositions in subspaces V_{j-1} and W_{j-1}, respectively. We continue this process until it stops at scale 0. The set $\alpha^0 \cup \beta^0 \cup \beta^1 \cup ... \cup \beta^{j-1}$ gives us the DWT of the sequence α^j.

Such a signal decomposition described can be achieved using a "filter bank", where the coefficients $h(n)$ correspond to a low pass filter giving us a "big picture" of the signal and the coefficients $g(n)$ correspond to a high pass filter providing us with "details" of the signal. We can assume the signal to be made up of some basic components, with different components residing at different frequencies. Taking a "perfect" low-pass filter and a perfect high-pass filter, we simultaneously apply this pair

of filters and divide the signal into two parts: one part contains only low-frequency components; the other part, high-frequency components. Typically, the low-frequency part is more important, and we want to know more about its structure. Hence we again deploy a pair of filters on the low-frequency part and repeat the process. In this way, we get a detailed structure in the low frequency part; at the same time, we keep the information in the high frequency part. This is shown schematically in Figure 4.4 (a). $L.P$ stands for a low-pass filter and $H.P$ stands for a high-pass filter.

Figure 4.4 (b) shows the decomposition of a noisy 1D signal using wavelet filter. cA_1 are the approximation coefficients and cD_1 are the detail coefficients at level 1 of decomposition obtained by convolving the signal with low-pass and high-pass wavelet decomposition filters (Figure 4.5 (top)) respectively. The signal reconstructed using just these approximation coefficients is shown in blue. The signal component obtained using coefficients cA_1 is then again convolved with low-pass and high-pass decomposition filters to get the approximation and detail coefficients cA_2 and cD_2 at level 2. The output of this wavelet decomposition process is the vector $c = \left[\left[cA_2\right]\left[cD_2\right]\left[cD_1\right]\right]$ which is then passed on to the "thresholding" step of the algorithm. Coefficients output from the thresholding step are used in the global "reconstruction" step to reconstruct the signal using thresholded wavelet coefficients and the low-pass and high-pass reconstruction filters (Figure 4.5 (bottom)). From (Figure 4.5 (top)) it can be seen that there are only a few filter elements with significant amplitudes and hence provide localization for capturing sharp features / abrupt changes in the signal.

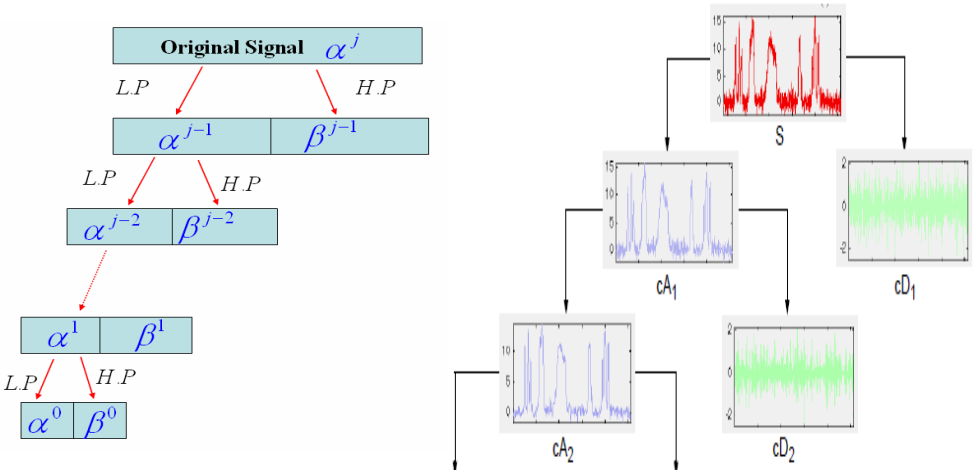

Figure 4.4: **(a) Discrete Wavelet Transform Coefficient Calculation (b) Components of a 1D surface signal reconstructed using approximation coefficients cA_i and detail coefficients cD_i at decomposition level i .**

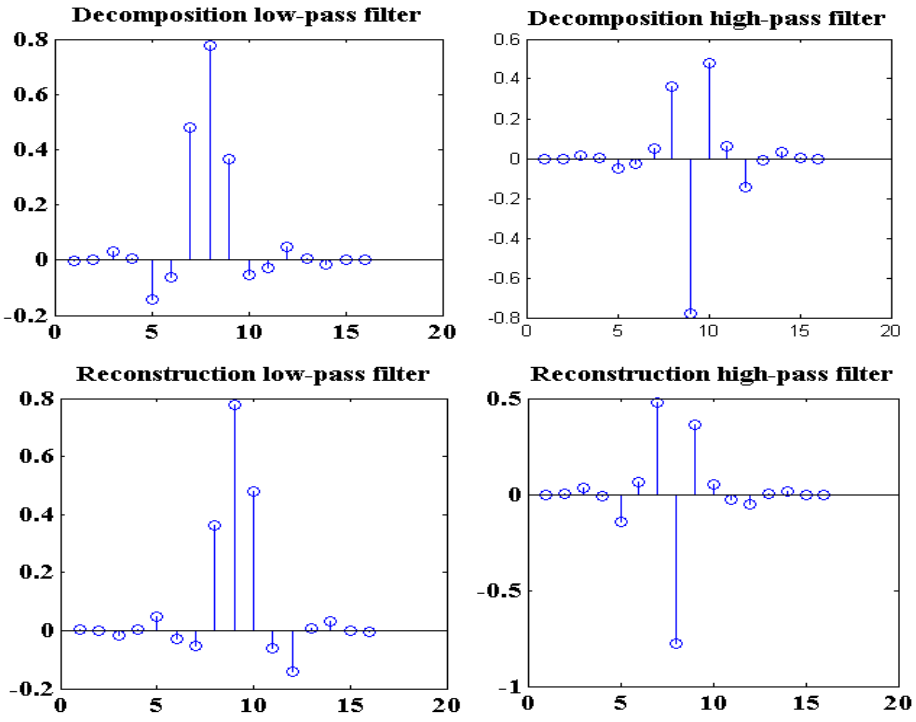

Figure 4.5: **Low-pass and high-pass decomposition and reconstruction filters obtained using Symlets of order 8.**

4.2.2 Using Wavelets for Surface De-noising

After attempting a wavelet decomposition of a 1D noisy signal as discussed in the previous section, now we use the wavelet decomposition for "intelligent" de-noising of the actual surface data obtained from optical profilometry on polyurethane seal surface. Since we are dealing with 2D surface data instead of 1D signal, we need to use 2D wavelets. The wavelet decomposition works on similar grounds as described in previous section, with little modifications as described below.

4.2.2.1 *2D Wavelet Decomposition*

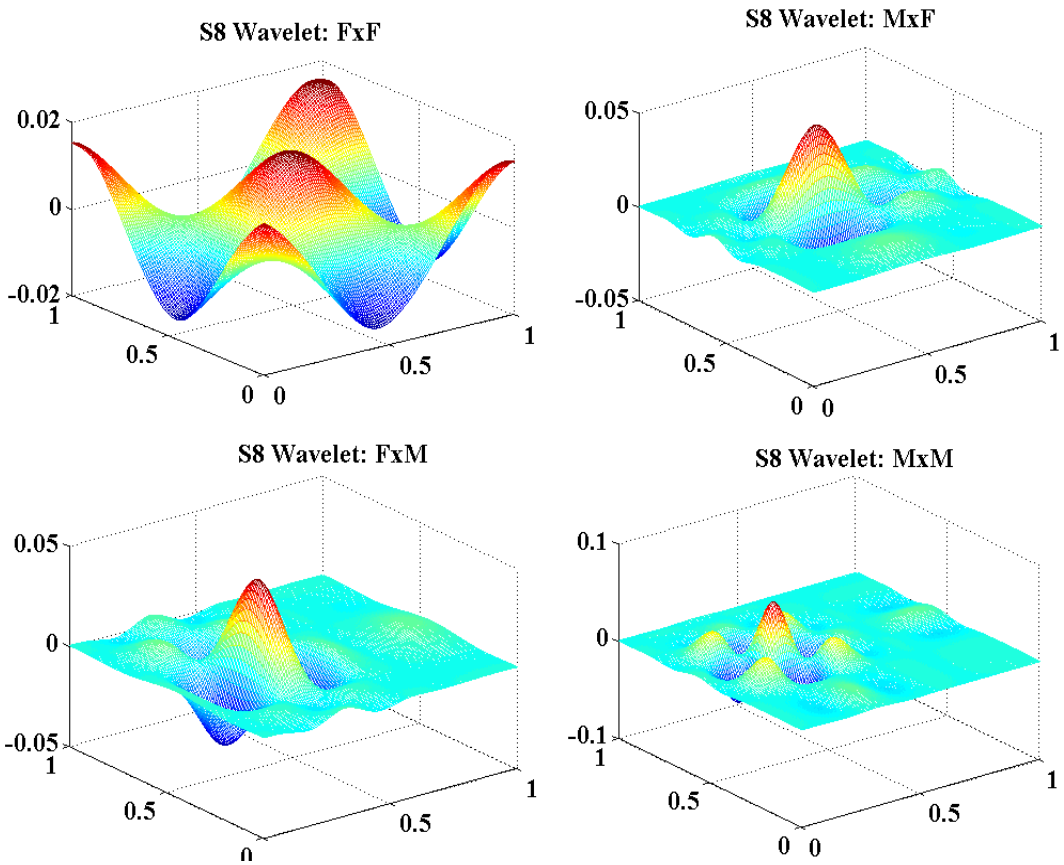

Figure 4.6: 2D Symlets of order 8 obtained from tensor products of Father Wavelet (F) and Mother Wavelet (M).

2-D wavelets are obtained by taking a tensor product of two 1-D wavelets and hence 2-D wavelet is a spatially localized function. Figure 4.6 shows Symlet wavelets of order 8 obtained from tensor products of a father wavelet and a mother wavelet. The decomposition structure for a 2D case works in a similar manner as a 1D case, but has convolutions with filters performed along both, the rows and the columns as shown in Figure 4.7. Operator "*" in the figure denotes the convolution operation. After the convolution of rows with L.P and H.P filters, columns are down-sampled by a factor of 2 as indicated by $Cols\downarrow$ and after convolution of columns with L.P and H.P filters, rows are down-sampled by a factor of 2 as indicated by $Rows\downarrow$.

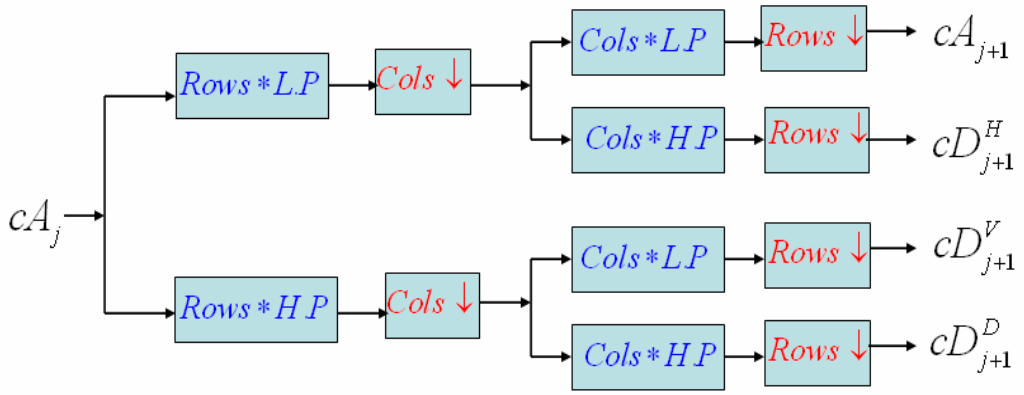

Figure 4.7: 2D wavelet decomposition algorithm.

In such a 2D discrete wavelet transform, the approximation coefficients at level j are decomposed into 4 components: 1 approximation coefficient vector at level j+1, and 3 detail coefficient vectors corresponding to 3 directions: horizontal (superscript H), vertical (superscript V), and diagonal (superscript D). At the start of the decomposition process, $cA_0 = original\ 2D\ signal$. This 2D wavelet decomposition strategy was applied to the surface profile of a real polyurethane seal surface. The profile of this surface

directly obtained from the optical profilometry is shown in Figure 4.9 (a) and indicates the presence of several "artificial" spikes as discussed before. This profile served as an input to the 2D wavelet decomposition algorithm. The 2D wavelets selected were Symlets of order 8 (Figure 4.6). Corresponding low-pass and high-pass decomposition and reconstruction filter coefficients were calculated and are same as the ones shown in Figure 4.5. Decomposition was performed up to level 3.

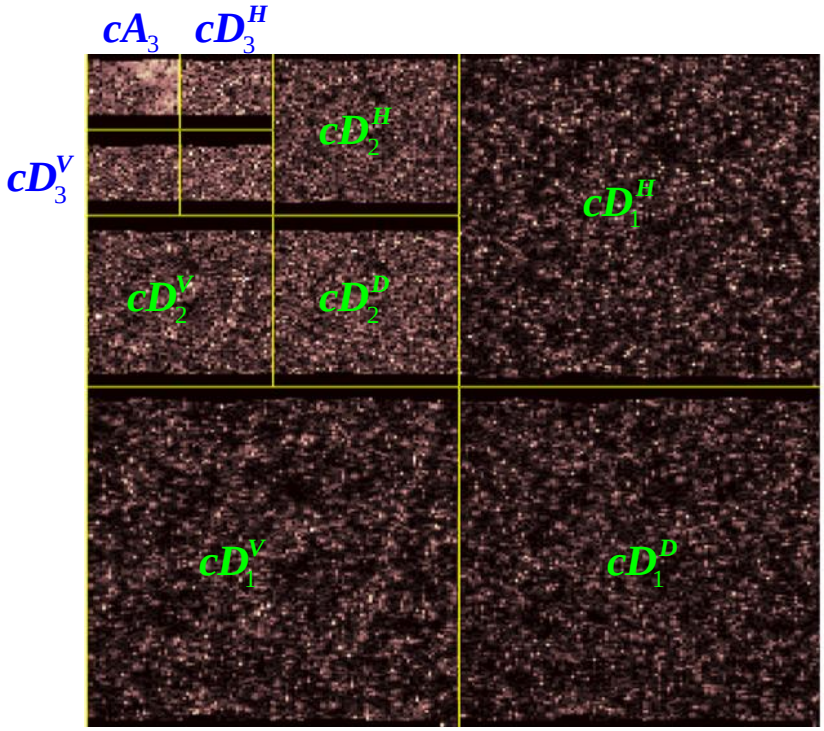

Figure 4.8: Wavelet decomposition of the surface profile of a polyurethane seal showing approximation and detail wavelet coefficients at 3 levels.

Figure 4.8 shows the result of this decomposition of the surface profile. Surface component corresponding to approximation coefficient at level 3 is shown by cA_3 and the surface components corresponding to the horizontal, vertical and diagonal detail

coefficients at level j are shown by cD_j^H, cD_j^V and cD_j^D respectively. As expected from "two-scale relationship", the size of the images at level 3 is 1/4th that at level 2 and 1/16th of that at level 1. cD_3^H, cD_3^V and cD_3^D capture finer details than cD_2^H, cD_2^V and cD_2^D which in turn capture finer details than cD_1^H, cD_1^V and cD_1^D. The output of this wavelet decomposition is the array,

$c = \left[\left[cA_3 \right] \left[cD_3^H \right] \left[cD_3^V \right] \left[cD_3^D \right] \left[cD_2^H \right] \left[cD_2^V \right] \left[cD_2^D \right] \left[cD_1^H \right] \left[cD_1^V \right] \left[cD_1^D \right] \right]$ which is then passed to the thresholding scheme.

4.2.2.2 *Wavelet Coefficient Thresholding*

After computing the wavelet decomposition coefficients as discussed above, thresholding of the detail coefficients is performed to get rid of the coefficients that approximately correspond to the unwanted noise and to retain only the ones of interest. Hard thresholding consists of setting to zero the elements whose absolute values are lower than the threshold, while in a soft thresholding scheme, first the elements whose absolute values are lower than the threshold are set to zero and then the nonzero coefficients are shrunk towards 0. Soft thresholding has some nice mathematical properties [93]. Here we choose to apply the soft thresholding scheme which is given by function η_T,

$$\eta_T(w_j) = sign(w_j)\left(\left|w_j\right| - T\right)_+ \tag{4.7}$$

where w_j are the wavelet coefficients, $sign()$ is the sign of the univariate argument, T is the threshold value and $(P)_+ = 0 \; if \; P < 0 \;\; and \;\; (P)_+ = P \; if \; P \geq 0$.

The value of the threshold T can be estimated using various methods. We have experimented with a couple of different methods in this work. In the first method, the threshold can be estimated based on a value of noise at a given level scaled by a factor,

$$T = \sigma_j \sqrt{2\ln(N)} \tag{4.8}$$

where N is the number of elements in the wavelet coefficient vector and σ_j is a measure of the median noise at level j and it can be approximated using $\sigma_j = median(abs(c_D))$. Here c_D is the output vector from wavelet decomposition as discussed earlier , except the first element, which is the approximation coefficients.

In the second method, an adaptive, level dependent scheme proposed by Donoho [93] and the Stein's unbiased risk estimate [94] is used to get a risk function, R_S. The threshold, based on the observed data, is then chosen such that it minimizes the risk function as follows:

$$\begin{aligned} T = & \quad \arg\min \quad R_S(x,T) \\ & 0 \le T \le \sqrt{2\log N} \end{aligned}$$
$$R_S(x,T) = N - 2\cdot\#\left\{i : |x_i| < T\right\} + \sum_{i=1}^{N}\left\{\min\left(|x_i|, T\right)\right\}^2 \tag{4.9}$$

where # denotes the cardinality of the set. This second method of threshold estimation is more conservative than the first one and is more convenient when small details of the signal lie near the noise range. On the other hand first method removes the noise more effectively.

4.2.2.3 ***Overall Algorithm***

The overall algorithm for wavelet transform based adaptive surface extraction works as follows:

1. A "mother" wavelet is selected as the basis function. The choice is made from a large number of available wavelets, e.g. Daubechies, Symlet, Coiflets, Haar etc (based on improvements in signal to noise ratio of sample 1D signals).
2. Low-pass and high-pass decomposition filters are created based on the mother wavelet chosen.
3. The level N of decomposition is chosen.
4. Signal is decomposed using discrete wavelet transform. For this, the original signal is convolved with the low-pass filter coefficients to get approximate coefficient vector and with high-pass filter coefficients to get the detail coefficient vector (H,V,D) at first level.
5. For each level from 2 to N-1 approximate coefficients are convolved again with low-pass and high-pass filters to get approximate and detail coefficients at next level.
6. At each level, the detail coefficient vector is thresholded using soft thresholding and the threshold selection scheme discussed earlier.
7. Low-pass and high-pass reconstruction filters are created based on the mother wavelet function.
8. Signal reconstruction is performed using inverse discrete wavelet transform. For this the approximation coefficients at level N and thresholded detail coefficients at levels 1 through N are convolved with the reconstruction filters from step 7 to obtain the signal reconstruction in the original spatial domain.

It should be noted that for any mathematical algorithm, it is not possible to classify a surface peak as "noise" with 100 % surety without the understanding or expectation of the true physical characteristic of the surface. This is true even for the wavelet algorithm. Since we have an approximate idea of how a seal surface profile should look like and knowing that the artifacts introduced by interferometry are of significantly higher amplitude than nominal roughness features of the seal surface, for our purpose, the signal component that is above a certain threshold value can be considered to be the noise. However, in this algorithm, the threshold value is not chosen manually but is decided adaptively using a threshold selection scheme based on the noise level at a given wavelet decomposition level. The advantage of wavelet algorithm lies in the fact that due to its multi-level decomposition and the thresholding at each of these levels, it can detect and remove the sharp spikes much more effectively than some of the other noise-removal methods.

4.2.2.4 ***Results from Wavelet De-noising of Polyurethane Seal Surface***

Optical profilometry results of several seal surfaces are processed through this wavelet transform based adaptive surface extraction algorithm to get de-noised surface profiles while still retaining high frequency surface features of interest. The results obtained for one such polyurethane seal surface are shown in Figure 4.9. Part (a) shows the surface profile obtained from optical profilometry. This is before wavelet de-noising. Part (b) shows the surface profile obtained after wavelet de-noising of the surface in part (a). It can be seen that almost all the spikes from noise are cleanly removed without removing much of the finer "real" surface features of interest.

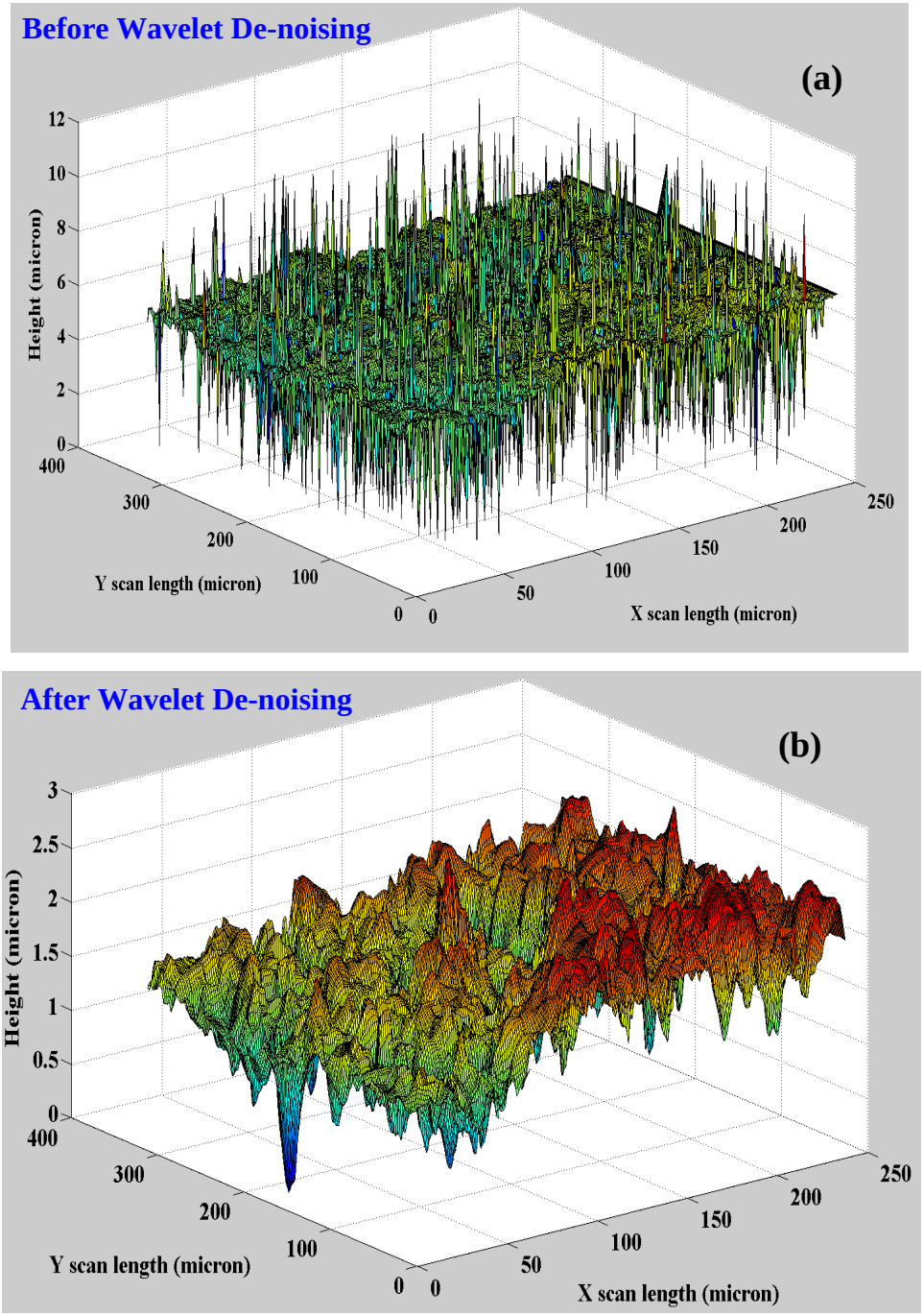

Figure 4.9: **Surface profile of a polyurethane seal before and after wavelet de-noising.**

The RMS roughness estimated from the raw data was much higher (~ 5.5 micron) while the RMS roughness value obtained after wavelet de-noising was 1.4 micron. Thus these artificial noise spikes if not removed could have seriously overestimate the roughness value. Applying a general low-pass filter to the raw data to get rid of noise spikes, also gets rid of some of the "real" details of the surface and reduces the RMS value (~ 0.7 micron) giving a false estimation of roughness statistics. This is the reason the wavelet based adaptive surface extraction method discussed in this study is a valuable tool for the seal's surface characterization and is needed for the accurate parameter estimation for the MSMP model.

4.3 Surface Characterization Results

Surface characterization studies are performed on several different seals (both, unused and used with long run-in periods) obtained from seal manufacturers and industrial seal users (Hallite, Trelleborg, Eaton etc.). The seals analyzed include PTFE, Nitrile and Polyurethane seals. After performing optical profilometry, least-squares surface is fit and removed to get rid of the overall form in the data. It also removes any z-axis offset and residual tilt present after nullifying the optical fringes. Profile is then decomposed into the waviness and roughness components using FFT based filtering. If needed, wavelet de-noising is performed to get rid of noise-induced spikes.

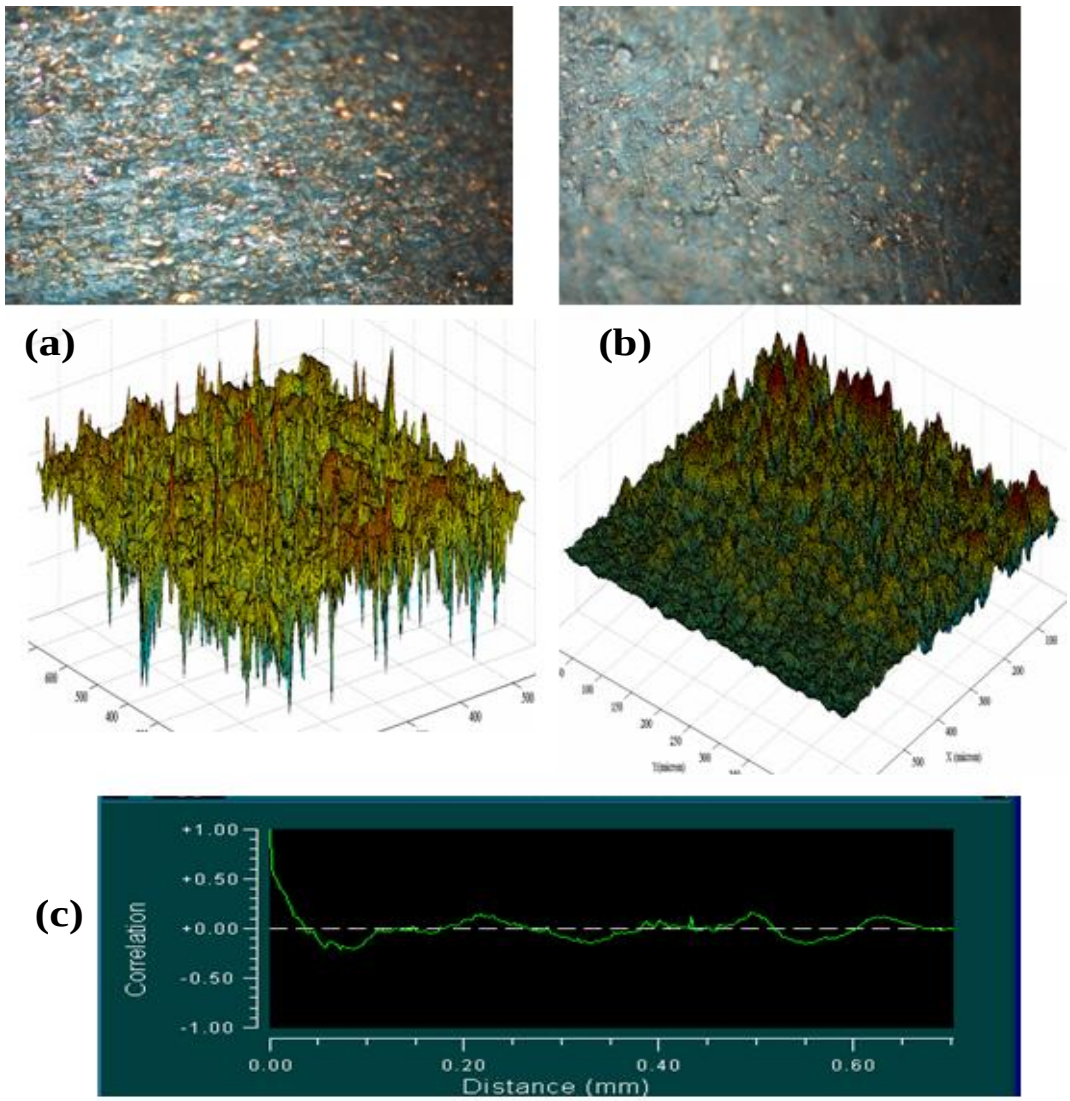

Figure 4.10: (a) Unused PTFE seal surface and its roughness profile. (b) Used PTFE seal surface and its roughness profile. (c) Auto-covariance function showing correlation length for the unused seal.

Table 4.1: Surface parameters obtained for the seals in Figure 4.10.

Seal	Ra (micron)	Rq (micron)	Average ACL (mm)	Asperity Density (# / m^2)
Unused PTFE	3.16	4.51	0.05	$5x10^{11}$
Used PTFE	6.52	9.116	0.03	$5x10^{11}$

The roughness profile thus obtained is then used for extracting Ra, Rq, ACL and Asperity density for each surface. The results for some sample seals are presented below. Figure 4.10 (a) shows the optical microscope image of an unused PTFE seal surface. It can be seen that the surface has no directionality and it is reflected in it's surface profile. The surface of a used PTFE seal on the other hand Figure 4.10 (b) can be seen to be smoothened out due to "run-in" period but at the same time it also starts to show some pattern and this is reflected in its autocorrelation length which decreases from that of unused seal. The autocorrelation function for the unused seal is plotted in part (c) of the figure. The surface parameters obtained for these two seals are listed in Table 4.1.

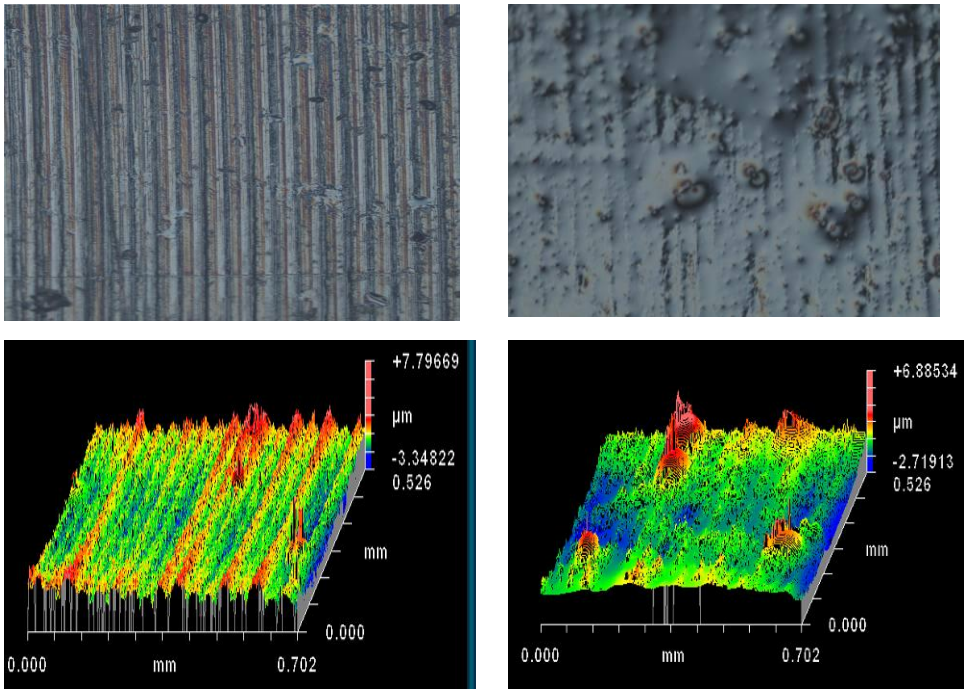

Figure 4.11: (a) Unused Hallite Polyurethane seal surface and its roughness profile. (b) Used Hallite Polyurethane seal surface and its roughness profile.

Table 4.2: Surface parameters obtained for the seals in Figure 4.11.

Seal	Ra (micron)	Rq (micron)	Average ACL (mm)	Asperity Density (# / m^2)
Unused Polyurethane	0.675	0.845	2.5	$1.5x10^{12}$
Used Polyurethane	0.598	0.830	3.2	$1.1x10^{12}$

Figure 4.11 (a) shows the surface of an unused Hallite Polyurethane seal. A homogeneous looking surface to a naked eye revealed a pattern of ridges along Y direction in the optical profilometry data as seen in the figure. This was a surprising finding and is thought to be arising from the seal manufacturing process. With this directionality in the surface, the statistical parameters can be expected to be very different than that for the seal of Figure 4.10. This indeed is found as seen from Table 4.2. Part (b) of the figure shows the surface of a used Hallite Polyurethane seal manufactured with the same manufacturing process but used in an industrial application for long run-in period. The microscope image shows the wear of the ridges. The profilometry data shows the reduction in the strength of directionality. As expected the ACL is found to increase from 2.5 micron for unused surface to 3.2 micron for the used surface.

Figure 4.12 shows heavily used and lightly used Hallite Polyurethane seals. In the lightly used seal (b), the surface still has a strong presence of ridges which gives it lower ACL than the heavily used seal surface. Table 4.3 lists the roughness parameters, autocorrelation lengths and asperity density values for these two seals.

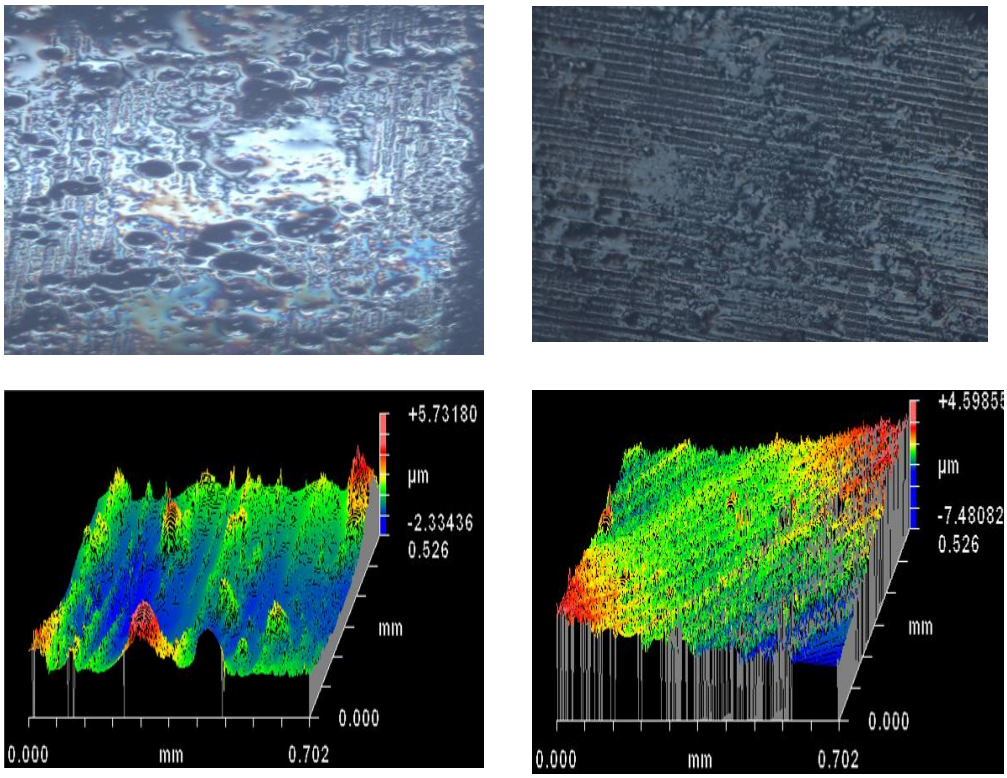

(a) **(b)**

Figure 4.12: (a) Heavily used Hallite Polyurethane seal surface and its roughness profile. (b) Lightly used Hallite Polyurethane seal surface and its roughness profile.

Table 4.3: Surface parameters obtained for the seals in Figure 4.12.

Seal	Ra (micron)	Rq (micron)	Average ACL (mm)	Asperity Density (# / m^2)
Polyurethane (a)	0.616	0.824	2.7	$8x10^{11}$
Polyurethane (b)	0.496	0.623	2.3	$1x10^{12}$

Figure 4.13 (a) shows a used PTFE seal surface which looks statistically random and "perfect" under small optical magnification. However this particular seal showed unusual leakage characteristics than rest of the seals in the same production batch and hence was selected for investigation. Upon performing optical profilometry, it showed missing data points in a circular pattern, (part (c) and (d) of the figure). This was

intriguing and hence the seal surface was again observed under 100x optical magnification. Under this magnification the seal surface revealed a large circular hole of ~ 150 micron diameter. This hole was a surface defect either from the manufacturing process or produced during run-in and is thought to be the cause of the unexpected fluid leakage observed experimentally. Corresponding roughness parameters obtained are listed in Table 4.4.

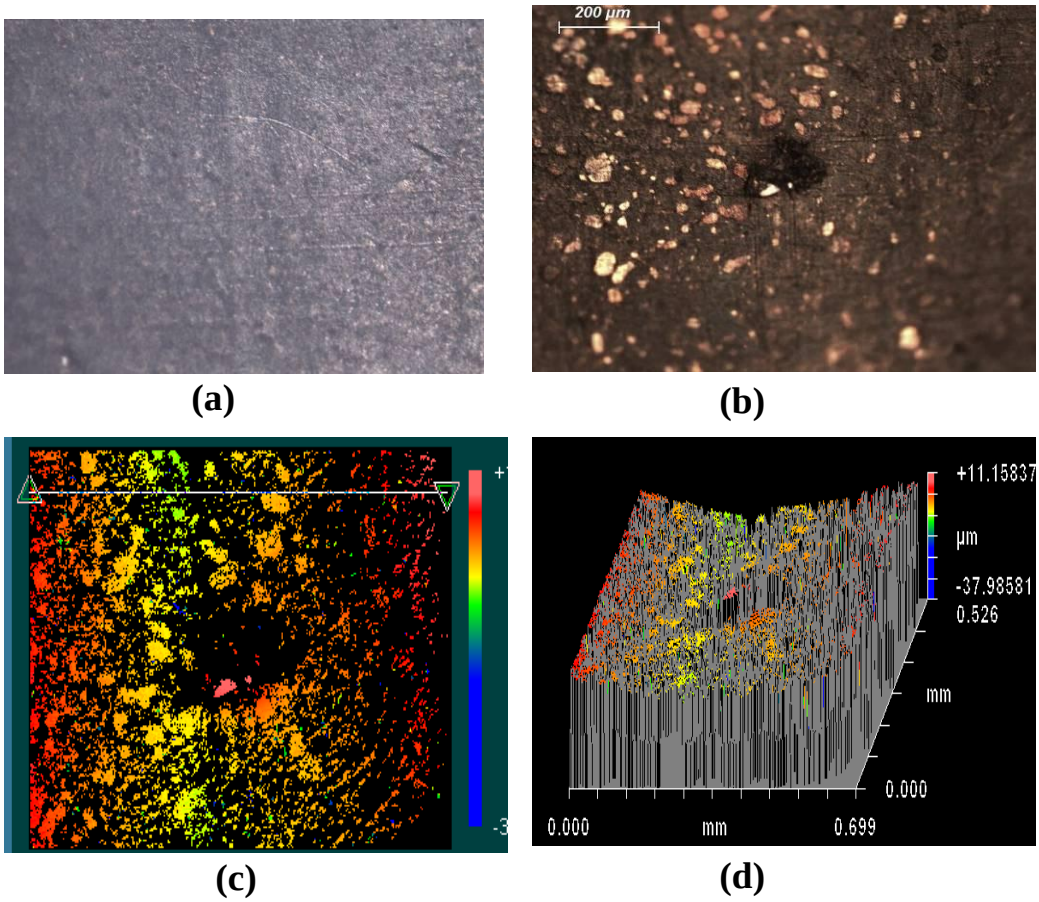

(a) **(b)**

(c) **(d)**

Figure 4.13: (a) Used PTFE seal surface at 10x optical magnification. (b) Seal surface at 100x optical magnification. (c) Color map of surface heights. (d) 3D surface profile

Table 4.4: Surface parameters obtained for the seals in Figure 4.13.

Seal	Ra (micron)	Rq (micron)	Average ACL (mm)	Asperity Density (# / m^2)
Used PTFE	2.52	3.58	—	—

4.4 Conclusions

Surface characterization of various seal surfaces is performed to get the surface parameters needed for the MSMP model. The optical profilometry proved to be a valuable tool to visualize surface features and extract statistical surface parameters like average roughness, RMS roughness, autocorrelation length, peak to valley distance and asperity density. It also revealed some of the defects in seal surfaces that were not visible to naked eye or to under small optical magnifications. Tracking such surface defects provided a rationale for understanding some of the anomalies in the seal performance characteristics that were observed experimentally.

A wavelet transform based adaptive surface extraction method is implemented to get rid of the noise-induced spikes in the surface profiles that occur during the acquisition of optical interference fringes. Such spikes can seriously overestimate the roughness values. Wavelets are localized and have a compact support. Using wavelet decomposition and a multi-resolution analysis, the noise-induced features can be effectively removed without removing the real high frequency surface features. The wavelet based method served as a valuable tool in accurate estimation of statistical surface parameters which are needed for the MSMP micro-scale contact mechanics calculations.

CHAPTER 5. MSMP SEAL MODEL WITH TRANSIENT SEALED PRESSURE

5.1 Introduction

Important details of rod seal operation were revealed by MSMP model of the reciprocating rod seal developed in previous chapter. That model traced the history of seal behavior resulting from a time varying rod speed. It was found that the behavior is quite different during outstroke and instroke: during the outstroke the fluid pressures in the interface decrease with increasing rod speed, while during the instroke they increase with increasing rod speed. Cavitation was observed during outstroke and the effect of hydrodynamics on the frictional characteristics was found to be quite different during outstroke than during the instroke. This transient study was performed holding the sealed pressure constant. However, in an actual sealing application like Injection Molding, the sealed pressure, as well as the rod velocity, varies with time. Since the time-varying sealed pressure produces significant time-variations in the seal geometry, the complexity of the analysis is significantly increased. With transient sealed pressure, the sealing zone changes with time and hence the whole computational domain for micro-mechanics calculations changes at each time step. To tackle this problem, significant modifications need to be made in the MSMP framework. Such an analysis is the subject of study in this chapter.

5.2 Model and analysis

Since the rod is much smoother than the seal lip due to polishing during the run-in period, the rod is treated as perfectly smooth while the seal lip is treated as rough, as discussed in the previous chapter. The MSMP model of such a seal consists of macro-and micro-scale deformation mechanics of the seal, a micro-scale fluid mechanics in the sealing zone, a micro-scale asperity contact mechanics and an iterative computational procedure as discussed previously. However a major difference between the model developed in previous chapter and the one developed here is the transient sealed pressure, the effects of which are discussed below.

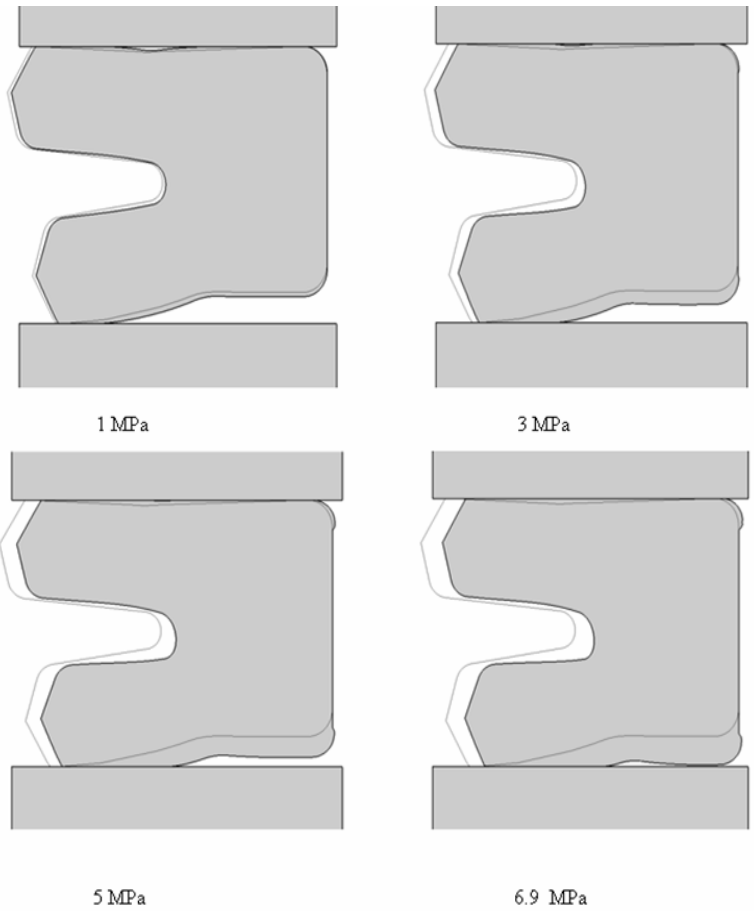

Figure 5.1: Geometrical configuration of the seal at various values of sealed pressure that changes with time.

5.2.1 Transience in Sealed Pressure

In several seal applications including an injection molding one, in addition to a time varying rod velocity, the sealed pressure also shows transience. Since the time-varying sealed pressure produces significant time-variations in the seal geometry, the complexity of the analysis is increased. Figure 5.1 shows the seal deformations at four different time instances obtained using macro-scale deformation and contact mechanics solution using FEM. The grey boundary shows the original undeformed configuration before applying sealed pressure. To solve this problem, we need to resolve the multi-scale fluid-structure interaction at each time step, as the micro-scale fluid domain and mesh is affected not only by the micro-scale structural deformations but also by the macro-scale changes in seal geometry taking place at each time step.

To tackle the problem mentioned above, an "Arbitrary Lagrangian-Eulerian" (ALE) formulation is implemented and a method called "Dynamic Domain Mapping" (DDM) is developed to capture the position and size of the moving fluid-structure interface accurately. ALE formulation facilitates the motion of points within a mesh with respect to their frame of reference by taking the convection of these points into account. Dynamic domain mapping ensures conservative transfer of information at the interface and mapping of field variables over a computational grid that changes with time. An efficient numerical strategy for the movement of mesh and an efficient solution algorithm are developed to ensure accurate multi-scale coupling between solid and fluid domains. While developing this ALE-DDM framework, the merits and de-merits of both, the monolithic methods as well as the partitioned methods are analyzed. In the monolithic approach, the discretized governing equations of fluid, solid and coupling conditions are

formulated as a grouped system and solved simultaneously with the pseudo-structural mesh motion subsequently resolved within the iteration loop. Whereas in a partitioned approach, each physical field is defined, discretized and solved separately with the coupling procedures applied to transfer the required interface information. For MSMP problems such as the ones at hand, the partitioned schemes are attractive in the sense that they allow for the modularity to be preserved, hence allowing the use of highly developed numerical algorithms for individual fields.

5.2.2 Changes in MSMP Modules for Fully Transient Algorithm

Micro-Scale fluid mechanics and micro-scale contact mechanics modules of the fully transient MSMP algorithm remain same as those discussed in Chapter 3. The major change in macro-scale deformation mechanics module is the implementation of ALE-DDM framework as discussed in the following sections. The other big change in the algorithm is that due to transient sealed pressure, now the macro-deformation and dry-contact calculations are performed at each time step and corresponding geometrical configuration is calculated under "dry" conditions. Under these dry condition, the finite element analysis yields a new dry contact pressure distribution, P_{dc}, as well as new sealing zone length at each time step. This time updated sealing zone is also used to compute the normal deformation of the sealing zone boundary, H_{def} as required by Eq. 3.35.

It should be noted that shear deformations of the seal are not taken into account in the MSMP model of this chapter. Such deformations are not believed to have a significant qualitative effect on reciprocating seal behavior. The quantitative effect is

estimated as less than 5% on the flow rate and less than 10% on the friction force, based on a steady-state analyses with and without shear deformation. For the sake of completeness, however, the shear deformations are eventually added in the viscoelastic MSMP model discussed in chapter 6.

5.3 Arbitrary-Lagrangian-Eulerian Method

Since the boundaries of the computational domain are moving greatly with time, a deforming mesh needs to be implemented. To implement such a temporally deforming mesh, a "Moving Mesh" method of Comsol is used with some changes made in the way the mesh motion and mesh smoothing is performed. The moving mesh method implemented forms the new mesh using the Arbitrary Lagrangian-Eulerian (ALE) description. In a total Lagrangian method, the mesh movement follows the movement of the physical material where the displacements often are relatively small. However, when the structural deformations are of the order of the size of the reference geometry, an Eulerian method, where the mesh is fixed, is needed to solve for the field variables. However this method cannot account for moving boundaries. ALE method is an intermediate between the Lagrangian and Eulerian methods, and it combines the best features of both as it allows moving boundaries without the need for the mesh movement to follow the material. Following discussion gives a brief overview of the ALE method implemented.

5.3.1 ALE Description

The ALE method implemented here closely follows that described by Donea *et. al.* [95]. In the total Lagrangian method we follow the material particles of the continuum in their motion and hence a computational grid which follows the continuum in its motion, where the grid nodes are fixed to the same material points. This is shown in Figure 5.2, where the original and deformed seal configurations are shown and corresponding finite element domain used in total Lagrangian and total Eulerian frame of reference is demonstrated. The motion of the material points relates the material coordinates, $\mathbf{X}$, to the spatial ones x using a mapping operator φ such that $\varphi : R_{\mathbf{X}}\left(t_0, t_{final}\right) \to R_x\left(t_0, t_{final}\right)$. The gradient of this mapping operator can be represented in terms of the "Material Velocity" v as,

$$\frac{\partial \varphi}{\partial(\mathbf{X}, t)} = \begin{bmatrix} \dfrac{\partial x}{\partial \mathbf{X}} & v \\ 0^T & 1 \end{bmatrix} \qquad [5.1]$$

where $v = \left.\dfrac{\partial x}{\partial t}\right|_{\mathbf{X}}$ is the "material velocity". With this, the history of the motion is tracked. However, with large material deformations, the total Lagrangian method undergoes a loss in accuracy and may not converge.

Problems caused by large grid distortions are overcome in the Eulerian formulation. In this method, the variables associated with the material particles passing through a fixed space are examined as time evolves. Finite element mesh is thus fixed and the continuum deforms with respect to the computational grid. This is demonstrated in Figure 5.2 for the case of large seal deformations.

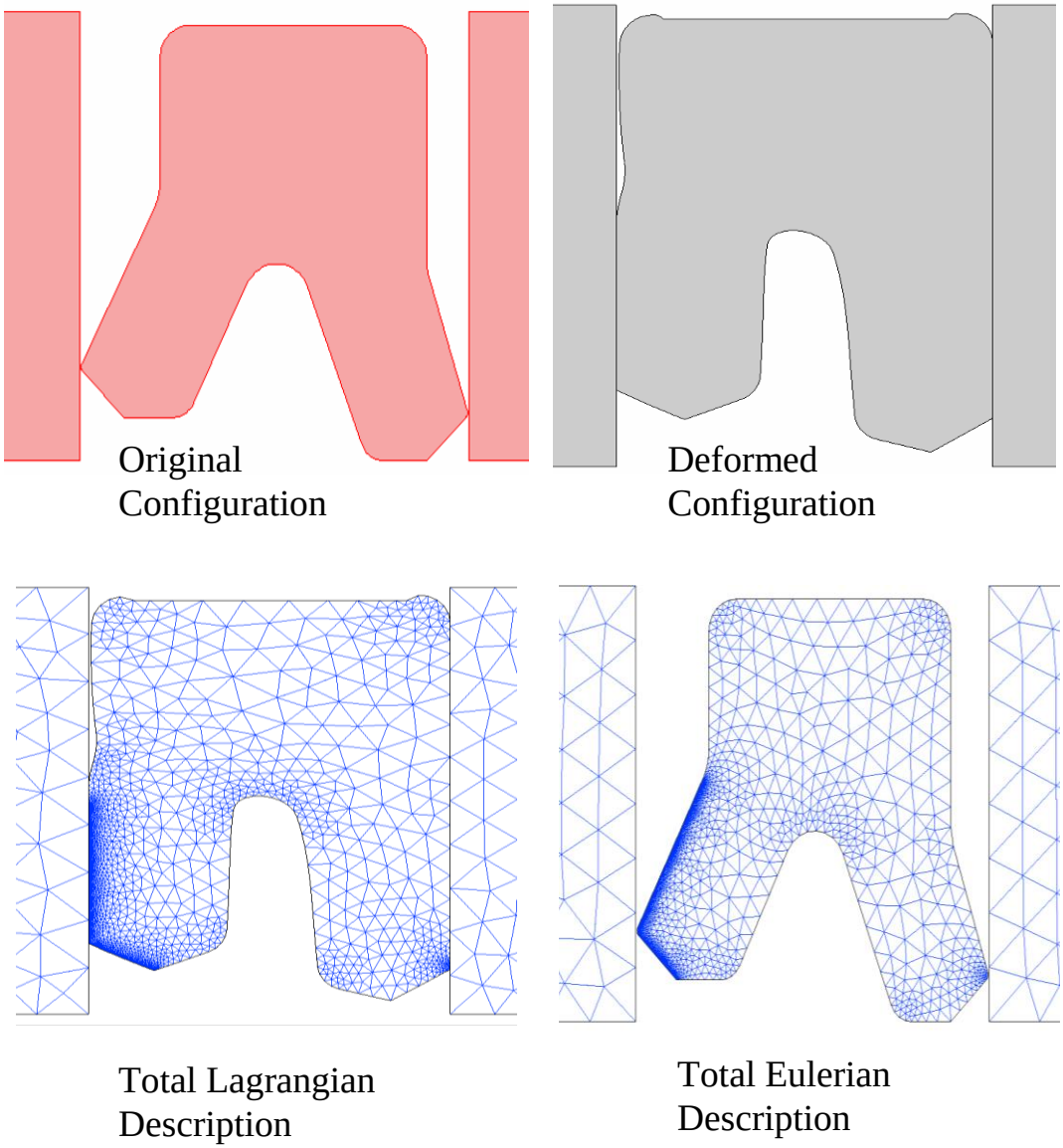

Figure 5.2: Original and deformed seal configurations and total Lagrangian and total Eulerian descriptions.

In Eulerian framework, the conservation equations are formulated in terms of the spatial coordinates x and the time t. The material velocity v at a given mesh node is the velocity of the material point at that node at time t. Since the mesh nodes are now

different from the material particles, convective effects appear due to the relative motion between the deforming material and the computational grid. However, the Eulerian algorithm often presents numerical difficulties due to the non-symmetric character of convection operators and creates problems for mobile boundaries [95].

In the ALE description of motion, neither the material configuration R_{X} nor the spatial one R_x is taken as the reference. Instead a third domain, the "Referential configuration", R_χ, is created where the reference coordinates χ are introduced to identify the grid points. Figure 5.3 shows these domains and the one-to-one transformations relating the configurations. The referential domain R_χ is mapped into the material and spatial domains by Ψ and Φ respectively. The particle motion φ can then be expressed as: $\varphi = \Phi \otimes \Psi^{-1}$ [95]. The mapping Φ from the referential domain to the spatial domain, which is the motion of the grid points in the spatial domain, is represented by $\Phi : R_\chi\left(t_0, t_{final}\right) \to R_x\left(t_0, t_{final}\right)$ and its gradient is

$$\frac{\partial \Phi}{\partial(\chi, t)} = \begin{bmatrix} \dfrac{\partial x}{\partial \chi} & \hat{v} \\ 0^T & 1 \end{bmatrix} \qquad [5.2]$$

where $\hat{v} = \left.\dfrac{\partial x}{\partial t}\right|_\chi$ is the "mesh velocity". In this description, both the material points and the mesh moves with respect to the observer.

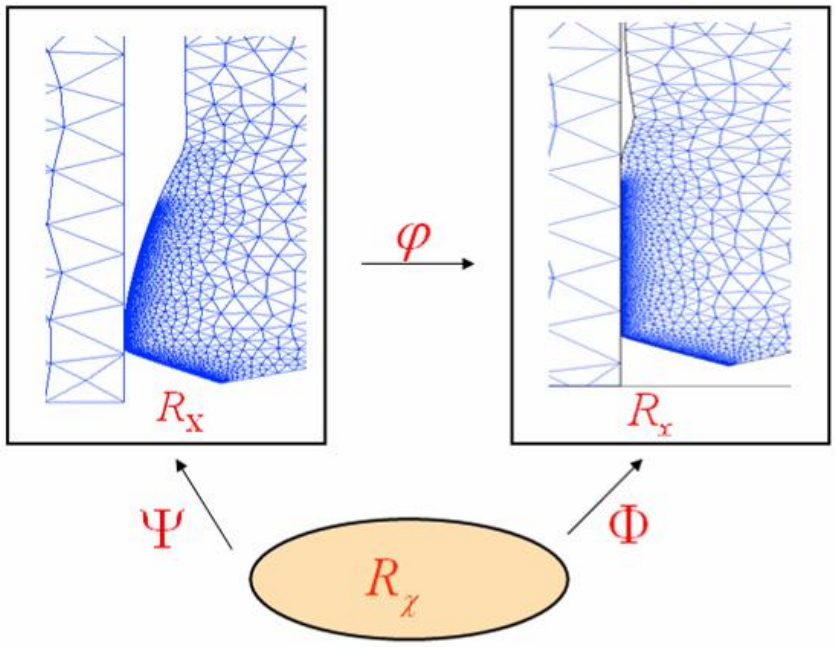

Figure 5.3: ALE technique: Mapping between different frames of reference: Material (R_X), Spatial (R_x) and Referential (R_χ).

The "particle velocity in the referential domain" is defined as, $w = \left.\frac{\partial \chi}{\partial t}\right|_X$. The relation between velocities $v, \hat{v}$ and w is obtained by differentiating φ and using a chain rule [95],

$$\begin{bmatrix} \frac{\partial x}{\partial \mathbf{X}} & v \\ 0^T & 1 \end{bmatrix} = \begin{bmatrix} \frac{\partial x}{\partial \chi} & \hat{v} \\ 0^T & 1 \end{bmatrix} \begin{bmatrix} \frac{\partial \chi}{\partial \mathbf{X}} & w \\ 0^T & 1 \end{bmatrix} \qquad [5.3]$$

This gives "Convective Velocity", c as the relative velocity between the material and the mesh, $c := v - \hat{v} = \frac{\partial x}{\partial \chi} \cdot w$. With this ALE description, now the time derivatives of any field variable σ_r (radial stress for example) in various frames are related by,

$$\left.\frac{\partial \sigma_r}{\partial t}\right|_{\mathbf{x}} = \left.\frac{\partial \sigma_r}{\partial t}\right|_{x} + v \cdot \nabla \sigma_r$$
$$\left.\frac{\partial \sigma_r}{\partial t}\right|_{\mathbf{x}} = \left.\frac{\partial \sigma_r}{\partial t}\right|_{\chi} + c \cdot \nabla \sigma_r \qquad [5.4]$$

which relate the material time derivative to the spatial and referential time derivatives using material velocity and convective velocity respectively. Similar equations can be written for rest of the field variables.

Finally, the ALE integral forms of the conservation equations described in section 2.2 can then be obtained by considering the rate of change of integrals of the field variables over a moving volume whose boundary moves with a mesh velocity $\hat{v}$ [95],

$$\left.\frac{\partial}{\partial t}\right|_{\chi} \int_{V_t} S_{ij}(x,t)\,\delta\varepsilon_{ij}(x,t)\,dV = \int_{V_t} \left.\frac{\partial S_{ij}(x,t)\,\delta\varepsilon_{ij}(x,t)}{\partial t}\right|_{x} dV + \int_{S_t} S_{ij}(x,t)\,\delta\varepsilon_{ij}(x,t)\,\hat{v}\cdot\hat{n}\; dS \qquad [5.5]$$

where V_t is an arbitrary volume whose boundary S_t moves with the mesh velocity $\hat{v}$.

5.3.2 ALE Implementation into the MSMP

Comsol's moving mesh algorithm is used to implement the ALE method into the macro-deformation-contact module of the MSMP framework. However, instead of using a free displacement for the internal material points and the boundaries, the solution of displacement variables from the previous iteration is used to assign the motion of internal and boundary nodes of the finite element mesh. Also in this method, the new mesh is not generated for each new configuration of the seal from scratch. Instead, the algorithm perturbs the mesh nodes so they conform to the moved boundaries. Movement of the

interior mesh nodes is then governed by physical displacement variables. To avoid inverted elements during large seal deformations, a combination of Laplace smoothing and Winslow smoothing is implemented which alternates between the two as needed to avoid large mesh distortions and numerical divergence. Laplace smoothing takes the second order derivatives with respect to material coordinates, while Winslow takes the second order derivatives with respect to the spatial coordinates. Winslow is slower and more memory intensive than Laplace smoothing but does a better job.

The solver assembles the discretized model on the deformed mesh, using the reference derivatives of the solution as an input. It then computes the spatial time derivatives using the above equations. With this implementation, the PDEs do not need to be re-formulated when using the deformed mesh for further calculations. With ALE implementation, deformation mechanics calculations are attached to the reference frame. Deformation analysis computes the mesh displacements that are used as input for the moving mesh calculations when they define the spatial frame. Micro-scale fluid mechanics and micro-scale contact calculations are attached to the spatial frame as defined by the moving mesh algorithm.

5.4 Dynamic Domain Mapping

Dynamic domain mapping method is developed for solving two major problems: 1) Following the boundary loads over surface area of the seal changing with time 2) Mapping the micro-scale computational domain and evaluation of the Reynolds equation squeeze term over changing sealing zone. These are discussed below.

5.4.1 Load Following over Changing Surface Area

With changing sealed pressure as a function of time, the seal undergoes large changes in its macro-scale as well as micro-scale geometrical configuration as seen in Figure 5.4. If the structural mechanics loads are defined in a fix reference frame, all forces need to be specified as force / undeformed area in a fixed coordinate system. This creates complications in modeling the pressure acting on a surface which is undergoing large deformations over time as the force keeps on changing direction due to the deformation. There is also an effect of change in area due to surface stretching. Hence, a relation between the deformed area, da, and the undeformed area, dA, is needed. To handle this, a dynamic domain mapping is performed. During dynamic domain mapping, the algorithm computes both the deformed area and the deformed normal direction, $\hat{n}$. The force is then calculated as,

$$F = -\tilde{P}\,\hat{n}\,da = -\tilde{P}\,\hat{n}\,\frac{da}{dA}\,dA \qquad [5.6]$$

where $\tilde{P}$ is the follower pressure. Such follower loads then change the direction as the body deforms. This pressure following then takes care of the changes in the magnitude of forces due to the stretching of the surface and in direction due to changes in normal directions of boundaries.

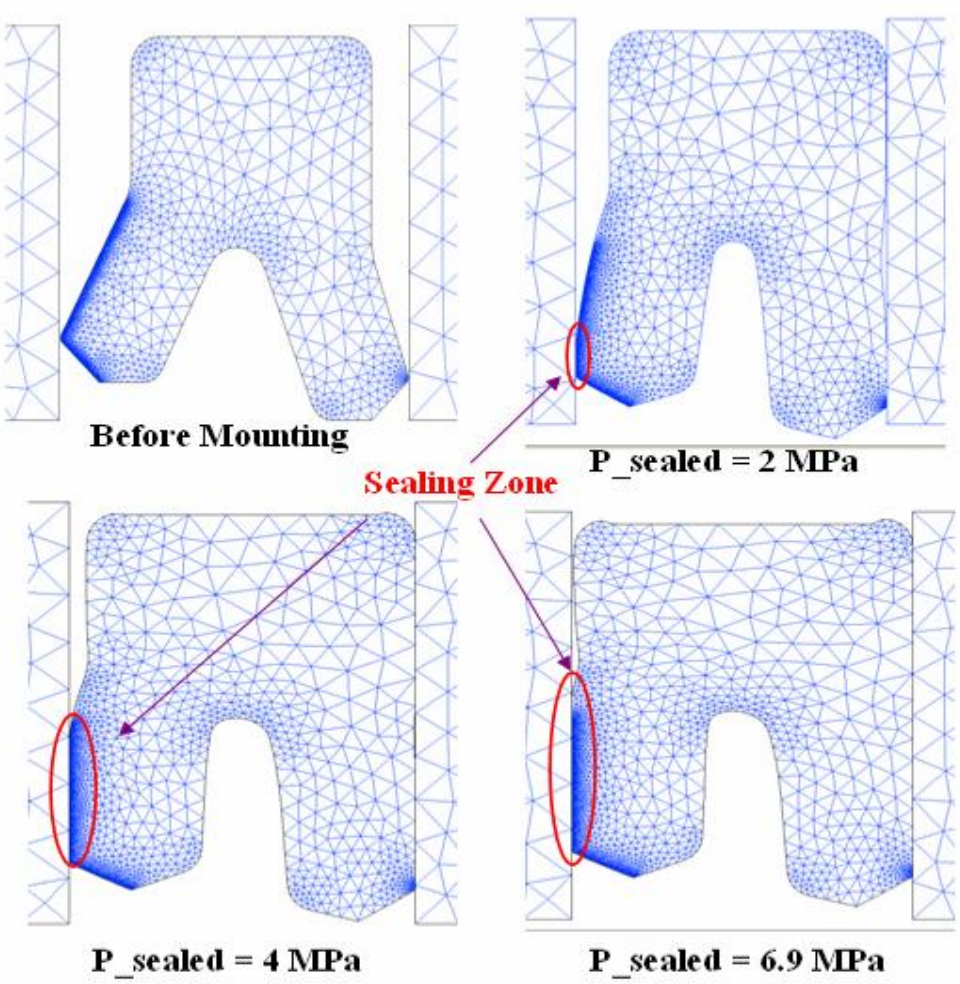

Figure 5.4: Mapping the sealing zones using Dynamic Domain Mapping. The sealing zone encircled in red shows the effect of time changing sealed pressure on sealing zone lengths and hence on micro-scale computational domain.

5.4.2 Mapping the Micro-Scale Computational Domain and Evaluation of the Reynolds Equation Squeeze Term over Changing Sealing Zone

Another need for dynamic domain mapping is for mapping the micro-scale computational domain from one time step to next when the seal is undergoing large deformations with time. In such a case, the sealing zone changes extensively in its length

and location as seen by red encircled region in Figure 5.4. This implies that the whole computational domain for micro-scale fluid / contact / deformation mechanics calculations changes at every time step. This creates complications in evaluating field variables like fluid pressure, cavitation index, density function and film thickness for the micro-mechanics computations. This is where dynamic domain mapping is needed to map all the field variables from one time step to next over a moving computational grid.

As an example, mapping of film thickness is demonstrated in Figure 5.5. One of the needs for mapping film thickness is for calculating the squeeze film term from Reynolds equation Eq. 3.22. Calculating the time derivative of film thickness in this term becomes tricky when the contact zone length is changing as a function of time. Quantities like H, F and ϕ are evaluated over the sealing zone at a particular time step. To differentiate these quantities with respect to time (which is a part of TDMA algorithm), their nodal values need to be time differenced. But since the spatial domain over which these quantities are defined, itself, is undergoing transience, we need to map the nodal values from the spatial domain at new time step into the domain at old time step. There are two scenarios that arise as seen from Figure 5.5.

i) If the contact length at the new time step is less than the contact length at the old time step, then the old variable mapped into new domain is given by:

$$H_{new\_1} = \Re_1(H_{prev}) = truncate\left(H_{prev}\right) \qquad [5.7]$$

where $\Re_1$ is the spatial mapping operator, which truncates the old variable at a spatial length equal to that of the new domain.

This is seen by comparing parts (a) and (b) of Figure 5.5, where Lprev is the old sealing zone length, Hprev is the old film thickness,

L_new1 is the new sealing zone length and H_new1 is the film thickness mapped from old sealing zone to new sealing zone.

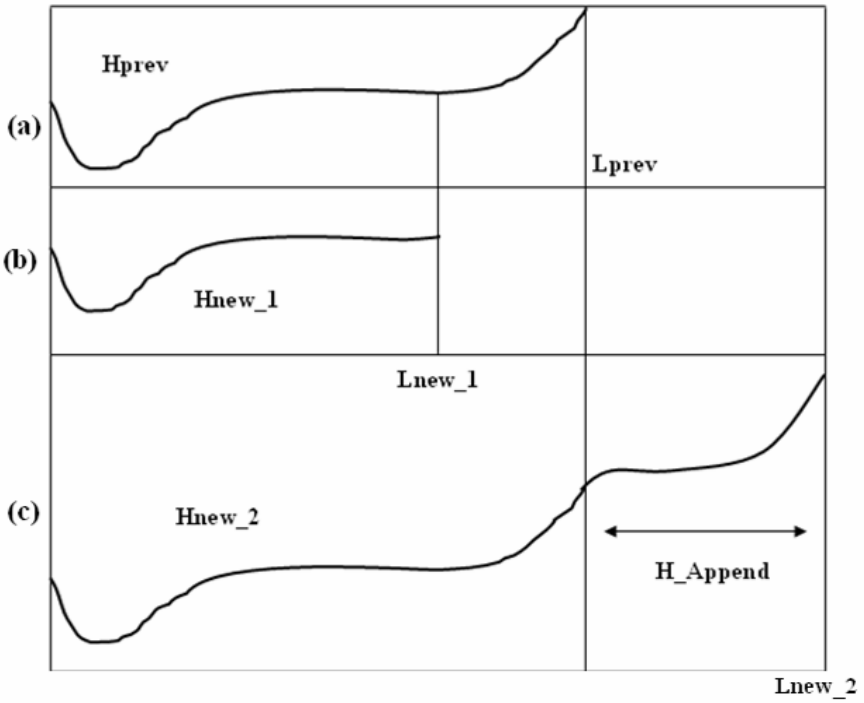

Figure 5.5: Mapping of film thickness from the sealing zone at old time step to that at new time step.

ii) If the sealing zone length at new time step is larger than the sealing zone length at old time step, then the old variable mapped into new domain is given by

$$H_{new\_2} = \Re_2(H_{prev}) = H_{prev} + append\left(H_{macro}\right) \qquad [5.8]$$

where $\Re_2$ is the spatial mapping operator, which appends a component H_{macro} to the old variable such that $length(H_{new}) = length(H_{new\_2})$. H_{macro} is calculated from the macroscopic geometrical configuration of the seal at the previous time step. This is seen

by comparing parts (a) and (c) of Figure 5.5, where Lprev is the old sealing zone length, Hprev is the old film thickness, L_new2 is the new sealing zone length and H_new2 is the film thickness mapped from old sealing zone and old macro-geometry to onto the new sealing zone. H_Append is additional film thickness component appended and which is calculated from old macro-geometry (e.g. from coordinates of the nodes next to the sealing zone).

5.5 Computational Procedure

The overall computational procedure used in this hybrid finite element- finite volume framework is shown in Figure 5.6. Due to the strong coupling, the above mentioned equations are solved iteratively.

Step a) At a given time step, the dry contact - deformation mechanics problem with a given sealed pressure is solved using the ALE modified finite element procedure explained earlier, to yield the deformed geometrical configuration, sealing zone and the dry contact pressure distribution.

Step b) Equations (3.22), (3.23), (3.24) along with boundary condition Eq. (3.25) are then solved for Φ and F numerically with a finite volume formulation and the tri-diagonal matrix algorithm. Time integration is carried out using a fully implicit method. This yields the fluid pressure distribution and locations of cavitation zones.

Step c) The asperity contact pressure is then evaluated using the Greenwood-Williamson statistical model. The integral in Eq. (3.34) is evaluated numerically using the Adaptive Gauss-Kronrod quadrature.

Step d) The fluid pressure, asperity contact pressure and dry contact pressure (from Step a) are fed into the finite element seal deformation analysis. The computed deformations and Eq. (3.35) are then used to update the film thickness and flow factors for the next iteration.

Step e) Steps (b) through (d) are run in an iterative loop in a coupled finite element – finite volume framework within the parent script until the converged solutions for fluid pressure and film thickness are obtained at the given time step.

Step f) The converged solutions at this time step are then used to calculate the transient squeeze term (in Eq. (3.22)) for the next time step. For this, dynamic domain mapping method developed in section 5.4.2 is used to handle the problem of sealing zone changing with time.

Step g) Steps (a) through (f) are repeated over the time interval of interest and a transient solution for the entire period of operation is obtained. The post processing calculations described in section 2.7.3 are then performed.

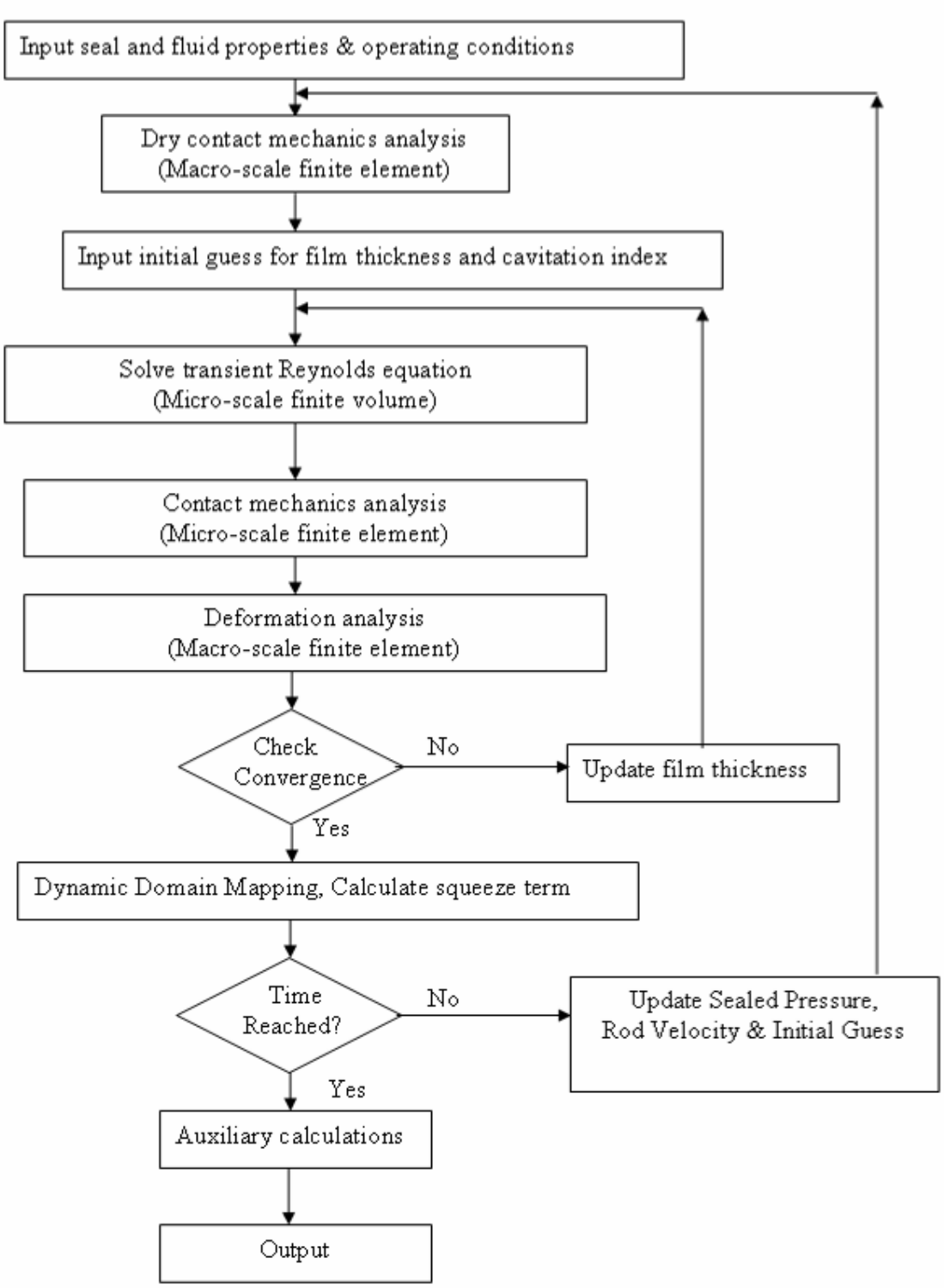

Figure 5.6: Transient sealed pressure MSMP computational algorithm.

5.6 Results

Computations are performed for a polyurethane seal used in an injection molding application, shown schematically in Figure 3.3. This seal prevents leakage from the actuator that moves the half-mold in and out of the injection molding machine. The motion is controlled by primarily varying the hydraulic pressure on the cap side of the piston. The base parameters are same as the ones described in Table 3.3 in chapter 3, except that the seal's RMS roughness is now fixed at 1.2 μm. The seal roughness is assumed to be isotropic. As described previously, the rod is treated as perfectly smooth.

Figure 5.7 and Figure 5.8 show the specified rod velocity and sealed pressure respectively as functions of time, over one cycle. The outstroke occurs from t = 0 to t = 10.50 sec., and the instroke from t = 10.51 sec. to t = 21.0 sec. Also shown on these figures are key times labeled 1 to 21.

5.6.1 Dynamic Deformations of the Seal

Figure 5.9 shows the displacement field (surface plot) and first principal stress field (contour plot) in the seal body at various time instances of seal operation. The sealed pressures at these times can be found from Figure 5.8. The maximum displacement (total magnitude of radial and axial displacements) at any given point in seal body is about 0.57 mm. However it still produces a maximum sealing zone length of about 2.4 mm. The shape of the stress contours changes significantly in going from t = 2.09 sec to t = 3.18 sec. Especially the contour lines converge into the sealing zone with very different slopes which in turn critically affects the dry contact pressure distribution in the sealing zone.

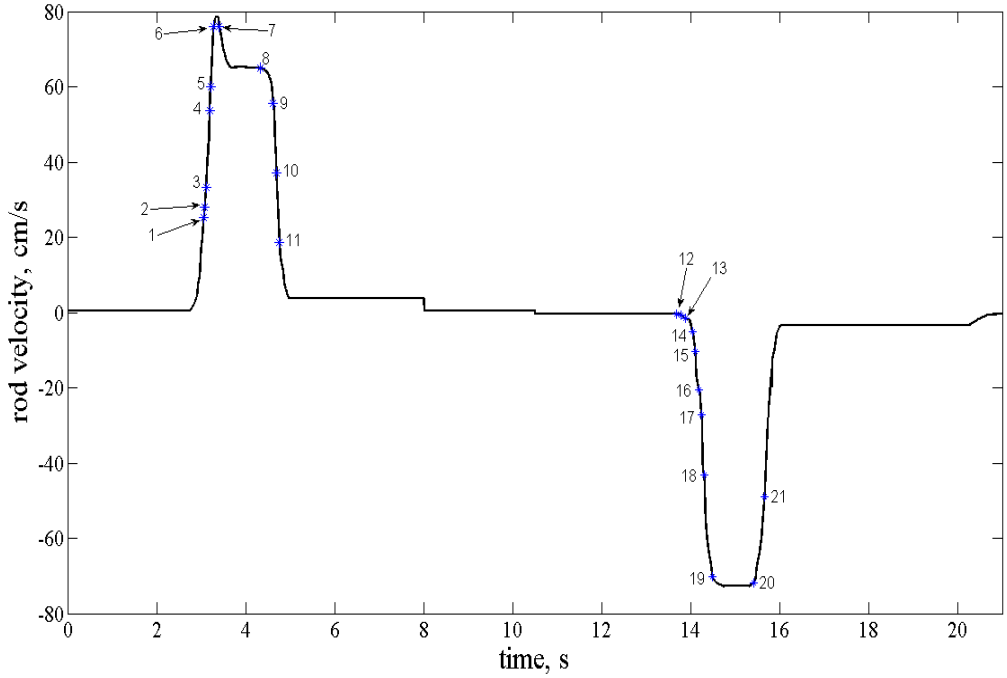

Figure 5.7 : Rod velocity history.

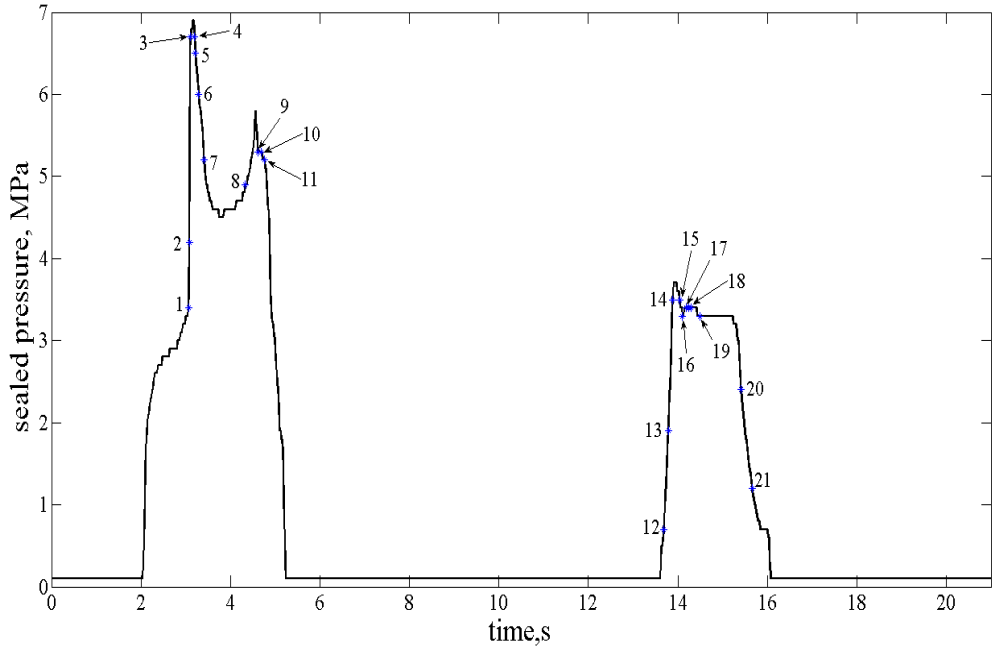

Figure 5.8: Sealed pressure history.

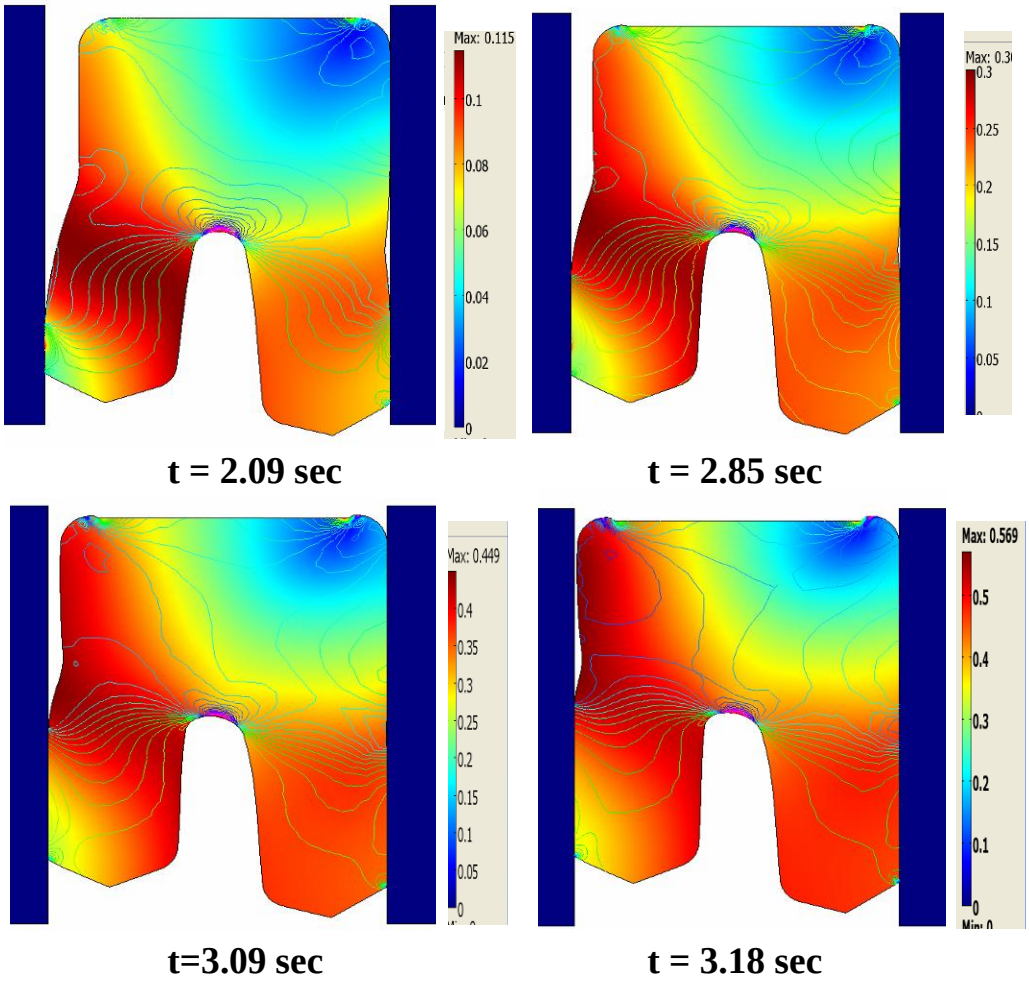

Figure 5.9: Displacement field (surface plot) and First Principal Stress field (contour plot) in the seal body at various time instances.

The seal characteristics most important to designers and users are the leakage and friction characteristics. These are presented and discussed below.

5.6.2 Leakage

The instantaneous volumetric flow rate (out of the cylinder) as a function of time is shown in Figure 5.10. The shape of the curve is almost identical to that of the rod

velocity history. This indicates that the Poiseuille (pressure-driven) contribution to flow is very small compared to the Couette contribution.

Figure 5.11, obtained by integrating the flow rate in Figure 5.10, shows the net fluid transport (out of the cylinder) as a function of time. During the outstroke it increases and during the instroke it decreases. At t = 15.7 s the fluid transport is zero, and then remains negative through the end of the cycle (t = 21.0 sec.), indicating zero net leakage. Since the model assumes flooded conditions at the inlet to the sealing zone, the model is no longer valid for times greater than 15.7 s. This is indicated by the broken vertical line on Figure 5.11 and on succeeding figures (and on Figure 5.10).

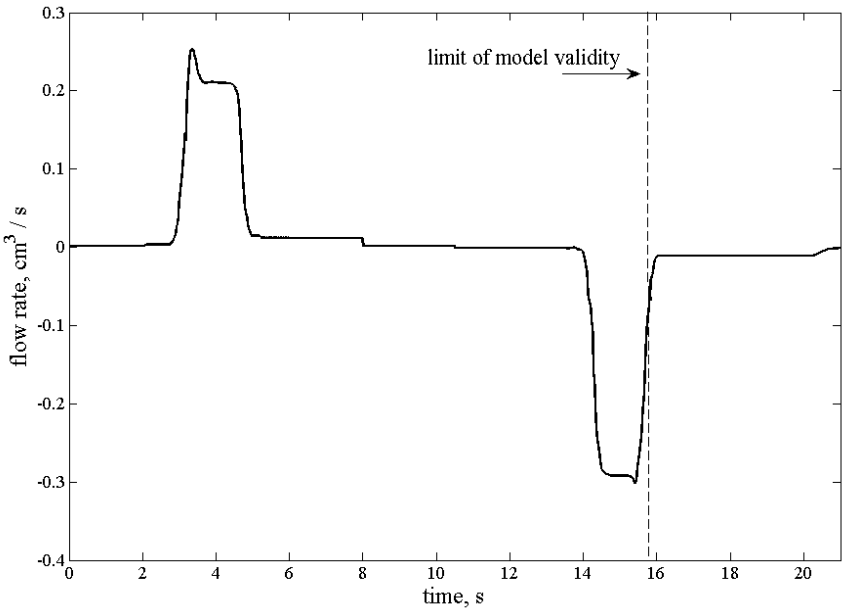

Figure 5.10: Flow rate vs time.

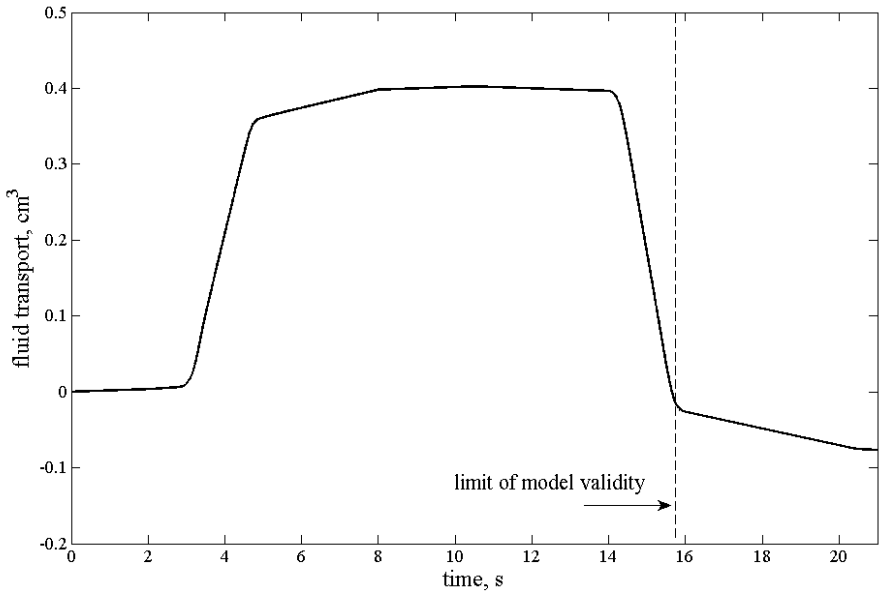

Figure 5.11: Net fluid transport vs time.

5.6.3 Fluid Pressure Distributions

To understand why this seal exhibits zero net leakage, it is useful to examine the fluid pressure and film thickness distributions in the sealing zone.

Figure 5.12 and Figure 5.13 show the fluid pressure distributions during outstroke and instroke respectively. The fluid pressure is affected by both the sealed pressure and the rod velocity. An increase in sealed pressure leads to an increase in fluid pressure since the former acts as a boundary condition on the latter. From the discussion in chapter 3, it was found that an increased rod velocity reduces the fluid pressure during the outstroke but increases it during the instroke. This is because during the outstroke the flow in the film is primarily diverging, and during the instroke it is primarily converging. Thus, due to this dual dependence, the detailed transient behavior of the fluid pressure distributions is quite complex. Nevertheless, it is seen from Figure 5.12 and Figure 5.13 that during the

outstroke the fluid pressures are generally lower than those during the instroke. Furthermore, during the outstroke there are significant regions where the pressure goes to zero (and Φ is negative). These are regions of cavitation. They do not occur during the instroke. Such cavitation during the outstroke and lack of cavitation during the instroke, promotes zero net leakage because the cavitation inhibits flow of the hydraulic fluid. This is consistent with previous steady-state studies of rod seals [44-46].

5.6.4 Film Thickness Distributions

The characteristics of the fluid pressure distributions are reflected in the film thickness distributions of Figure 5.14 and Figure 5.15, which indicate that mixed lubrication occurs, since the film thickness is generally less than 3σ. The lower fluid pressures during the outstroke result in a generally reduced film thickness (Figure 5.14), while the higher fluid pressures during the instroke result in a generally increased film thickness (Figure 5.15). Thus, the average film thickness during the instroke exceeds that during the outstroke.

This, as well as the cavitation during the outstroke, prevents net leakage since it allows higher flow rates during the instroke than during the outstroke. This, too, is in agreement with previous steady-state studies [44-46].

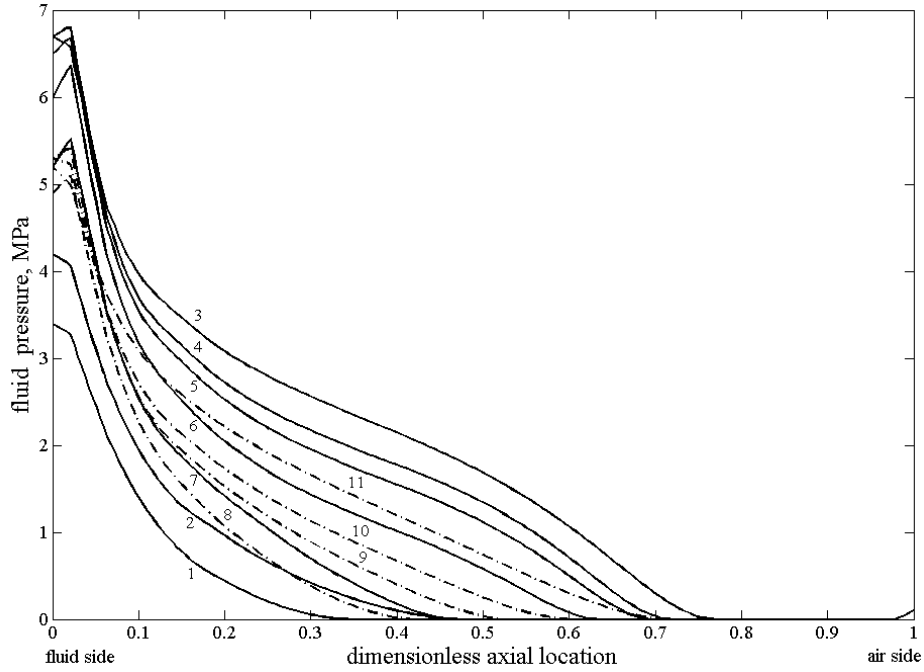

Figure 5.12: Fluid pressure distribution, outstroke.

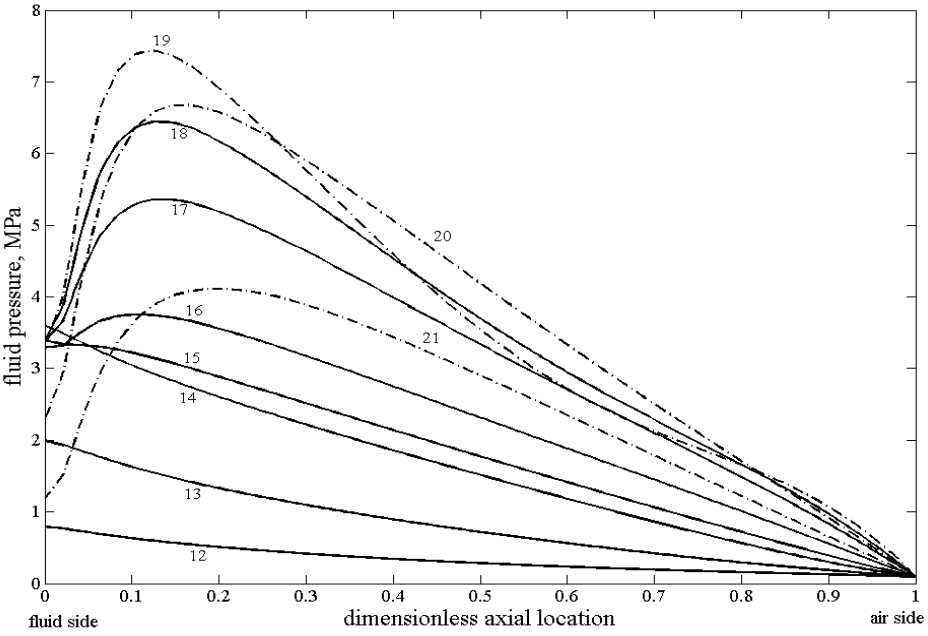

Figure 5.13: Fluid pressure distribution, instroke.

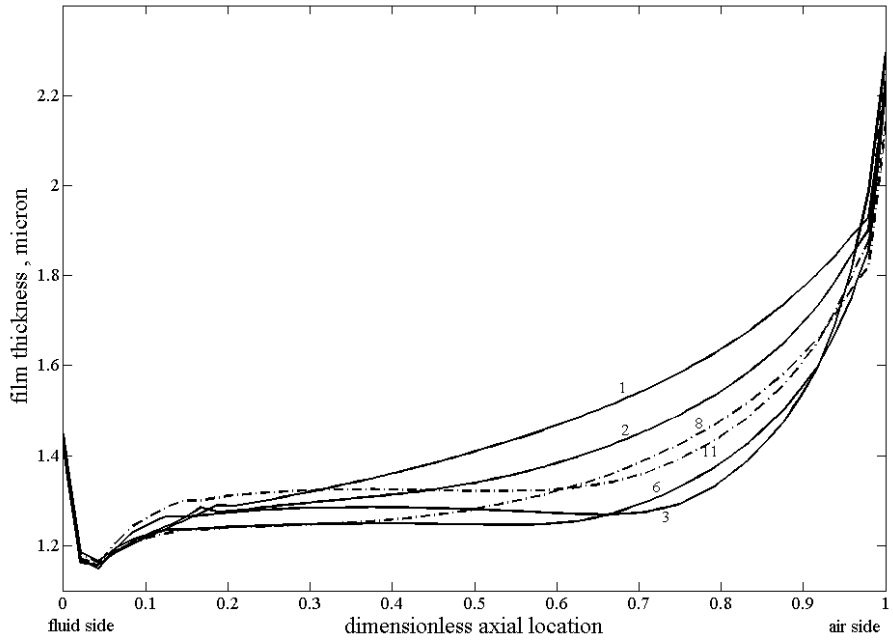

Figure 5.14: Film thickness distribution, outstroke.

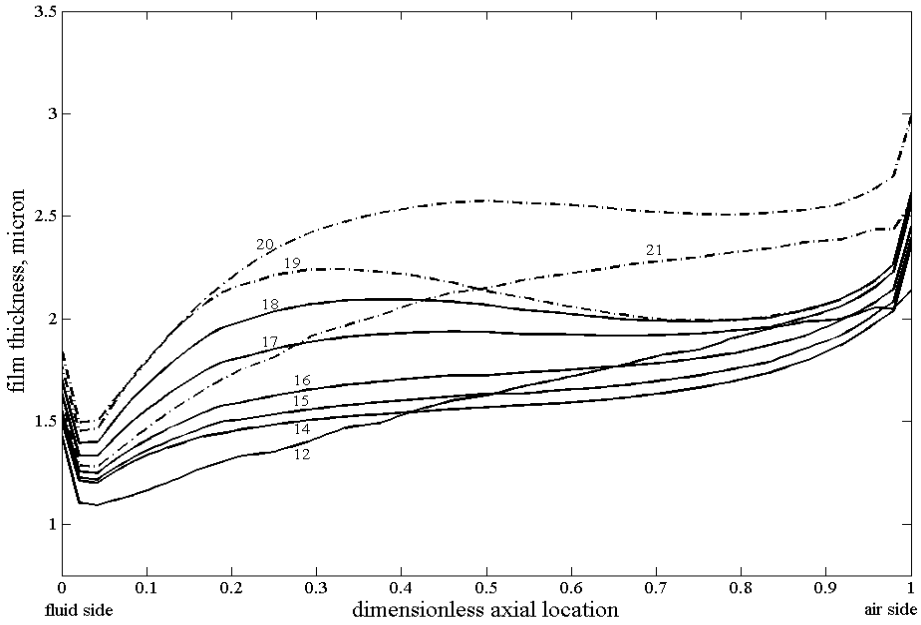

Figure 5.15: Film thickness distribution, instroke.

5.6.5 Friction

Figure 5.16 shows the total friction force on the rod. Its magnitude is significantly larger during the outstroke than during the instroke. To understand this behavior, it is necessary to examine both the shear stress on the rod and the sealing zone length, since the friction force is obtained by integrating the shear stress over the sealing zone length. The mean shear stress on the rod is shown in Figure 5.17 as a function of time. During the outstroke its magnitude is increased from its quasi-static value, while during the instroke its magnitude is decreased. The reduced film thickness during the outstroke (Figure 5.14) leads to a generally increased contact pressure, as shown in Figure 5.18, while the increased film thickness during the instroke (Figure 5.15) leads to a generally decreased contact pressure, as shown in Figure 5.19. Thus, the magnitude of the shear stress due to contacting asperities is increased during the outstroke and reduced during the instroke, following Eq. (3.61) (the viscous contribution to the shear stress is relatively small).

Figure 5.20 shows the sealing zone length as a function of time. Comparing Figure 5.20 with Figure 5.8, it is evident that the sealing zone length is governed by the sealed pressure; the higher the sealed pressure, the larger is the sealing zone length. This is a result of the macroscopic deformation characteristics of the seal, as is evident from Figure 5.4 and Figure 5.9.

Thus it is clear that the larger friction force during the outstroke, as compared with that during the instroke, is due to both the higher shear stress and longer sealing zone, and these latter two characteristics are readily understood, as described above.

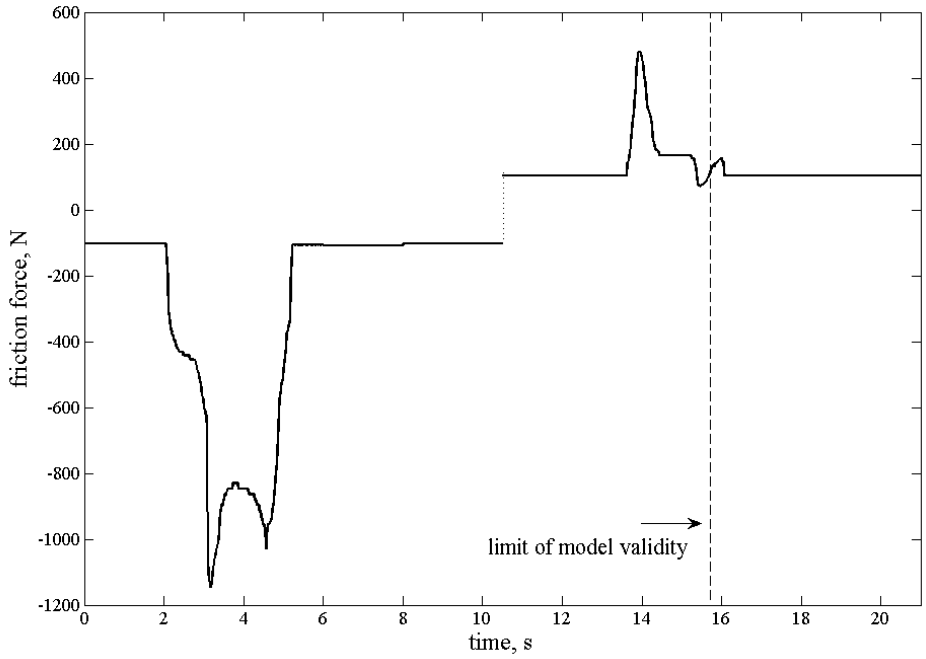

Figure 5.16: Friction force on the rod vs time.

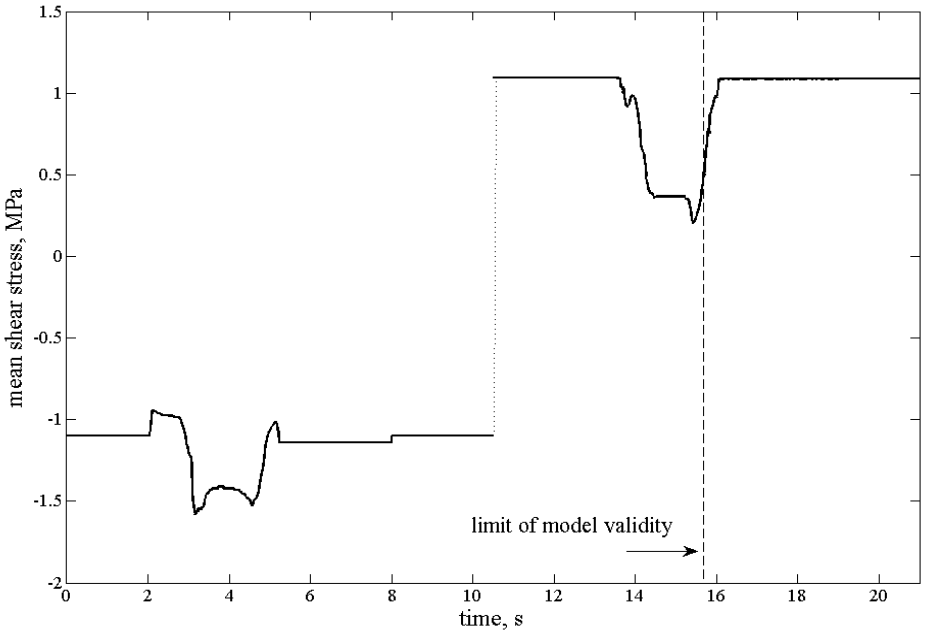

Figure 5.17: Mean shear stress on the rod vs time.

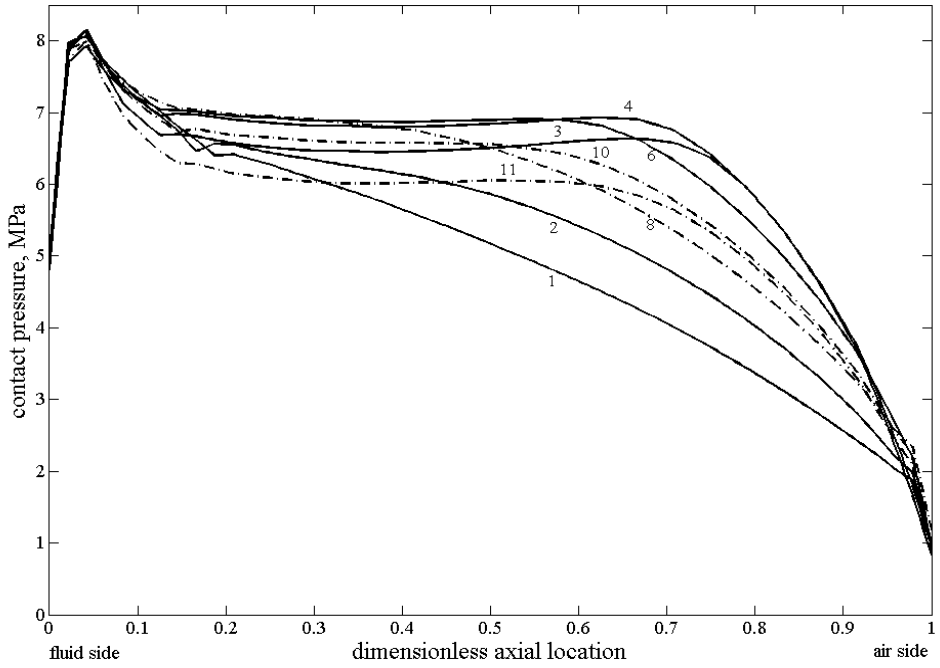

Figure 5.18: Contact pressure distribution, outstroke.

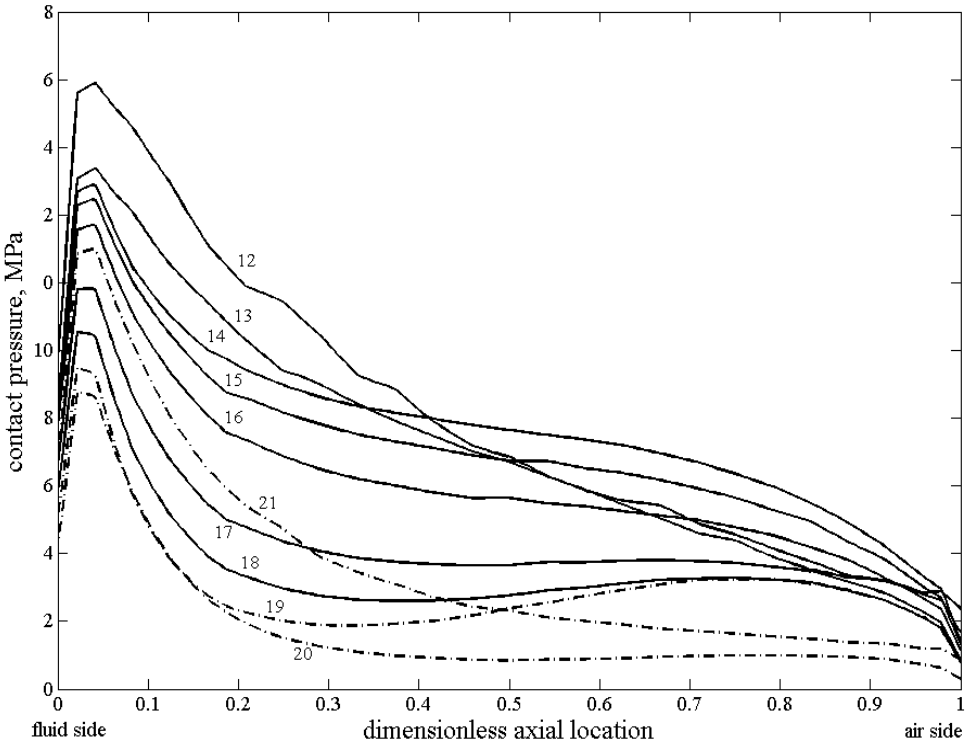

Figure 5.19: Contact pressure distribution, instroke.

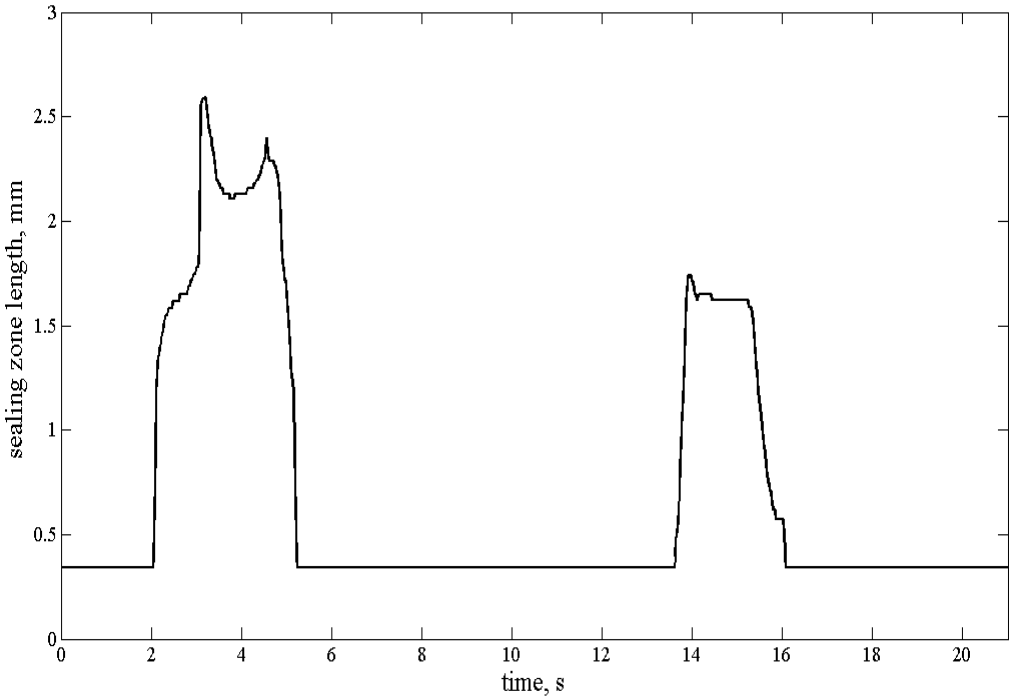

Figure 5.20: Sealing zone length vs time.

5.7 Conclusions

The MSMP framework is modified to handle an important problem of sealing dynamics with transient sealed pressure. The time varying sealed pressure is seen to produce significant changes in macro-deformation and contact mechanics of the seal, resulting in a micro-scale computational domain that constantly changes at each time step. Arbitrary Lagrangian-Eulerian and Dynamic Domain Mapping methods are implemented to tackle the problems caused by large variation in macro-scale and micro-scale geometrical configurations. With this implementation the MSMP framework was successful in solving the fully transient, coupled, elasto-hydrodynamic problems.

Modified MSMP framework is used to study the seals used in injection molding applications. The effects of transient seal pressure and rod velocity on fluid pressure, contact pressure and film thickness distributions as well as on leakage and friction characteristics are analyzed. The analysis has demonstrated that a fully transient EHL analysis reveals the detailed history of a reciprocating seal's behavior over a cycle. It is seen that the time variations in fluid pressure distributions are governed by a complex dual dependence on changes due to time varying sealed pressure boundary condition and those due to hydrodynamic effects produced by time varying rod velocity. The contact pressure distributions are largely affected by changes in sealed pressure and in turn they cause large variations in shear stress and friction characteristics of the seal with time. The leakage history is again governed by the Couette component of the flow rate, both during outstroke and instroke.

CHAPTER 6. COMPREHENSIVE MSMP MODEL: INCORPORATING VISCOELASTICITY

6.1 Background Analysis of Dynamic Response of Viscoelastic Solids

To incorporate viscoelasticity of seal under transient sealing conditions, first it is essential to understand the dynamic response of viscoelastic polymers. Understanding dynamic viscoelastic response is also needed to experimentally characterize the seal materials and to gain physical insight regarding viscoelasticity. The frequency of the applied load may be so slow that inertial terms can be neglected or high enough that the resonance can occur. At sufficiently high frequencies the dynamic behavior can result into the wave propagation through the viscoelastic solid.

Consider a strain input sinusoidal in time, $\varepsilon(t)=\varepsilon_0 e^{i\omega t}$, where ω is the angular frequency of the sinusoid. Using Boltzmann superposition integral (discussed later in section 6.3.1), we can write the stress as,

$$\sigma(t)=\int_{-\infty}^{t} E(t-\tau)\frac{d\varepsilon(\tau)}{d\tau}d\tau \tag{6.1}$$

If we decompose the relaxation function into a transient component and a long term (equilibrium) component as, $E(t)=E_\infty+\tilde{E}(t)$, substitute the strain history and make a substitution, $\tilde{t}=t-\tau$, then Eq. (6.1) becomes,

$$\sigma(t)=\varepsilon_0 e^{i\omega t}\left(E_\infty+\omega\int_0^\infty \tilde{E}(\tilde{t})\sin(\omega\tilde{t})\,d\tilde{t}+i\omega\int_0^\infty \tilde{E}(\tilde{t})\cos(\omega\tilde{t})\,d\tilde{t}\right) \tag{6.2}$$

and the stress-strain relation can be expressed as, $\sigma(t)=E^*(\omega)\varepsilon(t)$ where E^* is the

complex modulus and can be written in terms of real (storage modulus) and imaginary (loss modulus) parts,

$$E^*(\omega) = E'(\omega) + i\,E''(\omega) \tag{6.3}$$

where

$$\begin{aligned} E'(\omega) &= \text{storage modulus} = E_\infty + \omega\int_0^\infty \tilde{E}(\tilde{t})\sin(\omega\tilde{t})\,d\tilde{t} \\ E''(\omega) &= \text{loss modulus} = \omega\int_0^\infty \tilde{E}(\tilde{t})\cos(\omega\tilde{t})\,d\tilde{t} \end{aligned} \tag{6.4}$$

and the loss tangent or the damping ratio is given by,

$$\tan(\delta(\omega)) = \frac{E''(\omega)}{E'(\omega)} \tag{6.5}$$

Here, $\delta(\omega)$ represents the phase angle in the complex plane by which stress lags the strain input and is a frequency dependent material property. Hence the dynamic stress-strain relation can also be expressed as,

$$\sigma(t) = \left|E^*(\omega)\right|\varepsilon_0 e^{i(\omega t+\delta)} \tag{6.6}$$

If we consider only the real part of strain and stress sinusoids,

$$\begin{aligned} \varepsilon(t) &= \Re\left\{\varepsilon_0 e^{i\omega t}\right\} = \varepsilon_0\cos(\omega t) \\ \sigma(t) &= \Re\left\{E^*(\omega)\varepsilon_0 e^{i\omega t}\right\} = \varepsilon_0\left[E'(\omega)\cos(\omega t) - E''(\omega)\sin(\omega t)\right] \end{aligned} \tag{6.7}$$

then it shows the decomposition of total stress into its in-phase and out-of phase components. The component in-phase with the strain sinusoid is $\varepsilon_0 E'(\omega)\cos(\omega t)$ and the component 90^O out of phase is $-\varepsilon_0 E''(\omega)\sin(\omega t)$, i.e. $E'(\omega)$ is the part of the modulus that is in phase with the applied strain and $E''(\omega)$ is the part of the modulus that is 90^O out of phase.

Now, to measure the relaxation modulus of polymers, an experimental method called Dynamic Mechanical Analysis is employed (see section 7.1), which measures the Storage and Loss moduli of the polymer sample as a function of excitation frequency. The relaxation modulus is expressed using generalized Maxwell model and a Prony series. After substituting Generalized Maxwell Model (Eq. (2.6)) into Eq. (6.4) and evaluating the integrals (see section 7.1.2.1) we get,

$$E^{'}(\omega) = E_{\infty} + \sum_{i=1}^{N} E_i \frac{\omega^2 \tau_i^2}{1+\omega^2 \tau_i^2}$$
$$E^{''}(\omega) = \sum_{i=1}^{N} E_i \frac{\omega \tau_i}{1+\omega^2 \tau_i^2} \tag{6.8}$$

The resulting set of algebraic equations is solved in a constrained optimization sense to extract the parameters E_i and τ_i (see section 7.1.2.2) and the relaxation modulus is reconstructed by substituting these parameters into $E(t) = E_{\infty} + \sum_{i=1}^{N} E_i e^{-t/\tau_i}$.

To better understand and model the dynamic behavior of viscoelastic solids, it is desired to look at the behavior of storage and loss moduli and loss tangent as a function of frequency of applied load. Figure 6.1 shows such a plot for a viscoelastic polymer modeled using Generalized Maxwell model consisting of $E_{\infty} = 75$ MPa, $E_1 = 3000$ MPa and $\tau_1 = 0.1\,\text{sec}$. ω is the frequency of the applied strain. Storage moduli, loss moduli and loss tangent are calculated analytically using Eq. (6.8) and Eq. (6.5) respectively. As mentioned earlier, $\delta(\omega)$ represents the phase angle by which stress lags the strain input and is a frequency dependent material property.

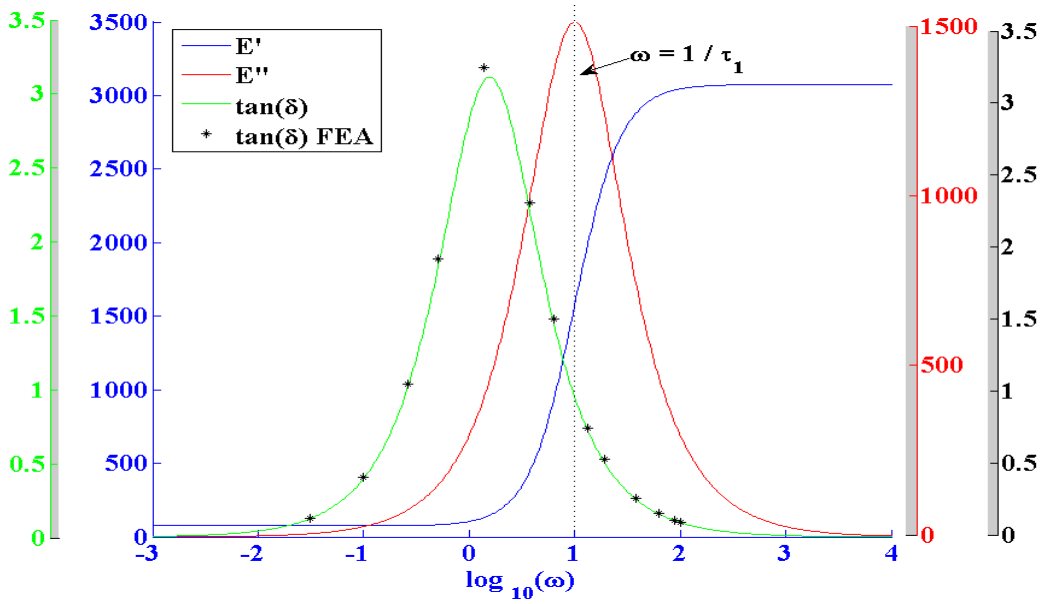

Figure 6.1: Analytical results for variation of storage and loss moduli and loss tangent as a function of frequency of applied load. Results for loss tangent obtained with FEA model are also plotted for validation.

To test this concept, a finite element model of a viscoelastic polymeric thin beam is developed using our MSMP framework (described in section 6.3) and is shown in Figure 6.2 (left). The material properties of the beam are modeled using the same parameters mentioned above. The beam is fixed at its top end and a cosine strain input of a fixed frequency (the real part of complex exponential; $\varepsilon(t) = \Re\left\{\varepsilon_0 e^{i\omega t}\right\} = \varepsilon_0 \cos(\omega t)$) is applied at its lower end. FE solution is obtained for time duration of interest for that particular frequency. The time history of normal stress σ_x and normal strain ε_x at a material point in the specimen is tracked. The results are shown in Figure 6.2 (right).

As discussed earlier, analytically we expect the stress to vary according to second equation of Eq. (6.7). We also expect the stress to lag the strain by a phase difference δ given by (6.5). This was indeed observed in the FEA results. The phase lag for this FE

example with $\omega = 13.44$ rad/s was obtained as $\delta = 3.768$ giving $\tan(\delta) = 0.7236$, which matches the analytical value of $\tan(\delta) = 0.725$ at that frequency. The procedure was then repeated for several frequencies to cover the broad range of relaxation spectrum. The results for $\tan(\delta)$ VS ω were obtained and are plotted over the analytical results in Figure 6.1.

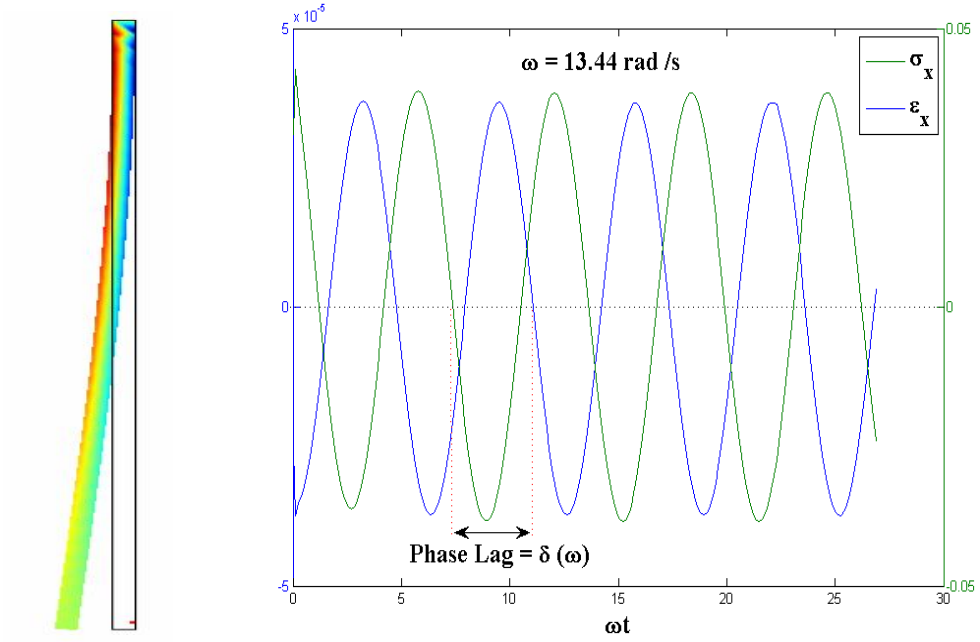

Figure 6.2: FEA model (left) and FEA result (right) showing phase lag between sinusoidal strain and corresponding stress at a material point in a viscoelastic solid.

It can be seen that the FEA results match very closely with the analytical results for loss tangent. Since variation in loss tangent is due to variation in storage modulus and loss modulus, the good agreement between the two results provides the confidence about

the accurate calculation of storage and loss moduli at broad range of frequencies and hence this is a good validation test for the viscoelastic model incorporated in the MSMP framework.

It can be seen that the storage modulus asymptotes at very low and very high frequencies. Storage modulus is a measure of the energy stored and recovered per cycle. Since both, $E(t)$ and $E'(\omega)$ are measures of stored elastic energy and a dynamic measurement at frequency ω is qualitatively equivalent to a transient one at $t = 1/\omega$, when plotted they are approximately mirror images of each other, reflected in the ordinate. This will be evident by comparing the two curves in Figure 6.3. Storage modulus provides important information on the order of magnitudes of energy distribution in the system. The magnitude of $E'(\omega)$ depends on what polymer chain rearrangements take place within the period of oscillatory deformation.

Loss modulus on the other hand is the component of the stress 90^O out of phase with the strain, divided by the strain. It is the measure of energy dissipated or lost as heat per cycle of sinusoidal deformation. An important characteristic of loss modulus is that for many thermoplastic and some thermoset polymers it shows a peak at frequency which corresponds to the inverse of the relaxation time constant of the system. It can be seen in Figure 6.1 that this, indeed, is observed for the simple one branch generalized Maxwell model considered above, where the peak in the loss modulus occurs at $\omega = 10 = \dfrac{1}{(\tau_1 = 0.1)}$.

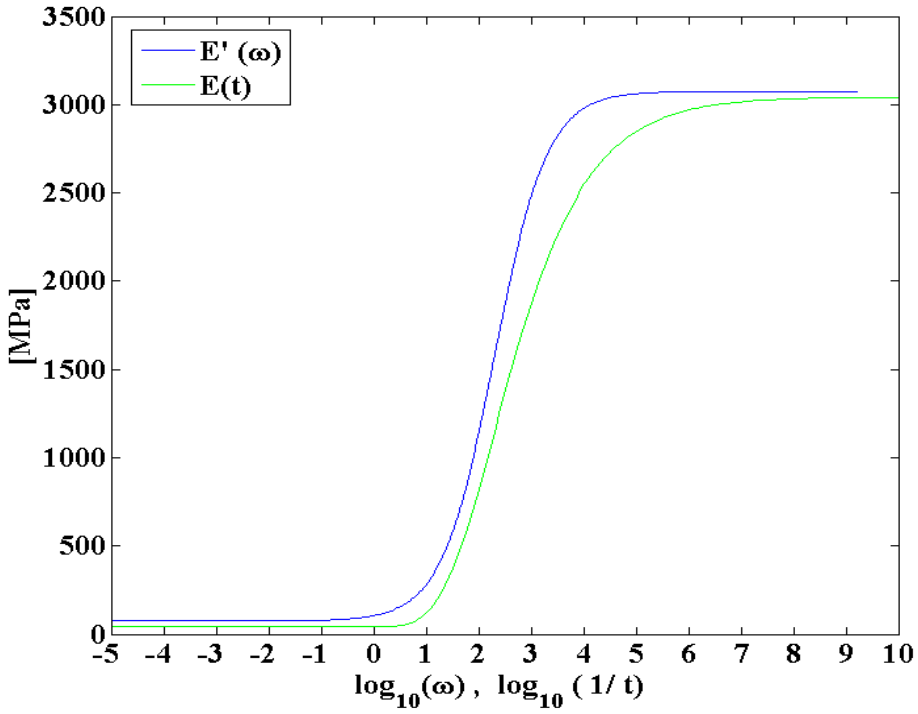

Figure 6.3: Comparison of storage modulus with relaxation modulus.

In the frequency regions where $E'(\omega)$ changes slowly, the behavior is close to purely elastic. In such regions, comparatively smaller amount of energy is dissipated and $E''(\omega)$ tends to be much smaller than $E'(\omega)$. Normally, for the polymers which exhibit the effect of entanglement coupling like amorphous polymers of high molecular weight (e.g. atactic PMMA) and lightly cross-linked amorphous polymers (e.g. styrene butadiene copolymer) , the flattening of E' at frequencies below the transition zone is accompanied by a plateau or minima in E'' [29]. At very high frequencies, the generalized Maxwell model is expected to approach a perfectly elastic behavior, as the motion of dampers becomes negligible compared to the springs. This should make $E''(\omega)$ approach zero. This indeed is observed in Figure 6.1. On a molecular basic, this corresponds to the

absence of atomic adjustments capable of dissipating energy within the period of deformation. However, for many soft polymers, the maxima in E'' occur at high frequencies beyond which the losses due to configurational changes diminish [29]. There can also be more than one local maxima in the loss modulus which correspond to the inverse of more than one relaxation time constants associated with other dissipative molecular process. For the linear viscoelastic solid with a simplified version of generalized Maxwell model without a free spring, it can be imagined that E'' will again be directly proportional to ω at very low frequencies.

Another important observation from Figure 6.1 is that the loss tangent shows a "bell" shaped profile, very typical of that obtained experimentally for many polymers (e.g. polycarbonates, PTFE and PMMA). Loss tangent is a measure of the ratio of energy lost to energy stored in a cyclic deformation. For the polymers in the transition zone (between glass-like and rubber-like consistency), the loss tangent demonstrates a pronounced maxima. It is interesting note that the maxima in E'' occurs to the right of that in $\tan(\delta)$ on the frequency scale. For very lightly cross-linked polymers (e.g. styrene-butadiene copolymer) there are subsidiary maxima at lower frequencies associated with losses involved in entanglement slippage of polymer chains [29]. Typically, smaller maxima also occur in glassy and highly crystalline polymers, which reflect other dissipative mechanisms. These secondary maxima are not seen in Figure 6.1, as the model for these plots is very simplistic. But the model for Figure 6.6 has 5 such local maxima in $\tan(\delta)$ (which occur at frequencies indicated by dotted black lines; 3 of them corresponding to $1/\tau_1, 1/\tau_3, 1/\tau_4$ can be clearly identified while other 2 corresponding to $1/\tau_2, 1/\tau_5$ are more subtle and hard to see in the plot) and hence does a

better job at covering losses occurring at broader range of frequencies. Also, typically, lightly cross-linked polymers attain a very small value of loss tangent at low frequencies. Loss tangent determines macroscopic physical properties like damping of free vibrations, attenuation of propagated waves and frequency width of resonance response and hence is of prime importance in dynamic modeling of viscoelastic structures.

To understand the effect of magnitude of instantaneous elastic moduli E_i on the sluggishness of the seal, analytical calculations for a thin linear viscoelastic material are performed to get stress-strain history for a range of values of E_1 (Although, the seal's MSMP model developed later will be 2D axisymmetric, the effects seen here will be qualitatively same). Figure 6.4 shows the phase lag obtained as a function of the ratio E_1 / E_∞ for various values of frequency. It is observed that for low frequencies as system becomes stiffer (increasing E_1), the phase difference between stress and strain increases, i.e. viscoelastic structure becomes more sluggish to react to the applied load. At higher frequencies too, this behavior is observed but only up to a certain critical instantaneous stiffness beyond which the phase angle asymptotes to a constant value. Also, in the range of frequencies considered here (typical of a reciprocating rod seal application), the phase lag increases with increase in frequency for a given modulus ratio.

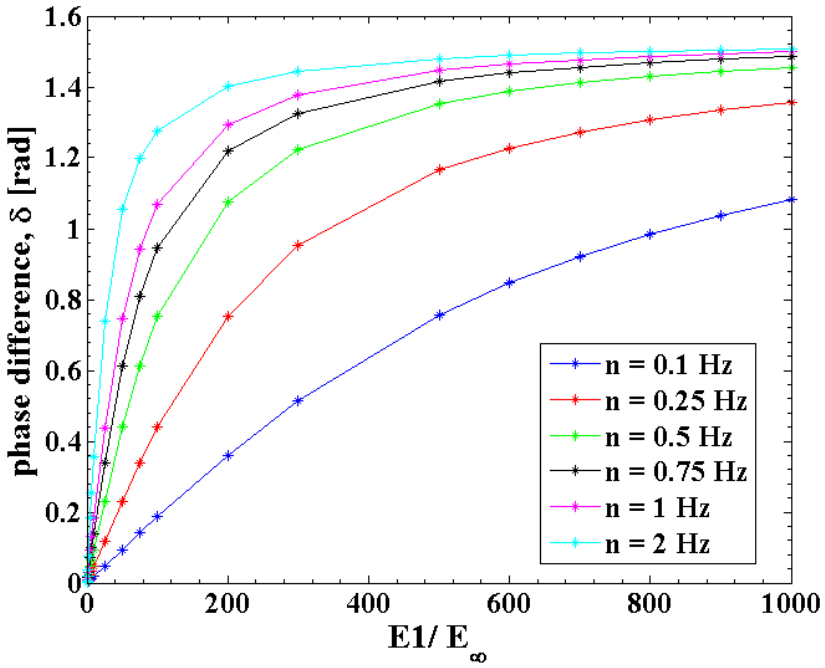

Figure 6.4: Phase lag as a function of stiffness ratio for a single branch Maxwell model.

Now, one may expect the phase difference to decrease monotonically with decrease in relaxation time constant for a fixed instantaneous stiffness. To test this hypothesis, calculations were performed for various values of time constants for a single branch Maxwell model and the calculations were repeated for range of stiffness ratios. Figure 6.5 shows the results from these calculations. It was observed that the above hypothesis is incorrect and in fact the curve shows a bell-shaped profile reminiscent of the $\tan(\delta)$ vs ω curve. Hence a reduced time constant does not always guarantee less sluggish response of the material to the applied load. Also, it was observed that increasing stiffness ratio seems to skew the curves towards left. i.e. with increasing stiffness, the maxima in phase difference occurs at lower and lower time constants. Also at very high stiffness ratios, the phase difference starts to form a plateau at the top, covering wide range of time constants. This is important in predicting dynamic

viscoelastic behavior of seals. For example, above result implies that polymeric seal materials with instantaneous stiffness ratios above 500 or so will be less prone to changes in relaxation time scales in the range 0.003 sec to 0.1 sec and will not show any improvement in instantaneous response even if the time constant is reduced. Hence the plots like the ones in Figure 6.1, Figure 6.4 and Figure 6.5 will provide critical information for choosing appropriate seal materials for particular dynamic applications.

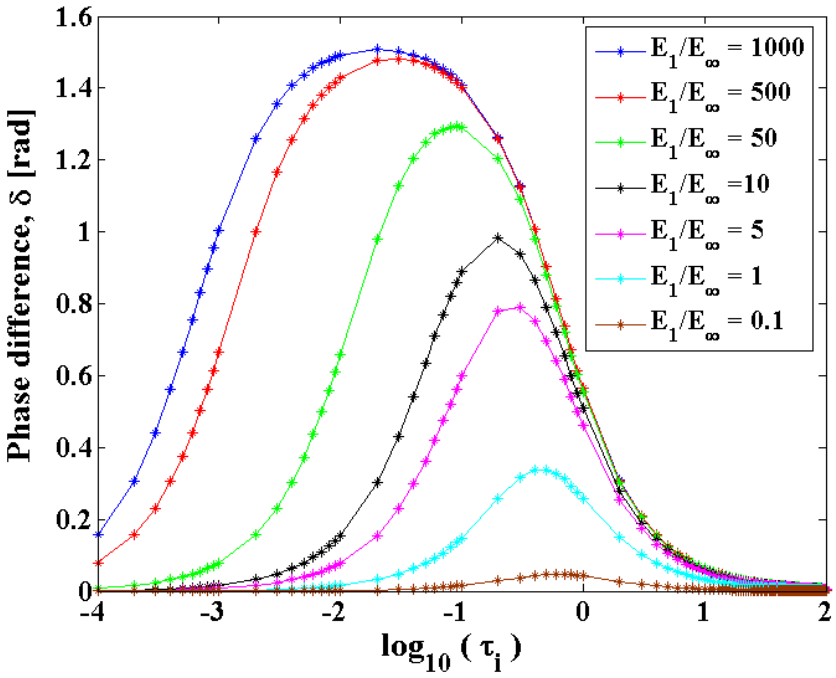

Figure 6.5: Phase lag as a function of relaxation time constant for a single branch Maxwell model.

Figure 6.6 shows the analytical results for storage moduli, loss moduli and loss tangent and it's comparison with FEA results for loss tangent obtained with the MSMP framework (developed in section 6.3.1) for a thin beam. The beam is made of viscoelastic seal material (polyurethane) with following viscoelastic parameters: $E_\infty = 43$ MPa, $E_i = [90, 15, 11, 7, 0.9]$ MPa, $\tau_i = [0.3, 3, 60, 300, 1000]$ sec. With more

time constants, it is expected that this material model would capture the true viscoelastic behavior at wide range of frequencies more accurately than a single branch Maxwell model of Figure 6.1. This indeed is reflected especially in the variation of loss modulus and loss tangent. The loss modulus now has 5 maxima that correspond to the five time constants of the system (which occur at frequencies indicated by dotted black lines; 3 of them corresponding to $1/\tau_1, 1/\tau_3, 1/\tau_4$ can be more easily identified, while other 2 corresponding to $1/\tau_2, 1/\tau_5$ are subtle and hard to see in the plot). These subsidiary maxima better capture the relaxation mechanisms occurring in polyurethane at much lower frequencies, which were observed during experimental measurements using Dynamic Mechanical Analysis. With respect to the transition region, the decay in storage modulus is less rapid as compared to the single branch Maxwell model. This transition region now extends across all five relaxation time scales instead of asymptoting right after the first peak as in Figure 6.1. This behavior is much more similar to that in a real polymer. In the MSMP framework for accurately modeling viscoelastic response over wide frequency range, it was necessary to capture a large range of relaxation time scales like the ones shown here. For this purpose Dynamic Mechanical Analysis was performed on several seal samples and using a novel algorithm, a spectrum of instantaneous moduli was extracted (see section 7.1.2.2). The moduli and time constants thus obtained were then used in the MSMP model to solve for the dynamic behavior of seal under time varying sealed pressure and rod velocity. The experimental investigation is explained in detail in Chapter 7.

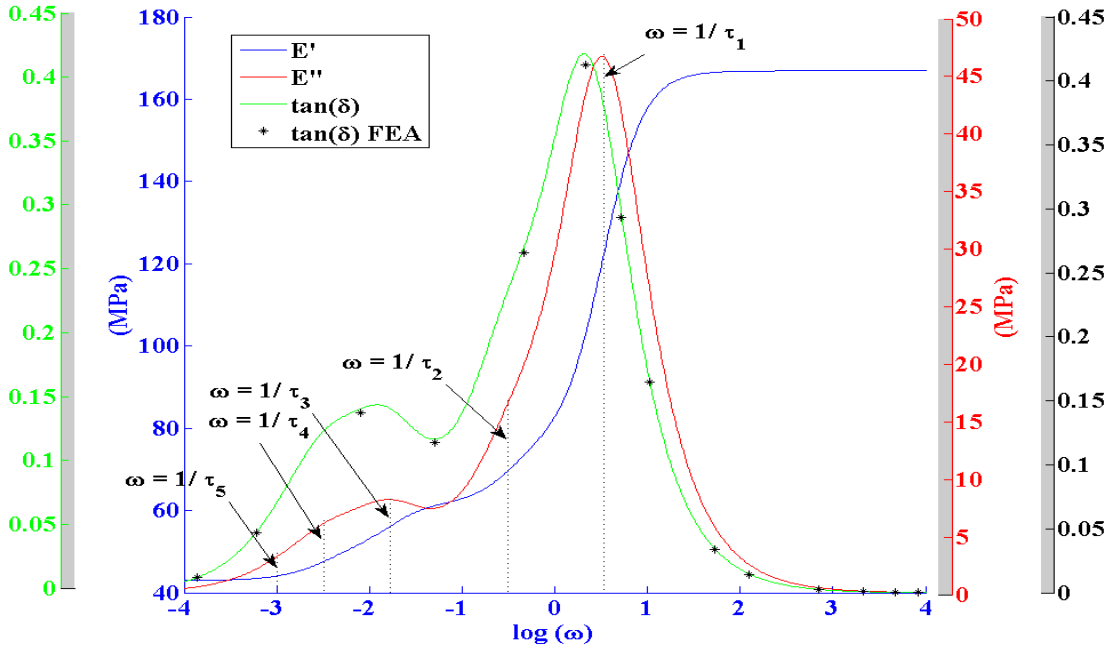

Figure 6.6: Analytical results for variation of storage and loss moduli and loss tangent as a function of frequency of applied sinusoidal strain; Results for loss tangent obtained with FEA model are over plotted for validation.

6.2 Macro-Scale Dynamic Response of a Rod Seal (without fluid film)

After investigating the basic dynamic viscoelastic behavior of simple polymer structure, the next logical step was to see how the actual seal of intricate shape and design would behave under real loading and contact conditions. Now, according to Fourier analysis, any signal can be constructed from a combination of sinusoidal waveforms, it would be interesting to see the viscoelastic response of the seal to these basis functions. For the linear viscoelastic seal material, the response to any other signal then can be imagined to be the superposition of the responses to individual basis signals. With this in mind, the seal of interest was subjected to a sinusoidally varying sealed pressure boundary condition. The displacement constraints and contact conditions were

maintained same as those for the linear elastic material model as discussed in chapter 3. To avoid tensile boundary conditions (as they do not occur in real sealing applications), only the absolute value of the signal was applied as sealed pressure boundary condition. The frequency of the applied sealed pressure was 0.125 Hz, which approximately is equivalent to the "active" cycle period for the injection molding application discussed in chapter 5. After 4 cycles (16 sec) the sealed pressure was removed (held constant at an ambient value) and the seal was allowed to relax for 4 more seconds (16 sec-20 sec). The time history of radial, axial and shear stresses, strains, particle displacements, contact pressures and sealing zone lengths as well as the overall seal deformations was tracked. The study was repeated for several seals with same elastic moduli but different time constants. The elastic moduli, same for all the seals, were:

$E_\infty = 43$ MPa and $E_1 = 3000$ MPa while time constants for four different seals were:

$\tau_1 = 0.001, 0.01, 0.1$ and 1.0 sec. Some of the results obtained from this study are presented in Figure 6.7 though Figure 6.13.

Figure 6.7 (top left) shows the applied time varying sealed pressure boundary condition and the corresponding deformation of the seals at the end of the 4^{th} cycle (t=16.0 sec) of loading. The surface plot shows the von-Mises stress distribution in the seal body. Also shown are the displacement streamlines in the seal body. It can be seen that the seal with smallest time constant immediately returns to its original undeformed shape as soon as the applied load is removed, while the seals with $\tau_1 = 0.01$ sec and $\tau_1 = 0.1$ sec are progressively farther away from their original configuration.

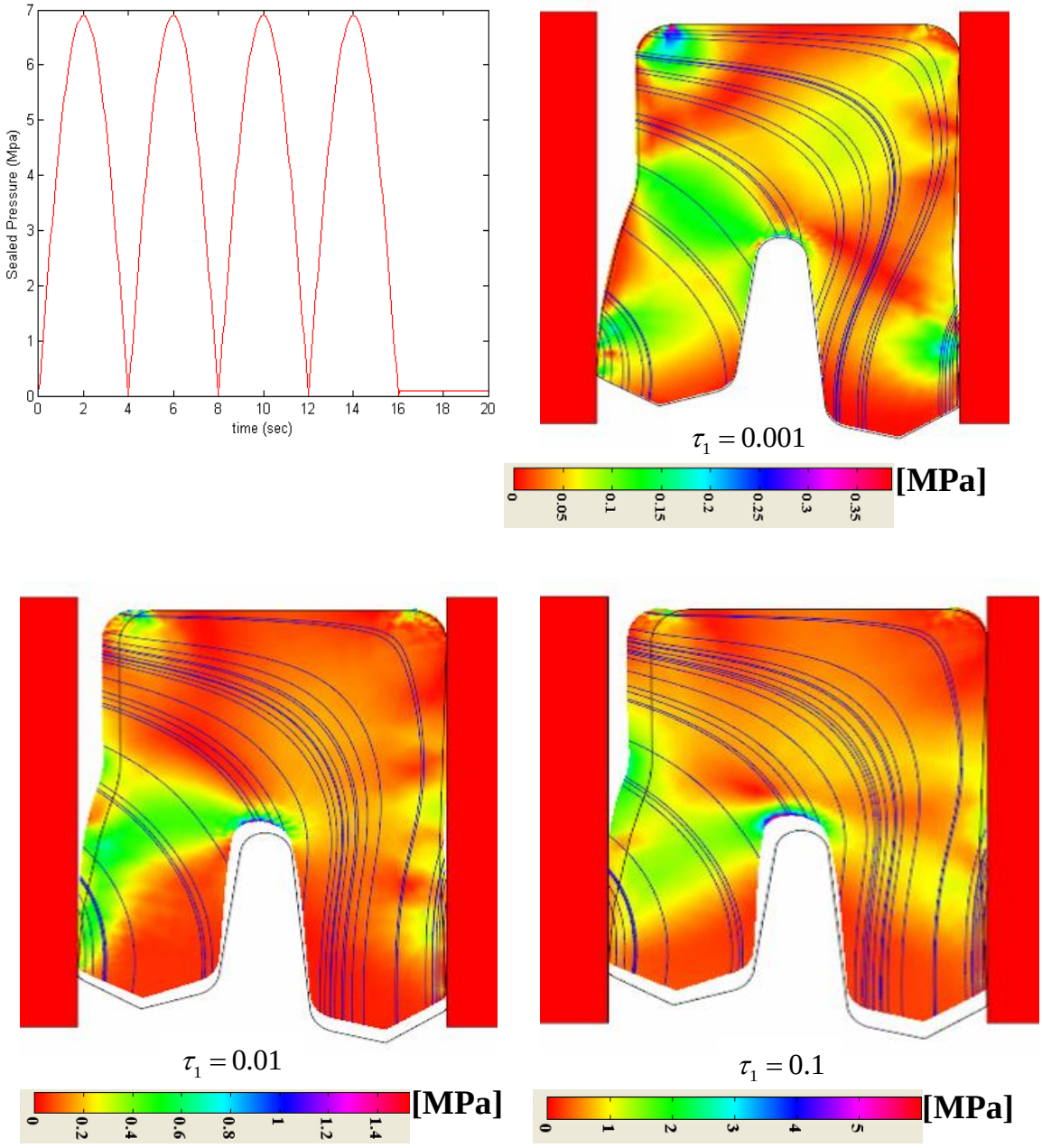

Figure 6.7 : Sealed pressure waveform (top left) applied to the seals of various relaxation time constants and corresponding seal deformations at the end of the 4th cycle (16 sec). Color plot shows the von Mises stress distribution in the seal and streamlines show the displacement field.

Another important difference is the length of the sealing zone is quite different for the three seals. Also there are differences in the curvature of streamlines and the stress

distribution near the sealing edge. Since the contact pressure in the sealing zone is directly related to the stress distribution near the sealing zone, it can be imagined that contact pressure distribution over the sealing zone would be very different for the three seals as well. Sealing zone length and contact pressure are some of the primary characteristics that govern the dynamics of sealing and hence it can be concluded that the relaxation time scales associated with the seal's polymer can have a major impact on the sealing performance.

Figure 6.8 (a) shows the Cauchy stress in the radial direction at a material point in the seal. As expected, it follows the exact same pattern as the pressure boundary condition. Parts (b),(c) and (d) show the radial strain at the same material point in the three different seals with increasing time constants. The strain can be seen to keep up with the stress for $\tau_1 = 0.001$ sec, but it starts to show the increase in the phase lag for $\tau_1 = 0.01$ sec and $\tau_1 = 0.1$ sec seals leading to a time lag of ~ 0.7 sec and ~ 2 sec respectively. The strain for $\tau_1 = 0.001$ sec shows double peaks. The reason for this is not entirely clear, but one possibility is due to the interference of excitation phases of neighboring material particles. This is not seen in other plots, as the phase lags are different for different time constants, as was seen from Figure 6.5. It can also be seen that in the "relaxed" period (16 sec-20 sec), the strain in $\tau_1 = 0.01$ sec seal shows a typical exponential decay reminiscent of a single branch Maxwell model. Even after 4 seconds of relaxed period, this seal has not completely returned to its base state, while the seal with $\tau_1 = 0.1$ sec time constant can be seen to be much farther from the un-strained state at the end of 20 seconds.

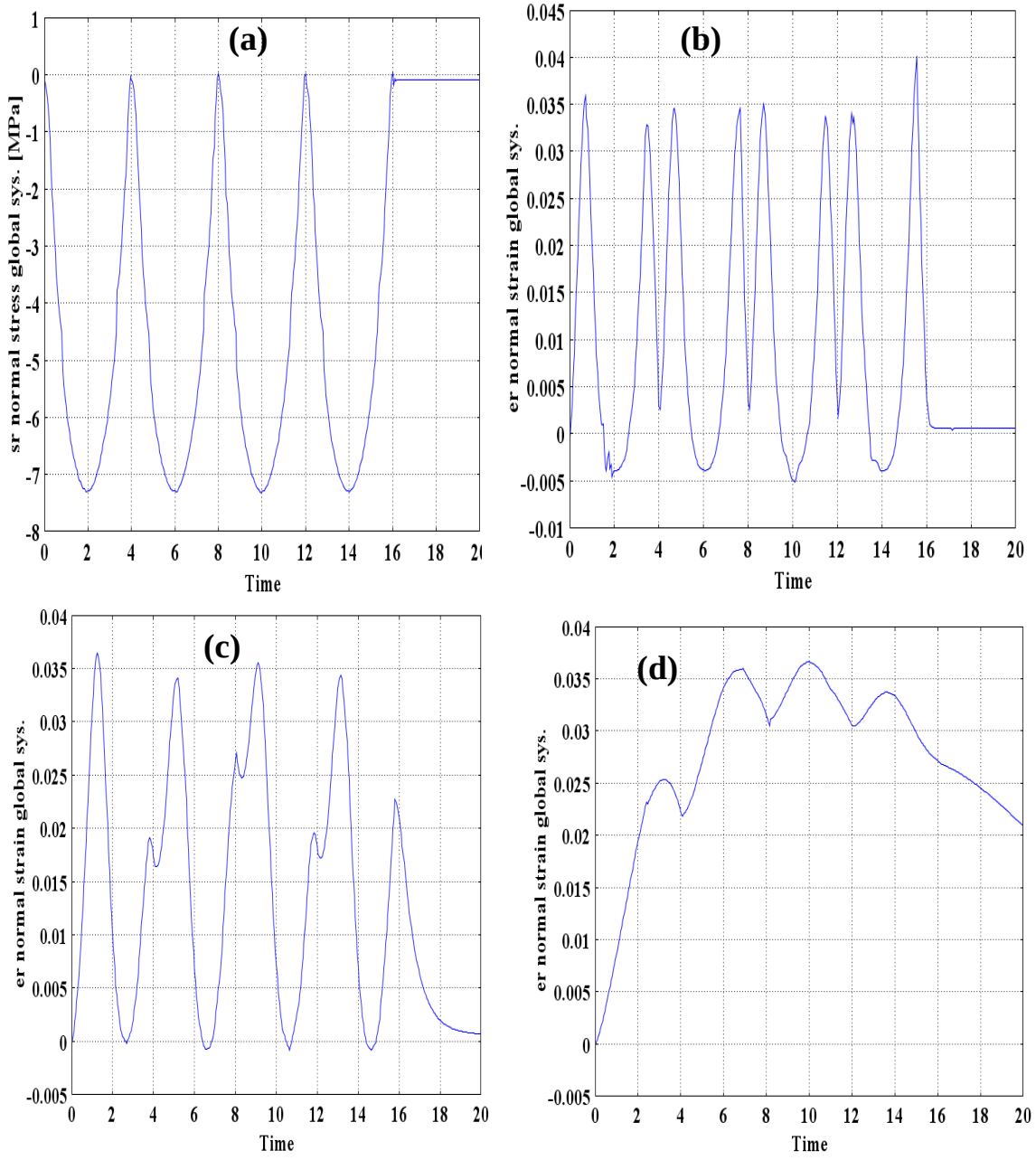

Figure 6.8: **Cauchy stress in radial direction at a material point in seal body (a) and corresponding radial strain for seals with** $\tau_1 = 0.001$ sec **(b),** $\tau_1 = 0.01$ sec **(c), and** $\tau_1 = 0.1$ sec **(d).**

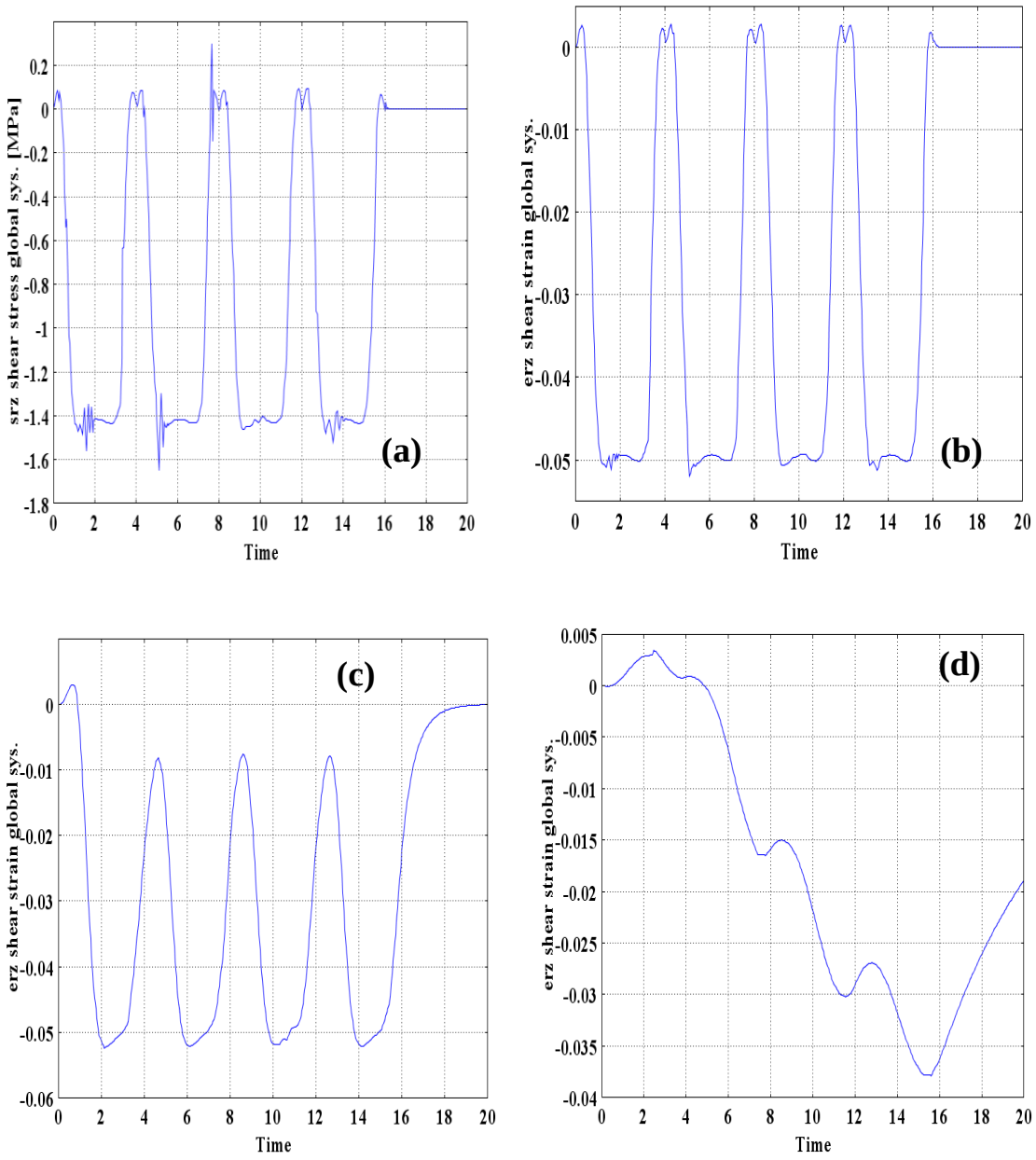

Figure 6.9: **Cauchy shear stress r-z direction at a material point in seal body (a) and corresponding shear strain for seals with Tau1=0.001 (b), 0.01(c),and 0.1 (d).**

Similar behavior is observed in the case of shear stress and strain curves of Figure 6.9. The phase-lag observed in the stress-strain history for different time constants makes it more clear why the seal deformations and sealing zone lengths seen in Figure 6.7 are so different at the end of the active sealing period.

Figure 6.10 shows the radial Cauchy stress vs radial strain and shear stress vs shear strain plots for seals with $\tau_1 = 0.001$ sec and $\tau_1 = 0.01$ sec. The typical elliptical shape of the curve shows the "Hysteresis loop" and is a consequence of linear viscoelastic behavior. The width of this hysteresis loop is a measure of the loss angle δ of a linear viscoelastic material. δ can quantitatively be approximated from such a hysteresis loop for a sinusoidal stress-strain. If A is the intercept of the return path with the strain axis and $B = \varepsilon\big|_{\sigma_{\max}}$, then it can be shown that $\tan(\delta) = A/B$. This is further elaborated in Figure 6.11 (a), where $\delta = 0.5$ was extracted back from the hysteresis loop.

Figure 6.11 (b) shows the hysteresis loops for various values of phase angles. Another important observation that can be made from Figure 6.10 is that the width of the hysteresis loop has increased substantially when going from with $\tau_1 = 0.001$ sec to $\tau_1 = 0.01$ sec seal. For a given viscoelastic material, the degree of phase lag and the width of hysteresis loop depend greatly on the frequency and temperature at which the loading is executed. If stress and strain are completely in phase with each other, we get a straight line instead of the loop. At a frequency and temperature where the material behaves in a "glassy" manner, the phase lag and hysteresis are very small. Also, the area inside the hysteresis loop represents the energy lost or dissipated during a cyclic deformation and hence gives an idea about magnitude of losses associated with the two seals for given operating conditions.

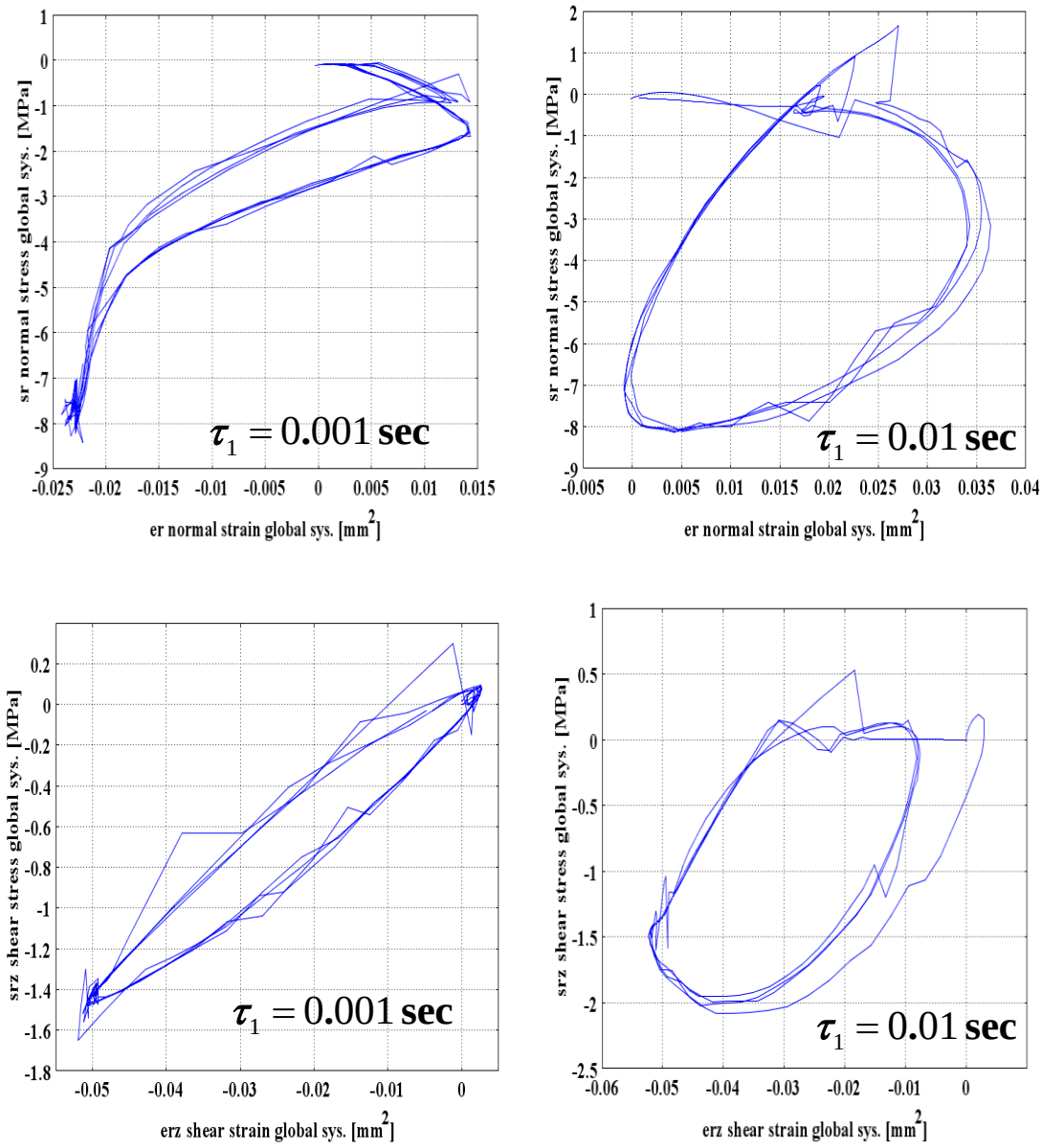

Figure 6.10: Radial (top plots) and shear (bottom plots) hysteresis loops for seals with different time constants.

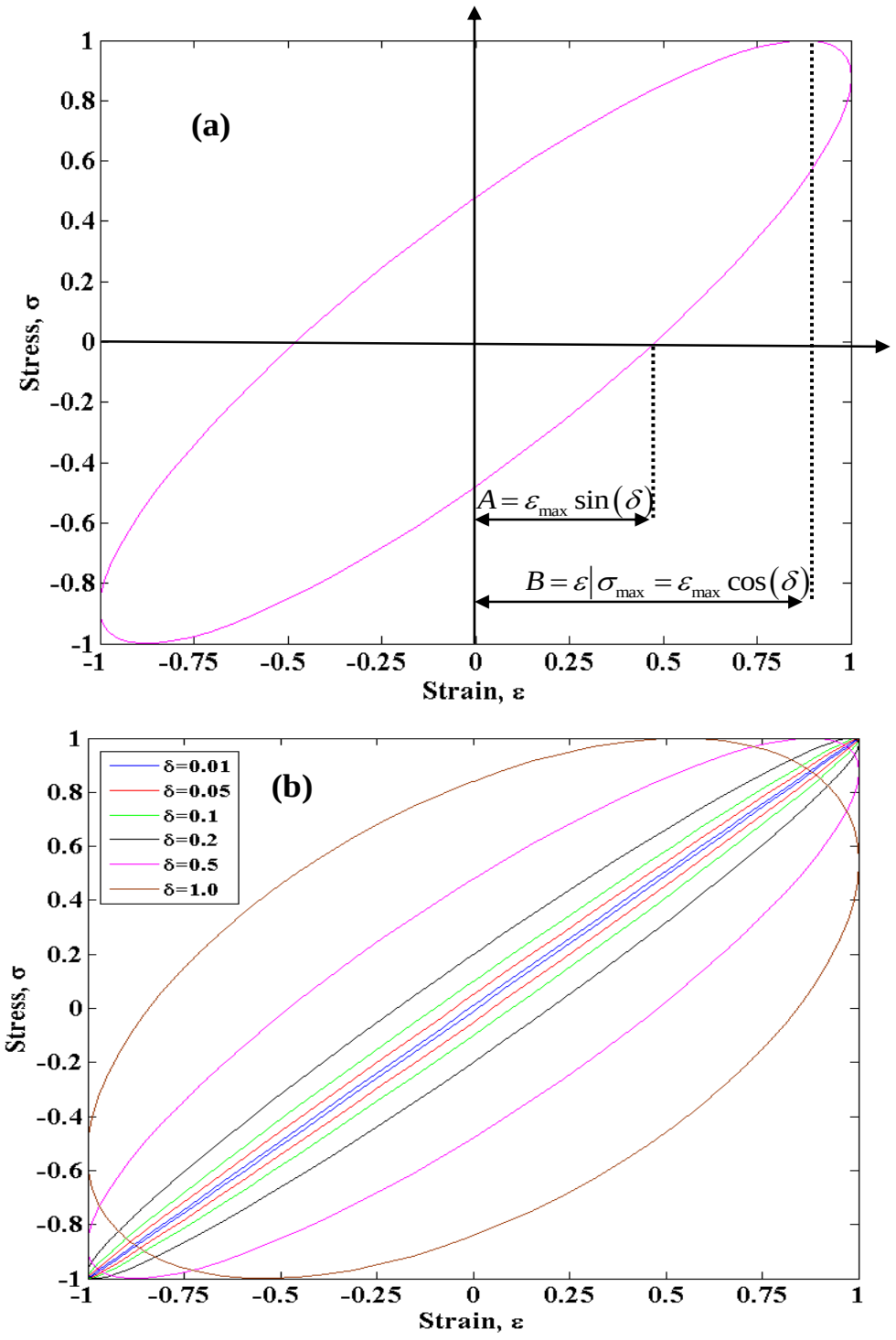

Figure 6.11: (a) Extraction of phase lag from hysteresis loop. (b) Hysteresis loop for various phase angles.

If the seal behaves in a perfectly elastic manner, the deformation energy supplied during loading is stored in stretching of the molecular chains and is recovered completely upon unloading the seal i.e. there will be no energy dissipated. For a complete cycle of symmetric oscillatory loading and unloading, the net energy stored is zero. However, the amount of energy dissipated in a complete cycle of oscillatory loading is given by Eq. (6.9) and can be seen to be proportional to the loss modulus as follows:

$$\text{Energy dissipated per cycle} = \int_{\text{cycle}} \sigma \, d\varepsilon = \int_{0}^{2\pi/\omega} \sigma \dot{\varepsilon} \, dt \tag{6.9}$$

For a perfectly elastic material, $\sigma = E\varepsilon$ and the evaluation of the above integral results in zero and hence the hysteresis loop reduces to a line. However, for a viscoelastic material,

$$\sigma(t) = E^{*}(\omega)\varepsilon(t) = E'(\omega)\varepsilon(t) + \frac{E''(\omega)}{\omega}\dot{\varepsilon}(t) \tag{6.10}$$

Substituting Eq.(6.10) into Eq. (6.9) and for a sinusoidal input strain $\varepsilon(t) = \varepsilon_0 \sin(\omega t)$ we get,

$$\text{Energy dissipated per cycle} = \int_{0}^{2\pi/\omega} \left[E'(\omega)\varepsilon_0 \sin(\omega t) + \frac{E''(\omega)}{\omega} \omega t \, \varepsilon_0 \cos(\omega t) \right] \omega t \, \varepsilon_0 \cos(\omega t) \, dt$$

Which after simplification reduces to,

$$\text{Energy dissipated per cycle} = \varepsilon_0^{\,2} \omega \pi E''(\omega) \tag{6.11}$$

Hence, the energy dissipated can be seen to be proportional to the loss modulus. In the frequency / temperature range where the loss modulus is low, the energy dissipation will be much smaller while in the regions where the loss modulus peaks, the dissipation will be maximum. This fact should be underlined when designing seals for particular frequency applications or for high temperature use.

To further understand the effect of relaxation time scales on sealing performance metric like sealing zone length, cyclic history of sealing zone length is calculated for the same four seals with same relaxation moduli but different time constants. The resulting plot is showed in Figure 6.12. Since the axial displacement of seal's material points plays a vital role in defining the sealing zone length, the history of axial displacement at such a material point in the seal body is shown in Figure 6.13. At $\tau_1 = 0.001$ sec the axial displacement at the material point follows the load history very closely. The magnitudes of displacement can be seen to be the same for all the cycles in this figure. At $\tau_1 = 0.01$ sec it starts to show the hysteresis, as the second cycle begins before the material point can come back to its undisplaced state. Little accumulation in displacement from cycle to cycle is visible. At $\tau_1 = 0.1$ sec the phase difference between stress and strain is clearly reflected in the axial displacement. The accumulation of displacement from cycle to cycle becomes prominent as the maximum displacement increases by almost 100 % from 1st cycle to 4th cycle for $\tau_1 = 0.1$ sec and by 160 % for $\tau_1 = 1.0$ sec. The seals with $\tau_1 = 0.1$ sec and $\tau_1 = 1.0$ sec are far displaced from base state even at the end of 4 sec of relaxed period. Another important observation is that the magnitude of axial displacements decays non-linearly with increasing time constant of the seal, reducing by almost 15 times for the first cycle while going from $\tau_1 = 0.001$ sec to $\tau_1 = 1.0$ sec. These observations are critical in understanding the sealing characteristics of seals with different polymeric materials and hence different time constants.

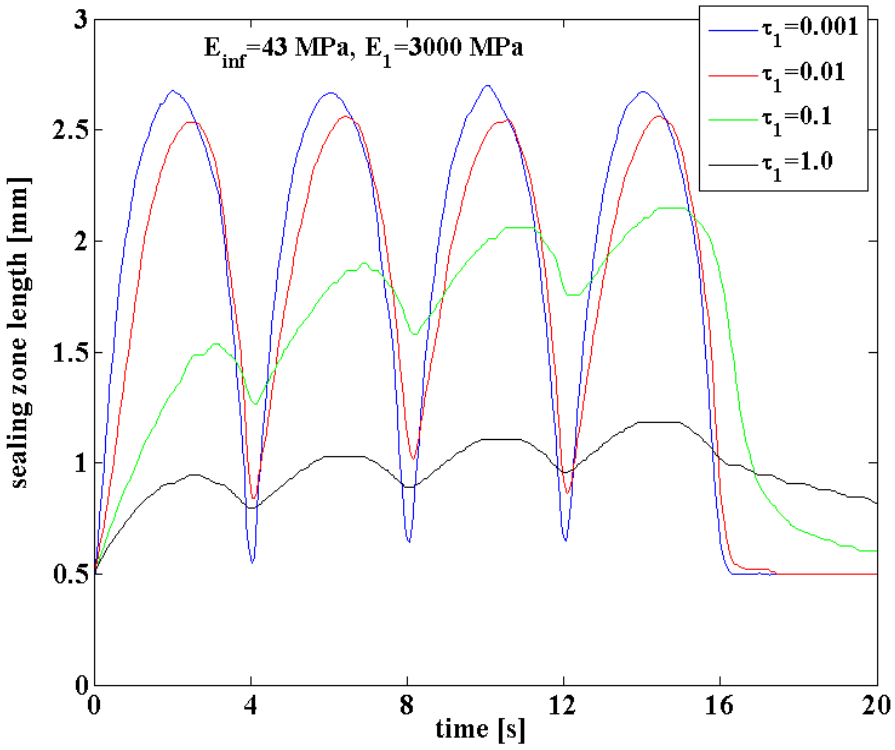

Figure 6.12: Sealing zone length obtained for seals with same elastic moduli but four different time constants.

The characteristics of axial displacement of material points are reflected in variation of sealing zone length with time constant as seen in Figure 6.12. The maximum sealing zone length in the first cycle is reduced by about 5 % , 43 % and 64 % in going from $\tau_1 = 0.001$ to $\tau_1 = 0.01$, $\tau_1 = 0.1$ and $\tau_1 = 1.0$ respectively. The accumulation effect is also visible in the sealing zone lengths for seals with $\tau_1 = 0.1$ and $\tau_1 = 1.0$. Since the sealing zone length is one of the key characteristics governing sealing performance, the polymeric material chosen while designing seals should be such that it caters to the desired sealing zone characteristics under given dynamic conditions.

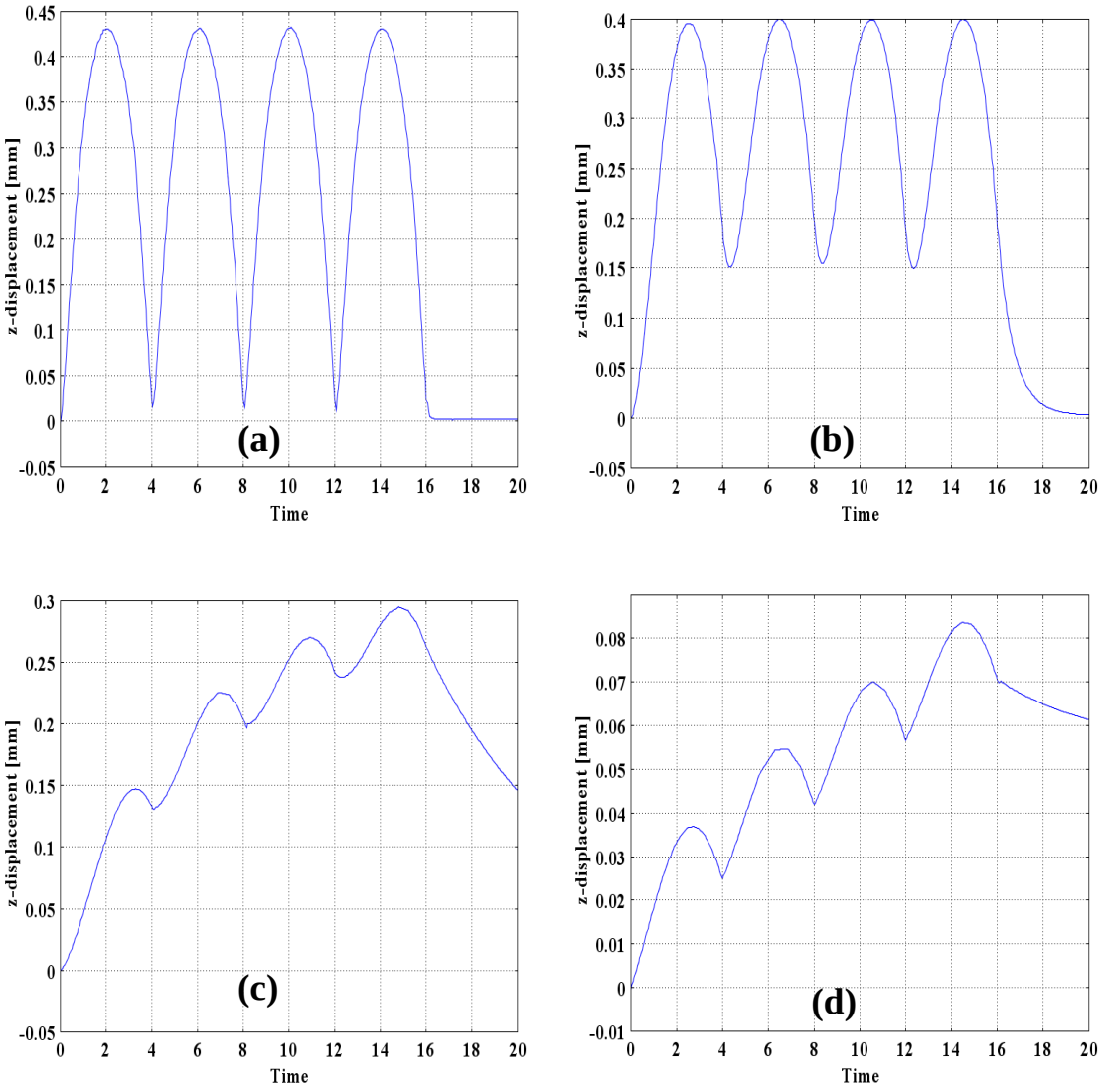

Figure 6.13: Axial displacement at a material point in seal body for seals with $E_\infty = 43$ MPa, $E_1 = 3000$ MPa but different time constants: (a) $\tau_1 = 0.001$ sec (b) $\tau_1 = 0.01$ sec (c) $\tau_1 = 0.1$ sec (d) $\tau_1 = 1.0$ sec.

The theoretical studies performed on the real seal designs using the MSMP framework as discussed in this section were useful in understanding the dynamic performance of these seals under various loading conditions of different frequencies, seal materials with different relaxation spectra and macro-scale contact. The effect of relaxation time scales of seal materials on phase angles, hysteresis and hence on dissipation characteristics was also revealed. MSMP framework allowed studying the dynamic viscoelastic response of intricate seal structures under fundamental oscillatory modes of loading, which would not have been feasible with analytical methods. It also revealed the effect of seal material relaxation spectra on critical seal performance characteristics like sealing zone length.

6.3 Incorporating Viscoelasticity into the MSMP Framework

6.3.1 Macro-Scale Viscoelastic Deformation and Contact Mechanics

The general stress-strain law for a linear viscoelastic solid is constructed with following considerations: 1) Material experiences small shape changes and rotations. 2) Assume that for time $t < 0$, the solid is stress free, and $\varepsilon_{ij} = 0$. 3) Assume that the material is isotropic. 4) Material response to a pure volumetric strain, $\varepsilon_{11} = \varepsilon_{22} = \varepsilon_{33} = \left(V - V_0\right)/3V$ is perfectly elastic (no time dependent behavior). Hydrostatic stress induced by the volumetric strain is $\sigma_{11} = \sigma_{22} = \sigma_{33} = \sigma$. The hydrostatic stress is related to the volumetric strain by $\sigma = 3K\delta V/V$ where K is the bulk modulus.

Now, the stress relaxation is the time variation of stress $\sigma(t)=\varepsilon_0 E(t)$ in response to a step function of strain history ($\varepsilon_0\tilde{\mathrm{H}}(t)$) and creep compliance is the strain output for a step input in stress history ($\sigma_0\tilde{\mathrm{H}}(t)$). According to "Boltzmann superposition principle", for a linear viscoelastic material, the effect of a compound cause is the sum of the effects of individual causes and hence for a rectangular pulse stress input, $\sigma(t)=\sigma_0\left[\tilde{\mathrm{H}}(t)-\tilde{\mathrm{H}}(t-t_1)\right]$, the strain is given by, $\varepsilon(t)=\sigma_0\left[J(t)-J(t-t_1)\right]$, where $J(t)$ is the compliance of the material. Similarly, if a random variable stress input is decomposed into infinitesimal pulses and represented by a series of step inputs,

$$\sigma(t)=\sigma_0\,\tilde{\mathrm{H}}(t)+\sum_k\left[\sigma_k-\sigma_{k-1}\right]\tilde{\mathrm{H}}(t-t_k) \tag{6.12}$$

then the corresponding strain output for a linear viscoelastic material becomes,

$$\varepsilon(t)=\sigma_0\,\tilde{\mathrm{H}}(t)\;J(t)+\sum_k\left[\sigma_k-\sigma_{k-1}\right]\tilde{\mathrm{H}}(t-t_k)\;J(t-t_k) \tag{6.13}$$

Multiplying and diving by the pulse width $\Delta\tau$ and taking the limit as the pulse width approaches zero, the summation converges to integration and we get,

$$\varepsilon(t)=\int_{0^-}^{t}J(t-\tau)\frac{d\left[\sigma(\tau)\tilde{\mathrm{H}}(\tau)\right]}{d\tau}d\tau \tag{6.14}$$

Here the upper limit is set at "t", as with the principle of "Causality", the pulses in the future have no effect on the state of strain at the present time. The lower limit is set at $t=0^-$ and includes the jump discontinuity in the stress at the beginning. Now noting that $\frac{d\tilde{\mathrm{H}}(\tau)}{d\tau}=\delta(\tau)$, where $\delta(\tau)$ is the Dirac Delta function , we get,

$$\varepsilon(t)=\int_{0^-}^{t}J(t-\tau)\left\{\frac{d\sigma(\tau)}{d\tau}\tilde{\mathrm{H}}(\tau)+\sigma(\tau)\,\delta(\tau)\right\}d\tau \tag{6.15}$$

Now, using the sifting property of $\delta(\tau)$, which states,

$$\int_a^b f(\tau)\delta(t-\tau)d\tau = f(t)$$

we get,

$$\varepsilon(t) = \sigma_0 \tilde{H}(t) J(t) + \int_{0^+}^{t} J(t-\tau)\frac{d\sigma(\tau)}{d\tau}d\tau \tag{6.16}$$

where integral is from $t = 0^+$ and does not take the discontinuity into account. Discontinuity is expressed explicitly as the first term on right hand side. An analogous derivation for the stress output obtained with the strain history as an input gives,

$$\sigma(t) = \int_{0^-}^{t} E(t-\tau)\frac{d\varepsilon(\tau)}{d\tau}d\tau \tag{6.17}$$

Eq. (6.17) is the constitutive equation that will be used for the viscoelastic material model of MSMP framework. However, as discussed earlier, the stiffness matrix for a nearly incompressible material becomes ill-conditioned. To bypass this problem, again the total stress is decomposed into the deviatoric and hydrostatic parts as, $\sigma_{ij} = S_{ij} + \frac{\sigma_{kk}\delta_{ij}}{3}$, the hydrostatic stress is given by, $\frac{\sigma_{kk}}{3} = K\left(\frac{\partial u_k}{\partial x_k}\right)$ and the constitutive relation for the viscoelastic deviatoric stress (S_{ij}) in terms of the deviatoric strain is written,

$$S_{ij} = \int_0^t 2G(t-\tau)\frac{d\left[\varepsilon_{ij}(\tau) - \frac{1}{3}\varepsilon_{kk}(\tau)\delta_{ij}\right]}{d\tau}d\tau \tag{6.18}$$

In Eq.(6.18), the shear relaxation modulus $G(t)$ can be expressed in terms of the elastic relaxation modulus $E(t)$ as,

$$G(t) = \frac{E(t)}{2(1+\upsilon)} \tag{6.19}$$

In the MSMP framework, the relaxation modulus $E(t)$ is defined using the Generalized Maxwell model with a Prony series representation as discussed earlier,

$$E(t) = E_\infty + \sum_{i=1}^{N_p} E_i e^{-t/\tau_i} \tag{6.20}$$

The equations of motion, kinematic equations and boundary conditions used for solving the macro-scale deformation and macro-scale contact mechanics are the same as those described in chapters 3 and 5. Using δu_i as the virtual displacement field and $\delta\tilde{\varepsilon}_{ij}$ as the virtual strain field, the principal of virtual work for the viscoelastic MSMP model is then written as,

$$\begin{aligned}\int_R S_{ij}\,\delta\varepsilon_{ij} dV_0 + \int_R p\,\delta\varepsilon_{qq} dV_0 + \int_R \delta p\left(\frac{\sigma_{kk}}{3K} - \frac{p}{K}\right) dV_0 + \int_R \rho_0 \frac{d^2 u_i}{dt^2}\delta u_i dV_0 \\ - \int_R \rho_0 F_{bi}\delta u_i dV_0 - \int_{\partial R_2} b_i^*\,\delta u_i dA = 0\end{aligned} \tag{6.21}$$

where p is the additional degree of freedom representing the unknown hydrostatic stress and δp is the arbitrary variation in the hydrostatic stress. Subscript "0" indicates the undeformed configuration. The above equations are discretized using the finite element method in a way similar to that described in sections 3.2.2 and 5.3. Second order Lagrange quadratic polynomials are used as shape functions. Computations are performed using an in-house MATLAB code coupled with the Comsol finite element solver. The finite element mesh consists of 13757 2nd order Lagrange elements (based on a mesh refinement study).

6.3.2 Macro-Scale Viscoelastic Contact Mechanics

In the viscoelastic MSMP model, the macro-scale contact mechanics at the seal-rod interface and the seal-housing interface are solved using the same augmented Lagrangian formulation as described in section 3.3. A contact map operator $\tilde{C}$, a gap distance variable g and contact normal penalty factor p_n are defined, and for each slave point of interest a corresponding master point is searched in the direction normal to the slave boundary. However, this contact mechanics problem becomes very stiff and hard to converge for viscoelastic material, especially in the regime of instantaneous deformation and loading. For this purpose "viscoelastic transient initialization" calculations are performed in Comsol to pre-compute the initial states for the time dependent studies. This assumes that any possible elastic pre-strain of the material is always fast enough to equally affect all the branches of the generalized Maxwell model, which implies that both viscoelastic strain and stress tensors are deviatoric. Also, with the time varying relaxation modulus, the normal penalty factor p_n used for defining the interaction between the master and slave boundary either becomes too stiff and prevents the boundaries from approaching each other or becomes too weak and allows the slave boundary to penetrate the master boundary, each of which is unacceptable. To remedy this problem, an adaptive form of penalty factor is chosen which adjusts its value proportional to the time varying sealed pressure and prevents p_n from becoming too stiff or two weak.

6.3.3 Micro-Scale Fluid Mechanics

In the viscoelastic MSMP model, the micro-scale fluid mechanics in the sealing zone is solved using the same set of equations as described in section 3.4. Equations (3.22) through (3.25) are solved for Φ and F at each time step with the finite volume method and TDMA algorithm. The finite volume mesh consists of 236 nodes selected following a mesh sensitivity study. This yields the fluid pressure distribution and location of cavitation zones at each time step. The flow rate and amount of fluid transport as well as the fluid viscous shear stresses are then computed using equations (3.55) through (3.62).

6.3.4 Micro-Scale Viscoelastic Contact Mechanics

For a perfectly elastic material, the Greenwood-Williamson model gives the contact pressure as

$$P_c = \frac{4}{3}\frac{1}{\left(1-\upsilon^2\right)}\hat{\sigma}^{3/2}\frac{1}{\sqrt{2\pi}}\int_H^\infty \left(z-H\right)^{3/2} e^{-z^2/2} dz \tag{6.22}$$

However, in a viscoelastic material, the previous history of asperity contact must be taken into account in calculating the contact pressure at current time instant. This needs to be done through something like a time convolution operation. From Hertzian theory, for contact of an elastic body with a much stiffer surface, the load due to a single asperity is given by

$$F_{k\ Elastic} = \frac{4}{3}\frac{1}{(1-\upsilon^2)}R^{1/2}E\delta^{3/2} \tag{6.23}$$

where δ represents the normal deformation of the asperity. If the two surfaces come together until their reference planes are separated by a distance , d then there will be contact at any asperity whose height was originally greater than d . Hence, $\delta = z - d$, where z is the height of the given asperity. For the transient case, $d = d(t)$ and hence, $\delta = \delta(t)$. Also, for the viscoelastic material, $E = E(t)$. Using the similar argument for describing viscoelastic indentation as by Sakai [96] and Hui *et. al.* [97] the viscoelastic version of Eq.(6.23) can be written as :

$$F_{k\,Viscoelastic}(t) = \frac{4}{3}\frac{1}{(1-\upsilon^2)} R^{1/2}\left(E(t) * \delta(t)^{3/2}\right) \tag{6.24}$$

where '$*$' is the time convolution operator. Now, the probability of having contact at any given asperity, of height z is :

$$\text{Prob}(z > d(t)) = \int_{d(t)}^{\infty} \psi(z)dz \tag{6.25}$$

If there are total N asperities, then total expected load is:

$$F_{k\,Viscoelastic}(t) = N \int_{d(t)}^{\infty} F_{k\,Viscoelastic} \cdot \psi(z)dz \tag{6.26}$$

Substituting Eq. (6.24) into Eq. (6.26) and writing $N = \eta A$, where $\eta = \text{asperity density}$ and $A = \text{nominal contact area}$, we get:

$$F_{k\,Viscoelastic}(t) = \eta A\frac{4}{3}\frac{1}{(1-\upsilon^2)} R^{1/2} \int_{d(t)}^{\infty} \left(E(t) * \delta(t)^{3/2}\right) \cdot \psi(z)dz \tag{6.27}$$

Hence total viscoelastic contact pressure at time t is :

$$P_c(t)_{\,Viscoelastic} = \eta\frac{4}{3}\frac{1}{(1-\upsilon^2)} R^{1/2} \int_{d(t)}^{\infty} \left(E(t) * \delta(t)^{3/2}\right) \cdot \psi(z)dz \tag{6.28}$$

Expanding the convolution operation into an integral form, we get:

$$P_c(t)_{Viscoelastic} = \eta \frac{4}{3} \frac{1}{(1-\upsilon^2)} R^{1/2} \int_{d(t)}^{\infty} \left\{ \int_0^t E(t-\tau) \frac{d}{d\tau} \left[\delta(\tau, z)^{3/2} \right] d\tau \right\} \cdot \psi(z) dz \quad (6.29)$$

Substituting $\delta(\tau, z) = z - d(\tau)$ into above equation, we get

$$P_c(t)_{Viscoelastic} = \eta \frac{4}{3} \frac{1}{(1-\upsilon^2)} R^{1/2} \int_{d(t)}^{\infty} \left\{ \int_0^t E(t-\tau) \frac{d}{d\tau} \left[(z - d(\tau))^{3/2} \right] d\tau \right\} \cdot \psi(z) dz \quad (6.30)$$

Now we can normalize the separation between reference planes with respect to the standard deviation of the asperity heights as $H(\tau) = d(\tau)/\sigma$ and also standardize $\psi(z)$ into standardized height distribution $\tilde{\psi}(\mathrm{s})$, such that $\tilde{\psi}(\mathrm{s})$ has standard deviation of unity ($\tilde{\sigma} = 1$). Then Eq. (6.30) becomes,

$$P_c(t)_{Viscoelastic} = \eta \frac{4}{3} \frac{1}{(1-\upsilon^2)} R^{1/2} \sigma^{3/2} \int_{H(t)}^{\infty} \left\{ \int_0^t E(t-\tau) \frac{d}{d\tau} \left[\left(s - H(\tau) \right)^{3/2} \right] d\tau \right\} \cdot \tilde{\psi}(s) ds \quad (6.31)$$

Assuming Gaussian distribution of asperity heights with zero mean,

$\tilde{\psi}(s) = \frac{1}{\tilde{\sigma}\sqrt{2\pi}} e^{-\frac{s^2}{2\tilde{\sigma}^2}} = \frac{1}{\sqrt{2\pi}} e^{-\frac{s^2}{2}}$ $\left(\text{since } \tilde{\sigma} = 1 \text{ as shown earlier}\right)$, Eq. (6.31) becomes,

$$P_c(t)_{Viscoelastic} = \eta \frac{4}{3} \frac{1}{(1-\upsilon^2)} R^{1/2} \sigma^{3/2} \frac{1}{\sqrt{2\pi}} \int_{H(t)}^{\infty} \left\{ \int_0^t E(t-\tau) \frac{d}{d\tau} \left[\left(s - H(\tau) \right)^{3/2} \right] d\tau \right\} \cdot e^{-\frac{s^2}{2}} ds \quad (6.32)$$

Let's consider

$$f(s) = \int_0^t \left| E(t-\tau) \frac{d}{d\tau} \left[(s - H(\tau))^{3/2} \right] \cdot e^{-\frac{s^2}{2}} \right| d\tau$$
$$\text{and } \int_{d(t)}^{\infty} f(s) ds < \infty \quad (6.33)$$

Using Tonelli's theorem we get,

$$\int \left| E(t-\tau)\frac{d}{d\tau}\left[(s-H(\tau))^{3/2}\right]\cdot e^{-\frac{s^2}{2}} \right| d(s,\tau) < \infty$$

As a result of bounded-ness of the above integral, we can use Fubini's theorem, to interchange the order of integration in Eq. (6.32).

$$P_c(t)_{Viscoelastic} =$$

$$\eta\frac{4}{3}\frac{1}{(1-\upsilon^2)}R^{1/2}\sigma^{3/2}\frac{1}{\sqrt{2\pi}}\int_0^t E(t-\tau)\frac{d}{d\tau}\left[\int_{H(\tau)}^{\infty}\left(s-H(\tau)\right)^{3/2}\cdot e^{-\frac{s^2}{2}}ds\right]d\tau \tag{6.34}$$

Let, $I(t)=\eta\frac{4}{3}\frac{1}{(1-\upsilon^2)}R^{1/2}\sigma^{3/2}\frac{1}{\sqrt{2\pi}}\int_{H(t)}^{\infty}\left(s-H(t)\right)^{3/2}\cdot e^{-\frac{s^2}{2}}ds$

Since there is jump in I(t) at t = 0, to capture this discontinuity , we can write $I(t)=I(t)\tilde{\mathrm{H}}(t)$. Hence,

$$P_c(t)_{Viscoelastic} = \int_{0^-}^{t} E(t-\tau)\frac{d}{d\tau}\left[I(\tau)\tilde{\mathrm{H}}(\tau)\right]d\tau \tag{6.35}$$

Now,

$$\frac{d}{d\tau}\left[I(\tau)\tilde{\mathrm{H}}(\tau)\right]=\tilde{\mathrm{H}}(\tau)\frac{d}{d\tau}\left[I(\tau)\right]+I(\tau)\frac{d}{d\tau}\left[\tilde{\mathrm{H}}(\tau)\right]=\tilde{\mathrm{H}}(\tau)\frac{d}{d\tau}\left[I(\tau)\right]+I(\tau)\delta(\tau)$$

Hence, Eq. (6.35) becomes,

$$P_c(t)_{Viscoelastic} = \int_{0^+}^{t} E(t-\tau)\left\{\tilde{\mathrm{H}}(\tau)\frac{d}{d\tau}\left[I(\tau)\right]+I(\tau)\delta(\tau)\right\}d\tau \tag{6.36}$$

Applying sifting property of $\delta(\tau)$, i.e. $\int_0^t f(t)\,\delta(t-t_1)\,dt = f(t_1)$, we get :

$$\int_{0^+}^{t} E(t-\tau)I(\tau)\delta(\tau)d\tau = E(t)I(0^+)\tilde{\mathrm{H}}(t)$$

Substituting in Eq.(13) we get :

$$P_c(t)_{Viscoelastic} = I(0^+)E(t)\tilde{\mathrm{H}}(t) + \int_{0^+}^{t} E(t-\tau)\frac{d}{d\tau}\left[I(\tau)\right]d\tau \tag{6.37}$$

where, $I(t) = \eta\frac{4}{3}\frac{1}{(1-\upsilon^2)}R^{1/2}\sigma^{3/2}\frac{1}{\sqrt{2\pi}}\int_{H(t)}^{\infty}\left(s-H(t)\right)^{3/2}\cdot e^{-\frac{s^2}{2}}ds$.

In discrete form Eq. (6.37) can be written as:

$$P_c(t)_{Viscoelastic} = I(0^+)E(t)\tilde{\mathrm{H}}(t) + \sum_n E(t-t_n)\lim_{\Delta\tau\to 0}\frac{I(t_n)-I(t_{n-1})}{\Delta\tau}\cdot\tilde{\mathrm{H}}(t-t_n)\cdot\Delta\tau$$

or

$$P_c(t)_{Viscoelastic} = I(0^+)E(t)\tilde{\mathrm{H}}(t) + \sum_n E(t-t_n)\left[I(t_n)-I(t_{n-1})\right]\cdot\tilde{\mathrm{H}}(t-t_n) \tag{6.38}$$

Eq. (6.37) and (6.38) gives us the expression for contact pressure at time ‘t’ which takes into account the entire history of contact between rough viscoelastic seal surface and the rigid rod surface.

6.3.5 Dry Film Thickness during Viscoelastic Contact

It was discussed in previous chapters that for calculating the film thickness distribution using MSMP deformation mechanics module, the “dry” film thickness distribution was needed. For perfectly elastic seal, it was computed by equating the dry contact pressure obtained from the macro-scale deformation and macro-scale contact analysis of the smooth seal surface under pressurized conditions, P_{dc}, with the micro-scale contact pressure distribution under dry conditions. However for viscoelastic seal material, the procedure is not as straightforward as now we will have to invert time convolution equation (6.37) in extracting the dry film thickness from it. This section describes this extraction process.

Consider Eq. (6.37) for viscoelastic contact pressure at time t and let: $\tilde{E}(t) = E(t)/E_\infty$ (E_∞ is the long term relaxation modulus),

$$C_1 = \frac{4}{3}\eta \frac{1}{(1-\upsilon^2)} R^{1/2}\sigma^{3/2} \frac{1}{\sqrt{2\pi}} E_\infty$$

and

$$G\left(H(\tau)\right) = \frac{d}{d\tau}\left[\int_{H(\tau)}^{\infty} \left(s - H(\tau)\right)^{3/2} \cdot e^{-\frac{s^2}{2}} ds\right]$$

Then,

$$P_c(t)_{Viscoelastic} = I(0^+)E(t)\tilde{H}(t) + C_1 \int_{0^+}^{t} \tilde{E}(t-\tau)\cdot G\left(H(\tau)\right) d\tau \qquad (6.39)$$

The first term on right hand side is retained as it is, since it can be evaluated directly without the knowledge of the film thickness history. This is because, $I(0^+)$ depends only on the value of film thickness at the jump condition which occurs at the start of the transient process. Equating $P_c(t)_{Viscoelastic}$ from Eq. (6.39) to viscoelastic dry contact pressure $P_{dc}(t)_{Viscoelastic}$ evaluated from macro-deformation finite element calculations, we get:

$$P_{dc}(t)_{Viscoelastic} = I(0^+)E(t)\tilde{H}(t) + C_1 \int_{0^+}^{t} \tilde{E}(t-\tau)\cdot G\left(H_{dry}(\tau)\right) d\tau \qquad (6.40)$$

Our aim is to solve Eq. (6.40) for $H_{dry}(t)$.

Since we can directly calculate first term on right hand side, we can bring it on left and write:

$$\tilde{P}_{dc}(t) = P_{dc}(t)_{Viscoelastic} - I(0^+)E(t)\tilde{H}(t) = C_1 \int_{0^+}^{t} \tilde{E}(t-\tau)\cdot G\left(H_{dry}(\tau)\right) d\tau \qquad (6.41)$$

Now, since $\tilde{P}_{dc} \in L^1\left(R^n\right)$, we can write its Fourier Transform as:

$$\begin{aligned}\hat{P}(\upsilon) &= \int_{R^n} \tilde{P}_{dc}(t) e^{-2\pi i t\cdot\upsilon} dt \\ &= C_1 \int_{R^n}\int_{R^n} G(\tau)\tilde{E}(t-\tau)\, d\tau\, e^{-2\pi i t\cdot\upsilon} dt\end{aligned} \tag{6.42}$$

Also, $\left|G(\tau)\tilde{E}(t-\tau)e^{-2\pi i t\cdot\upsilon}\right| = \left|G(\tau)\tilde{E}(t-\tau)\right|$, and $\int\left|G(\tau)\tilde{E}(t-\tau)\right| d(\tau,t) < \infty$,

hence the integral taken with respect to the product measure over the combined space is bounded. Therefore we can interchange the order of integration in Eq. (6.42), i.e.

$$\hat{P}(\upsilon) = C_1 \int_{R^n} G(\tau)\left[\int_{R^n} \tilde{E}(t-\tau) e^{-2\pi i t\cdot\upsilon} dt\right] d\tau \tag{6.43}$$

Let, $y = t - \tau \Rightarrow dy = dt$, then

$$\begin{aligned}\frac{\hat{P}(\upsilon)}{C_1} &= \int_{R^n} G(\tau)\left[\int_{R^n} \tilde{E}(y) e^{-2\pi i (y+\tau)\cdot\upsilon} dy\right] d\tau \\ &= \int_{R^n} G(\tau) e^{-2\pi i \tau\cdot\upsilon}\left[\int_{R^n} \tilde{E}(y) e^{-2\pi i y\cdot\upsilon} dy\right] d\tau \\ &= \left[\int_{R^n} G(\tau) e^{-2\pi i \tau\cdot\upsilon} d\tau\right]\cdot\left[\int_{R^n} \tilde{E}(y) e^{-2\pi i y\cdot\upsilon} dy\right]\end{aligned}$$

Hence we get,

$$\frac{\hat{P}(\upsilon)}{C_1} = \hat{G}(\upsilon)\cdot\hat{E}(\upsilon) \tag{6.44}$$

where, $\hat{G}(\upsilon)$ is the Fourier transform of $G(t)$ and $\hat{E}(\upsilon)$ is the Fourier transform of $\tilde{E}(t)$. This further gives,

$$\hat{G}(\upsilon) = \frac{1}{C_1}\frac{\hat{P}(\upsilon)}{\hat{E}(\upsilon)}$$

Taking inverse Fourier transform,

$$G(t) = \frac{1}{C_1} \int_{R^n} \frac{\hat{P}(\upsilon)}{\hat{E}(\upsilon)} e^{2\pi i t \cdot \upsilon} d\upsilon \tag{6.45}$$

Now since,

$$G(t) = \frac{d}{dt}\left[\int_{H(t)}^{\infty} \left(s - H_{dry}(t)\right)^{3/2} \cdot e^{-\frac{s^2}{2}} ds \right],$$

we can write, $\int_{H(t)}^{\infty} \left(s - H_{dry}(t)\right)^{3/2} \cdot e^{-\frac{s^2}{2}} ds = \int_0^t G(t)\, dt$

Let $M(t) = \int_0^t G(t)\, dt$, and hence now we can solve,

$$\int_{H(t)}^{\infty} \left(s - H_{dry}(t)\right)^{3/2} \cdot e^{-\frac{s^2}{2}} ds = M(t) \tag{6.46}$$

for $H_{dry}(t)$ using regression as follows:

$$H_{dry}(t) = a + b\left[\log\left(m(t)\right)\right] + c\left[\log\left(m(t)\right)\right]^2 + d\left[\log\left(m(t)\right)\right]^3 + e\left[\log\left(m(t)\right)\right]^4 + f\left[\log\left(m(t)\right)\right]^5 \tag{6.47}$$

where, $m(t) = -\log_{10}\left|M(t)\right|$ and a = 0.86197, b = 1.16979, c = 0.34673,

d = 3.57134 x 10^{-2}, e = 1.07985 x 10^{-3}, f = 1.68629 x 10^{-3}.

6.3.6 Micro-Scale Viscoelastic Deformation Mechanics

Having obtained the micro-scale contact pressure distribution from Eq.(6.37) and fluid pressure distribution as described in section 6.3.3, a net pressure load of $\left(P_{fluid} + P_c - P_{dc}\right)$ is applied over the sealing edge obtained from the macro-scale viscoelastic deformation & contact analyses. The corresponding radial deformations $H_{def}(t)$ of the sealing edge are then obtained using the viscoelastic finite element

analysis similar to that described in section 6.3.1. From the second time step onwards, the macro-scale as well as the micro-scale deformation mechanics are incorporated to get the macro-scale seal configuration at the next time step and in turn the updated sealing edge configuration and contact zone length. This assures that whole time history of deformations, strains and stresses needed for viscoelastic calculations is preserved both at the macro-scale and micro-scale. The dry film thickness, $H_{dry}(t)$, is computed as explained in previous section. The total film thickness is then computed as,

$$H(t) = H_{dry}(t) + H_{def}(t) \tag{6.48}$$

Another improvement that has been made in the viscoelastic MSMP model is that of incorporating shear deformations. Shear stresses from contacting asperities and from fluid viscous forces deform the sealing edge and such shear deformations of the sealing edge can, in principle, affect the overall sealing dynamics. For the viscoelastic model, again the entire time history of such shear deformations needs to be taken into account and hence the MSMP algorithm is modified to calculate the total shear stress on the sealing edge (total of those given by Eq. (3.57) and Eq. (3.61)) within the main time loop and not as a post-processing step. Once computed, these shear stresses are then applied as boundary condition on the sealing edge in solving the macro and micro-scale deformation mechanics for the next time step.

6.4 Visco-Elasto-Hydrodynamic MSMP Model: Computational Procedure

The overall computational procedure used in this Visco-Elasto-Hydrodynamic MSMP framework is shown in Figure 6.14. Again, due to the strong coupling between governing equations, an iterative procedure is used. Various steps of the algorithm are as follows:

Step a) Eq. (6.18) through Eq. (6.21) coupled with Eq. (3.12-3.13) that govern the macro-scale deformation and dry contact mechanics are solved using the finite element procedure explained earlier, to yield the deformed geometrical configuration, sealing zone and the dry contact pressure distribution for the entire operation cycle. The sealing zone length and configuration obtained for the first time step are passed to other modules. P_{dc} distributions are stored for the entire time history and are retrieved as required by other modules.

Step b) The sealing zone configuration is passed to the micro-scale fluid mechanics module and equations (3.22-3.24) along with boundary condition Eq. (3.25) are then solved for Φ and F. This yields the fluid pressure distribution and locations of cavitation zones.

Step c) The micro-scale viscoelastic contact pressure is then evaluated using Eq. (6.37). The integral in the equation for I(t) is evaluated numerically using the Adaptive Gauss-Kronrod quadrature.

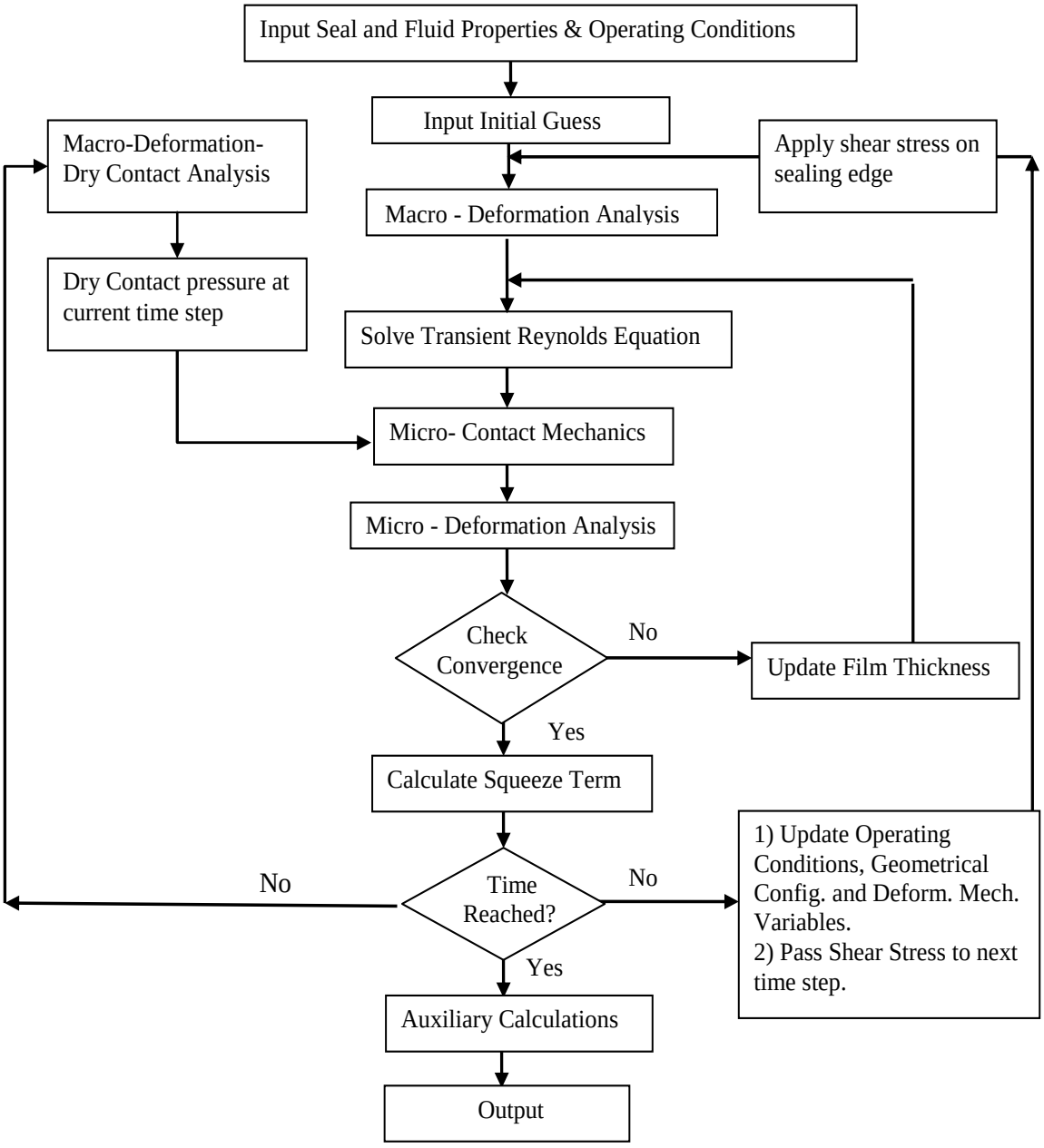

Figure 6.14: Visco-elasto-hydrodynamic model: computational algorithm.

Step d) The fluid pressure, micro-scale contact pressure, macro-scale dry contact pressure as well as the deformed seal configuration (from Step a) are fed into the micro-scale finite element deformation analysis of the sealing edge. The computed micro-scale deformations and the dry film thickness obtained using Eq.(6.47) are substituted in Eq. (6.48) to update the film thickness and flow factors for the next iteration.

Step e) Steps (b) through (d) are run in an iterative loop until the converged solutions for fluid pressure and film thickness are obtained at the given time step.

Step f) The converged solution for H, F, Φ and P_c at the current time step are used to calculate the total shear stress acting on the seal, which induces the shear deformation at the sealing edge. The total shear stress is the sum of the fluid viscous shear stress (Eq. (3.57)) and the asperity contact shear stress (Eq. (3.61)). This is applied over the sealing edge as an additional boundary condition in the deformation mechanics calculations for the next time step.

Step g) The converged solutions at the current time step are used to calculate the transient squeeze term (in Eq. (3.22)) for the next time step. Computing this squeeze term, for step b, is not straightforward since the sealing zone length is changing as a function of time. Quantities like $H, F \text{ and } \Phi$ are evaluated over the sealing domain at a particular time step. To differentiate these quantities with respect to time, their nodal values need to be time differenced. But since the spatial domain over which these quantities are defined, itself, is changing, one must map the nodal values from one spatial domain to the next. As discussed for the elastic model, there are two scenarios that arise. If the contact length at the new time step is less than that at the old time step, then the old time step domain is truncated. If the contact length at the new time step is larger than that

at the old time step then the old time step domain is extended to match the new time step domain, and the additional variable values are appended to the old time step solution.

Step h) The geometrical configuration of the seal (from the micro-deformation analysis) as well as values of all the stored solution variables like deformations, stresses, strains etc. at the end of the current time step are then passed onto the macro-deformation analyses of the next time step. This ensures that the entire strain history is preserved for the viscoelastic calculations. The converged solutions for H, F, Φ, P_c etc. are also passed for the calculations at the next time step.

Steps (b) through (h) are repeated over the time interval of interest and a transient solution for the entire period of operation is obtained. After arriving at the solution for the entire cycle, auxiliary calculations are performed for quantities such as the fluid flow rate, total fluid transport, and friction force (equations (3.55) through (3.62)).

6.5 Results from the Visco-Elasto-Hydrodynamic MSMP Model

Computations have been performed for a typical seal that is used in an injection molding application. This seal prevents leakage from the actuator that moves the half-mold in and out of the injection molding machine. The motion is controlled by primarily varying the hydraulic pressure on the cap side of the piston. Base parameters used in these calculations are same as those given in Table 3.3 except the material properties and some surface parameters that are listed in Table 6.1. Dynamic mechanical analysis was performed on a polyurethane seal sample and a multi-variate constrained optimization algorithm was implemented (discussed in chapter 7) to extract the values of the

parameters E_∞, E_i and τ_i that are given in this table. It was determined that $N_p = 5$ gives a reasonable estimate of the relaxation time scales covered by the seal material.

Table 6.1: Parameters used in the visco-elasto-hydrodynamic MSMP seal model.

Seal material	Polyurethane
E_∞	43 MPa
E_i for i = 1: 5	[90 ;15; 11; 7 ; 0.9] MPa
τ_i for i = 1: 5	[0.3; 3; 60; 300; 1000] s
Asperity radius	4 μm
Asperity density	$5 \times 10^{11} m^{-2}$

The specified rod velocity and sealed pressure histories as functions of time are shown in Figure 6.15 and Figure 6.16 respectively and are exactly same as those for the linear elastic model of chapter 5. The outstroke occurs from *t* = 0 to t = 10.50 s., and the instroke from *t* = 10.51 s. to *t* = 21.0 s. Also shown on these figures are key states labeled 1 to 9. The results obtained with the viscoelastic (VE) model are compared with those obtained with the previous linear perfectly elastic model (LE).

6.5.1 Dynamic Deformations of the Seal

Due to the transient sealed pressure, a new geometrical configuration is calculated at each time step under the "dry" condition (i.e. no fluid pressure in the sealing zone). Figure 6.17 shows the deformed geometries of the seal, von Mises stress distributions and displacement streamlines under the "dry" condition at various instants of time (different values of sealed pressure). The original undeformed configuration is also shown. Comparing the deformation at 2.09 s with that at 5.19 s (same value of sealed pressure)

the effect of viscoelasticity is seen. The curvatures of the particle displacement streamlines show the effect of the relaxation process.

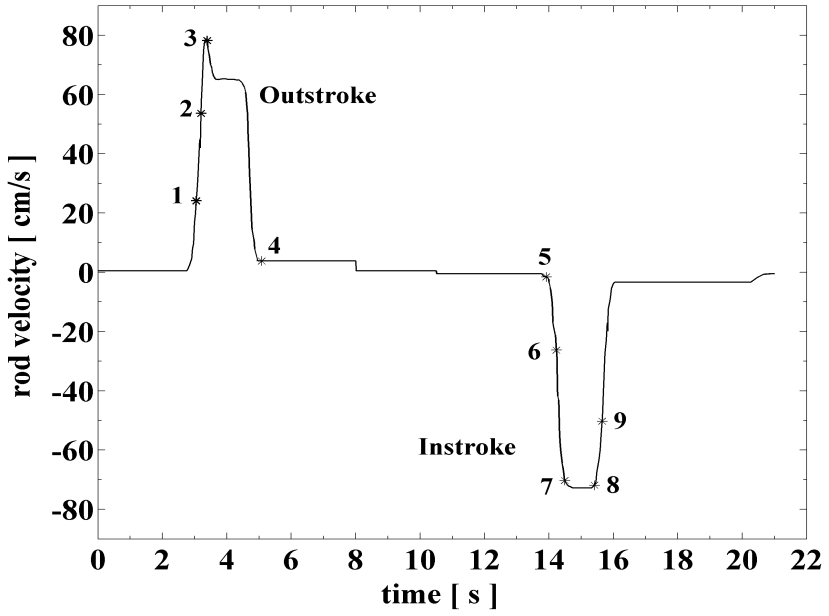

Figure 6.15: Rod velocity vs time.

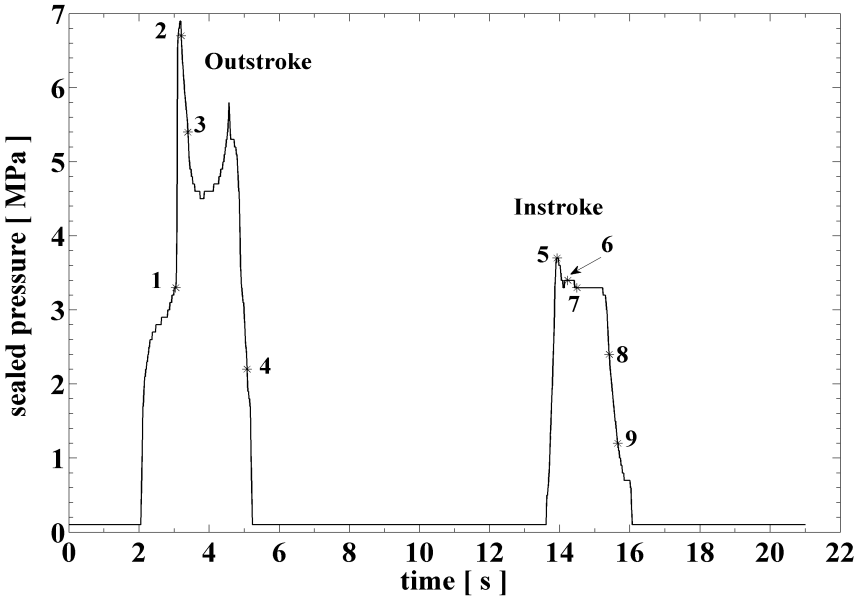

Figure 6.16: Sealed pressure vs time.

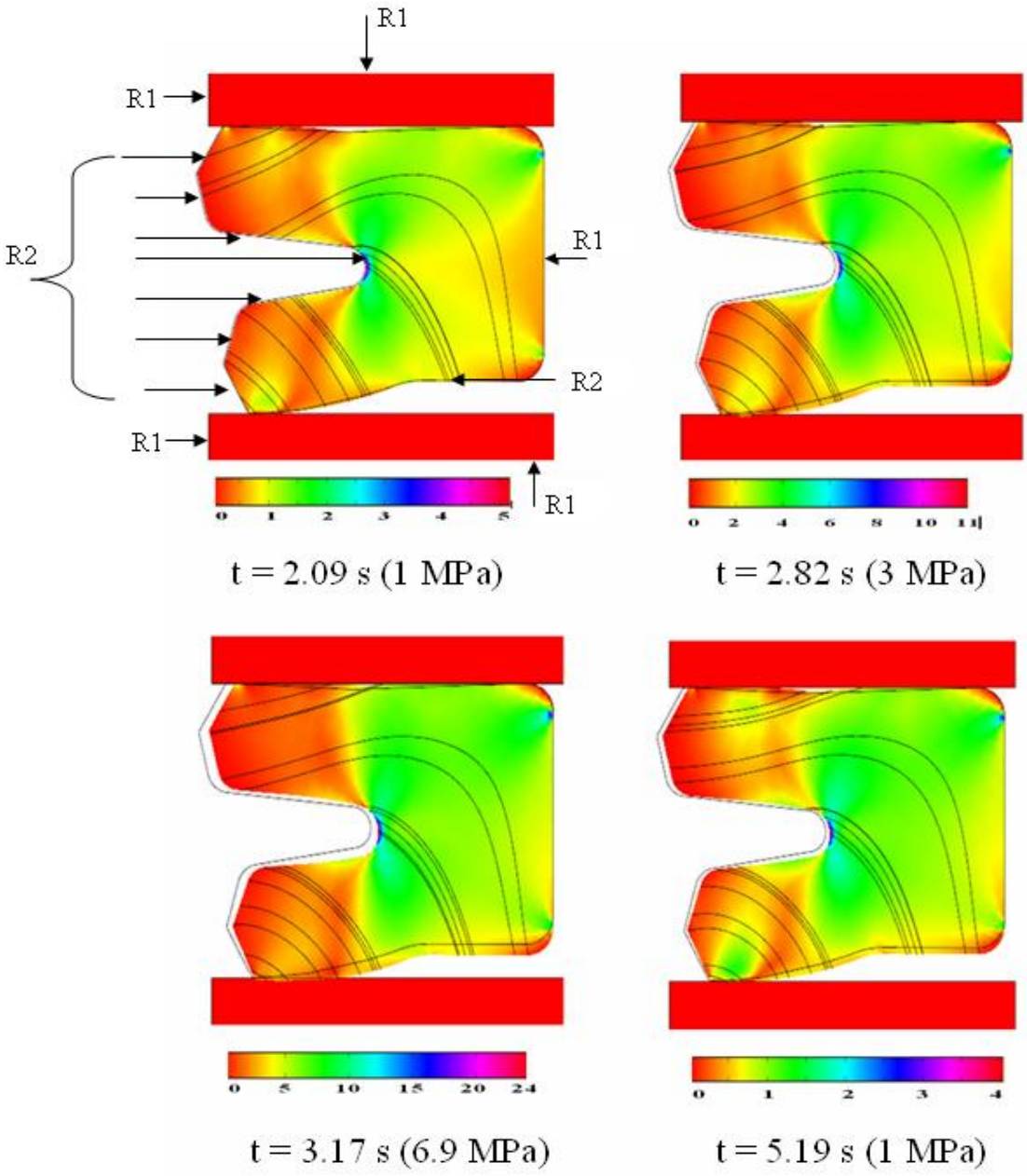

Figure 6.17: Deformed seal configurations at various time instances. R1 and R2 are the boundary conditions as described by Eq. (3.5). The von Mises stress distribution in the seal is shown using the color map (units of the color-scale are [MPa]). Also shown are displacement streamlines.

6.5.2 Fluid Pressure Distribution and History

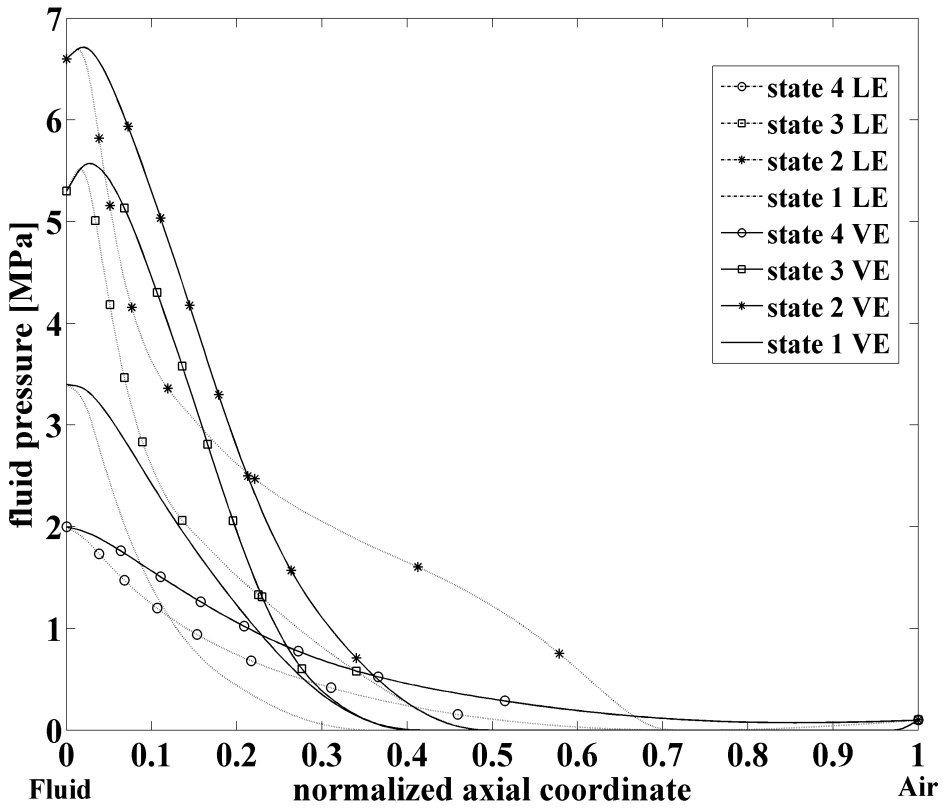

Figure 6.18: Fluid pressure distribution, outstroke.

Figure 6.18 shows the fluid pressure distributions during the outstroke, calculated using the VE model and the LE model. As was demonstrated in section 5.6.3 the transient fluid pressure distribution is governed by a complex dependence on the hydrodynamic effects produced by the changing rod velocity, the boundary condition effects produced by the changing sealed pressure, and the effects on the film thickness produced by the changing sealed pressure acting on the cup side of the seal lip. Through the viscoelastic model one observes a comparable level of complex dependence, along with some new effects that arise from the viscoelastic behavior of the seal. During the outstroke, the flow through the film is diverging (see the following section, Film

Thickness Distribution) so the fluid pressure decreases with increasing rod velocity for a given sealed pressure. An increase in sealed pressure increases the boundary value of the fluid pressure and hence leads to an increase in fluid pressure. In addition, an increased sealed pressure produces a higher pressure on the seal lip from the cup side and reduces the film thickness, which in turn affects the fluid pressure in the film. By comparing the curves for states 1 and 2, it can be seen that the sealed pressure increase of 3.4 MPa going from state 1 to state 2 dominates over the hydrodynamic effect caused by the approximately 30 cm/s increase in rod velocity. As a result, the fluid pressure at state 2 is generally larger than that at state 1 for the entire sealing zone except for the region with cavitation. Going from state 2 to state 3, both the increasing velocity and the decreasing sealed pressure simultaneously reduce the fluid pressure and increase the length of the cavitation region. State 4 demonstrates the fact that despite a low sealed pressure, a low value of the rod velocity keeps the cavitation from occurring.

The effect of viscoelasticity becomes evident by comparing the VE fluid pressure curves with the LE curves at the same instants of time. The VE distributions are significantly different from the corresponding LE ones. In general, the VE pressures are higher than the LE pressures in the region closest to the sealed end, while in the region farthest from the sealed end, the VE fluid pressures can be lower than the corresponding LE pressures. The viscoelasticity can also produce an increased length of the cavitation region (pressure is zero and Φ is negative) as seen by comparing the two curves for state 2 and state 3. With the VE model the cavitation region occupies 52% of the sealing zone, while with the LE model it occupies 29%. The increase in the cavitation region further limits the fluid flow out of the cylinder and hence is helpful in preventing leakage.

From the instroke fluid pressure distributions of Figure 6.19, it can be seen that the sealed pressure variation has the same effect as during the outstroke, while the rod velocity variation has the opposite effect since the flow is converging during the instroke (see the following section on film thickness distribution).

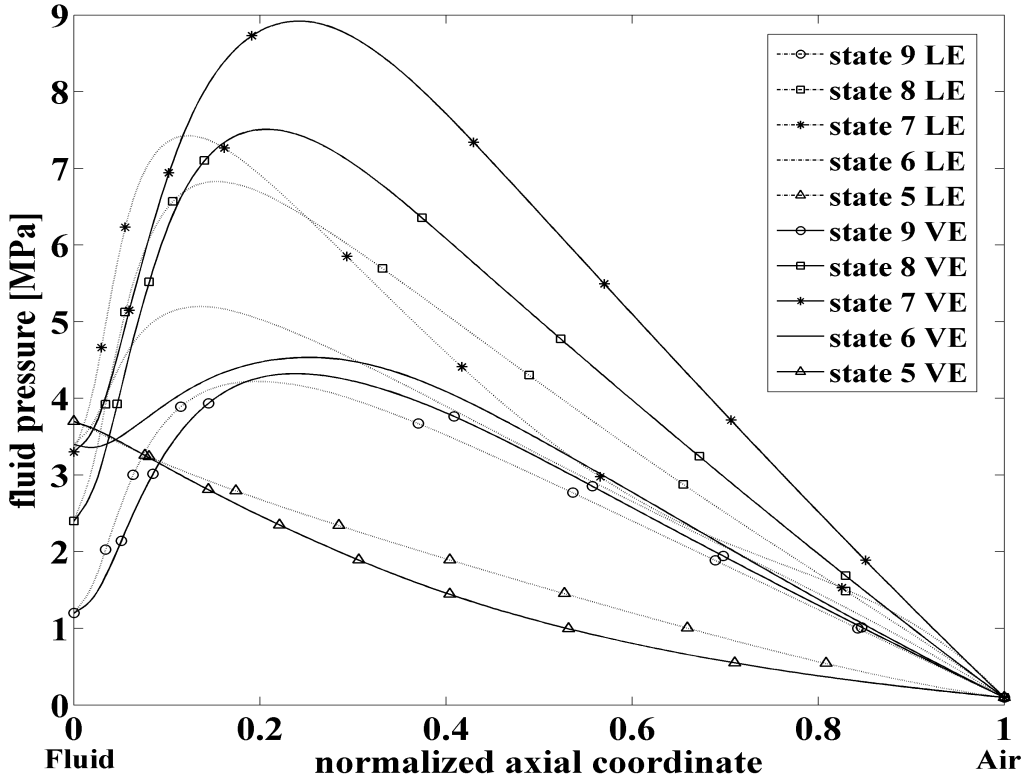

Figure 6.19: Fluid pressure distribution, instroke.

The increasing velocity from state 5 to state 6 increases the fluid pressure and dominates over the reduction caused by the small reduction in the sealed pressure. Comparing state 7 with state 6 demonstrates the large hydrodynamic pressure increase produced by the sharp rise in the rod velocity while the sealed pressure remains almost constant. Comparing state 8 with state 7 demonstrates the sole effect of reduced sealed pressure, which is much more pronounced at high velocities than at lower ones.

By comparing the VE and LE curves, it can be seen that during the instroke, the fluid pressures obtained by the VE model are generally higher in most of the sealing zone (state 5 is an exception) compared to those obtained with the LE model. Also in the VE model the peak in the fluid pressure is shifted away from the sealed pressure end, indicating the effect of viscoelasticity on the complex interplay between hydrodynamic effects and the boundary condition and film thickness effects due to sealed pressure variations.

It is important to note how the viscoelastic effect plays a role in determining the fluid pressure distribution. As mentioned earlier, the transient fluid pressure distribution is governed by a complex dependence on the hydrodynamic effects produced by the changing rod velocity, the boundary condition effects produced by the changing sealed pressure, and the effects on the film thickness produced by the changing sealed pressure acting on the cup side of the seal lip. For an elastic seal, changes in rod velocity and sealed pressure are immediately reflected in the fluid pressure distribution throughout the sealing zone. For a viscoelastic seal, the situation is quite different. The larger are the time constants of viscoelasticity, the slower the seal is in structurally reacting to pressure variations. Thus, there will be delays in the changes in the macro-deformation of the seal due to the changes in sealed pressure acting on the cup side of the seal lip, and the changes in the micro-deformation of the seal due to the changes in rod velocity and sealed pressure (acting as a boundary condition). These macro and micro deformation changes will affect the film thickness distribution, and hence the fluid pressure distribution, and therefore will result in a delayed response of the fluid pressure distribution. Furthermore, the deformation changes will be affected by the entire prior

history of the seal. It should be noted, however, that while changes in the fluid pressure distribution resulting from deformation changes will be delayed due to viscoelasticity, the direct effect of the sealed pressure acting as a boundary condition on the fluid pressure distribution will be instantaneous. Thus, the changes in the fluid pressure distribution will be governed by a combination of instantaneous effects and delayed viscoelastic effects. It is therefore clear that, with such a complex situation, it is difficult to attribute the net viscoelastic effects on the fluid pressure distributions to any single specific physical phenomenon.

It can be seen from Figure 6.18 and Figure 6.19, for both the LE and VE cases, that during the outstroke the fluid pressures are generally lower than those during the instroke. Furthermore, as mentioned earlier, during the outstroke there are significant cavitation regions. They do not occur during the instroke. Such cavitation during the outstroke and lack of cavitation during the instroke, inhibits leakage. These results are consistent with previous steady-state studies [43-46] and the transient studies with the linear elastic material performed in chapter 5. As pointed out above, the viscoelasticity tends to increase the length of the cavitation region during the outstroke, further inhibiting leakage compared to the LE case.

In Figure 6.20, the fluid pressure histories during the 2-6 s. of outstroke operation at locations x = 0.2L, 0.4L, 0.6L and 0.8L are plotted. The fluid pressure histories close to the sealed end at x = 0.2L, predicted by the two models, are quite different. While both resemble the sealed pressure history between times 3 and 5 s., the magnitudes of the slopes of the VE history following the first peak and prior to the second peak, times 3.19 s and 3.60 s, are much smaller than those of the LE history. This is the result of the

delayed viscoelastic response, and leads to significantly higher fluid pressures during this time period with the VE seal than with the LE seal. Such higher fluid pressures are consistent with the fluid pressure distributions, discussed earlier. The histories at $x =$ 0.4L and 0.6L show that the VE seal experiences a larger cavitation region than the LE seal, again consistent with the previously discussed fluid pressure distributions.

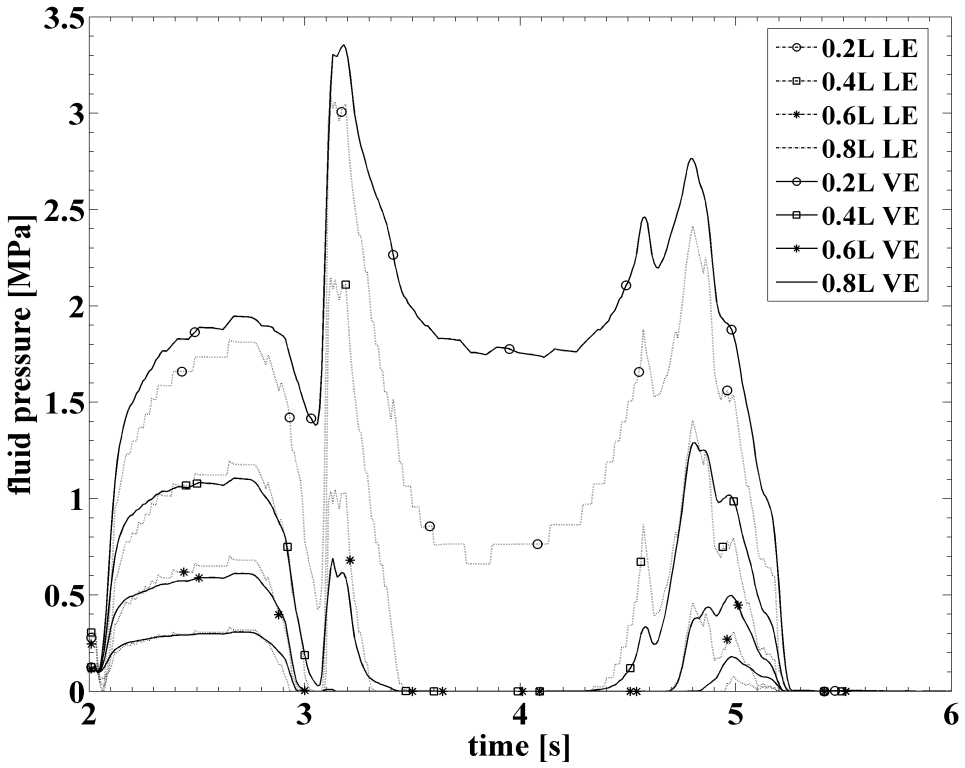

Figure 6.20: Fluid pressure history, outstroke.

Figure 6.21 shows a similar comparison of the fluid pressure histories during the 13-17 s period of instroke. The VE model gives higher fluid pressures than the LE model over almost the entire sealing zone during the period 14-16 s, consistent with the fluid pressure distributions.

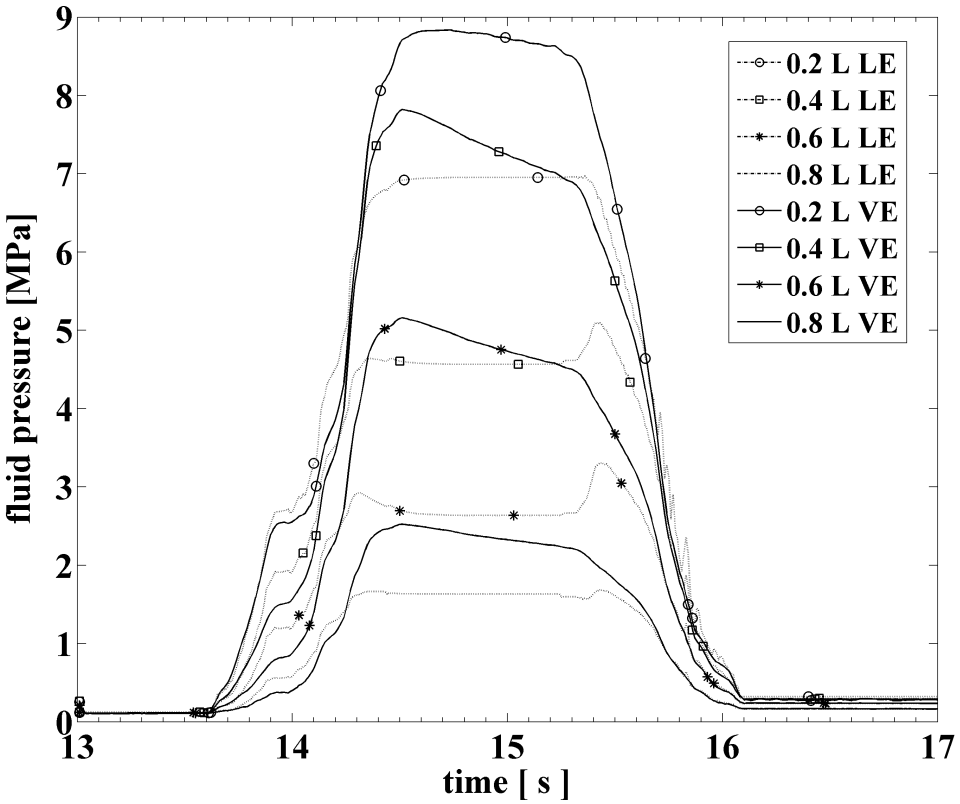

Figure 6.21: Fluid pressure history, instroke.

A 3D surface plot of fluid pressure distribution during outstroke as a function of time is shown in Figure 6.22. Part (a) shows the one obtained with VE model and part (b) shows that obtained with LE model. The discussion regarding Figure 6.18 and Figure 6.20 becomes clearer by looking at this simultaneous space-time distribution of fluid pressure. It can be seen that the "bulge" in fluid pressure in the lower-right side obtained with LE model is absent in the VE mode. This in turn produces a larger cavitation region for the viscoelastic seal (compare red vs green ellipse), as was seen in Figure 6.20.

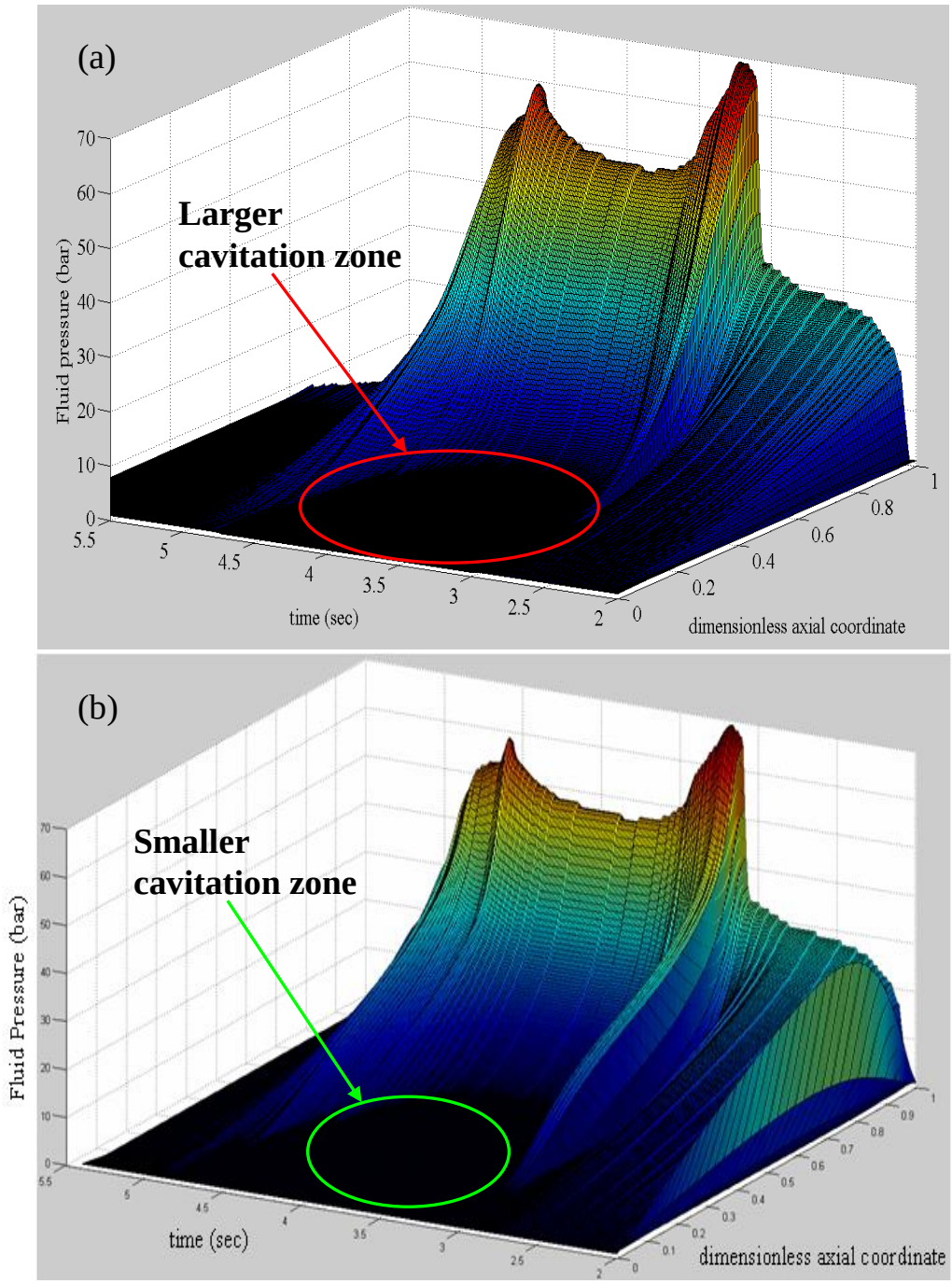

Figure 6.22: Fluid pressure distribution during outstroke as a function of time obtained with VE model (a) and LE model (b).

6.5.3 Film Thickness Distribution and History

The characteristics of the fluid pressure distributions are reflected in the film thickness distributions, Figure 6.23 and Figure 6.24, which indicate that mixed lubrication occurs, since the film thickness is generally less than 3σ. These figures show that the film generally diverges from the sealed side to the air side, resulting in diverging flow during the outstroke and converging flow during the instroke, as pointed out in the preceding section. The lower fluid pressures during the outstroke result in a generally reduced film thickness, Figure 6.23, while the higher fluid pressures during the instroke result in a generally increased film thickness, Figure 6.24. Thus, the average film thickness during the instroke exceeds that during the outstroke. This, as well as the cavitation during the outstroke, aids in inhibiting leakage from the system as was demonstrated in chapter 5. The very significant differences in shape between the VE and LE curves are due to the delayed and complex structural response of the viscoelastic seal to fluid pressure changes. The generally higher fluid pressures with the VE seal, during both outstroke and instroke, result in generally increased film thicknesses compared with the LE seal.

The history of the film thickness is shown in Figure 6.25 and Figure 6.26. These are consistent with the film thickness distributions, discussed above. The increased film thicknesses obtained with the VE model, compared to the LE model, are consistent with the film thickness distributions described above. The film thickness, during instroke, obtained with the VE model is 20%-30% higher than that obtained with the LE model, while during outstroke it is 22%-25% higher than that with the LE model. However, the ratio of outstroke to instroke film thickness for the VE and LE models are comparable.

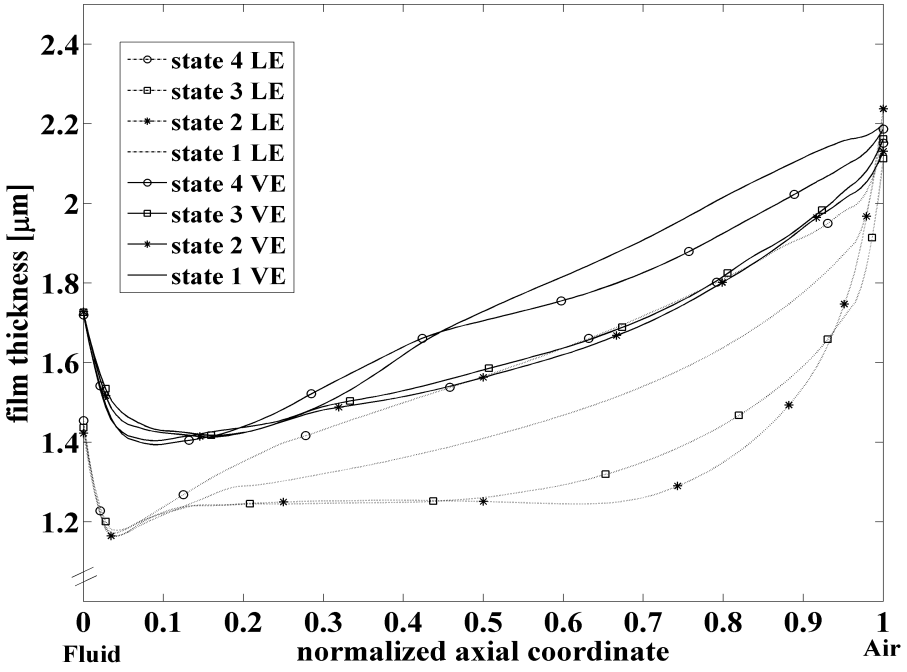

Figure 6.23: Film thickness distribution, outstroke.

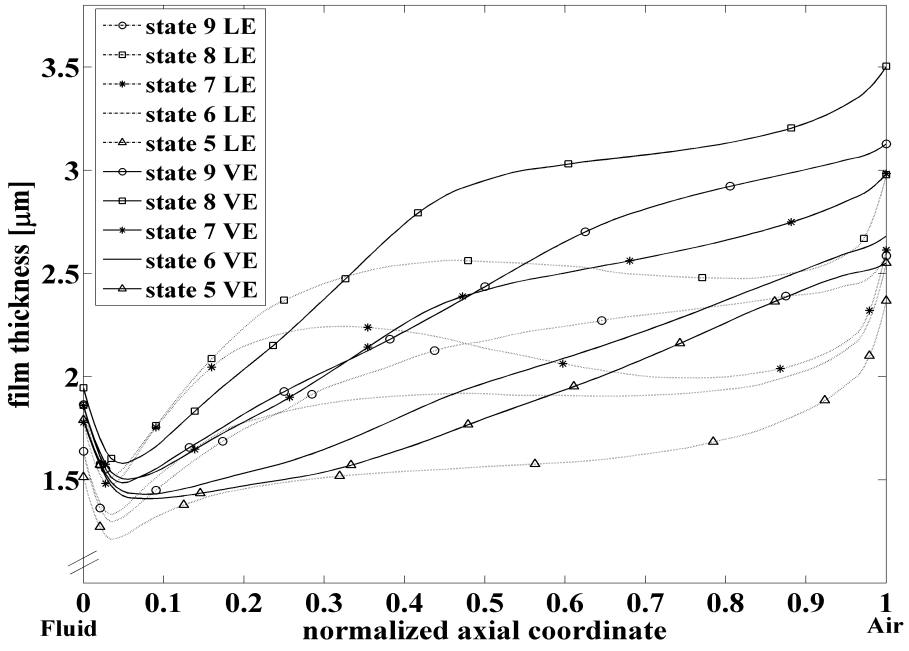

Figure 6.24: Film thickness distribution, instroke.

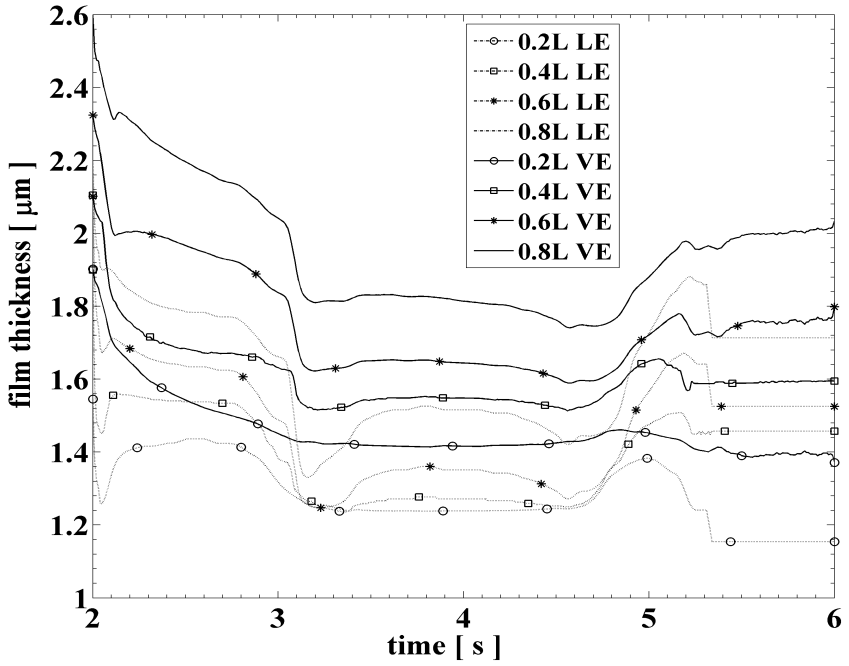

Figure 6.25: Film thickness history, outstroke.

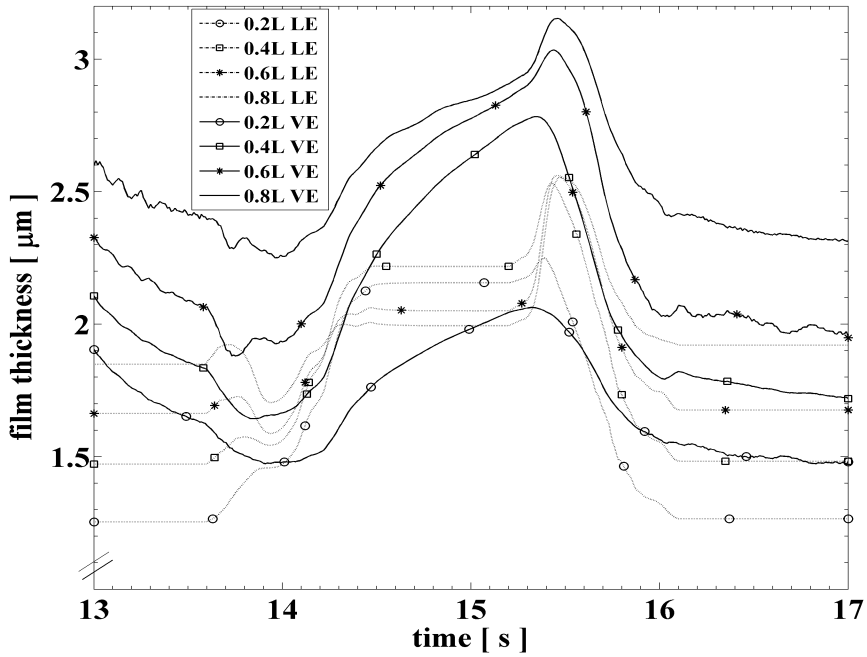

Figure 6.26: Film thickness history, instroke.

6.5.4 Contact Pressure Distribution and History

The dynamic contact pressure distributions during the outstroke and instroke are presented in Figure 6.27 and Figure 6.28 respectively. The generally higher contact pressures during the outstroke compared to the instroke are consistent with the film thickness results, discussed above. The VE distributions are significantly different from the ones obtained with the LE model, both in shape and magnitude. These differences are a result of the delayed and complex response of the viscoelastic seal.

The contact pressure results can be interpreted by noting that the total load exerted by the seal lip is supported by the fluid pressure and the dynamic contact pressure. The plots of contact pressure clearly reflect the interplay between these pressures as the sealed pressure varies. For example, during the outstroke (Figure 6.27) as the sealed pressure increases and the load exerted by the seal lip increases (state1 to state 2), the load on the contacting asperities increases and the contact pressure increases except for a small region close to the sealed end. In this latter region the contact pressure drops with increasing sealed pressure because the sealed pressure's effect in raising the fluid pressure is maximum in the region nearest to the sealed end. In the remaining portion of the sealing zone the hydrodynamic effects produced by the increasing rod velocity and the effects due to film thickness variations become significant. In that region, the reduced fluid during the outstroke leads to a generally increased contact pressure, while the increased film thickness during the instroke leads to a reduced contact pressure.

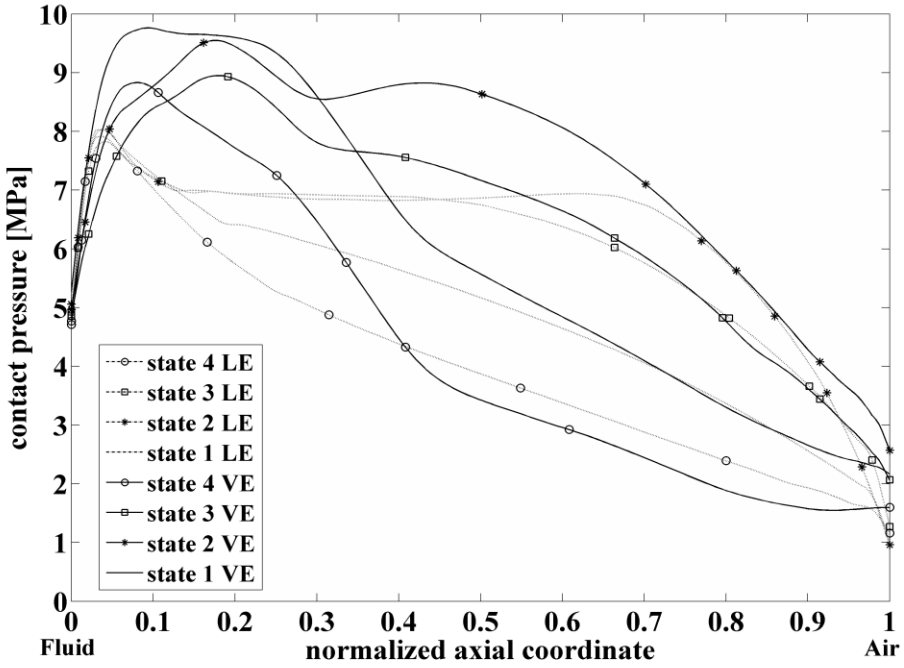

Figure 6.27: Contact pressure distribution, outstroke.

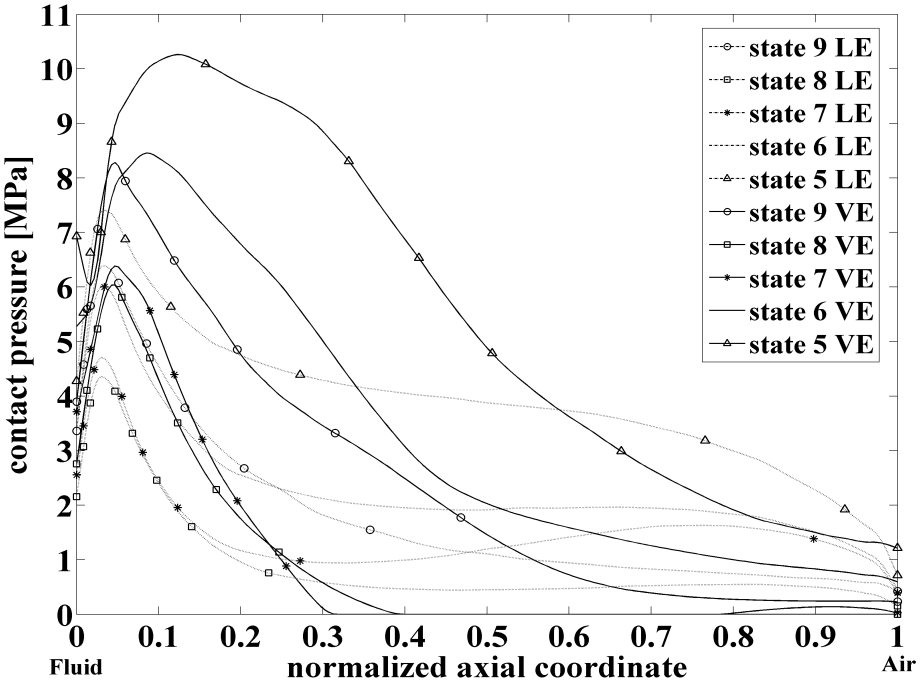

Figure 6.28: Contact pressure distribution, instroke.

The history of the outstroke contact pressure is shown in Figure 6.29. The viscoelastic relaxation of the contact pressure is evident from the slopes of the VE curves at x = 0.2L and 0.4L compared to the flat regions of the corresponding LE curves. The contact pressures from the VE model exceed those from the LE model in the contact zone nearest the sealed side (x = 0.2L). As x increases, the differences between the VE and LE model results decrease.

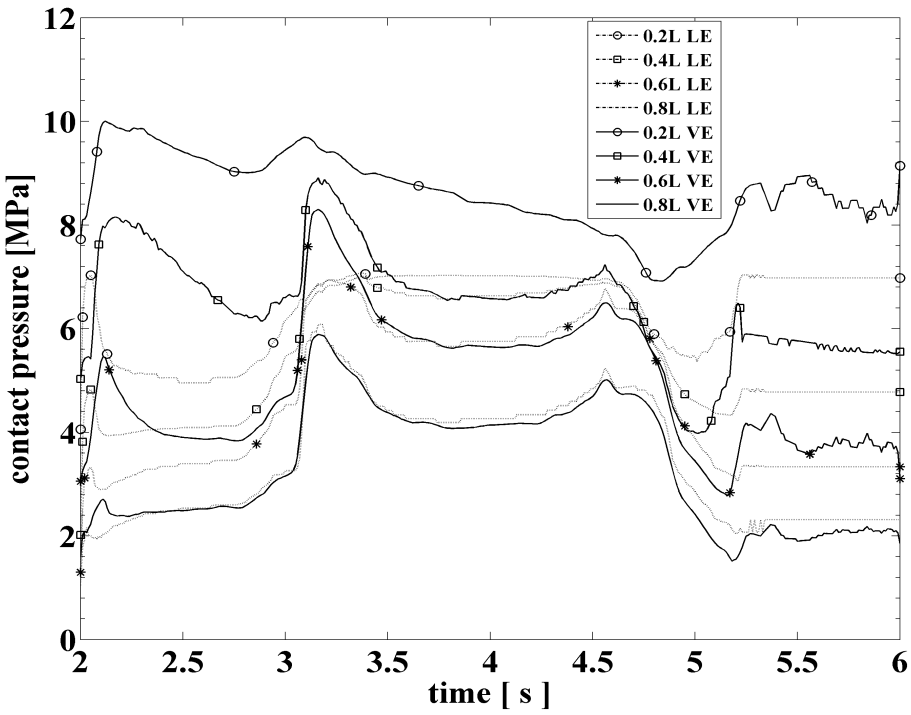

Figure 6.29: Contact pressure history, outstroke.

Somewhat similar behavior is observed in the history of the instroke contact pressure, Figure 6.30. However there is a difference in these histories during the periods of high rod velocity (3.25 s - 4.45 s for outstroke, 14.5 s - 15.5 s for instroke). During such a period of the outstroke, in the 80% of the sealing zone farthest from the sealed end, the VE and LE contact pressures are almost the same, while during the

corresponding period of the instroke the VE contact pressures are lower than the LE contact pressures.

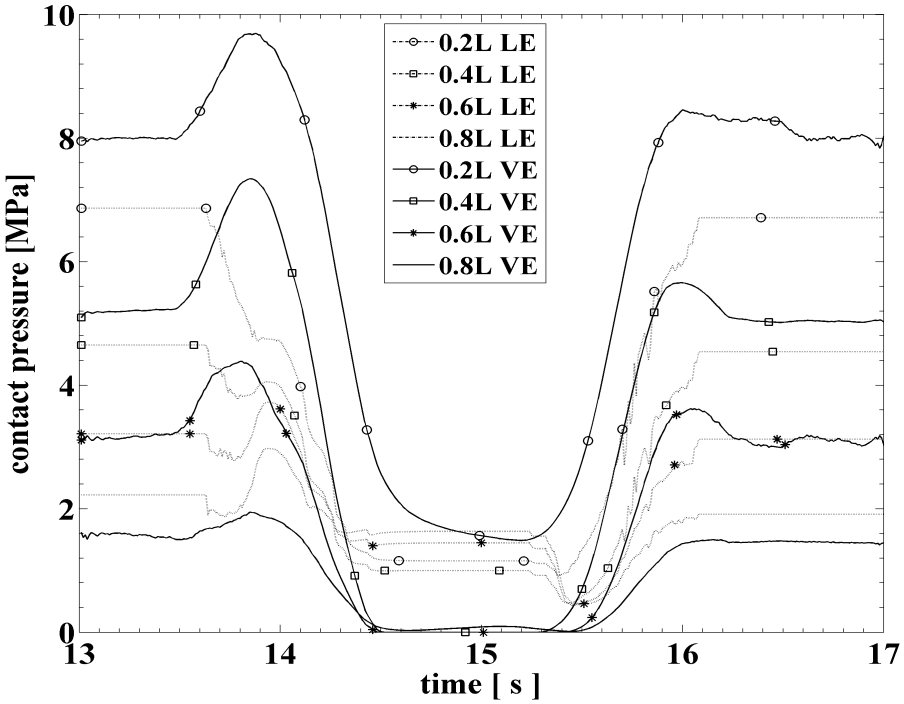

Figure 6.30: Contact pressure history, instroke.

A 3D surface plot of contact pressure distribution during outstroke as a function of time is shown in Figure 6.31. Part (a) shows the one obtained with VE model and part (b) shows that obtained with the LE model. The discussion regarding Figure 6.27 and Figure 6.29 becomes clearer by looking at this simultaneous space-time distribution of contact pressure. The contact pressures for the viscoelastic seal closest to the sealed end between 3-5 sec are much smaller than those at rest of the times. This difference is more pronounced than that obtained for the perfectly elastic seal. Also the curvature of the contact pressure distribution between 3-5 sec obtained with the VE model is much smaller than that obtained with the LE model.

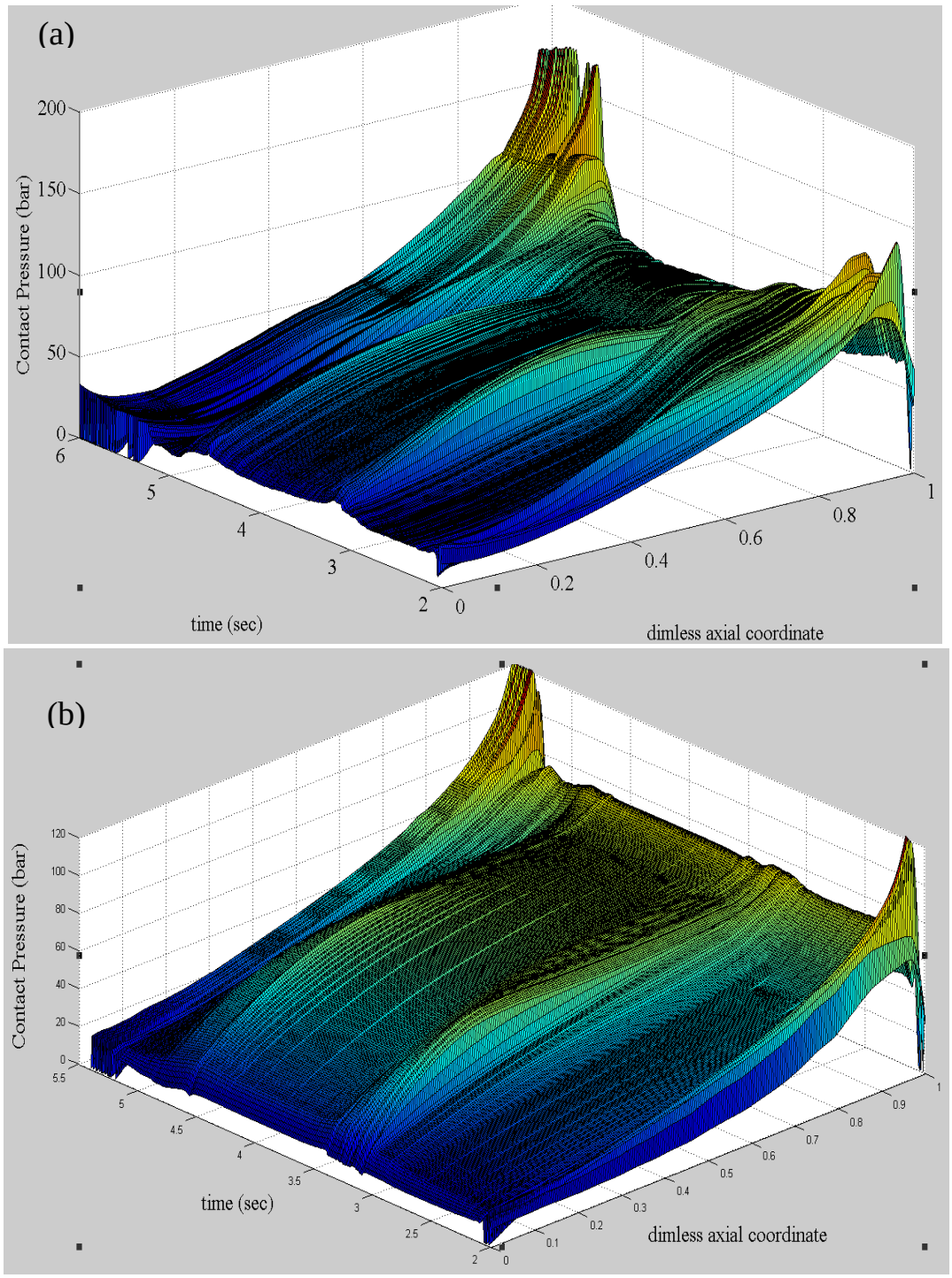

Figure 6.31: Contact pressure distribution during outstroke as a function of time obtained with VE model (a) and LE model (b).

6.5.5 Fluid Transport

Figure 6.32 shows the fluid transport out of the cylinder versus time. It can be seen that with the VE model, despite more cavitation, the increased film thickness during the outstroke raises the outward transport to a higher value at the end of the outstroke, compared to the LE model. The instroke transport has to begin its descent from this higher level. With the higher film thickness during the instroke, one would expect this descent to be steeper than that for the LE model. But in reality the slope is not very different from that with the LE model. The reason for this is revealed by decomposing the total flow rate into Poiseuille and Couette components as shown in Figure 6.33 and Figure 6.34.

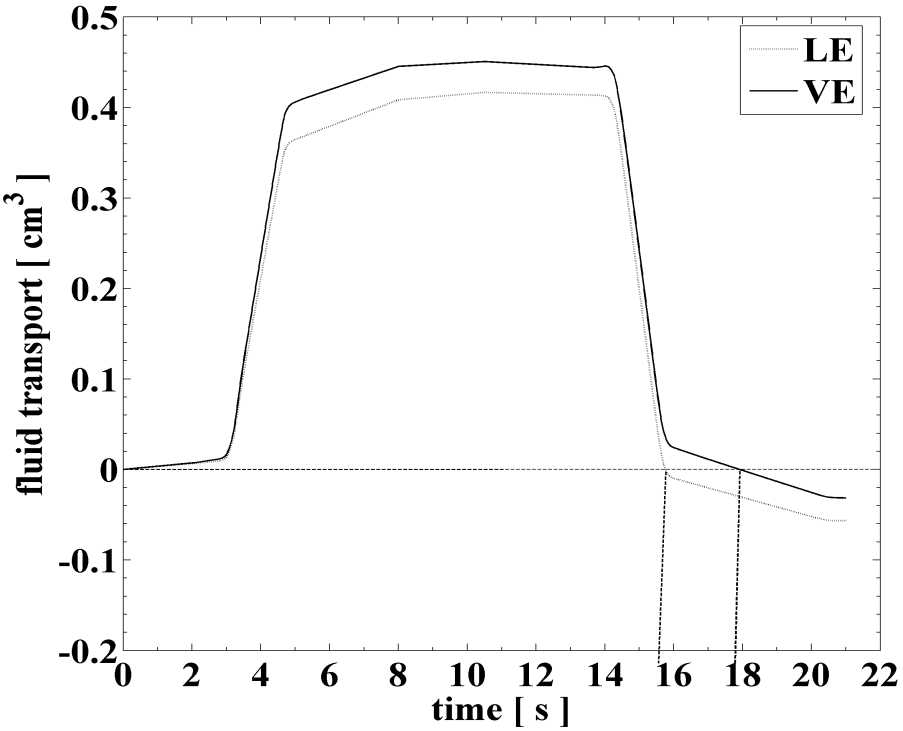

Figure 6.32: Fluid transport out of cylinder vs. time.

It can be seen that, with the VE model, during the outstroke the Couette component dominates the Poiseuille component and almost entirely accounts for the total flow rate, while during the instroke a substantial amount (approximately 17 %) of the Poiseuille component contributes to the total flow rate. In addition, the direction of the Poiseuille flow is opposite to that of the Couette flow and hence it reduces the total inward flow. This is a new phenomenon that was not observed with the LE model (with the LE model, the Poiseuille component is negligible during both outstroke and instroke). Hence this additional Poiseuille flow counteracts the effect of the increased film thickness. Hence due to the combined effect of the increased outstroke film thickness and the instroke Poiseuille component, the net outward fluid transport curve takes longer to reach the zero leakage state with the VE model (approximately 18 s with the VE model as compared to approximately 15.8 s with the LE model). That is, the LE model under predicts the time required to reach the zero leakage state. This is an important result, as it emphasizes the importance of modeling the viscoelastic material behavior in predicting the seal's leakage characteristics. With a small change in the input sealed pressure/ rod velocity history, the above curves could shift to the right such that the LE model would predict a non-leaking seal at the end of the cycle, while in reality the true viscoelastic behavior of the seal would lead to leakage.

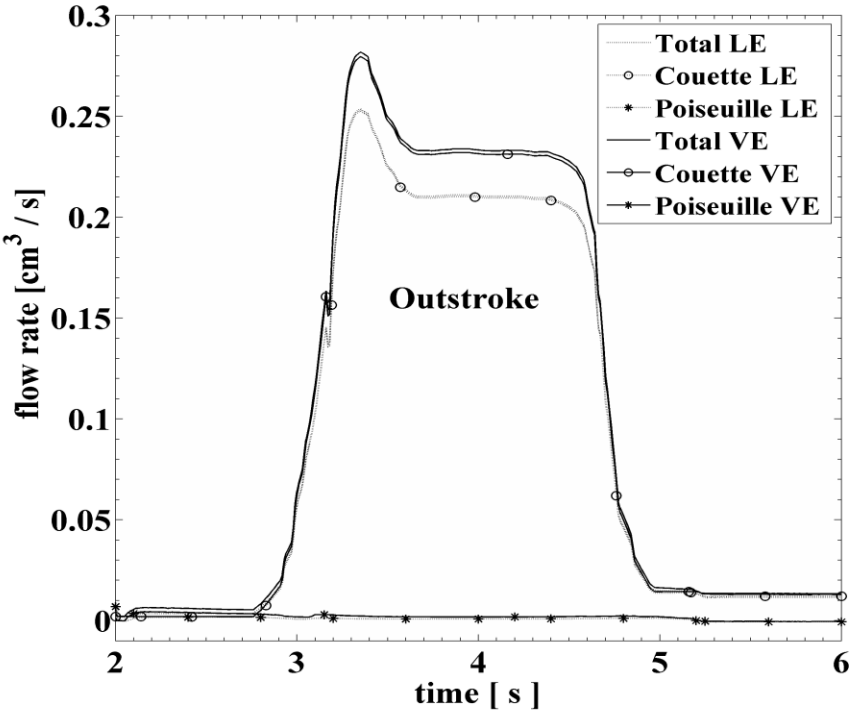

Figure 6.33: Flow rate vs. time, outstroke.

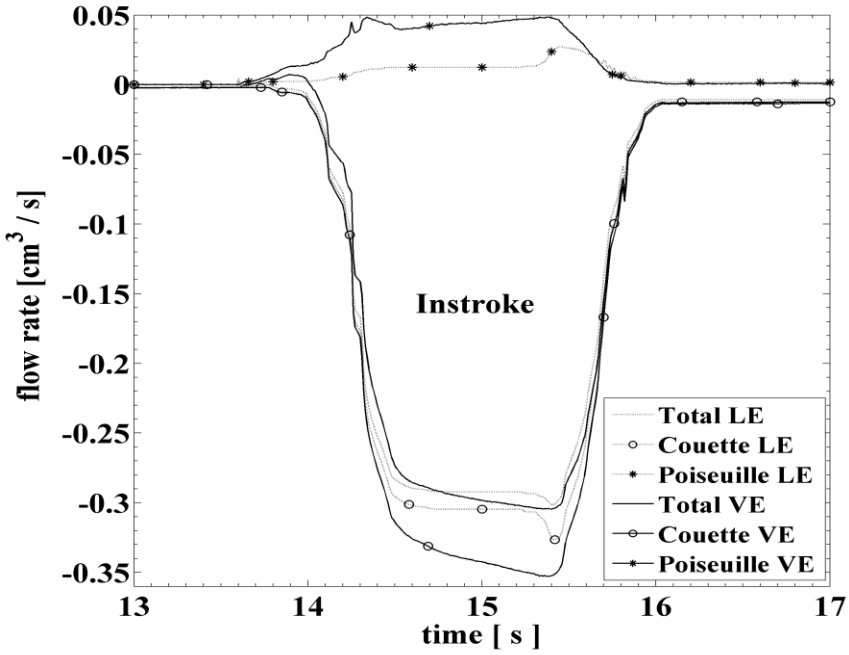

Figure 6.34: Flow rate vs. time, instroke.

6.5.6 Friction

Figure 6.35 shows the total friction force on the rod versus time. The magnitude is significantly larger during the outstroke than during the instroke The VE curves show significant viscoelastic decay during both outstroke and instroke, after the sealed pressure load is removed. VE reduces peak amplitudes during the outstroke by 10% but maintains a higher friction force than with the LE model during the relaxed period . During the instroke, the viscoelasticity has a mixed effect on the friction magnitude. During the period of increasing rod velocity, the friction force reduces to as little as 50% lower than that with LE model, while it rises to as much as 100 % higher than with the LE model during the drop in rod velocity (15.4-16.0 s). To get insight into this friction behavior, it is necessary to examine the shear stress on the rod and the sealing zone length, since the friction force is obtained by integrating the shear stress over the sealing zone length.

6.5.6.1 ***Shear Stress***

The mean shear stress on the rod is shown in Figure 6.36 as a function of time. The shape of the LE shear stress history closely resembles the contact pressure histories shown in Figure 6.29 and Figure 6.30. In general, during the outstroke its magnitude is increased from its quasi-steady value, while during the instroke its magnitude is decreased. This is because of the increased contact pressure during the outstroke and the decreased contact pressure during the instroke, as discussed earlier. Thus, the magnitude of the shear stress due to contacting asperities is increased during the outstroke and reduced during the instroke, while the viscous contribution to the shear stress remains relatively small. However, viscoelasticity strongly affects the shear stress history in both

shape and magnitude. During the outstroke, it increases the shear stress peak magnitude by about 20 %. During the instroke, the drop/rise due to hydrodynamic effects caused by the increasing (13.9-14.5 s) / decreasing (15.4-16.0 s) rod velocities can be seen to be much more pronounced with the VE model than with the LE model. This pronounced drop/rise in the shear stress magnitudes results in the friction behavior with the VE model described above. The difference between the quasi-steady value and maximum peak /valley value obtained with VE model is as much as 22 % higher than that with the LE model.

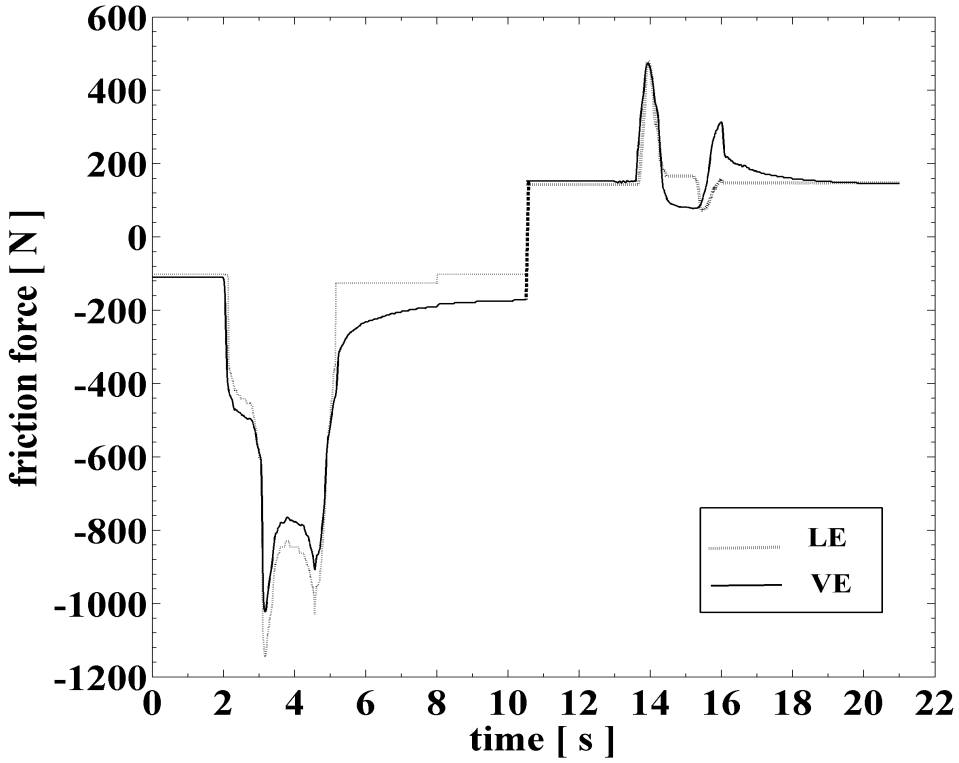

Figure 6.35: Friction force on rod vs. time.

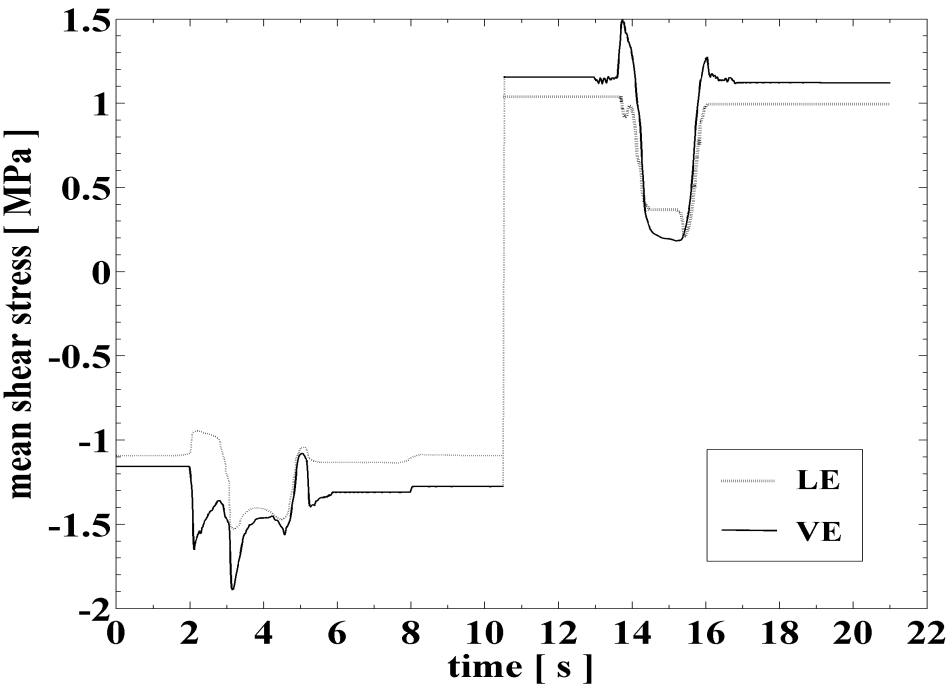

Figure 6.36: Mean shear stress on rod vs. time.

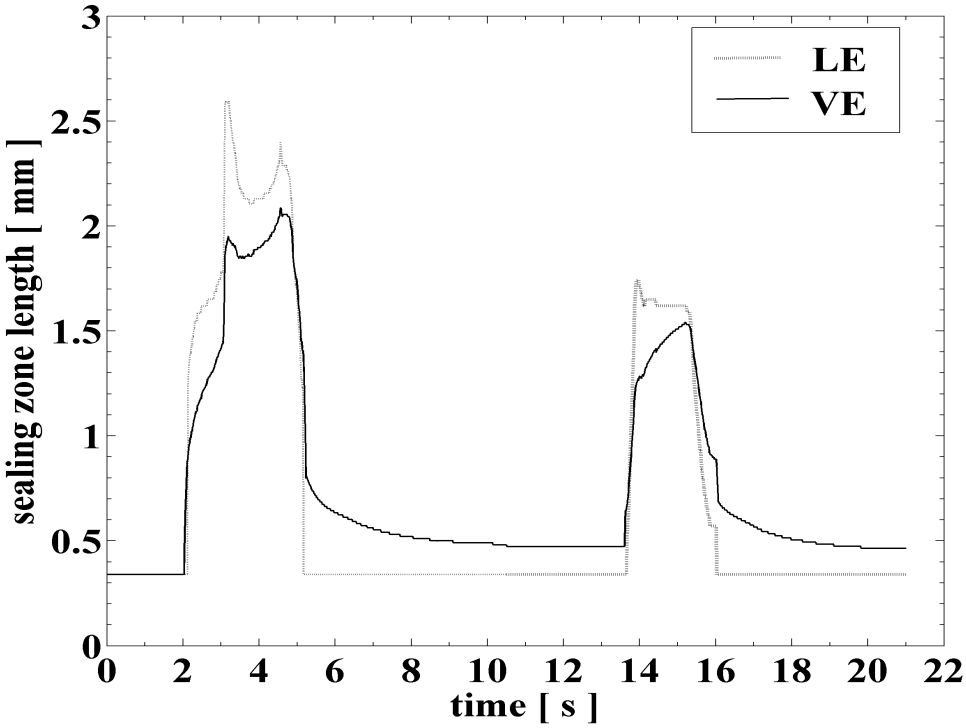

Figure 6.37: Sealing zone length vs. time.

6.5.6.2 ***Sealing Zone Length***

Figure 6.37 shows the sealing zone length as a function of time. Comparing Figure 6.37 with Figure 6.16, it is evident that the sealing zone length is governed by the sealed pressure; the higher the sealed pressure, the larger is the sealing zone length. This is a result of the macroscopic deformation characteristics of the seal, as is illustrated in Figure 6.17. One can conclude that the larger friction force during the outstroke, as compared with that during the instroke, is due to both the higher shear stress and longer sealing zone.

The sealing zone length vividly demonstrates the effect of viscoelasticity. The maximum sealing zone length obtained with the VE model is approximately 23 % lower during outstroke and about 13 % lower during instroke than those with the LE model. The VE curve also shows the viscoelastic decay after the sealed pressure load is released; hence, a longer contact length is maintained with the VE model than with the LE model. This longer contact length results in the higher frictional force observed during the "relaxed period" as discussed earlier. The rate of this decay depends on the combination of the viscoelastic relaxation moduli at the various time scales and can be controlled by an appropriate choice of the seal material. Another important observation is that, with the VE model, the instroke begins when the seal is still not fully relaxed and has not come back to its original base state. This differs from the results with the LE model, where each instroke begins at the exact same base state. It can be imagined that for multiple cycles, the rate of viscoelastic decay will play an important role and the viscoelastic effects will accumulate from cycle to cycle. This in turn will affect the fluid and contact pressures and film thickness characteristics of the succeeding cycles.

6.6 Conclusions

The dynamic response of viscoelastic solids is analyzed using analytical and finite element models. Effect of excitation frequency and relaxation time scales on storage and loss moduli and loss tangent is investigated. The effect of ratio of instantaneous moduli and relaxation time scales on the loss tangent and hence on hysteresis characteristics of viscoelastic polymers is analyzed. The macro-scale dynamic response of polyurethane rod seal under dry conditions is investigated by tracking displacements, stresses and strains at specific material points. The effect of viscoelastic relaxation time scales on hysteresis and sealing zone length of such seals is also quantified. These preliminary analyses facilitated the theoretical framework needed for choosing appropriate seal materials for particular dynamic applications and for developing comprehensive MSMP seal model incorporating polymer viscoelasticity.

With this knowledge, a MSMP model incorporating viscoelasticity is developed for predicting the rod seal behavior during the transient operation. A new analytical model for micro-scale contact of viscoelastic rough surfaces is developed and is incorporated into the MSMP framework. The inclusion of viscoelastic effects in the macro and micro-scale deformation mechanics as well as in the macro and micro-scale contact mechanics is a significant step forward in the pursuit of a realistic seal model. Viscoelasticity is seen to affect the leakage and friction characteristics through its effects on the fluid pressure and contact pressure distributions. It critically affects the interplay between the transient sealed pressure effects and the hydrodynamic effects produced by the changing rod velocity. Viscoelasticity increases both the fluid pressure and the contact pressure significantly in the sealing region closest to the sealed end, shifts the

fluid pressure peaks away from the sealed end during instroke and enhances the cavitation during the outstroke. It produces thicker fluid films during both, the outstroke and the instroke, and produces a significant increase in the Poiseuille component of the flow during the instroke. Through its effects on mean shear stress and sealing zone length, viscoelasticity significantly alters the friction force behavior. Importantly, it is found that ignoring viscoelasticity leads to under prediction of the time required to reach the zero leakage state during a cycle.

Limitations of the MSMP Model:

The comprehensive MSMP seal model discussed here takes into account several physical phenomena that occur over wide range of length and time scales. However, there are some limitations on the validity of the model. The model does not take into account the phenomena like wear or fracture of hydraulic seals. Such phenomena are often observed during long periods of sealing operation. Due to object-oriented nature of the MSMP framework, analytical / FE models for these phenomena can be included as separate modules into the current framework in the future. Also, the current model has not been tested at temperatures below 20^{o} C or above 120^{o}C. Such extreme temperatures can occur in applications like cryogenics equipments or aerospace actuators and the results predicted using MSMP in such environments need to be validated using appropriate experimental investigation. The model assumes linear viscoelastic behavior of the seal, however, at high temperatures, several polymers show a non-linear viscoelastic response which can produce deviations of the results from those predicted using current MSMP framework. Currently, the thermal transport due to friction between

seal and rod is neglected. Preliminary investigation showed negligible temperature rise due to friction at least in injection molding applications. However, in very high frequency, high pressure applications, such frictional heat can be non-negligible and hence the MSMP model needs to be upgraded to include the thermal transport into the MSMP coupling.

CHAPTER 7. MACRO SCALE AND NANO SCALE MATERIAL CHARACTERIZATION

The ability to handle viscoelasticity is of significant importance to the MSMP framework. Accurate prediction of the viscoelastic response of the seal requires input of accurate relaxation moduli and time constants that span a broad relaxation spectrum of the polymer. Macro-scale viscoelasticity parameters can be estimated using techniques like Dynamic Mechanical Analysis (DMA). However, extracting the parameters needed for MSMP from a typical output of DMA is not trivial. Also, with the inclusion of micro-scale viscoelastic contact analysis, it is interesting to see if the micro / nano scale viscoelastic properties of the contacting asperities are any different than the macro-scale viscoelastic properties of the bulk of the polymer. Characterizing such macro-scale and micro/nano scale viscoelastic properties of the seals is the focus of this chapter. The experiments conducted for this purpose are described in the following sections.

7.1 Characterizing Macro-Scale Viscoelasticity

7.1.1 Dynamic Mechanical Analysis

To find the macro-scale viscoelastic properties of the polyurethane and PTFE seals, DMA was performed on the samples of these materials. The seal samples were obtained from industrial partners, namely, Trelleborg and Hallite. The samples used in DMA machines need to be of standardized shape. Seals were precisely cut into rectangular cross-sections with dimensions: 5.3 mm x 3 mm x 3 mm. Since the linear

variable differential transformer (LVDT) of DMA measures the small changes in sample dimensions based on a standardized original sample geometry, all the sample curvatures were eliminated before mounting the sample.

TA Instruments DMA 2980 was used to perform multi-frequency single cantilever analysis. The experimental setup is shown in

Figure 7.1. The DMA instrument shown belongs to the lab of Prof. C.P. Wong at Georgia Tech and the measurements were obtained with the help of Dr. Jack Moon and Mr. Liang Qizhen. During DMA operation a variable sinusoidal stress was applied to the end of the sample cantilever and the resultant sinusoidal strain was measured. If the material is purely elastic, the phase difference between the stress and strain waves is zero. If the material is purely viscous, the phase difference is 90°. Polymers exhibit a phase difference between these extreme values. This phase difference, together with the amplitudes of the stress and strain waves, was used to determine storage and loss modulus, $\tan(\delta)$, complex and dynamic viscosity, transition temperatures and creep. For extracting the Prony series coefficients for the seal sample, it was required to obtain the storage and loss moduli as functions of excitation frequency (see discussion in next section). For this, frequency scans were performed on each sample at various temperatures. To obtain the multi-temperature frequency scans following steps were performed on a polyurethane seal sample:

1) Equilibrate the sample at 30^{o}C

2) Keep the sample on isothermal condition for 5 mins.

3) Perform frequency sweep by driving the sample at monotonically varying frequencies and record storage & loss moduli, $\tan(\delta)$, amplitude of excitation, stress and strain at

each frequency. Since the viscoelastic relaxation time scales span over several decades, the excitation frequencies uniformly distributed from 0.1 Hz to 200 Hz on a logarithmic scale were chosen. These frequencies were : [0.1, 0.16, 0.25, 0.4, 0.63, 1.0, 1.6, 2.5, 3, 6.3, 10, 15.8, 25, 39.8, 63, 100, 158, 200] Hz.

4) Equilibrate the sample at 75^{o}C.

5) Keep the sample on isothermal condition for 5 mins.

6) Perform frequency sweep at same frequencies as in step 2 and record the data.

7) Equilibrate the sample at 120^{o}C

8) Keep the sample on isothermal condition for 5 mins.

9) Perform frequency sweep and record the data at each frequency.

The steps performed for PTFE seal sample are same as above except that the temperatures selected were: 30^{o}C, 50^{o}C, 80^{o}C, 100^{o}C and 120^{o}C

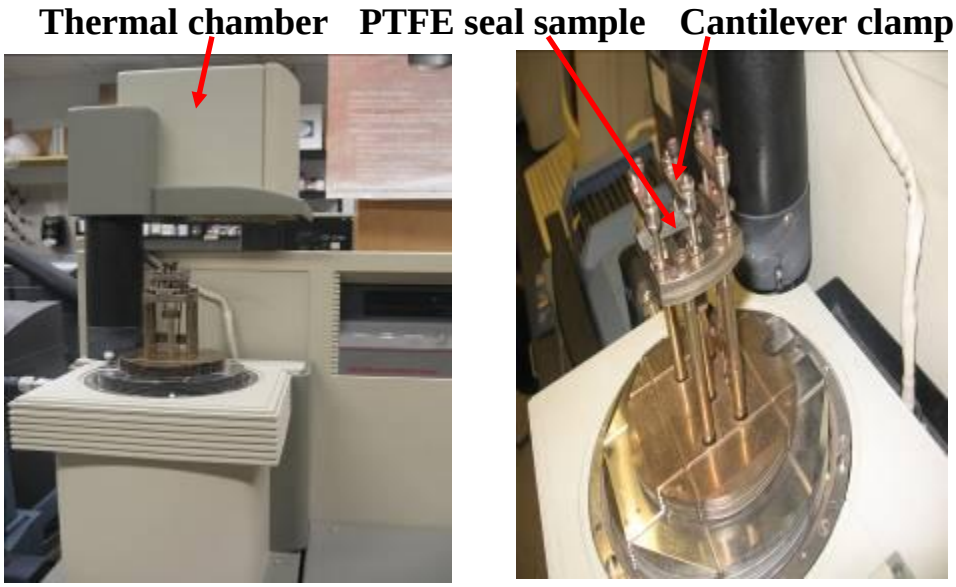

Figure 7.1: Dynamic mechanical analysis machine (left) and the clamp used to hold and oscillate the sample in the cantilever mode (right) (DMA setup belongs to Prof. C.P. Wong's lab at Georgia Tech).

The results from the frequency sweep on polyurethane at 30^{o}C are shown in Figure 7.2 and Figure 7.3. Figure 7.2 shows the storage and loss modulus. The error bars shown indicate the standard error on mean. It can be seen that the storage modulus increases significantly with increase in excitation frequency. The storage modulus increases by ~ 45 % in going from 0.1 Hz to 158 Hz. This is due the fact that at higher frequencies polymer chains re-arrange in such a way that the bulk of the polymer behaves more "elastic-like" than "viscous-like". However, the behavior of storage modulus with frequency also depends on the transitions involved and hence on the temperature at which the frequency scan is performed. At higher temperatures such a sharp rise in storage modulus will not be observed and material response will plateau towards an equilibrium value. The loss modulus also shows significant increase with frequency indicating that the hysteresis losses in the polyurethane seal will increase with frequency if operated at around room temperature. Since loss tangent, $\tan(\delta)$ is the ratio of loss modulus to storage modulus, the features of these moduli are reflected in loss tangent behavior as seen in Figure 7.3 which shows a large peak at 158 Hz. The peak is an indication of transition due to the ability of polymer chains to move past each other. This also indicates that the transition is dependent not only on the temperature but also on the strain rate.

7.1.2 Extracting Prony Series Coefficients from Storage and Loss Moduli

As seen from Figure 7.2, the output of dynamic mechanical analysis was the storage and loss moduli for various values of frequency. However for the generalized Maxwell model used in our MSMP framework, we need to input the Prony series

coefficients namely, instantaneous relaxation moduli (E_i) and relaxation time constants (τ_i) for i=1: N. Hence there was a need to develop a method for extracting viscoelastic Prony coefficients from the DMA data.

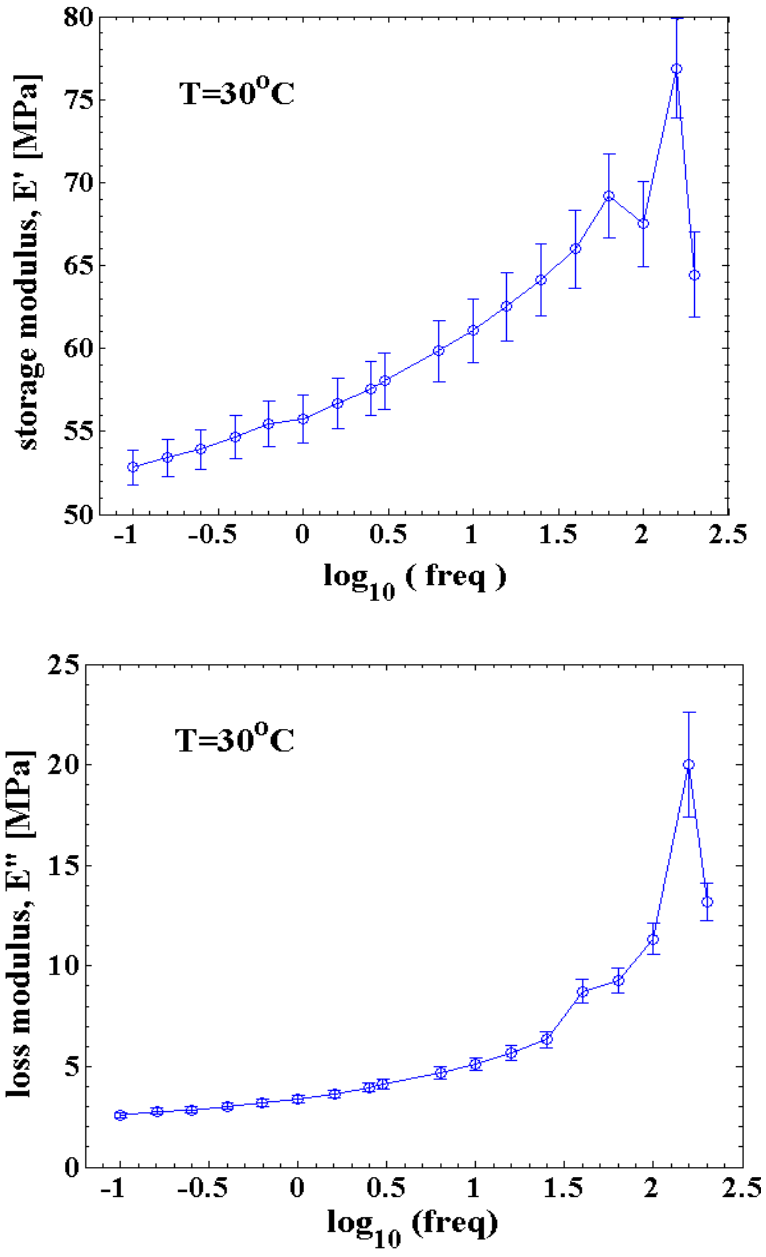

Figure 7.2: Storage modulus (top) and loss modulus (bottom) obtained from DMA with the frequency sweep at 30°C.

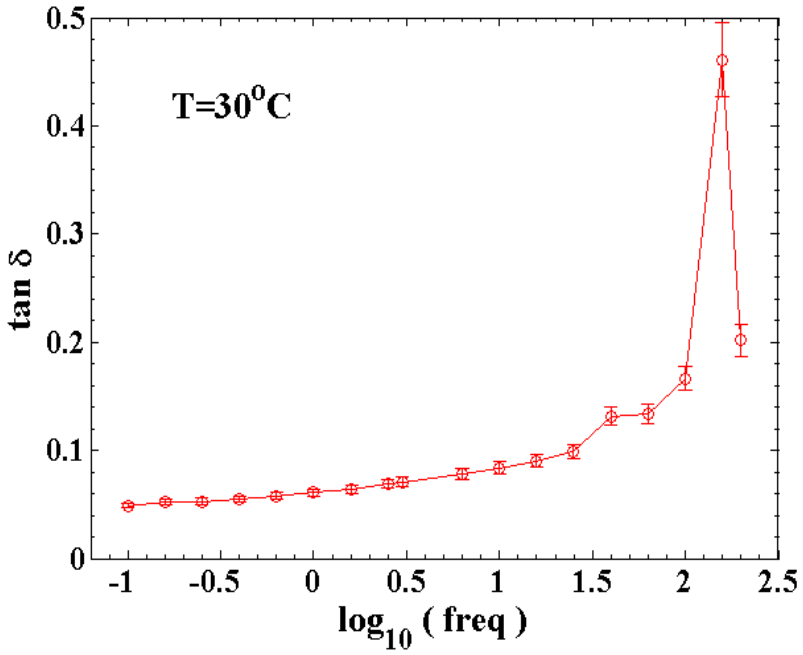

Figure 7.3: Loss tangent obtained from the frequency sweep at 30°C.

This section discusses the development of a *Multi-Variate Constrained Optimization* method for extracting the viscoelastic coefficients.

7.1.2.1 *Analytical Relation between Dynamic Moduli and Prony Coefficients*

Consider the complex modulus ($E^*(i\omega)$), which is the Fourier transform of the time dependent relaxation modulus ($E(t)$),

$$E^*(i\omega) = i\omega \int_0^\infty E(\tilde{t})\, e^{-i\omega\tilde{t}}\, d\tilde{t} \tag{7.1}$$

and its real (storage) and imaginary (loss) parts are,

$$E^{'}(\omega) = \text{storage modulus} = E_{\infty} + \omega\int_0^{\infty} \tilde{E}(\tilde{t})\sin(\omega\tilde{t})\,d\tilde{t}$$
$$E^{''}(\omega) = \text{loss modulus} = \omega\int_0^{\infty} \tilde{E}(\tilde{t})\cos(\omega\tilde{t})\,d\tilde{t} \tag{7.2}$$

where, $\tilde{E}(\tilde{t}) = E(\tilde{t}) - E_{\infty}$. If we express the time dependent modulus using Prony series as, $E(t) = E_{\infty} + \sum_{i=1}^{N} E_i\, e^{-t/\tau_i}$ and substitute it into Eq. (7.2), we get,

$$E^{'}(\omega) = E_{\infty} + \omega\int_0^{\infty}\left(\sum_{i=1}^{N} E_i\, e^{-\tilde{t}/\tau_i}\right)\sin(\omega\tilde{t})\,d\tilde{t} \tag{7.3}$$

$$E^{''}(\omega) = \omega\int_0^{\infty}\left(\sum_{i=1}^{N} E_i\, e^{-\tilde{t}/\tau_i}\right)\cos(\omega\tilde{t})\,d\tilde{t} \tag{7.4}$$

Considering the integration of the first term from the series expansion in Eq. (7.3) ,

$$\omega\int_0^{\infty} E_1\, e^{-\tilde{t}/\tau_1}\sin(\omega\tilde{t})\,d\tilde{t} = E_1\omega\int_0^{\infty} e^{-\tilde{t}/\tau_1}\sin(\omega\tilde{t})\,d\tilde{t} \tag{7.5}$$

Noting the Laplace Transform relation, $\mathcal{L}\{\sin(\omega\tilde{t})\} = \int_0^{\infty} e^{-s\tilde{t}}\sin(\omega\tilde{t})\,d\tilde{t} = \frac{\omega}{s^2+\omega^2}$,

integration of the first term of the series expansion in Eq. (7.3) becomes,

$$\omega\int_0^{\infty} E_1\, e^{-\tilde{t}/\tau_1}\sin(\omega\tilde{t})\,d\tilde{t} = E_1\frac{\omega^2\tau_1^{\,2}}{1+\omega^2\tau_1^{\,2}}$$

Using the same analysis, equations (7.3) and (7.4) reduce to,

$$E^{'}(\omega) = E_{\infty} + \sum_{j=1}^{N}\frac{E_j\,\omega^2\,\tau_j^{\,2}}{1+\omega^2\tau_j^{\,2}}$$
$$E^{''}(\omega) = \sum_{j=1}^{N}\frac{E_j\,\omega\,\tau_j}{1+\omega^2\tau_j^{\,2}} \tag{7.6}$$

Having obtained an implicit relation between (E_j, τ_j) and ($E^{'}(\omega), E^{''}(\omega)$), it is now required to develop a method to extract (E_j, τ_j) from the DMA data for ($E^{'}(\omega), E^{''}(\omega)$).

7.1.2.2 ***Multi-Variate Optimization Algorithm for Viscoelastic Parameter Extraction***

Eq. (7.6) cannot be inverted and hence a non-linear regression model needs to be developed for this purpose, where the problem is to find in some optimal way, the set of coefficients ($\{E_j\}$, $\{\tau_j\}$) that will minimize the error between analytical solution for ($E^{'}(\omega), E^{''}(\omega)$) given by Eq. (7.6) and the experimentally observed values of ($E^{'}(\omega), E^{''}(\omega)$) from DMA over a given range of frequency, ω. A couple of different methods are implemented to solve this nonlinear optimization problem, which are described below.

Method I) <u>Mixed Linear-Nonlinear Regression (Unconstrained Method):</u>

In this method, the experimentally found storage-loss modulus data vector $F(\omega)$

$$F(\omega) = \begin{cases} E_\infty + \sum_{j=1}^{N} \dfrac{E_j \omega^2 \tau_j{}^2}{1+\omega^2 \tau_j{}^2} & \forall \omega \geq 0 \\ \sum_{j=1}^{N} \dfrac{E_j \omega \tau_j}{1+\omega^2 \tau_j{}^2} & \forall \omega < 0 \end{cases} \tag{7.7}$$

is written as a multiplication of a matrix A and a vector E ,

$$F_i = A_{ij} E_j \tag{7.8}$$

in which , sum over repeated indices is implied and where,

$$A_{i,j} = \begin{cases} \dfrac{\omega_i \tau_j}{1+\omega_i^2 \tau_j^2} & \forall\ i \le Q \\ \dfrac{\omega_i^2 \tau_j^2}{1+\omega_i^2 \tau_j^2} & \forall\ i > Q \end{cases}$$

Then Eq. (7.8) is a mixed linear-nonlinear regression problem with N linear parameters E_i and N nonlinear parameters containing τ_j. This optimization problem is solved in the following manner:

1) Using the initial guess for τ_j , matrix A is constructed.

2) The linear regression problem $F = A * E$ is solved for E using linear least squares method where $norm(A * E - F)$ is minimized.

3) The solution of E thus obtained is then used to get the estimated value of $F_{est} = A * E$

4) Norm of the residual error is calculated : $norm(\varepsilon) = norm(F - F_{est})$.

5) Non-linear regression problem: "*find* τ_j *such that* $\left[norm(\varepsilon)\right]$ is minimized" is solved iteratively using Nelder-Meade algorithm. In the new iteration, the new values of τ_j are used in step 2 and steps 2-5 are repeated until convergence is reached.

The advantage of this method is that the relaxation time constants need not be fixed as in method (II) and it returns simultaneously optimized solution for both E_j and τ_j . However, the values of E_j and τ_j produced by this method can be negative.

Now, a constraint that makes this optimization problem non-trivial is that the values of the regression coefficients ($\{E_j\}$, $\{\tau_j\}$) cannot be negative, as these are real material properties and their negative values do not carry any physical meaning. Hence

the problem at hand is a constrained optimization problem. To remedy this issue, a second method is implemented which works on a similar ground as the one described by Bradshaw and Brinson [98] and is described below.

Method II) Minimize the RMS Error between Analytical and Experimental Values (Constrained Method):

In this method, a single universal function similar to that described in [98] is created to describe both, the storage modulus and loss modulus. An extended set of $2Q$ frequency domain points is created from Q original frequency data points as, $\{0,...,\omega_Q\} \rightarrow \{-\omega_Q,..0...,\omega_Q\}$. Negative ω are assigned to loss modulus and positive ω are assigned to storage modulus. The form of this universal function is shown below,

$$f(\omega) = \begin{cases} E_\infty + \sum_{j=1}^{N} \dfrac{E_j \omega^2 \tau_j{}^2}{1+\omega^2 \tau_j{}^2} & \forall \omega \geq 0 \\ \sum_{j=1}^{N} \dfrac{E_j \omega \tau_j}{1+\omega^2 \tau_j{}^2} & \forall \omega < 0 \end{cases} \tag{7.9}$$

Now, we can choose to solve for both $\{E_j\}$ and $\{\tau_j\}$ or we can choose to fix the time constants, $\{\tau_j\}$ and get the instantaneous relaxation moduli corresponding to that set of time constants. If we choose to fix the set of time constants, then a reasonable way to distribute these relaxation time constants over a range of frequencies of interest is using a logarithmic scale (since time constants of a viscoelastic Prony series typically span several decades) as,

$$\log_{10}(\tau_j) = \log_{10}(\tau_{\min}) + \left(\frac{j-1}{N-1}\right)\left[\log_{10}(\tau_{\max}) - \log_{10}(\tau_{\min})\right] \tag{7.10}$$

for $j = 1, 2, 3, ..., N$ where, $\tau_{\min}$ is the shorted and $\tau_{\max}$ is the longest relaxation time constant. These limiting time constants can be estimated from the maximum and minimum experimental frequencies as, $\tau_{\min} = 2\pi / 3\omega_{\max}$, $\tau_{\max} = 3 \cdot (2\pi / \omega_{\min})$ where, the factor of 3 extends the time constant range little beyond the experimental frequency range. Eq.(7.10) is then used to distribute the relaxation time constants over the broad range of frequencies of interest.

Now, our objective is to "globally" minimize the error between the universal modulus function $f(\omega)$ evaluated at frequencies $-\omega_Q \le \omega \le \omega_Q$ and storage modulus ($E'_{data}(\omega_j)$) data and loss modulus ($E''_{data}(\omega_j)$) data. One of the measures of such error is given by the RMS error defined as,

$$\varepsilon_{RMS} = \sqrt{\frac{1}{2Q}\left[\sum_{j=1}^{Q}\left(\frac{f(\omega_j) - E'_{data}(\omega_j)}{E'_{data}(\omega_j)}\right)^2 + \sum_{j=1}^{Q}\left(\frac{f(-\omega_j) - E''_{data}(\omega_j)}{E''_{data}(\omega_j)}\right)^2\right]} \qquad (7.11)$$

With this definition of error, the optimization problem now becomes,

$$Find\ E_j > 0\ \ for\ \ j = 1:N\ \ \ such\ that\ \ \varepsilon_{RMS} < \varepsilon_{tolerance} \qquad (7.12)$$

This minimization problem is solved using "Nelder-Meade" Simplex algorithm of MATLAB. A simplex in Q-dimensional space is characterized by the Q+1 vectors that are its vertices. During each step of the search, a new point near the current simplex is generated. The function value at the new point is compared with the function's values at the vertices of the simplex and one of the vertices is replaced by the new point, giving a new simplex. This step is repeated until the diameter of the simplex is less than the specified tolerance. The algorithm proceeds in the following manner [99]:

1) Functions are ordered according to the values at their vertices.

2) Reflection point is calculated and if it is not better than the best point of the current simplex, then a new simplex is generated by replacing the worst point with the reflected point. The algorithm is re-directed to the first step.

3) If the reflection point calculated is the best point then the expansion point is computed. If the expansion point is better than the reflected point then a new simplex is obtained by replacing the worst point of current simplex with the expanded point. Else the worst point is replaced by the reflected point to obtain the new simplex. If the reflected point is not better than the second worst point of current simplex then the algorithm is directed to step 4.

4) Contraction point is computed. If the contraction point is better than the worst point then a new simplex is obtained by replacing the worst point with the contracted point and algorithm is re-directed to step 1. Else algorithm is directed to step 5.

5) All the points except the best point are shrunk using the shrink coefficient.

The values of the Prony coefficients $\{E_j\}$ and $\{\tau_j\}$ obtained with this method are strictly positive and hence are physically interpretable.

As a test of feasibility of using above methods for Prony series parameter extraction, we applied these methods to several DMA data sets obtained from both, the literature and through our experiments. Figure 7.4 shows one such test where the blue circles are the data points obtained by [100] from the DMA experiments on poly(ester) urethane. The data points corresponding to positive ω are the storage moduli and those corresponding to negative ω are the loss moduli. We used our unconstrained optimization algorithm on this data set and were able to successfully extract the Prony coefficients E_j and τ_j . Top part of Figure 7.4 shows the DMA data (blue circles) for

storage and loss moduli and the analytical (Eq. (7.6)) curve obtained using the initial guess for parameters E_j and τ_j . It can be seen that the initial guess is far from the correct values that would agree with the experimental data. Bottom part of the figure shows the results obtained after successful convergence of the optimization algorithm. Successful convergence reduced the norm of the error below the tolerance value and produced a set of coefficients E_j and τ_j that when inserted in Eq. (7.6) gave exact same analytical curve as the experimentally observed data.

Figure 7.5 shows the results from the application of the "unconstrained" algorithm to our DMA test data described in section 7.1.1. Figure 7.6 shows the results from the application of the "constrained" algorithm to the same data set. It can be seen that extracted values of E_j and τ_j from the constrained version produced fairly good approximation to the experimentally observed behavior over a decent frequency range. The unconstrained algorithm (Figure 7.5) does a much better job of capturing the peaks in the DMA data. However, the values of E_j and τ_j obtained from such an unconstrained version may be negative and hence may not be always physically interpretable, as described earlier.

The relaxation modulus was reconstructed with $E(t) = E_\infty + \sum_{i=1}^{N} E_i e^{-t/\tau_i}$ using the extracted values of E_j and τ_j for the experimental data of polyurethane and PTFE seal samples. One such relaxation modulus vs time curve is shown in Figure 7.7. The values of E_j and τ_j for this relaxation modulus are also listed in the figure. These are the values that are used in the MSMP framework's viscoelastic macro and micro-scale deformation and contact mechanics modules described in chapter 6.

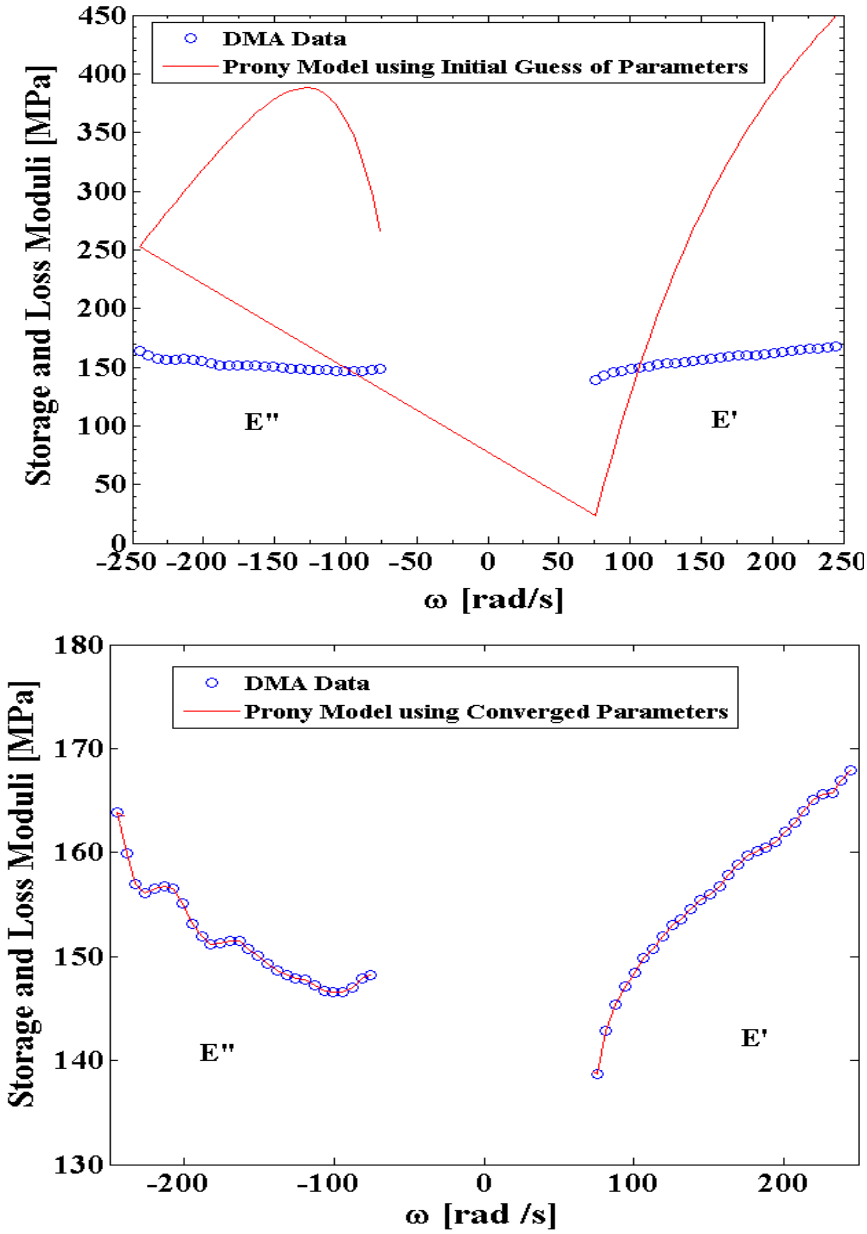

Figure 7.4 **DMA test data and the analytical curve obtained using initial guess (top) and converged solution (bottom) using constrained algorithm.**

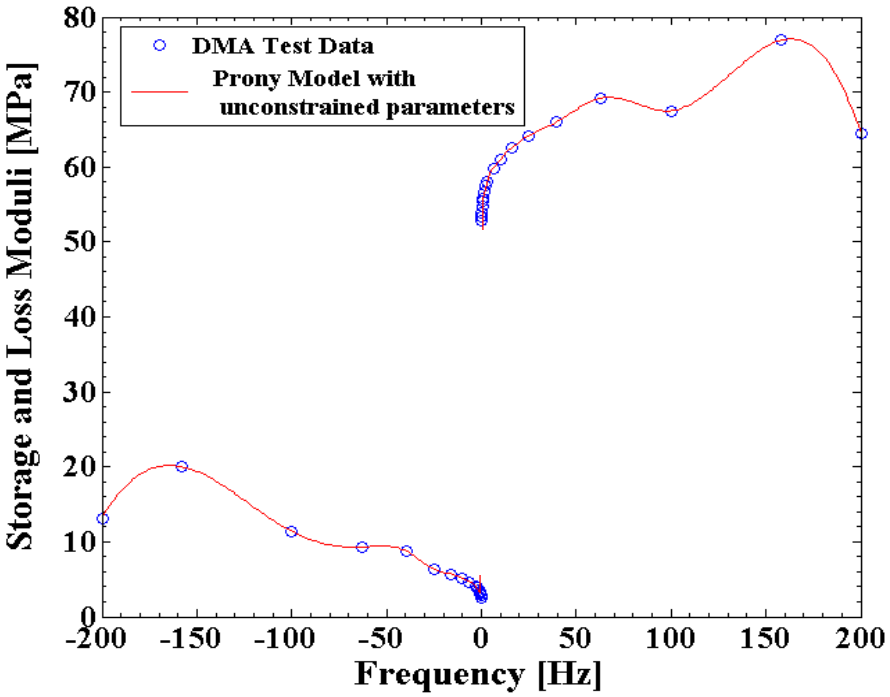

Figure 7.5: **DMA test data and the analytical curve obtained using the converged solution using unconstrained algorithm.**

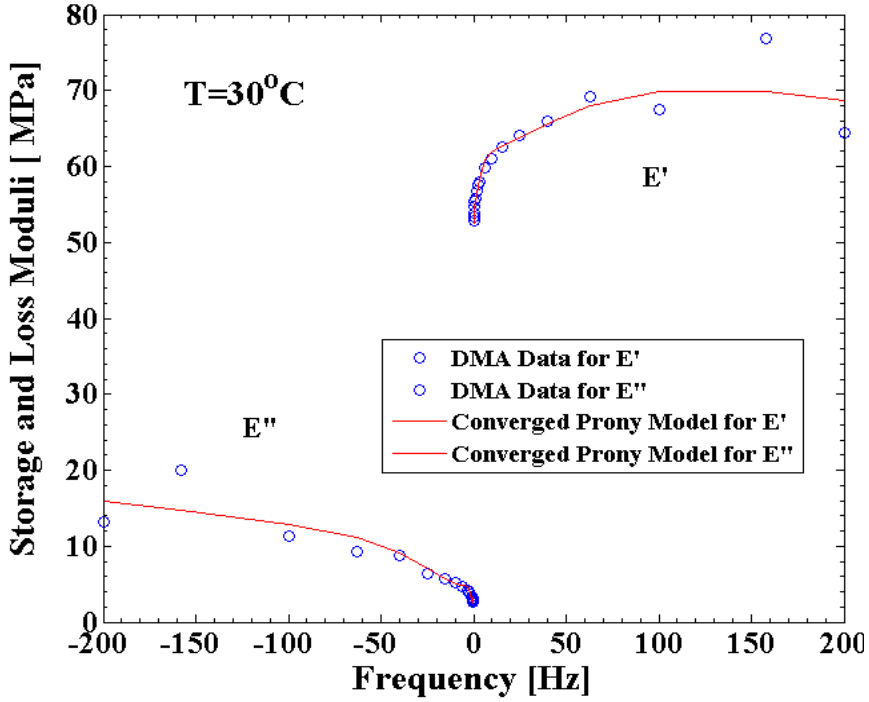

Figure 7.6: **DMA test data and the analytical curves obtained using the converged solution using constrained algorithm.**

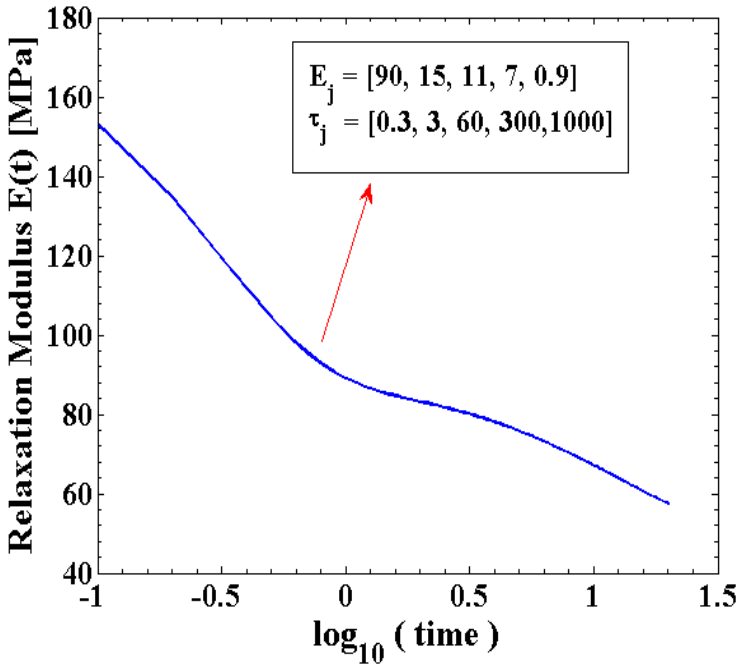

Figure 7.7: Relaxation modulus vs time curve constructed using the Prony series coefficients obtained from the constrained optimization algorithm.

7.1.3 Effect of Temperature on Viscoelastic Properties

To understand the effect of temperature on viscoelastic response of sealing polymers, it is useful to look at the molecular mechanisms that govern the polymer's viscoelastic response. In thermoset polymers both covalent and secondary (e.g., dipole, van der Waal) bonds connect individual chains to each other, while in thermoplastic polymers only secondary bonds connect the individual chains. These distinctions between the molecular characteristics of thermoplastics and thermosets cause the differences in behavior throughout the five regions of viscoelastic behavior, namely, Glassy, Transition, Rubbery, Rubbery Flow and Liquid Flow.

7.1.3.1 *Molecular Theory Describing Temperature Dependence*

The level of polymerization, characteristics of side groups of polymer chains, deformability of the molecular bonds, the thermal energy of the chains and the level of cross-linking are some of the important factors that typically dictate the macroscopic response of a polymer. However, one of the most important parameter to define the state of a polymer is its glass transition temperature, T_g. Below T_g, polymers show glass-like nature with minimal viscoelastic behavior. In this temperature region, the stretching/compression of molecular bonds produces deformations that manifest instantaneous elastic response. However, as the temperature increases and approaches T_g, the viscoelastic nature starts to become stronger. This behavior can be explained on the basis of vibrational modes of the polymer chains. Below T_g, the amplitudes of vibrations are typically much smaller and the molecular vibrations occur in confined regions. As the temperature is raised above T_g, the chain vibrations increase in frequency and amplitude, resulting in translational motions of the polymeric chains [27]. The molecular chains start to slide past other chains, and start inducing a more viscous response. In this temperature range, the secondary bonds are constantly broken and reformed hence causing pronounced configurational changes in the molecular chains that can produce irreversible strains in the bulk of the polymer.

With such a strong temperature dependence of viscoelastic moduli it is not possible to quantify the polymer's viscoelastic regions just based on absolute relaxation time range. There is a strong duality between the time and the temperature that defines the viscoelastic nature of the polymers. This duality is also responsible for a very useful concept of "Time-Temperature-Superposition" which is discussed later.

7.1.3.2 *Variation of Polyurethane and PTFE Viscoelastic Properties with Temperature*

Figure 7.8 shows the storage and loss moduli obtained from DMA measurements of polyurethane seal samples using frequency sweep at three different temperatures, 30^{o}C, 75^{o}C and 120^{o}C. The maximum modulus decreases by 45 % when temperature increases from 30^{o}C to 75^{o}C and by 58% when it is increased further to 120^{o}C. This is due to significant softening of polyurethane in the transition and rubbery regions. At low temperatures, the polyurethane shows a substantial increase (46%) in storage modulus with increasing frequency. The increase in modulus with frequency is not as significant at higher temperatures with only 14 % rise in storage modulus in going from 0.1 Hz to 200 Hz. A similar behavior is observed for loss modulus, where a very large increase in the loss modulus at 30^{o}C indicates that the high rise in out-of-phase component of stress with increase in applied frequency is much more pronounced at low temperatures.

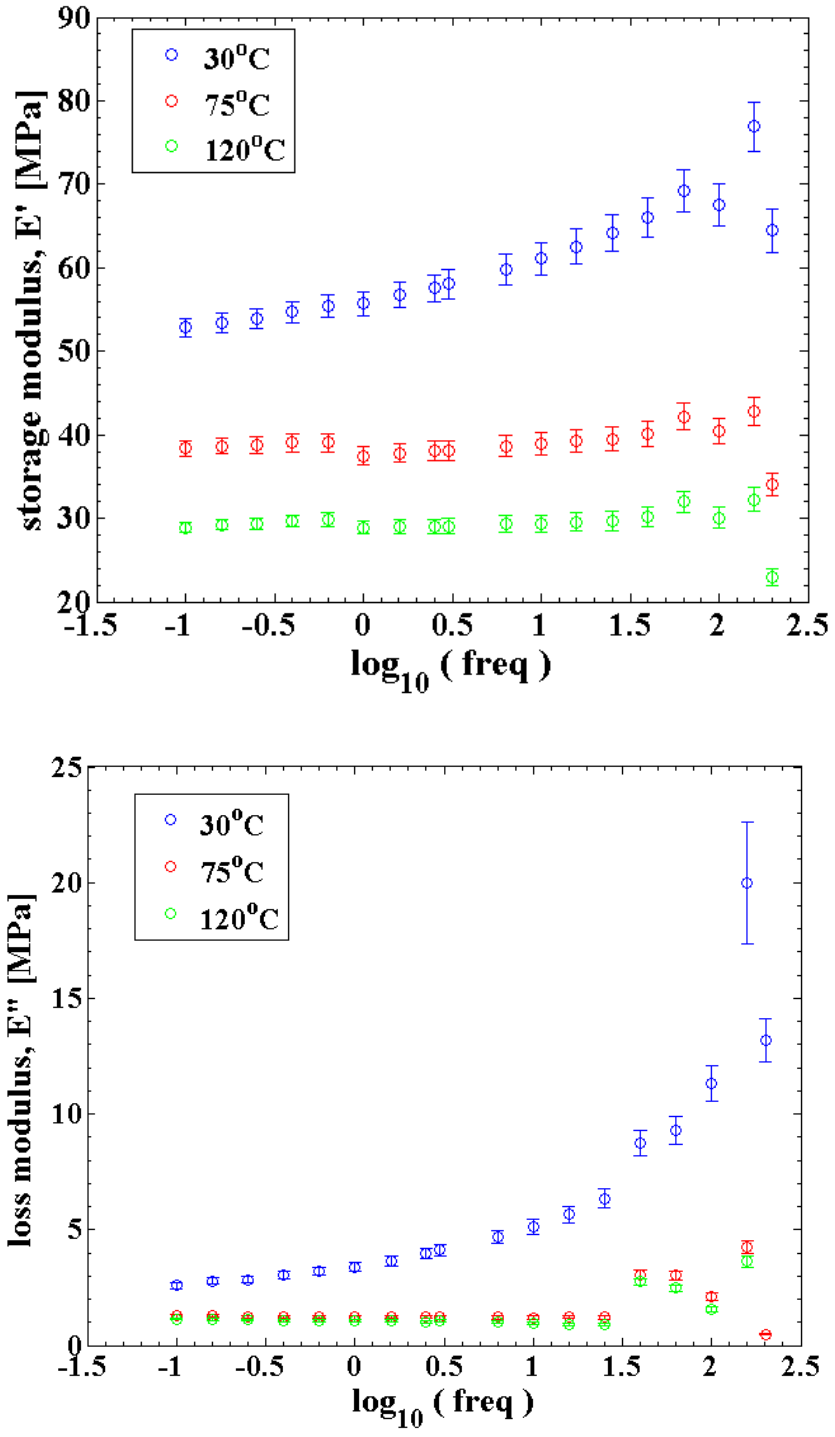

Figure 7.8 **Storage and loss moduli obtained from dynamic mechanical analysis of polyurethane seal samples using frequency sweep at 3 different temperatures.**

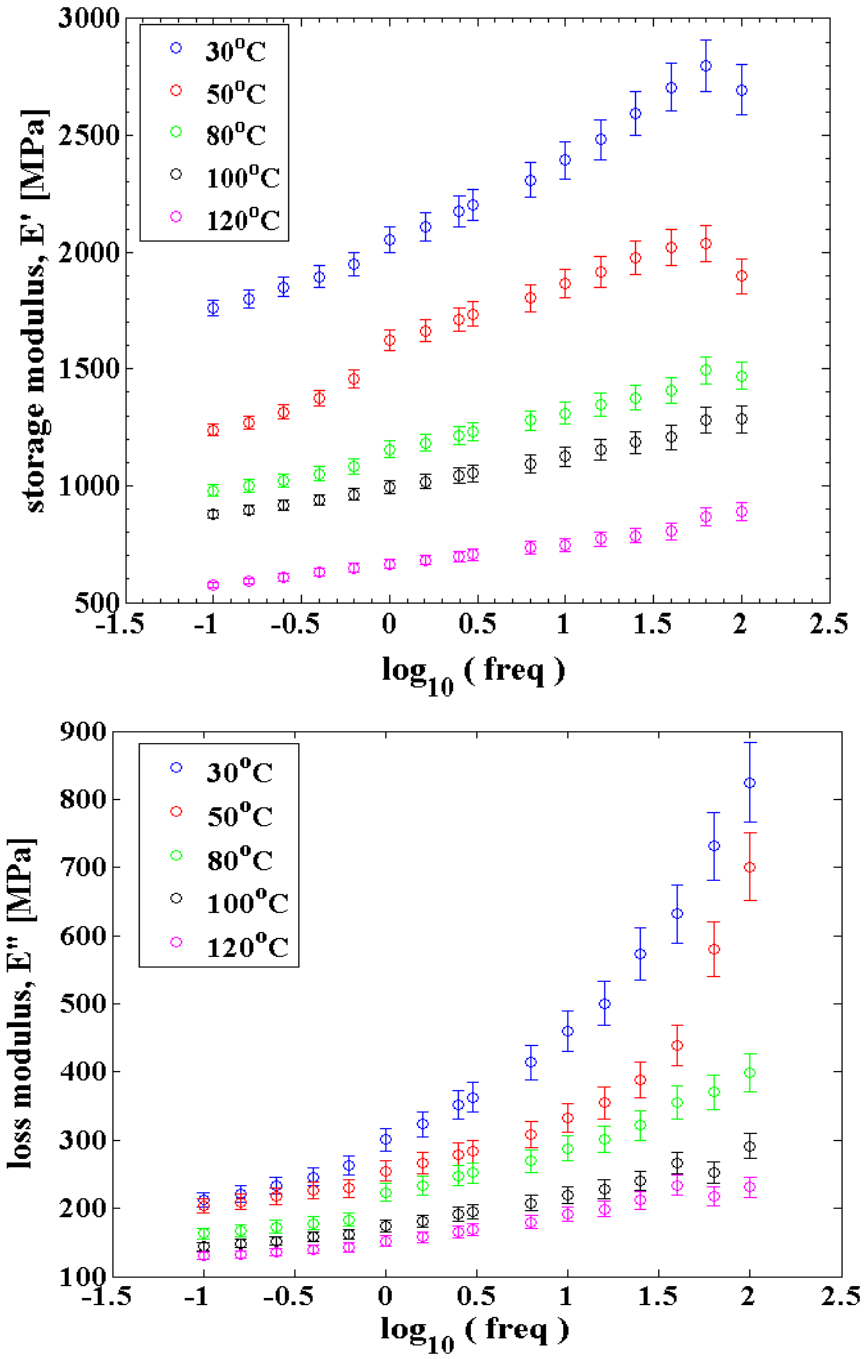

Figure 7.9: **Storage and loss moduli obtained from dynamic mechanical analysis of PTFE seal samples using frequency sweep at 5 different temperatures.**

The temperature dependence of storage and loss moduli of polyurethane seen here will be reflected in the values of Prony series coefficients and in the variation of relaxation modulus with time. This indicates that the polyurethane seal used in the viscoelastic MSMP model at 30^{o}C will be more than twice as stiff as the one at 120^{o}C. From the results of chapter 6, it can be imagined that if this seal is operated at 120^{o}C , it will produce much larger sealing zone lengths at same values of sealed pressures and will be more instantaneous to react than if operated at 30^{o}C. Comparing the loss modulus data at 30^{o}C and 120^{o}C , it can also be concluded that the hysteresis losses will be much higher at 30^{o}C than at 120^{o}C. It can also be seen that the fluid pressure and contact pressure distributions and hence leakage and friction characteristics will also be very different at 120^{o}C than those if operated at room temperature. It becomes apparent that the viscoelastic material parameters needed for any polymer seal model need to be extracted from the data obtained at approximately the same temperature as the operating temperature of interest. For the calculations in chapter 6, the properties were extracted at 30^{o}C.

DMA results for a PTFE seal sample are shown in Figure 7.9. It can be seen that PTFE is a much stiffer material with almost 40 times larger storage moduli than polyurethane at the room temperature. The temperature variation of storage and loss moduli is much more pronounced for PTFE than that for polyurethane, even at high temperatures. The storage modulus drops by almost 70% when temperature is increased from 30^{o}C to 120^{o}C. The loss modulus shows a more gradual decay with temperature than that observed in polyurethane. Unlike polyurethane, even at high temperatures, PTFE shows a significant increase in loss modulus with frequency. This indicates that the

out of phase component and the hysteresis losses will not be negligible even if the PTFE seal is operated at high temperatures. The experimental investigation here indicates that similar to polyurethane seals, for modeling the dynamic viscoelastic operation of PTFE seal, the material model should account for significant temperature variation of material properties and hence the material coefficients should be extracted from the data obtained at temperatures close to the operating range.

7.1.3.3 *Time-Temperature Superposition*

Since the hydraulic seals operate in a wide range of temperatures, our objective is understand how the viscoelastic moduli found at some reference temperature can be used to estimate the value of the moduli at some other temperature. More importantly, since the time scale of polymer relaxation at a given temperature may be so long that it may be impractical to conduct experiment to characterize such long time scales. In such a situation, time-temperature superposition comes extremely handy, as it allows the measurement of modulus to be conducted at a temperature higher than the reference temperature but for a shorter period of time and then converting this measurement into an equivalent modulus value at the reference temperature but over a much longer period of time.

H. Leaderman (NIST) first proposed the time-temperature superposition principle in 1940's. It was later verified by Rouse, Zimm and others using the "kinetic theory of polymers". Ferry and coworkers extended it to the bulk polymers in a rubbery state. The Rouse equation for the relaxation time of the p^{th} segment is given by [101], $\tau_p = \frac{6\eta M}{\pi^2 p^2 \rho RT}$ where, η is the viscosity of the solution, M is the molecular weight of

the segment, p is the number of segments per molecule, ρ is the solution density, R is the gas constant and T is the absolute temperature. Since M, p and R are constants, rearranging, we get, $\frac{\tau_p \rho T}{\eta} = \text{constant}$ and hence we can write,

$$\tau_p\big|_T = \tau_p\big|_{T_0} \frac{\eta}{\eta_0}\left(\frac{\rho_0 T_0}{\rho T}\right) \tag{7.13}$$

Thus, the relaxation time of a "thermorheologically simple" bulk polymer at one temperature can be found from that at another temperature by multiplying each relaxation time by a "shift factor" given by,

$$a_T = \frac{\tau_j\big|_T}{\tau_j\big|_{T_0}} = \frac{\eta}{\eta_0}\left(\frac{\rho_0 T_0}{\rho T}\right) \tag{7.14}$$

Since we are interested in finding the equivalence of modulus between the two temperatures / time scales, consider the Prony series modified to include the temperature dependence,

$$E(t)\big|_{T_0} = \rho_0 T_0 \sum_{j=1}^{N} E_j e^{-t/\tau_j\big|_{T_0}} \tag{7.15}$$

where, $E(t)\big|_{T_0}$ and $\tau_j\big|_{T_0}$ respectively denote the modulus and relaxation time constant evaluated at a reference temperature. Using the definition of "shift factor" defined earlier, the modulus at any other temperature can be expressed as,

$$E(t)\big|_T = \rho T \sum_{j=1}^{N} E_j e^{-(t/a_T)/\tau_j\big|_{T_0}} \tag{7.16}$$

Comparing Eq. (7.16) with Eq. (7.15), we get,

$$E(t)\big|_T = \frac{\rho T}{\rho_0 T_0} E\left(t' = \frac{t}{a_T}\right)\Bigg|_{T_0} \tag{7.17}$$

Now, since $t' = t / a_T$, hence $\log_{10}(t') = \log_{10}(t) - \log_{10}(a_T)$. Therefore the modulus calculated at one temperature can be converted into modulus at a different temperature by vertically shifting the modulus curve by a factor of $\log_{10}\left(\frac{\rho_0 T_0}{\rho T}\right)$ and then horizontally shifting it by a factor of $\log_{10}(a_T)$ as shown in

Figure 7.10 (Left). This is how the time-temperature superposition is used in this study.

William, Landel and Ferry [102] applied the time-temperature superposition method to a large number of polymers and have found empirically the following expression for the shift factor,

$$\log_{10}(a_T) = \frac{-C_1(T - T_0)}{C_2 + (T - T_0)} \tag{7.18}$$

where, the values of constants $C_1 = 17.44$ and $C_2 = 51.6$ have been found to give reasonable accuracy for a large number of commonly used polymers if the glass transition temperature T_g is used as the reference temperature T_0.

Figure 7.10 (right) shows the relaxation modulus curves obtained for polyurethane at 4 different temperatures. To form a master curve at 80^{o}C, the relaxation modulus curve at 30^{o}C is shifted to the left and the relaxation curves at 100^{o}C and 120^{o}C are shifted to the right to form a continuous smooth master curve that spans a much broader range of relaxation times. Hence the time-temperature superposition method provides a broad spectrum of relaxation time scales for the polymeric seal materials that in turn can be used in the MSMP viscoelastic framework to capture the viscoelastic seal response over a much wider range of excitation frequencies.

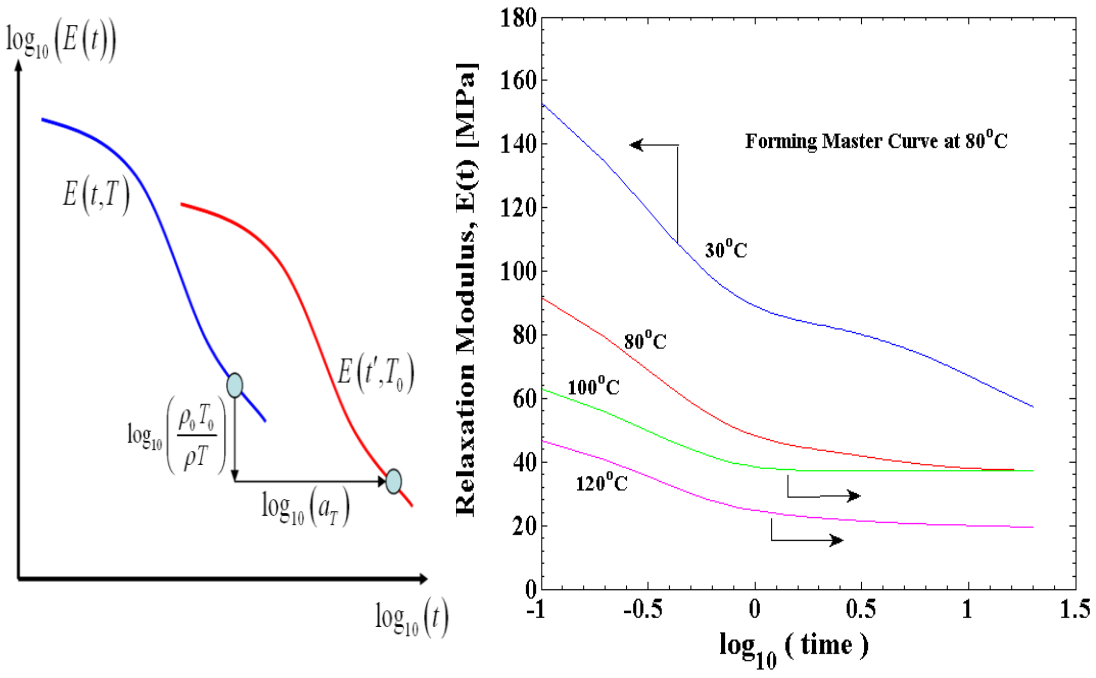

Figure 7.10: (Left): shifting the modulus data for $T_0 < T$. (Right): implementation of time-temperature superposition by shifting the polyurethane master curves at various temperatures.

7.2 Micro/Nano Scale Material Characterization

A micro-scale viscoelastic contact mechanics model was developed in chapter 6. This model defines the viscoelastic contact between seal surface asperities. In the calculations and results showed in chapter 6, the viscoelastic properties of asperities were assumed to be the same as that of the bulk of the polymer. However, recent developments in surface characterization techniques have shown that this may not be always the case. The surface force field like van der Waals attraction, electrostatic repulsion etc. also plays a significant role in the interaction between two surfaces that come in contact. Such surface force fields can alter the "effective" elastic properties of one surface as seen by the other. In addition, the polymer surfaces are often treated with surface enhancement methods like ion beam depositions, laser treatments, plasma treatments, metallization or surface coating. These techniques can significantly alter the surface elastic properties at macro/nano scale. In order to investigate the micro/nano scale elastic / viscoelastic surface properties of our seals, we have performed atomic force microscopy (AFM) on the polyurethane seal surfaces.

7.2.1 Topography

Figure 7.11 shows the results from an AFM study on a polyurethane seal surface. To acquire the topography, an MFP-3D AFM (Courtesy of Prof. Todd Sulchek at Georgia Tech) was used in the "contact mode". AFM operates by scanning a tip attached to the end of a cantilever across the sample surface while monitoring the change in cantilever deflection with a split photodiode detector. The tip contacts the surface through the adsorbed fluid layer on the sample surface.

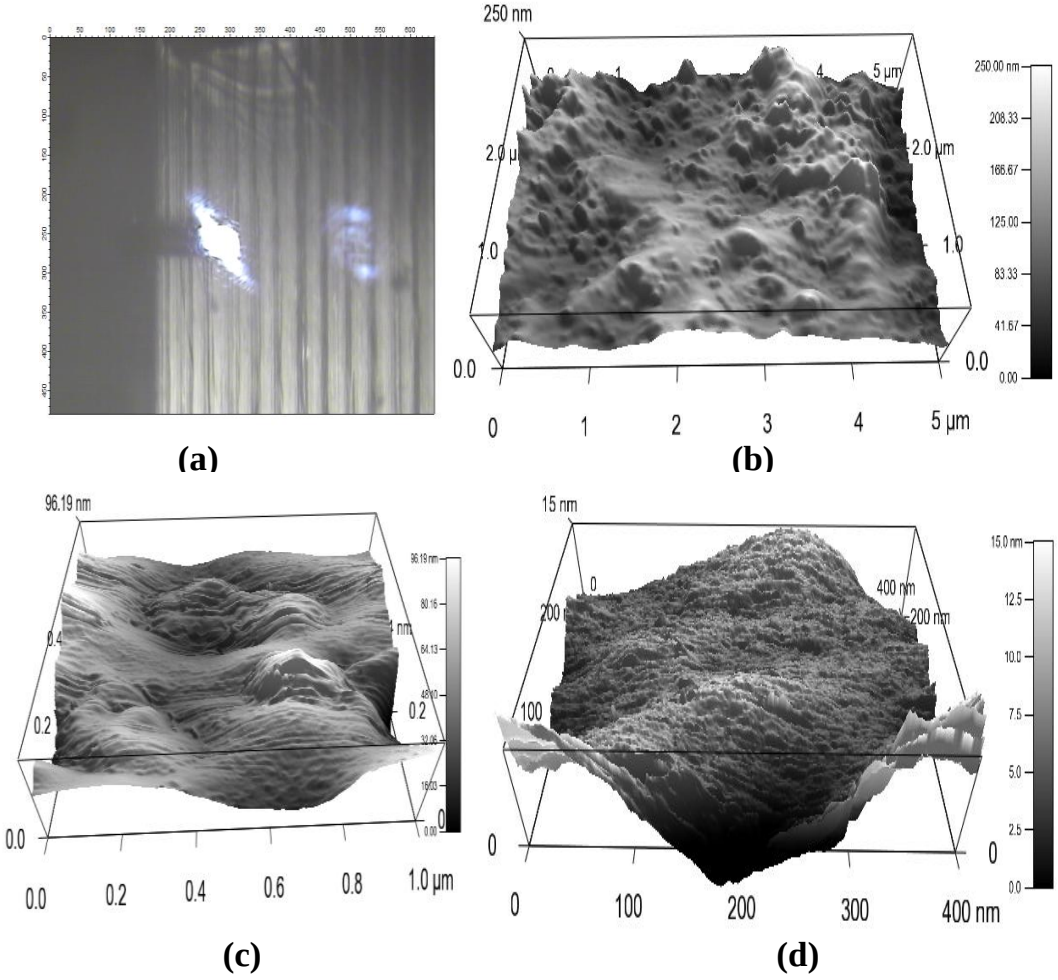

Figure 7.11: Atomic force microscopy of a polyurethane seal surface. (a) shows the seal surface and the cantilever tip over it. (b) through (d) show the topography of the same area scanned at different spatial resolutions.

A feedback loop maintains a constant deflection between the cantilever and the sample by vertically moving the scanner at each (x, y) data point to maintain a "set point" deflection. By maintaining a constant cantilever deflection, the force between the tip and the sample was maintained constant. The probe used was made of silicon nitride. For contact mode imaging, it is necessary to have a cantilever which is soft enough to be deflected by small forces and has a high enough resonant frequency to not be susceptible

to vibrational instabilities. The spring constant of the cantilever was 0.13 N/m. The seal surface and the probe cantilever over it is shown in Figure 7.11 (a). Parts (b),(c) and (d) show the scans performed at increasingly higher resolutions: $5\mu m \times 5\mu m$, $1\mu m \times 1\mu m$ and $400nm \times 400nm$ respectively, with a spatial resolution as low as $10nm$ and a vertical resolution as low as $1nm$. The images obtained are a good demonstration of "protuberance-on-protuberance" theory indicating various levels of roughness. The maximum asperity height observed at $400nm$ resolution was 15 nm.

7.2.2 Imagine Local Micro/Nano Scale Elastic Properties using AFM

After looking at the nano scale surface characteristics of the seal and the phase plot, next task was to actually scan the surface at this nano resolution and acquire the elastic properties at individual pixels. It was also of interest to see how the local elastic moduli vary with time from which the viscoelastic response of asperities, if any, can be extracted. For this purpose a modified Veeco-Multimode AFM was used in the "Tapping Mode". The experimental setup shown in Figure 7.12 is developed by Prof. Levent Degertekin's lab at Georgia Tech. The experimental data presented here was collected with the help of Ms. Zehra Parlak, a Ph.D student of Prof. Degertekin. Tapping mode AFM used here operates by scanning the probe attached to the end of an oscillating cantilever across the sample surface. The cantilever is oscillated near its resonance frequency with amplitude ranging from 20 nm to 100 nm. The tip lightly taps on the sample surface during scanning, contacting the surface at the bottom of its swing. The feedback loop maintains constant oscillation amplitude by maintaining a constant RMS of the oscillation signal acquired by the split photodiode detector.

Figure 7.12: Atomic force microscopes (top) used for imaging local micro/nano scale viscoelastic properties of seal surfaces. Also shown is the cantilever driving and data acquisition circuit (bottom left) and a seal sample used (bottom right). (AFM setup from the lab of Prof. Levent Degertekin at Georgia Tech.)

To obtain material properties dynamically, the sample is vibrated such that both the attractive and repulsive parts of the interaction force are experienced by the tip. RMS value of the measured tip displacement is used in the feedback circuitry. A version of this method is described in detail in [103]. This tapping method provides the time resolved interaction force (TRIF) signal for each tap. During TRIF measurements static tip–sample contact is avoided by selecting proper modulation amplitude and a set point value. By obtaining the interaction force at each point on the sample surface, and applying a proper interaction model, the local sample properties are extracted and images are formed.

If $F(t)$ is the time dependent value of TRIF signal, k is the stiffness of the cantilever, Z_1 is the peak amplitude of sinusoidal oscillation of the sample with ω as frequency and Z_0 is the rest position of the tip, then the tip-sample distance as a function of time is given by,

$$d(t) = Z_0 + Z_1 \cos(\omega t) + \frac{F(t)}{k} \tag{7.19}$$

By obtaining the interaction force $F(t)$ at each pixel on the sample, and applying a Hertzian or DMT (Derjaguin–Muller–Toporov) contact model [104] model, we can extract the material properties at each pixel of the sample. The experimental parameters used for out AFM material property imaging study are listed in Table 7.1.

Phase Imaging is also a powerful extension of tapping mode AFM that provides nanometer scale information about surface structure often not revealed by topography maps. By mapping the phase of the cantilever oscillation during the tapping mode scan,

phase imaging can detect variations in composition, adhesion, viscoelasticity , friction and capillary forces.

Table 7.1 : AFM experimental parameters for material property imaging.

Parameter	**Value**
Cantilever stiffness, k	25 N / m
Platinum tip radius, R_{tip}	15 nm
Excitation frequency, ω	2.02 kHz
Peak excitation amplitude	27 nm
Photo-diode sensitivity	55 mV/ nm
Sampling frequency, $1/\Delta t$	606.1 kHz

Such phase plots can then be used to identify the changes in micro/nano scale local material properties due to underlying layered materials, functionally graded seal surfaces, mapping of different components in composite materials like glass fibers or graphite embedded PTFE seals and differentiating regions of high and low surface adhesion and hardness. Figure 7.13 (a) shows the topography of a 5 micron x 5 micron polyurethane sample area obtained from the amplitude of the AFM tapping signal. Bright and dark areas correspond to peaks and valleys respectively. Part (b) shows the phase of the AFM signal on exact same area. It is interesting to note that some of the bright (higher amplitude) parts seen in the topography image have completely disappeared in the phase image. For example, the areas shown with red and blue circles in the topography image, both have same high topography. However those exact same areas, red and blue circles, in the phase image are completely different from each other. Red is with a high phase and blue is with a very low phase. This indicates that apparently similar looking 2 peaks in the topography map have very different local material properties. Red is probably much harder than the blue one. Also their viscoelastic relaxation would probably be very different from each other.

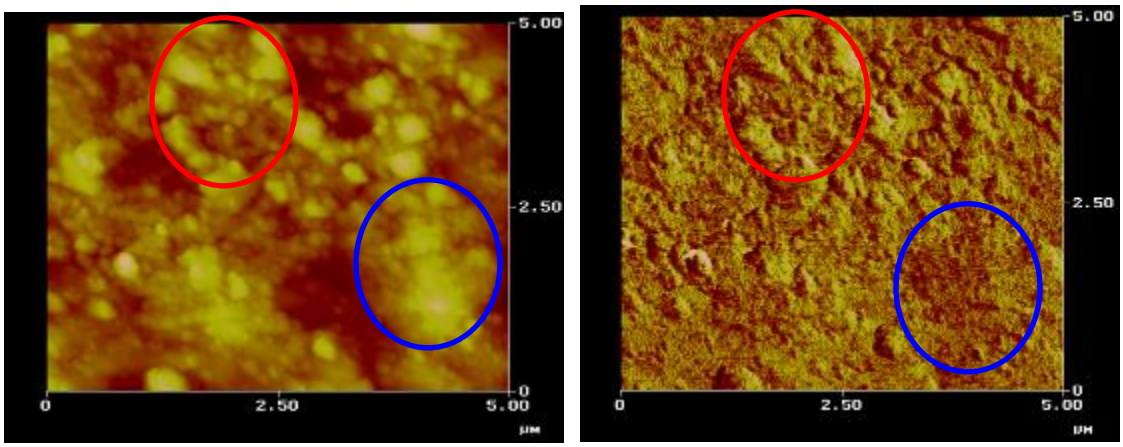

(a) **(b)**

Figure 7.13: Amplitude (a) of the AFM cantilever signal on seal sample shows the topography and phase (b) shows the variations in composition, adhesion and viscoelasticity.

Figure 7.14 shows the data obtained from a single tap at a material point on polyurethane seal sample. Z-piezo displacement, tip deflection (from which TRIF is obtained by multiplying by cantilever stiffness, k) signals are plotted from which indentation of the tip into the material as a function of time is retrieved. The five time zones of the tapping process, namely, tip approach, jump to contact, contact , adhesion and tip retract are also indicated on the plot. Corresponding cantilever positions are shown schematically in the top part of the figure. It can be seen that at this particular material point, the tip indents the surface to a depth of 21 nm.

Figure 7.15 (top) shows the corresponding "force curve" obtained by plotting cantilever deflection vs Z-piezo displacement during extension and retraction process of the tip. It can be seen that during the contact period (left of dotted vertical line) the deflection curves during extension and retract are almost overlapping, indicating that there are no viscoelastic losses during contact at this particular location. However in the

bottom plot of the figure (which was obtained at a different sample point), it can be seen that the curves during extension and retraction do not match during the contact period.

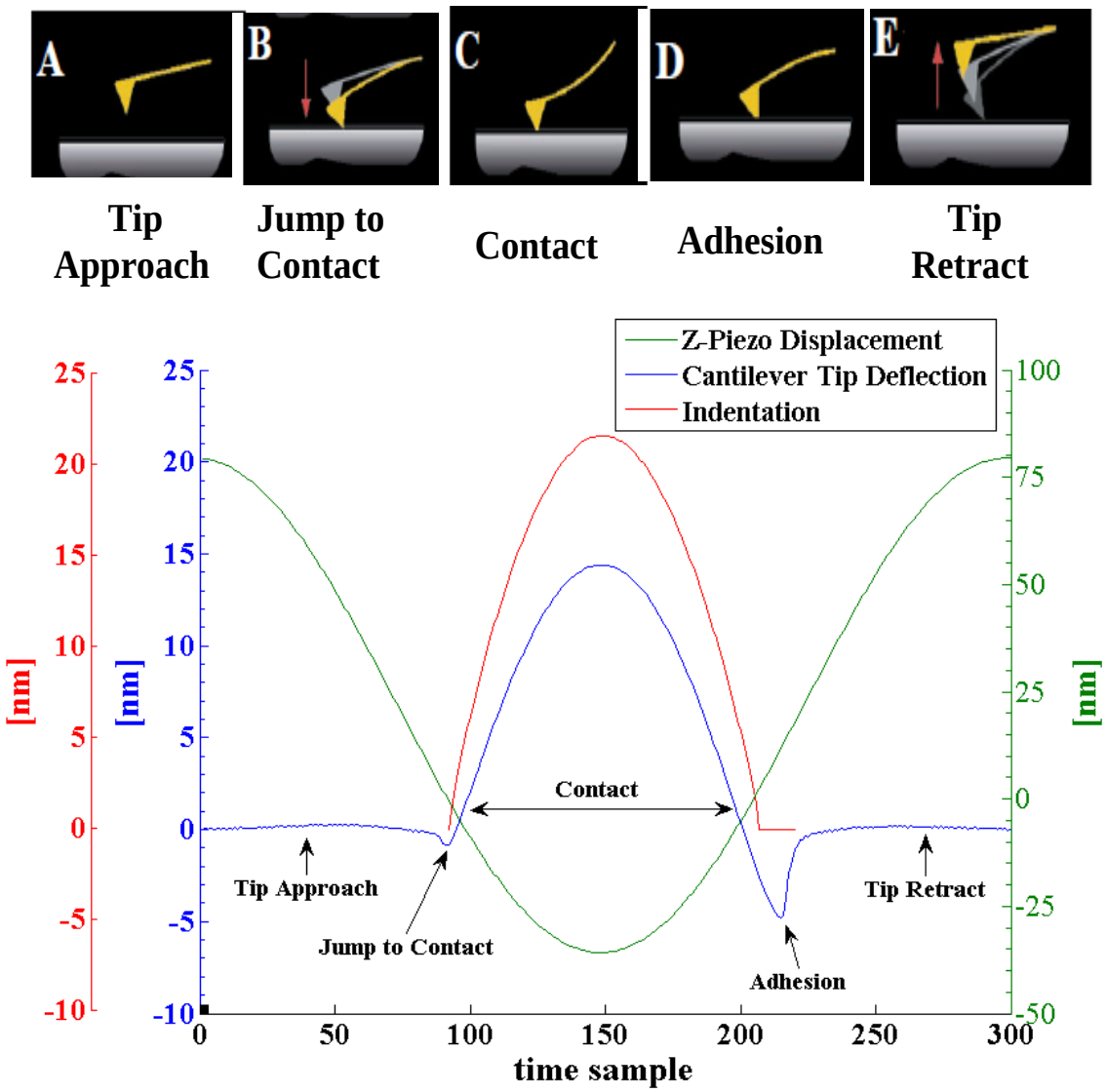

Figure 7.14: AFM tapping mode signals on polyurethane seal sample showing how the TRIF curves are extracted.

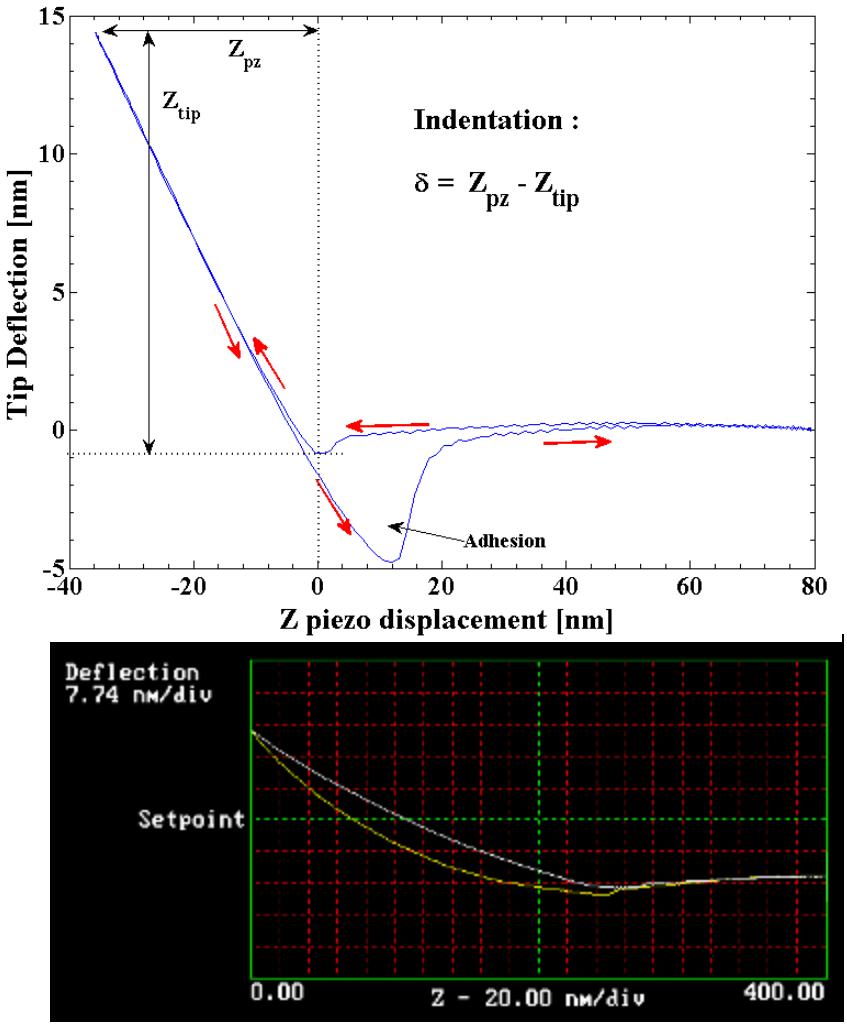

Figure 7.15: AFM cantilever tip deflection vs Z-piezo displacement at two different sample locations. Top showing no viscoelasticity, bottom showing viscoelastic losses.

This difference is attributed to the viscoelastic losses during contact period. It can also be seen in the top plot that there are strong "adhesive" forces during the retraction process as seen from the large dip that accounts for almost 33 % of the forces during contact. Such large adhesion is an important new finding about seal's contact surface. Although, such adhesion has been often observed in rubber, it has not yet been experimentally characterized for polymeric seal surfaces. These force curves again

provide us the value of indentation δ from which elastic modulus can be calculated using Hertzian or advanced contact theories like DMT.

Figure 7.16 shows the time resolved interaction force signals extracted at various sample locations. The slopes of these curves give us the information about stiffness of the material, the dips at two time locations (one close to 0.125 ms and other close to 0.375 ms) provide us the information about the magnitudes of capillary and adhesive forces and the hysteresis during the contact process. The width of the contact peak quantifies the contact duration for each contact and the differences in contact times for different spatial locations. For example, comparing the red and blue curves, it can be seen that the red point has 21 % higher peak contact force but 0.04 ms shorter duration of contact. This indicates that the material point indicated by red curve is much stiffer with a larger local elastic modulus than the material point of blue curve which is locally softer. In general, a softer material point will produce a much "broader" curvature of TRIF signal when compared to a stiff material point. This information on contact durations is also very valuable in understanding the differences in viscoelastic relaxation time scales of different surface asperities, which in turn will change the local micro-scale viscoelastic contact mechanics.

Once the time resolved interaction force signal is obtained, the local elastic modulus is obtained by using the contact theories. Using Hertzian theory for contact between a spherical tip and a elastic half space, we can write,

$$F_{contact} = \frac{4}{3} E^* R_{tip}^{1/2} \delta^{3/2} \tag{7.20}$$

where, $F_{contact}$ is the contact force, E^* is the reduced modulus, R_{tip} is the tip radius and δ is the indentation depth. From this we get the local elasticity of a material point, E_m as,

$$E^* = \left[\frac{1-\upsilon_{tip}^{\ 2}}{E_{tip}} + \frac{1-\upsilon_m^{\ 2}}{E_m}\right]^{-1} = \frac{3}{4}\frac{F_{contact}}{R_{tip}^{\ 1/2}\delta^{3/2}}$$

$$\rightarrow E_m = \frac{1-\upsilon_m^{\ 2}}{\left[\frac{4}{3}\frac{R_{tip}^{\ 1/2}\delta^{3/2}}{F_{contact}} - \frac{1-\upsilon_{tip}^{\ 2}}{E_{tip}}\right]} \tag{7.21}$$

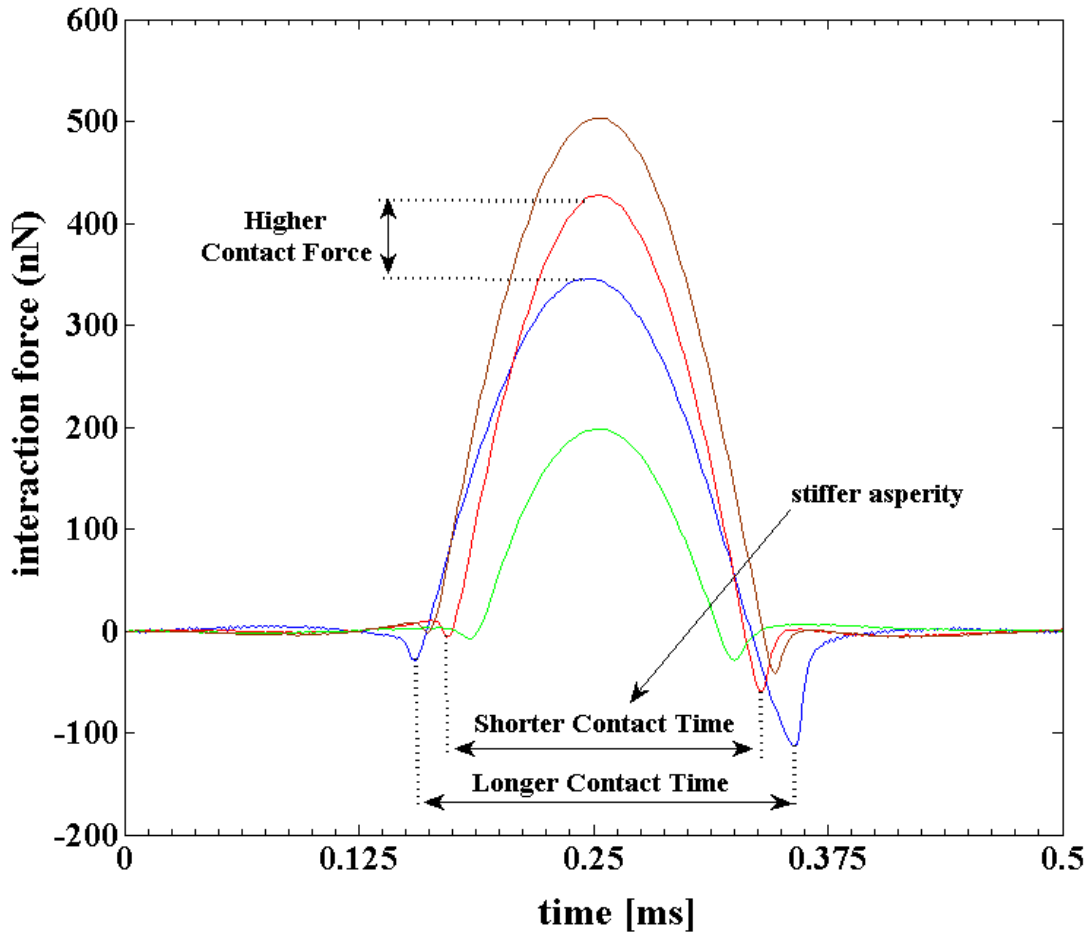

Figure 7.16: Time resolved interaction force curves at various sample locations indicate that some asperities are stiffer than the others and they have different viscoelastic responses than the others.

The values of AFM tip parameters are: $R_{tip} = 15\,nm$, $E_{tip} = 130\,GPa$, $\upsilon_{tip} = 0.27$ and $F_{contact}$ and δ are obtained from force curve plots shown earlier. In this way, the local elastic moduli were obtained for each individual material point on the sample.

More sophisticated contact theory like DMT model and taking into account the long-range attractive forces due to charge on AFM tip (Patch-charge model [105]) results in:

$$F_{contact} = \begin{cases} \dfrac{-4\pi\gamma R_{tip}}{\left(1 + d / Z_q\right)^2} & d \geq 0 \\ E^* \sqrt{R_{tip}} \left(-d\right)^{3/2} - 4\pi\gamma R_{tip} & d < 0 \end{cases} \tag{7.22}$$

where γ is the surface energy , d is the tip-sample distance and Z_q is the distance from the charge to the tip. The local elasticity can then be obtained by minimizing the error between expected and observed transient force signals as described in [103],

$$Error = \frac{\int \left| E^* \sqrt{R_{tip}} \left| d \right|^{3/2} + F_{pull} - F_{contact}\left(t\right) \right|}{\int \left| F_{contact}\left(t\right) \right|} \tag{7.23}$$

The results in Figure 7.17 and Figure 7.18 are obtained using this error minimization method.

There are some limitations, however, of the above models, e.g. they can not account for differences in adhesion between approach and retraction phases of indentation. Also, some can argue that the differences in measurements from one sampling point to the next are more due to changes in surface energy than due to changes in elastic modulus. However, the modulus measured by fitting the Hertzian model gives us the "effective" modulus at the surface as "seen" by the indenter and since our micro-contact model is based on Hertzian theory, this "effective modulus as seen by the

approaching rod surface" is what we are interested in and hence the method used here gives us a sufficiently accurate description of the elastic properties of the surface for our purpose.

Figure 7.17 shows sample results obtained from AFM taps on a 3 micron x 2 micron polyurethane seal surface. Part (b) shows 2D color indexed image plot showing the local elastic modulus at each pixel. A couple of horizontal edges that appear in the plot are from the fact that to map the entire area, the tapping had to be stopped and restarted 6 times. Each re-start began at the same material point where the last scan had stopped. Also, the darkest blue area corresponds to the regions where data could not be obtained with confidence. Other than this, the rest of the area seems to have preserved the continuity quite well. A 3D surface plot of the same data is shown in part (d) of the figure.

Looking at these plots, it immediately appears that the local elastic modulus varies significantly from one surface point to the next, especially outside ~1 micron radius. Another important observation is that the magnitudes of local nano-scale elastic moduli of polyurethane seal surface are much higher than the elastic modulus of bulk of the material (43 MPa). The local modulus at some pixels reaches as high as 3000 MPa. It is thought that these points correspond to the ones having underlying hard filler materials like glass fibers or brass particles. Although, most of the area has modulus between 500-700 MPa, there are some homogeneous regions with moduli between 1000-1500 MPa and some scattered much stiffer points. This is a very surprising finding which shows that local nano-scale elastic properties of seal surfaces can vary within two orders of magnitude from that of the bulk of the polymer, which is against the common belief in

the seal literature that normally assumes similar elastic moduli for macro-mechanics and micro-mechanics.

Figure 7.17 (a) shows the topography image of the same 3 micron x 2 micron area of which the elastic properties were mapped. Part (c) shows the 3D surface plot of the same topography data. Another observation that comes through by comparing plot (c) with plot (d) is that the topography and elastic properties of asperities are not correlated. Some asperity peaks are much softer than the others. Also there are some regions between the asperities that are much stiffer than the asperities themselves. These observations show that the polymeric seal asperities will respond to micro scale contact pressures very differently than what is thought in the literature. In addition to the effects from the surface roughness and directionality of the roughness, there will be differences in elastic / viscoelastic response of asperities due the inhomogeneity in the elastic properties at micro/nano scale.

So far we have seen the variation in the time averaged local elastic properties of seal asperities. The next objective was to see how the elastic modulus of each asperity changes with time, if there are any signs of nano-scale viscoelastic relaxation and if yes are the relaxation time scales similar for all the asperities. In the micro-scale asperity contact model developed in chapter 6 we had assumed the same viscoelastic relaxation time constants as that of the bulk polyurethane. As an improvement to this model, it is of interest to experimentally characterize the micro-scale viscoelasticity of asperities and extract the instantaneous moduli and relaxation time constants associated with individual asperities. With this in mind, the transient interaction force signals were used to extract the time variation of elastic modulus at each of the 16384 material points.

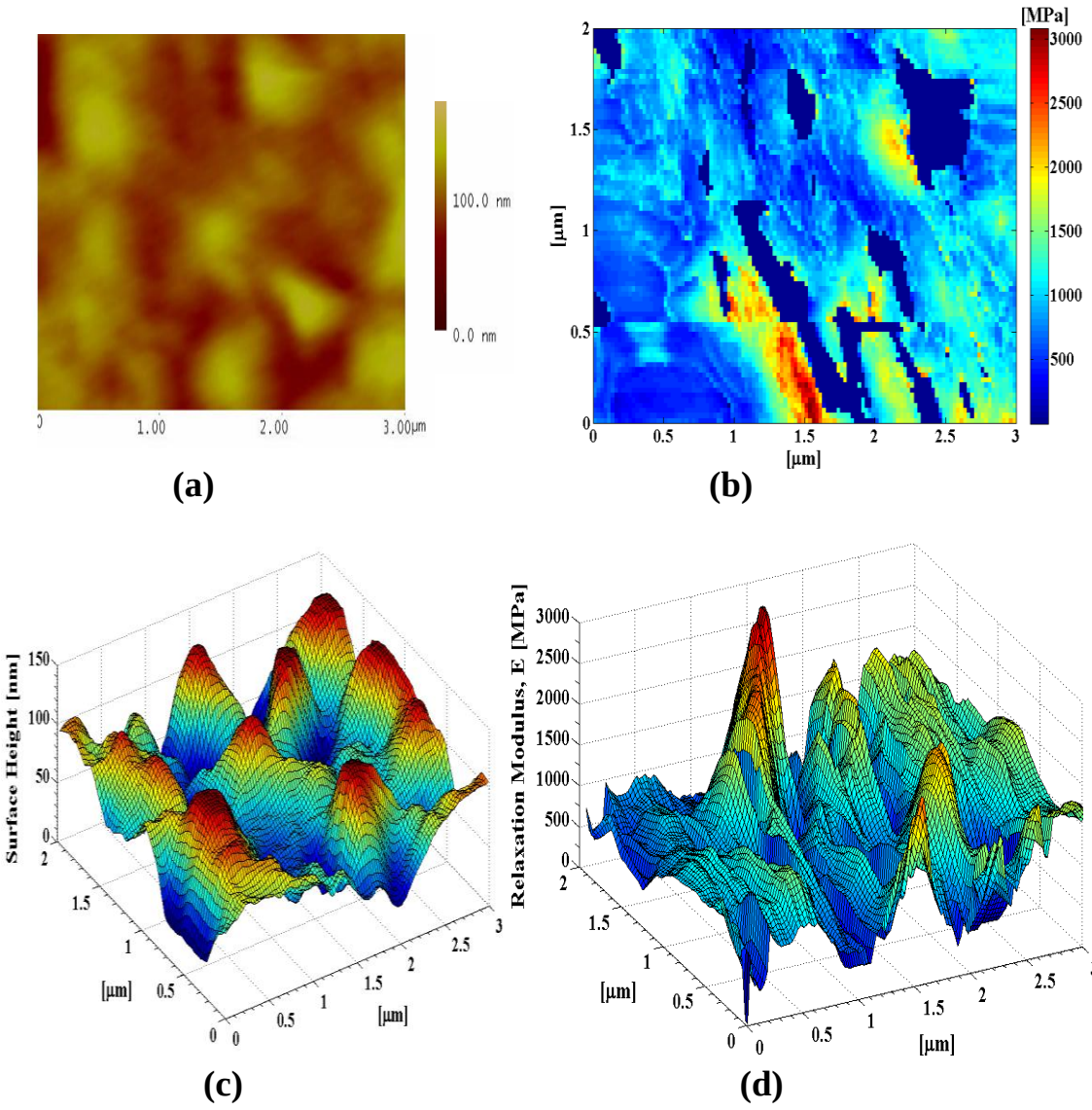

Figure 7.17: Nano-Scale topography [(a) and (c)] and elasticity [(b) and (d)] maps of a polyurethane seal surface obtained using Tapping Mode of AFM. Both, the topography and elasticity maps are of the exact same 2 micron x 3 micron sample area.

Figure 7.18 shows the results from this extraction at some representative locations. The modulus is plotted as a function of indentation, which in turn is a function of time. If the asperities were perfectly elastic (no stress relaxation), then these curves would be lines almost parallel to the abscissa as the elastic modulus would remain fairly constant with indentation. However the modulus dropping with indentation (and hence

with time) is an indication of the viscoelastic relaxation of the polyurethane asperities.

Figure 7.18 top plot shows the curves tracked at relatively soft sample locations (observed from elasticity map) and bottom plot shows the curves at relatively stiffer sample locations. It can be seen from the slopes of these curves that the viscoelastic relaxation time scales for these asperities are very different from each other. The blue asperities at both the soft and the stiff locations have much smaller relaxation time constants than the red asperities. Also, in the same relaxation time range, the red asperity has higher instantaneous elastic modulus than the green asperity and the black asperity. From these observations it becomes apparent that the micro/nano scale viscoelastic response of the polymer surface asperities differs from asperity to asperity. Some asperities have much higher instantaneous moduli than the others while some asperities have smaller relaxation time constants than the others. The relaxation spectrum of individual asperities would look very different from each other. From the plot of elastic modulus vs time, the Prony series coefficients needed for the micro-contact mechanics model can be extracted using the optimization method discussed in section 7.1.2.2.

These observations is a proof of concept that the micro/nano scale spatially and temporally varying elastic modulus of polymer seal surface asperities can be effectively extracted. From this, the viscoelastic parameters can be obtained using the algorithms described in section 7.1.2.2. These viscoelastic parameters can then be used in the micro-contact mechanics algorithm of chapter 6 to estimate the average time dependent contact pressure due to all the asperities. Understanding the nano-scale elastic and viscoelastic properties of seal asperities and variations in their response to applied pressures is a valuable addition to the fundamental understanding of multi-scale sealing dynamics.

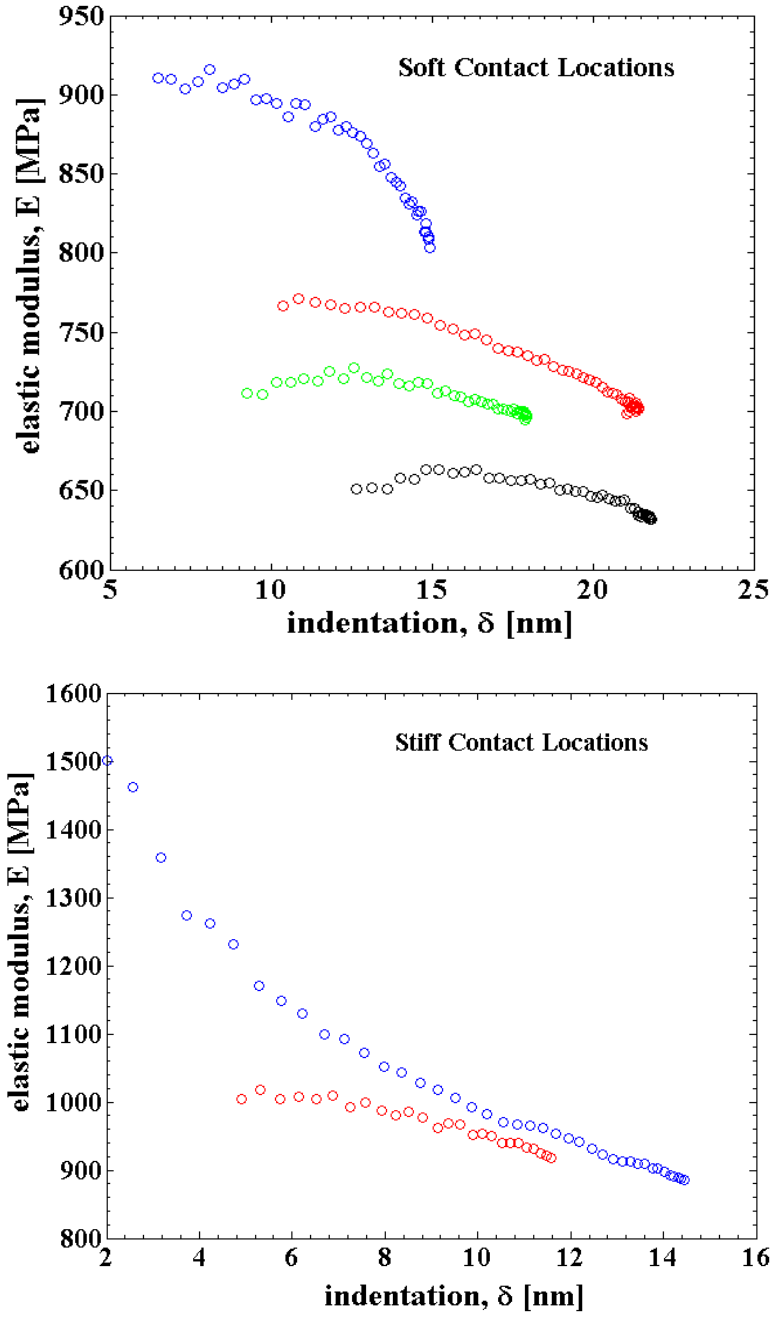

Figure 7.18: Variation of elastic modulus with indentation (hence time) obtained at various soft (top) and stiff (bottom) locations on polyurethane seal sample. The drop in elastic modulus indicates the nano scale viscoelastic response of the asperities.

CHAPTER 8. EFFECT OF VISCOELASTICITY ON HIGH PRESSURE - HIGH FREQUENCY SEALING APPLICATIONS

The sealing applications studied in the previous chapters were mainly in the field of injection molding. The typical cycle times for them are tens of seconds and stroke lengths are few meters. The sealing pressures are typically less than 2000 psi (~14 MPa). There are several hydraulic sealing applications which consist of much higher cycle frequencies and shorter strokes. Hydraulic pistons in excavators, drilling actuators, food processing equipments and automotive plants are some of these applications. Also, the operating pressures are much higher (3000 psi or higher). With this in mind, the next step of the current study was to use the MSMP framework developed to analyze the performance of short stroke, high frequency, high pressure sealing applications. With high cycle frequencies it is expected that the viscoelastic seal would get much lesser time to relax after the high pressure period ends and the seal may not be able to come to its base state before the beginning of the next cycle. This would cause the build-up of viscoelastic lag between applied stress and corresponding seal deformations and the seal performance may be quite different from cycle to cycle. Looking at the current seal literature, no existing model seems to have the capability to predict such performance differences from one cycle to the next that can be attributed only to the "material memory" and hence studying the effect of viscoelasticity on such high frequency dynamic sealing applications is thought to be a valuable addition to the field. Considering this, study of the effect of viscoelasticity on high frequency, high pressure sealing applications is the focus of this chapter.

8.1 High Frequency, High Pressure Dynamic Sealing Application

8.1.1 Deformation Mechanics and Secondary Contact

Figure 8.1 shows the time variation of sealed pressure and rod velocity in a short stroke, high frequency sealing application. The two cycles are shown where each cycle is 1.5 sec in duration. Here instroke is the primary "active" stroke while during outstroke the operating pressure is held at ambient value. Sealed pressure reaches a maximum value of 20.7 MPa at 0.27 sec, stays constant at this value until 0.63 sec and then drops rapidly to the ambient value at 0.75 sec. The maximum rod velocity reaches unto 72 cm/s during both instroke and outstroke. The sign convention is consistent with the positive direction for outstroke and negative direction for instroke as earlier.

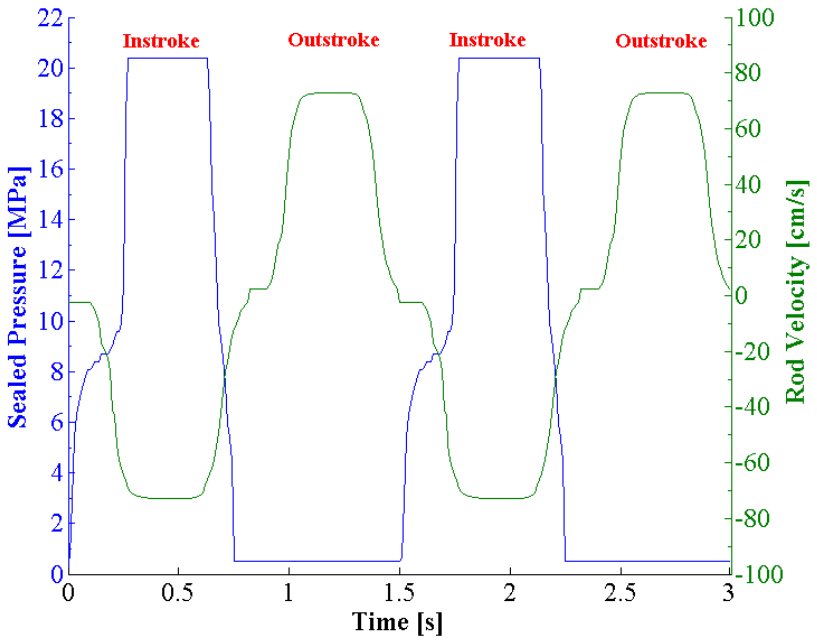

Figure 8.1: Sealed pressure and rod velocity history during 2 cycles of high pressure, high frequency sealing application.

Figure 8.2 shows the deformed seal geometries and von-Mises stress distribution in the seal body at various time instances. Configurations in (a), (c) and (d) all have same value of sealed pressure = 7.5 MPa, still their deformations are quite different. This is a result of viscoelastic lag associated with the seal material. For (a) the sealing pressure is still to reach its maximum value of 20.7 MPa and hence the deformations are moderate. At the end of the high operating pressure (20.7 MPa) period, the seal has deformed substantially and a "secondary" contact has occurred between the rear side of the seal and the rod (part (b) of the figure). This secondary contact was not observed in the analyses discussed in chapter 5 and is a consequence of much higher operating pressures here. From 0.63 sec to 0.71 sec operating pressure drops sharply to back again to 7.5 MPa as in case (a), however the seal's sluggish viscoelastic response does not allow seal to respond fast enough to this drop and the seal is still in a greater deformed state (c) than in (a). From the narrow gap between rear side of seal and the surface of the rod, it can be seen that the secondary contact has vanished, however the sealing zone length in (c) (1.7 mm) is still much larger than the sealing zone length in (a) (2.5 mm). Part (d) of the figure shows the seal at 2.21 sec which is towards the end of the second instroke period. The sealed pressure again is at 7.5 MPa, same as that in (a) and (b), but the deformation of the seal is larger than that in (b) and much larger than that in (a). Also, it can be seen that the secondary contact is present at this time which was not observed in (a) or (b). The stress distribution is also very different than that in (a). Comparing (a),(b) and (c) , it is evident that during such high pressure, high frequency sealing applications, viscoelasticity can induce significant differences in seal configurations, stress field and sealing zone lengths from cycle to cycle.

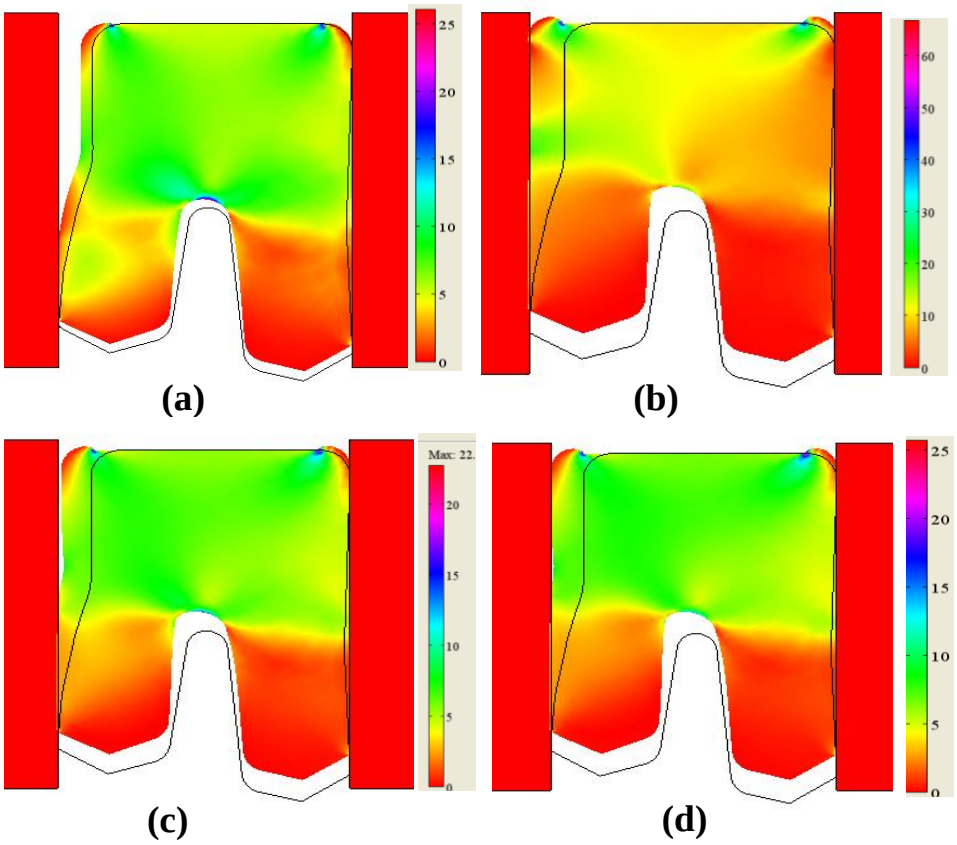

Figure 8.2: Deformed seal configurations and von Mises stress field in the seal body at various time instances. (a) t = 0.07 sec, P_sealed = 7.5 MPa (b) t = 0.6 sec, P_sealed = 20.7 MPa (c) t = 0.71 sec, P_sealed = 7.5 MPa (d) t = 2.21 sec, P_sealed = 7.5 MPa.

Figure 8.3 (a) shows the sealing zone length for the 2 cycles of operation. It can be seen that the secondary contact occurs at 0.27 sec and the sealing zone length shows a jump from 2.7 mm at 0.26 sec to 5.4 mm at 0.27 sec for the first cycle and from 2.53 mm at 1.76 sec to 5.4 mm at 1.77 sec for the second cycle. During the ambient pressure period of outstroke (0.76 sec to 1.5 sec and 2.26 sec to 3 sec) , the seal shows viscoelastic relaxation as the seal slowly tries to return to its base state (but does not reach there during the given period) as seen from the gradual decay in sealing zone length.

8.1.2 Effect of Viscoelastic Creep on Dry Contact Pressures

The effect of secondary contact on sealing becomes evident from the dry contact pressure distributions as observed in Figure 8.3 (b). Please note that these distributions are normalized by their respective sealing zone lengths (different for different distributions). At t = 0.09, 0.24 and 0.26 sec the seal has only primary (lip) contact with the rod and the dry contact pressure distributions are similar to those seen in chapter 5. As the seal jumps to secondary contact at t = 0.27 sec, the pressure distributions at t = 0.39, 0.49 and 0.59 sec all show two distinct high pressure regions, one over the primary contact area (left side of the plot) and other over the secondary contact area (right side) with a low pressure region connecting them. The low pressure region corresponds to the change in geometrical slope going from the lip region to the rear side of the seal. This change in slope causes this connecting region to be farther away from the rod surface than the lip and the rear part of the seal and hence produces smaller contact pressures than the primary and secondary contact regions.

It was a surprising finding to see the dry contact pressure in the secondary contact area increase from t = 0.39 sec to t = 0.49 sec to t = 59 sec while the operating pressure is held constant at 20.7 MPa. This increase in contact pressure is thought to be arising from the creep in the seal body at constant applied stress (constant sealed pressure). With the boundaries of the seal constrained between housing and the rod, the material points have nowhere to go but to push against the rod surface and this generates higher pressures at the sealing edge. These creep induced pressures then cause the dry contact pressure in the sealing zone to rise as the time passes from t = 0.27 sec to t = 0.59 sec.

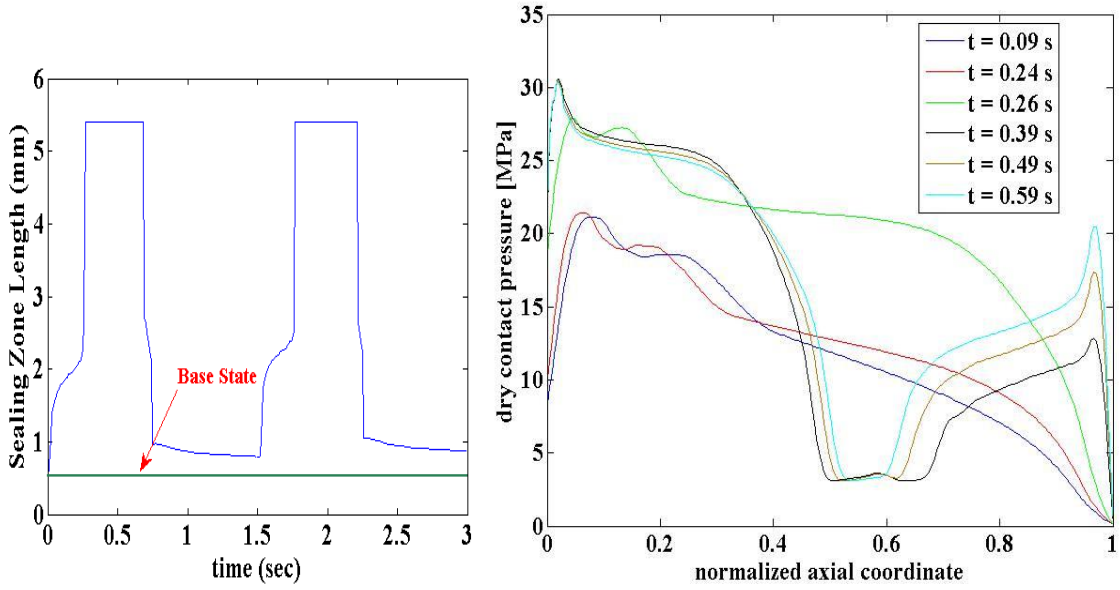

Figure 8.3: (a) Sealing zone length for 2 cycles. (b) Dry contact pressure distributions during outstroke of 1st cycle.

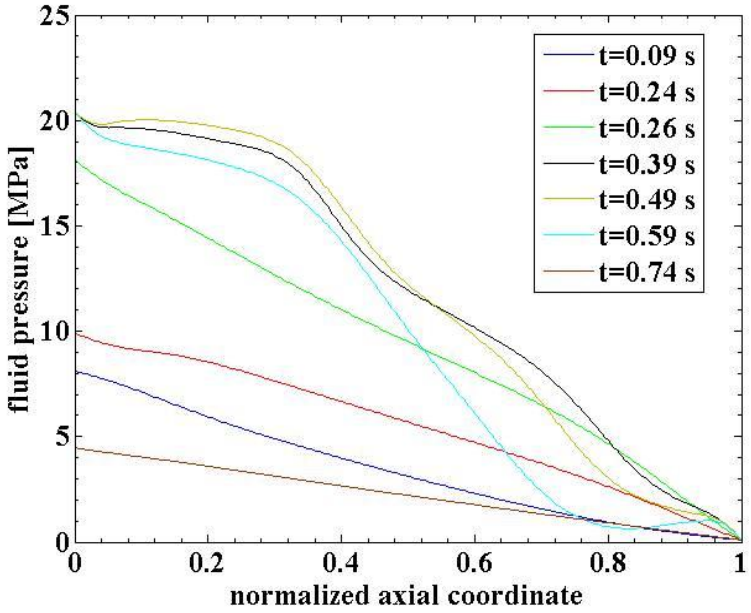

Figure 8.4: Fluid pressure distribution during instroke of 1st cycle.

The secondary contact and the viscoelasticity induced increase in the dry contact pressures (in secondary contact) are two key characteristics of the high pressure, high frequency sealing dynamics.

8.1.3 Effect on Fluid Pressure, Contact Pressure and Film Thickness

Figure 8.4 shows the fluid pressure distribution during instroke of the 1st cycle. As discussed in chapter 6, the transient fluid pressure distribution is governed by a complex dependence on the hydrodynamic effects produced by the changing rod velocity, the boundary condition effects produced by the changing sealed pressure, and the effects on the film thickness produced by the changing sealed pressure acting on the cup side of the seal lip. It can be seen that at t = 0.09s, the sealed pressure boundary condition is the primary factor deciding the fluid pressure distribution as the rod velocity is minimal and hence hydrodynamic effects are minimal and the distribution is close to linear. At t = 0.24 s onwards the hydrodynamic effects due to increased velocity become important and the distribution departs from linearity. Viscoelasticity causes the changes in the fluid pressure distribution resulting from deformation changes to be delayed while the direct effect of the sealed pressure acting as a boundary condition on the fluid pressure distribution is instantaneous as discussed previously. This is reflected in large increase in fluid pressures from time 0.09 s to 0.26 s.

Time instances t = 0.39 s, 0.49 s and 0.59 s have the exact same sealed pressure and rod velocity values and in the absence of viscoelasticity, fluid pressure distributions at these times would have shown very little differences (only arising from squeeze term in Reynolds equation). However, from the figure it can be see that although all of them

have same boundary value at fluid end (20.7 MPa), they differ significantly in the 50 % of the region away from the sealed end. Investigation of this phenomenon finds its roots in the contact pressure distribution at these time instances as shown in Figure 8.6. It can be seen that the dynamic contact pressures at t = 0.59 s in the secondary contact area is larger than that at t = 0.49 s which in turn is larger than t = 0.39 s. The reason for this increase in contact pressures is discussed below.

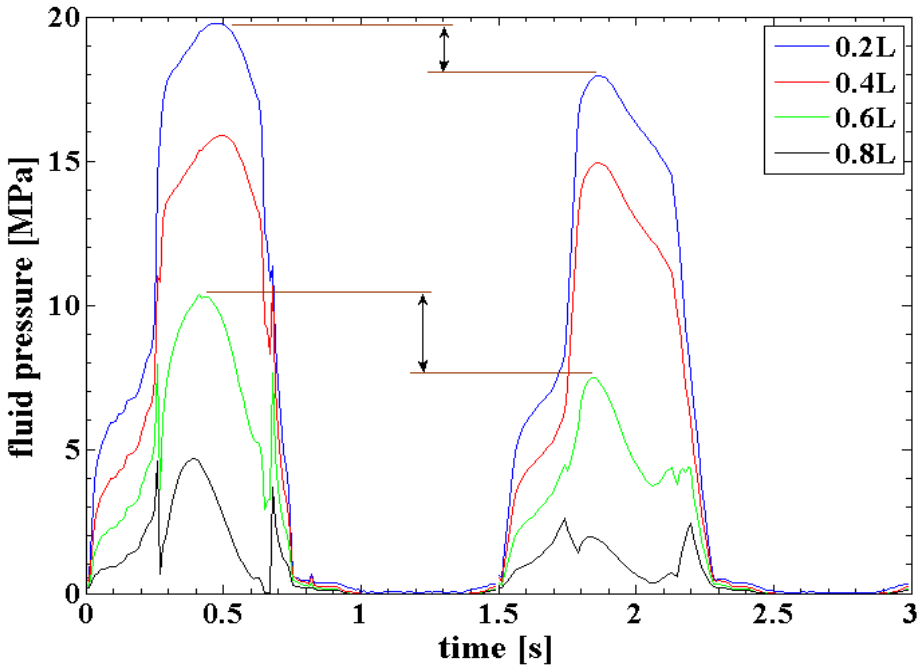

Figure 8.5: Fluid pressure history at four different locations along sealing zone.

Figure 8.5 shows the fluid pressure history at four key locations along the sealing zone during the 2 cycles. It becomes evident that there exist significant differences, both, in magnitude and in profile of fluid pressure in going from one cycle to the next. The fluid pressures during second cycle are ~ 10% lower than the first cycle in the region closer to the sealed end and ~26 % lower in regions closer to the air side. These

differences arise from viscoelastic nature of seal's response to applied pressure and rod velocity and could not have been predicted without the current comprehensive MSMP framework. The effect of viscoelastic decay can further be seen from the slope of the fluid pressure profiles in 1.87 s to 2.13 s period.

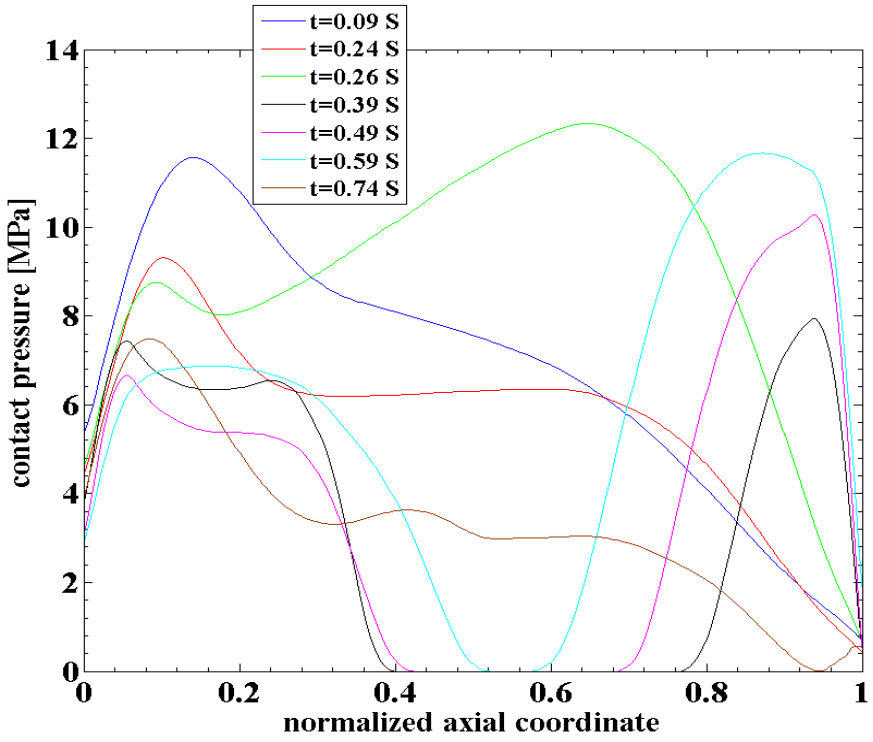

Figure 8.6: Contact pressure distribution during instroke of 1st cycle.

Figure 8.6 shows the contact pressure distributions during instroke of the 1st cycle. The characteristics of dry contact pressure are reflected in dynamic contact pressures as well. For t = 0.39s , 0.49 s and 0.59 s, two distinct regions corresponding to primary and secondary contact can be observed in contact pressure distributions. In the nearest 20% region of the primary contact area (left side of the plot), increasing fluid pressures cause the contact pressures to drop as we go from t = 0.09 s to t = 0.49 s. This is the region that

is primarily governed by sealed pressure boundary condition as discussed previously. However, in the secondary contact region (right side of the plot), increasing dry contact pressures (viscoelastic creep induced) produce large increase in the dynamic contact pressure as we go from t = 0.39 s to t = 0.49 s to t =0.59 s. The sealed pressure and rod velocity is constant during this time period and hence creep induced increase (as discussed earlier in reference to Figure 8.3 (b)) in dry contact pressure is the dominant factor in increasing dynamic contact pressure distribution in the secondary contact area during this time period.

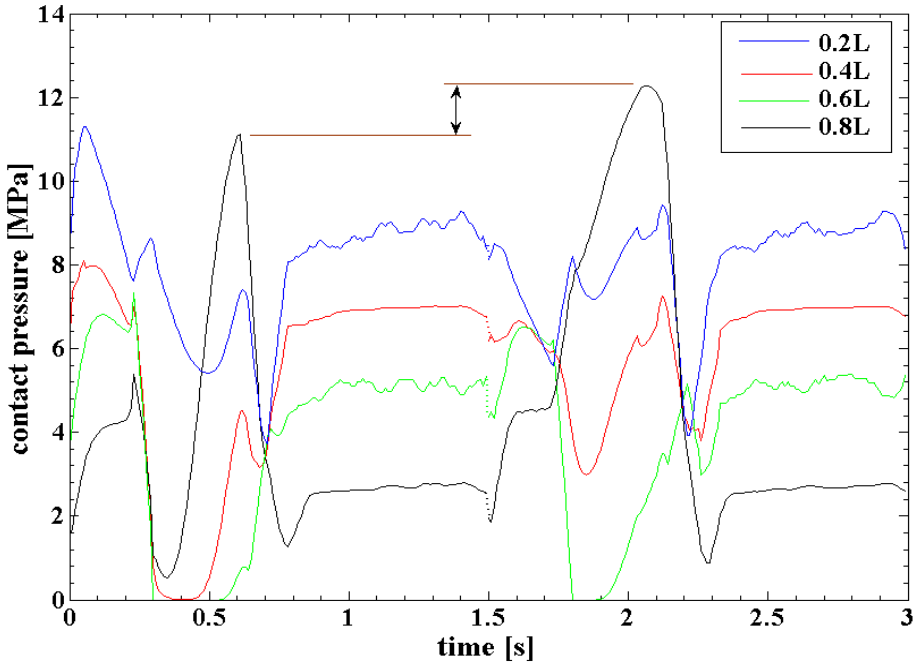

Figure 8.7: Contact pressure history at four different locations along sealing zone.

Figure 8.7 shows the history of the contact pressure at four key locations along the sealing zone. Again, the differences in contact characteristics between the two cycles can be seen from these profiles. The contact pressure history in this region looks very

different from the rest of the curves due to the presence of the secondary contact which increases the contact pressures in this region during 0.27-0.68 sec and 1.77-2.21 sec period significantly. Also, the contact pressures in this region during the 2nd instroke are larger than those in the same region during 1st instroke. This is an indication of the accumulation of creep at constant operating pressure in going from one cycle to the next, which causes an increase in the creep-induced contact pressure. Such a rise in contact pressures can cause significant differences in frictional characteristics from one cycle to the next and is of much interest for designing better seals.

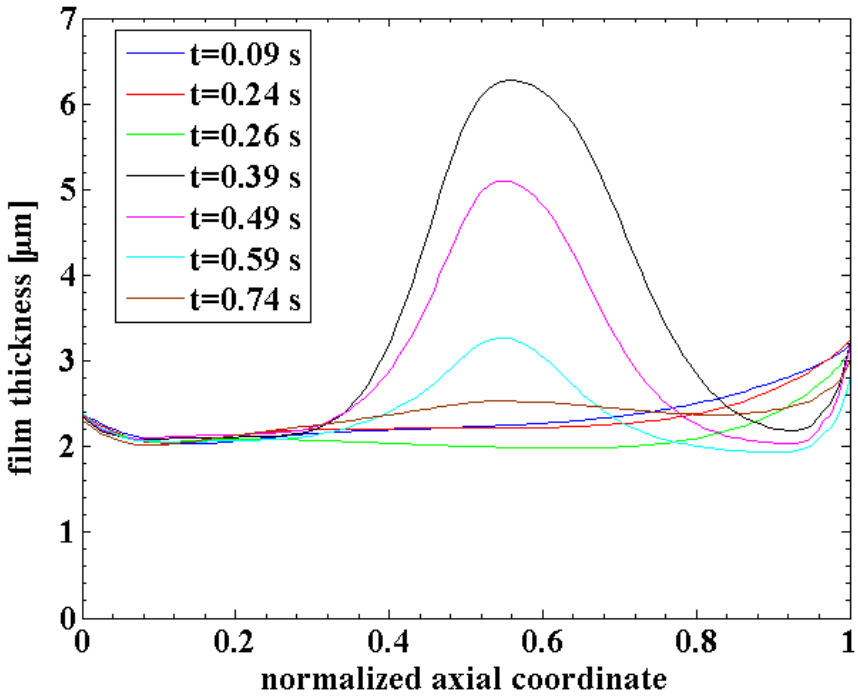

Figure 8.8: Film thickness distribution during instroke of 1st cycle.

Characteristics of fluid pressure and contact pressure distributions are further reflected in the film thickness distribution during instroke, as shown in Figure 8.8. A

large bell shaped rise observed between the 40% to 70% region of the sealing zone is a new characteristic that was not observed earlier at the low operating pressures (chapters 5, 6). This bell shaped profile is a consequence of the occurrence of the secondary contact and corresponds to the change in slope of the seal profile in going from lip region to the rear seal region, which increases the film thickness due to the "lift off". This is consistent with the low dry contact pressures observed in the same region in Figure 8.3 (b).

Since the sealed pressure is held constant at ambient value during outstroke, the viscoelastic effect on fluid pressure, contact pressure and film thickness distributions are not significant. The outstroke period mainly acts as a "relaxation period" for the seal to try to come back to its base state as seen from the sealing zone length history of Figure 8.3 (a).

8.1.4 Effect on Poiseuille Flow, Fluid Transport and Leakage

Figure 8.9 shows the total flow rate as well as the flow rate components vs time during the 2 cycles of operation. To be consistent, the same sign convention as used in the previous chapters (outstroke: positive velocity, instroke: negative velocity) is used here. The shape of the total flow rate profile is similar to that of the rod velocity profile which may give a false indication that Couette flow is the only major component of flow. However after decomposing flow rate into its Poiseuille and Couette components, it can be seen that during instroke of 1^{st} cycle, Poiseuille flow account for as much as 35 % of the total flow. This is a significant increase in Poiseuille flow that was not observed with linear elastic seal of chapter 5 or with the low-frequency seal operation of viscoelastic seal of chapter 6. This is one of the key findings from this model and demonstrates the

role of viscoelastic time scales on pressure driven flows through micro-channels of sealing zone as the strokes become shorter and frequencies become higher. This increase in pressure driven flow comes from the dependence of fluid pressure distributions on viscoelasticity of the seal, as discussed in chapter 6. Couette flow still remains the dominant component of the flow and demonstrates the viscoelastic decay in its profile during the instroke of both the 1st and the 2nd cycle. During the 2nd cycle however, the Poiseuille flow contribution diminishes and account to a maximum of 12 % of the total flow. This is a demonstration of change in sealing characteristics from cycle to cycle that arises due to viscoelastic nature of the seal material and has not been discussed in the literature before.

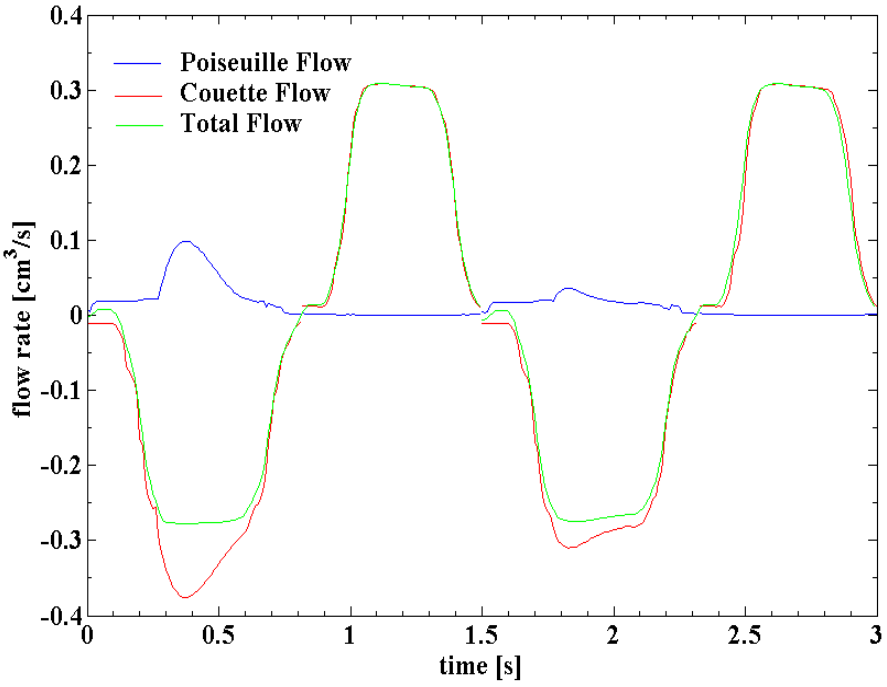

Figure 8.9: Flow rate (out of the cylinder) components vs time.

Figure 8.10 shows the net fluid transport out of the cylinder as a function of time. The negative sign seen for net fluid transport is a consequence of the consistent sign convention described earlier (negative sign for flow into the cylinder). The fluid transport into the cylinder increases during instroke and decreases during outstroke as expected from the discussion of chapter 5, 6. At the end of both the 1st cycle and the 2nd cycle, it has a negative value, indicating that there is no net leakage out of the cylinder. Hence with a 1.5 sec cycle time, this seal remains a non-leaking seal. From above discussion of flow decomposition and the discussion in chapter 6, it seems that due to the viscoelastic relaxation time scales associated with the seal material, a seal that is non-leaking for a particular frequency of operation may become leaking for a different operational frequency and stroke length. It is interesting to see the effect of viscoelasticity on leakage for different frequencies of operation and hence several such studies are performed with the current MSMP framework. These studies will be discussed in chapter 8.

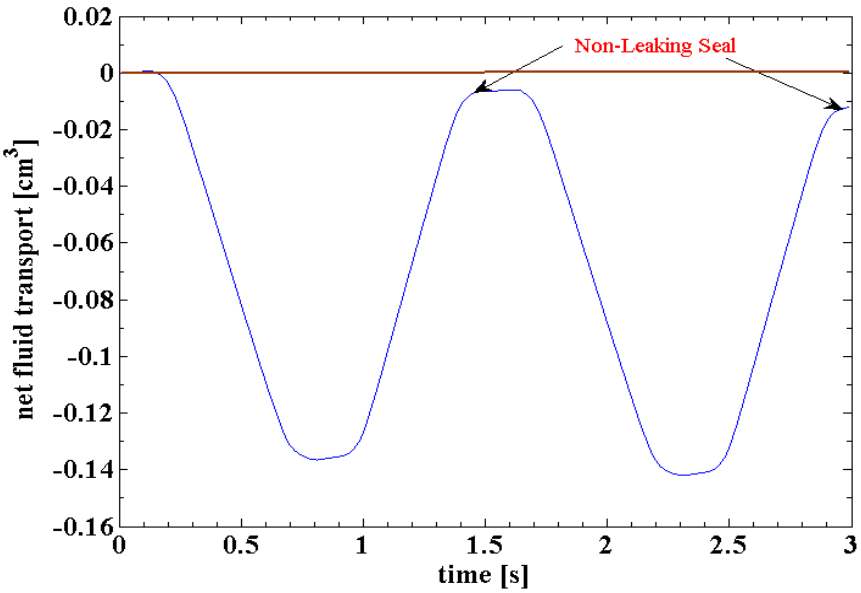

Figure 8.10: Net fluid transport out of the cylinder.

8.1.5 Effect on Shear and Friction Characteristics

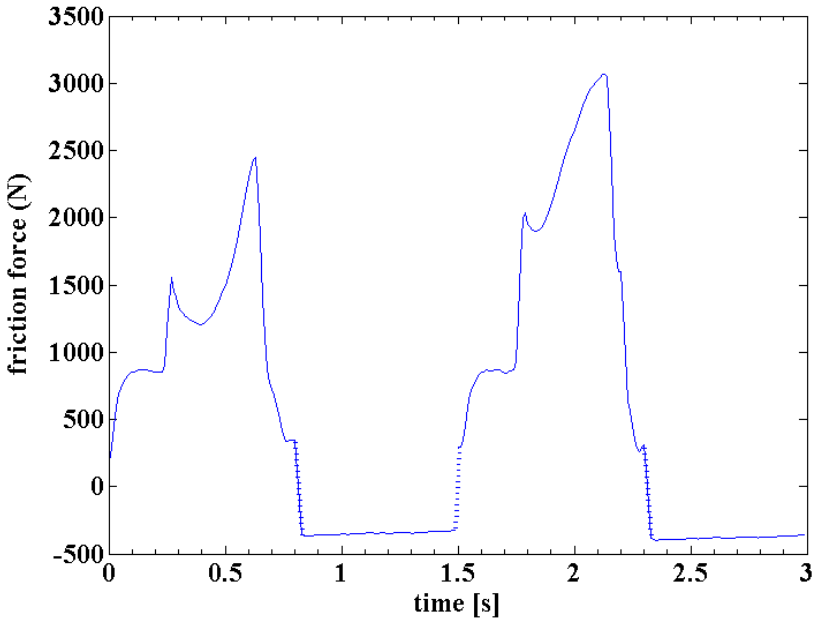

Figure 8.11: Friction force on the rod vs time.

Figure 8.11 shows the friction force on the rod vs time during the 2 cycles. It is evident that the frictional characteristics change significantly from one cycle to the next, with maximum friction increasing by as much as 26 %. It is interesting to see that even with the sealed pressure held constant from 0.27 s to 0.63 s, the friction force continues to increase significantly during this period. Similar is true for the second cycle. Also, for the second cycle it shows much more pronounced rise from base state to the first maxima than that for the first cycle and does not dip down thereafter as much as in the first cycle. The reason for this behavior becomes clearer from the discussion of contact pressure histories of Figure 8.7. The accumulation of creep at constant sealed pressure indeed causes a significant increase in friction force from 1st cycle to the 2nd and this phenomenon needs to be taken into account in designing seals with certain friction characteristics in mind.

The mean shear stress history over 2 cycles as shown in Figure 8.12 also provides more insight into the friction behavior above. With the higher fluid pressures during the first instroke (Figure 8.5), the contact pressures reduce and correspondingly shear stress decreases from its base value. It then shows a sharp rise due to the secondary contact. Since the fluid pressures are lower during the second instroke than those in the first, the shear stress does not drop much from its base value, in this case, before increasing due to the secondary contact. Also, the accumulated creep sustains a little larger contact pressure (at least in the 60% of the sealing zone away from the sealed end) than during the first cycle. Such creep accumulation is also a consequence of the high frequency of seal operation and depends on the relation between the viscoelastic time constants and the operational frequency. This shear behavior coupled with the contact length histories of Figure 8.3 (a) explain the observed friction behavior.

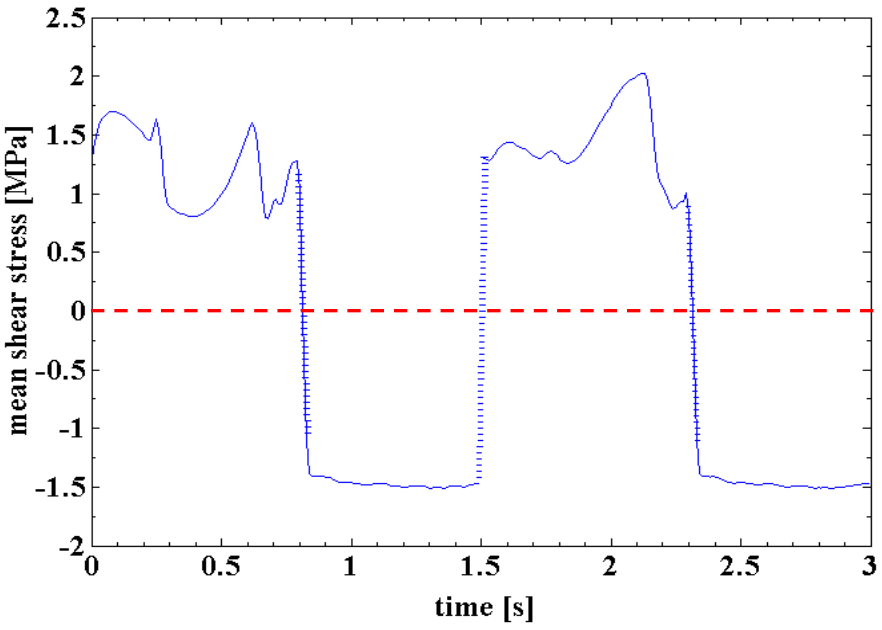

Figure 8.12: Mean shear stress on the rod vs time.

It is evident from the discussion in this section that the high pressure, high frequency sealing dynamics shows characteristic that are different from the ones observed in an application like injection molding where the frequencies are much lower. The differences can be attributed to the relation between the viscoelastic time constants and the characteristic cycle times. It is seen that, it is not realistic to assume the dynamic sealing cycle to be repetitive over the entire period operation. Viscoelasticity of the seal material produces critical differences in the key sealing characteristics like Poiseuille flow, contact pressures and friction from one cycle to the next. Analyzing such differences was possible due to the comprehensive capabilities of the MSMP framework developed in this work. This study is a significant step forward in understanding the effect of "material memory" on the performance of seal during consecutive high pressure, high frequency cycles.

8.2 Effect of Cycle Frequency on the Visco-Elastohydrodynamic Behavior

After looking at the viscoelastic seal response to high frequency cycle of 1.5 sec duration, the next logical step of the study was to understand how the visco-elastohydrodynamic behavior would look like if the cycle duration is gradually increased. It was observed in the previous section that the fluid pressure and contact pressure behavior during the consecutive cycles depends on the relation between the viscoelastic relaxation time constants and the characteristic time of the cycle. With this in mind, MSMP calculations were performed for two more cycle frequencies, one with 3 second cycle duration and other with a 6 second cycle duration. Operating parameters like the sealed pressure and rod velocity profiles for these new calculations were exactly the same

as those for 1.5 sec cycle, except stretched over the new cycle duration. The results from these calculations were then compared with those from 1.5 second cycle discussed before.

8.2.1 Effect of Cycle Frequency on Fluid Pressures and Contact Pressures

Figure 8.13 and Figure 8.14 show the fluid pressure histories for the 3 sec cycle and 6 sec cycle respectively. Comparing them with the 1.5 sec cycle of Figure 8.5, it can be seen that increasing the cycle duration (hence reducing the cycle frequency) , gives the seal material more time to respond to the applied stress and also to come back to it's base state after the stress is removed. This in turn reduces the differences in fluid pressure in going from one cycle to the next.

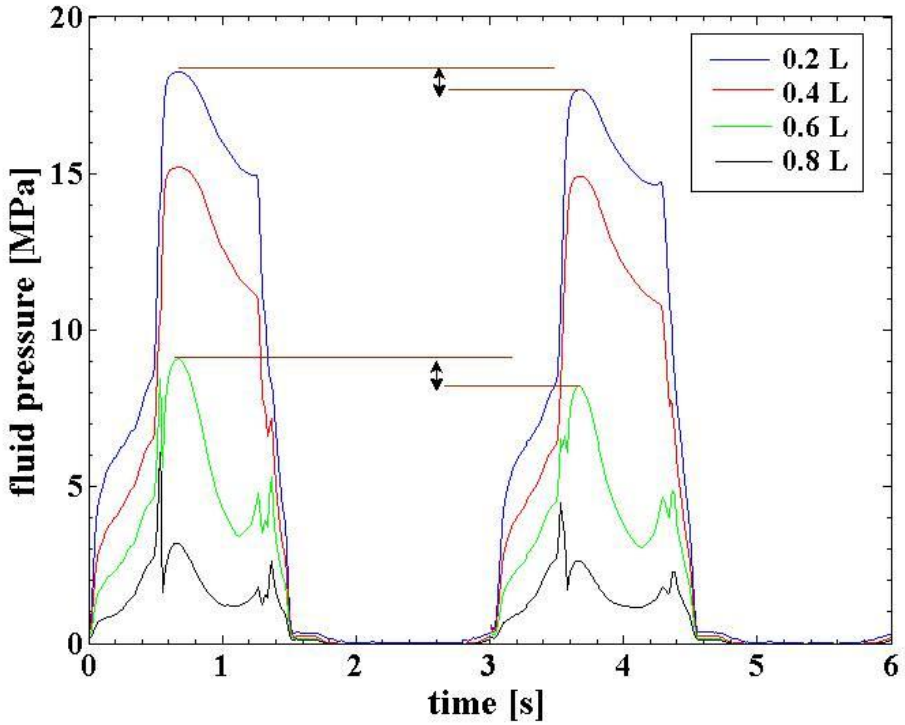

Figure 8.13: 3 sec cycle: fluid pressure history at four key points.

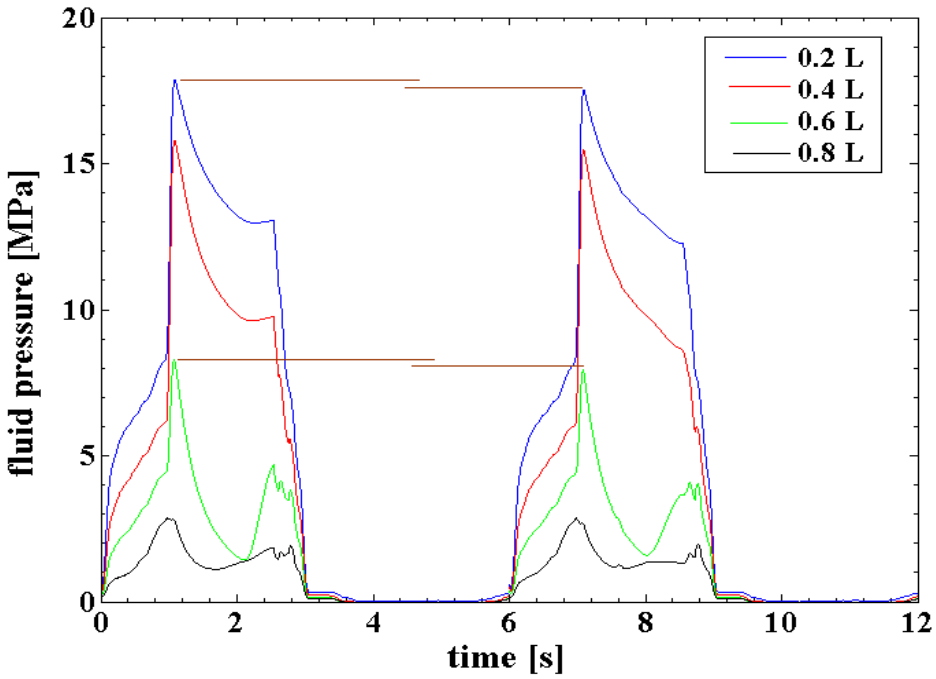

Figure 8.14: 6 sec cycle: fluid pressure history at four key points.

For example, the difference in peak fluid pressure from 1st cycle to 2nd reduces from about 10% for 1.5 sec cycle to 4 % for 3 sec cycle to 1.6 % for 6 sec cycle. As we go farther from the sealed end (e.g. at 0.6 L), the difference between 3 frequencies is more pronounced as seen from about 26% difference between the 2 cycles for 1.5 sec duration , 11 % for 3 sec duration and less than 5 % for 6 sec duration cycle. This indicates that at 4 times slower cycle frequencies, the seal is actually getting just enough time to come back to its base state before beginning the next operating cycle. This is certainly not true for cycles with higher frequencies.

Figure 8.15 and 8.16 shows the contact pressure histories for 3 sec cycle and 6 sec cycle respectively. Difference between the consecutive cycles is again seen to decay as the cycle duration is increased. The difference reduces from 11 % to 2 % to ~ 0 % for 1.5 sec, 3 sec and 6 sec cycle respectively.

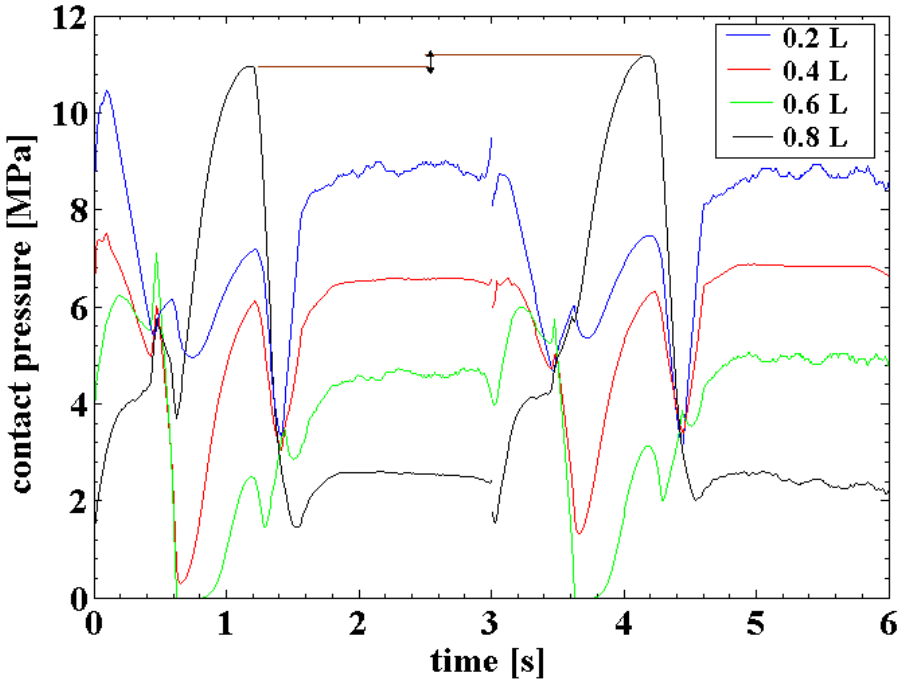

Figure 8.15: 3 sec cycle: contact pressure history at four key points.

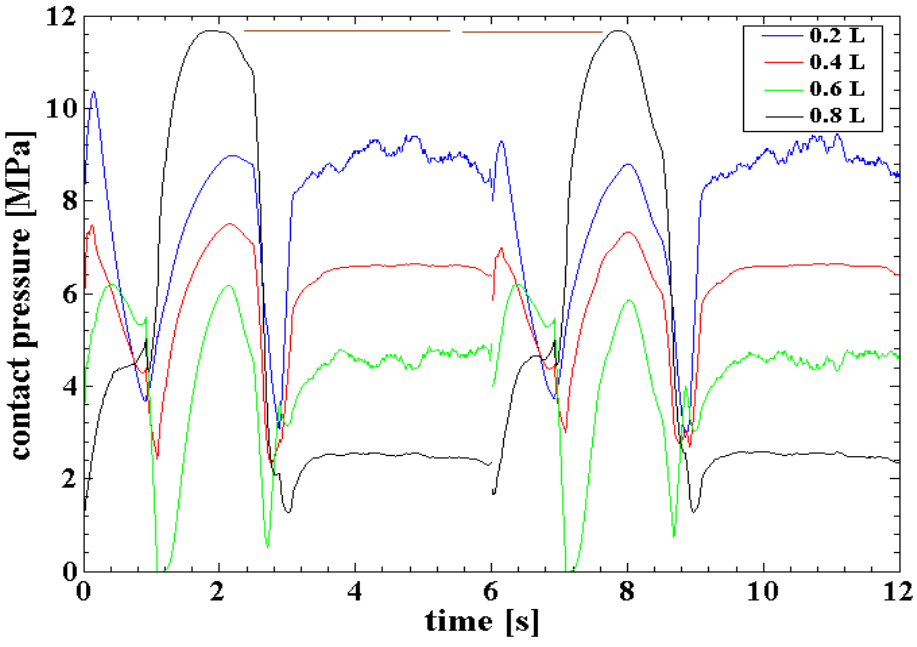

Figure 8.16: 6 sec cycle: contact pressure history at four key points.

8.2.2 Effect of Cycle Frequency on Fluid Transport and Flow Decomposition

Figure 8.17 and 8.18 show the total flow rate and Poiseuille and Couette flow components for the 3 sec and 6 sec cycle respectively. Comparing them with Figure 8.9 indicates that the flow decomposition depends on the frequency. During the first instroke, the magnitude of Poiseuille contribution decreases in going from highest frequency (35 % of the magnitude of total flow for 1.5 sec cycle) to a mid-range frequency (21 % for 3 sec cycle) to the lower frequency (11% for 6 sec cycle). It is interesting to see that the Couette flow contribution also decreases accordingly with decreasing frequency and keeps the total flow rate at about the same level for all the frequencies. However, during second instroke Poiseuille contribution first increases from 12 % for 1.5 sec cycle to 16 % for 3 sec cycle and then decreases to 10% for the 6 sec cycle.

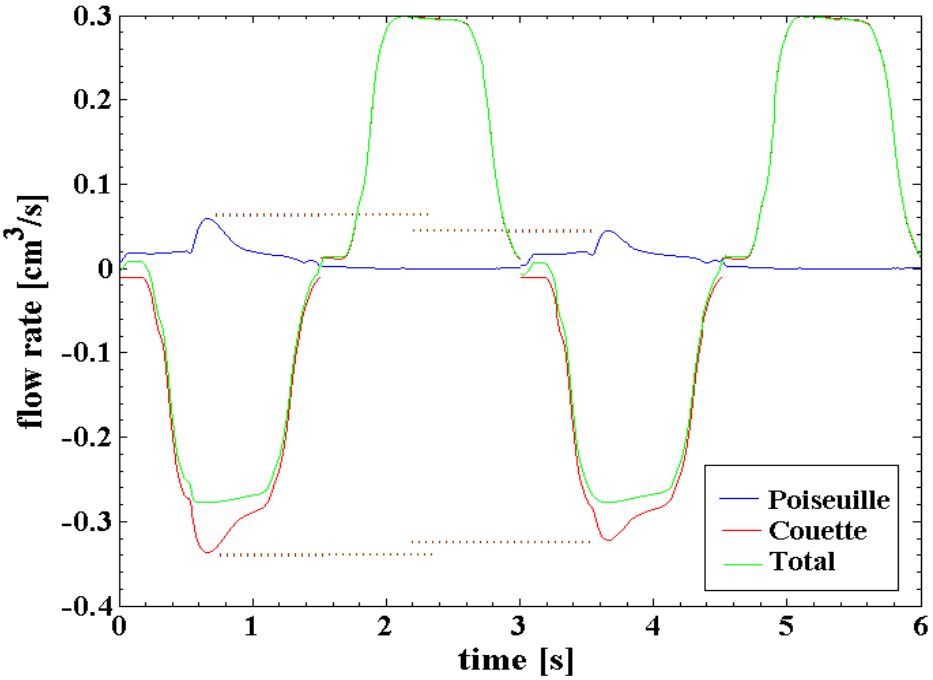

Figure 8.17: 3 sec cycle: flow rate vs time.

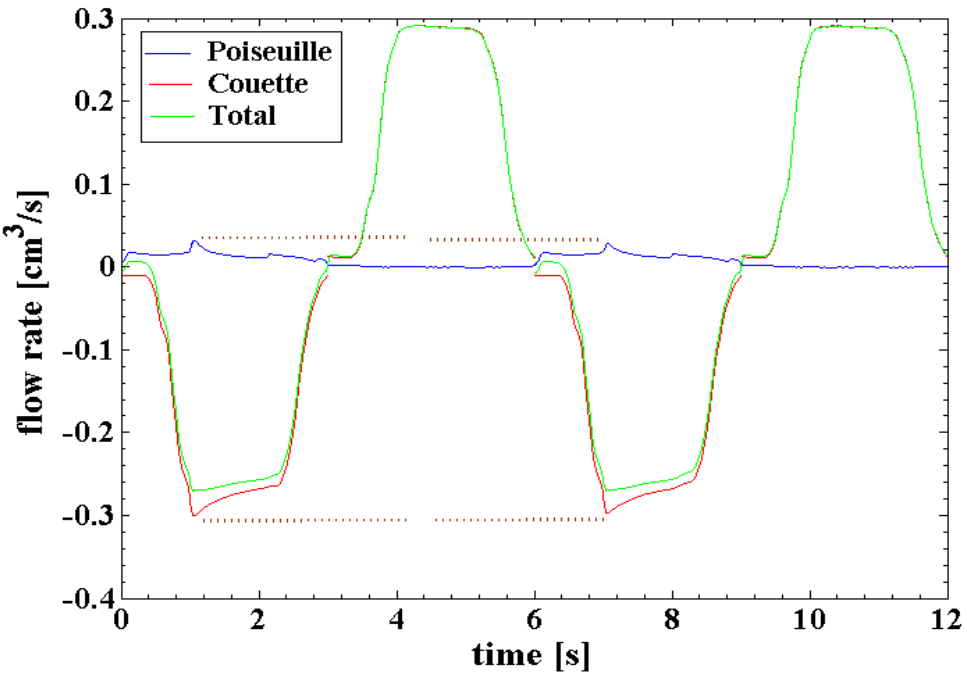

Figure 8.18: 6 sec cycle: flow rate vs time.

The role of viscoelasticity and cycle frequency on such a flow decomposition becomes clearer from Figure 8.19. It demonstrates that the difference in Poiseuille components between the consecutive cycles substantially decreases as the frequency of cycle decreases. This difference reduces from 64% to 24 % to 6 % as the cycle duration increases from 1.5 sec to 3 sec to 6 sec. Poiseuille component is a good measure of gauging the role of interrelation between viscoelasticity and cycle frequency on seal performance, as it is the component which mainly depends on pressure distribution in the fluid film and since viscoelastic time scales affect the fluid pressure distribution in the film, tracking the Poiseuille distribution over time for difference cycle frequencies provides an insight into their dual effect on seal performance. It becomes evident that with increasing cycle duration, seal gets more and more time to relax and come to the internal equilibrium before the next cycle begins. Reaching this internal equilibrium of molecular motions allows the seal material to behave the same during the repeating

cycles as during the very first one. It is clear from Figure 8.19 that 1.5 sec cycle and 3 sec cycle are far from reaching this state of internal equilibrium while 6 sec cycle is coming close to reaching that state.

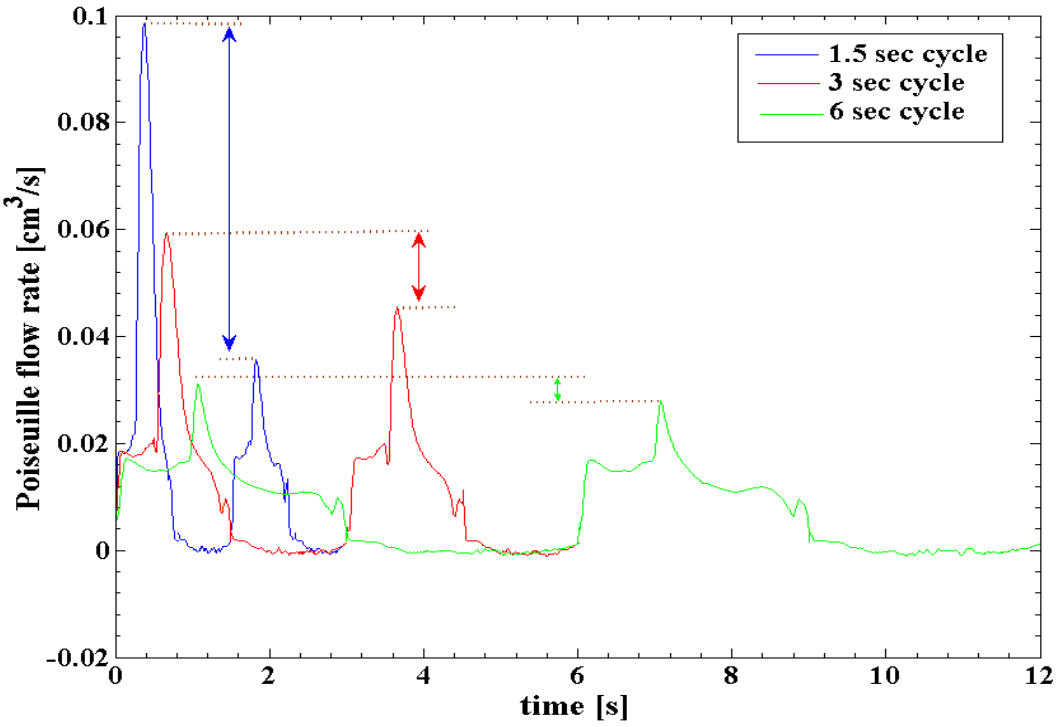

Figure 8.19: Comparison of Poiseuille flow components for 1.5 sec, 3 sec and 6 sec cycles.

Figure 8.20 shows the net fluid transport out of the cylinder for cycles with three different cycle durations. It is one of the most important results from this study and shows that the viscoelastic times scales coupled with operational frequency can critically affect the leakage characteristics of the seal. The current seal material makes this seal "non-leaking" when operated at high frequency (1.5 sec cycle duration) but the same seal with same viscoelastic relaxation spectrum when operated at moderate (3 sec cycle) and low frequency (6 sec cycle) starts to leak well before the cycle ends.

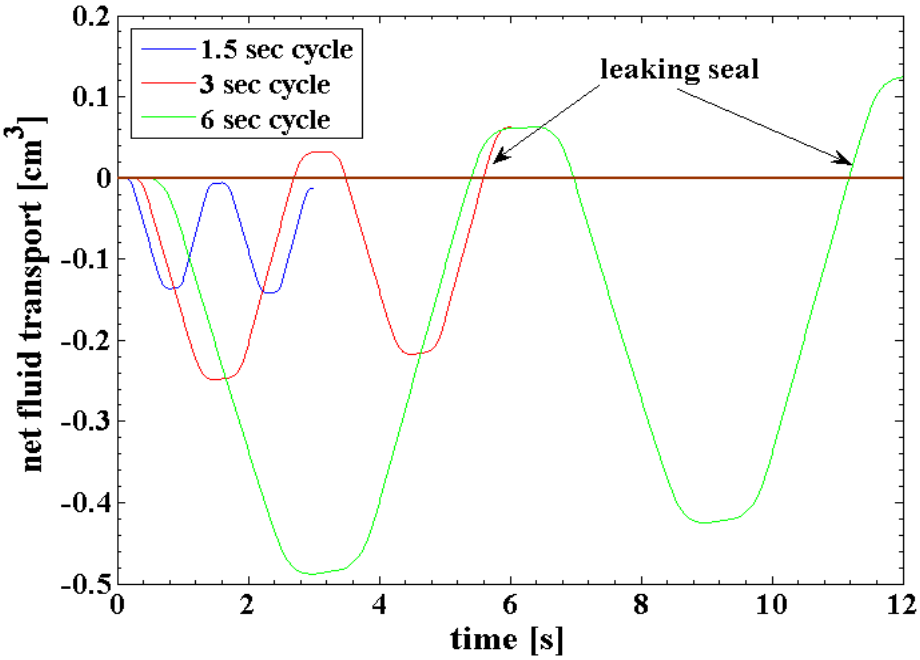

Figure 8.20: Comparison of net fluid transport out of the cylinder for 1.5 sec, 3 sec and 6 sec cycles.

This is a critical result that needs to be paid attention to when designing seals for operating in high pressure variable frequency environments. With this in mind, the relaxation time scales of the seal material chosen also need to be carefully analyzed for their dynamic response characteristics over a broad frequency range. It can also be seen from the figure that with lower cycle frequencies, the amount of fluid leaked would accumulate from cycle to cycle and would constitute a large loss of operating fluid even over a few hundred cycles of operation.

8.2.3 Effect of Cycle Frequency on Sealing Zone Length and Friction

Figure 8.21 shows the sealing zone lengths obtained with 1.5 sec, 3 sec and 6 sec cycle durations. It is interesting to note that even with high operating pressures for longer periods than 1.5 sec cycle, the 3 sec and 6 sec cycles reach the same maximum sealing

length as that of 1.5 sec cycle, however the 3 sec and 6 sec cycles progressively reach higher lengths of primary sealing zone, before jumping to the secondary contact (instantaneous sharp rise seen from the vertical line). It is observed that the end state of 1.5 sec cycle is farther away from the base state than the end state of 3 sec cycle which in turn is farther away than the end state of 6 sec cycle. This is as expected from the viscoelastic relaxation process. Also, the 1.5 sec cycle shows accumulation of creep from first cycle to the second (difference between end states of consecutive cycles), which is not seen in the 3 sec and 6 sec cycles. However, it is interesting to see that even at the end of 2nd cycle of 6sec duration, the seal has not completely returned to its undeformed configuration. The rate of creep recovery can be seen to be extremely slow in this case and with respect to characteristic cycle times, this creep behavior surprisingly looks like that of a thermoplastic.

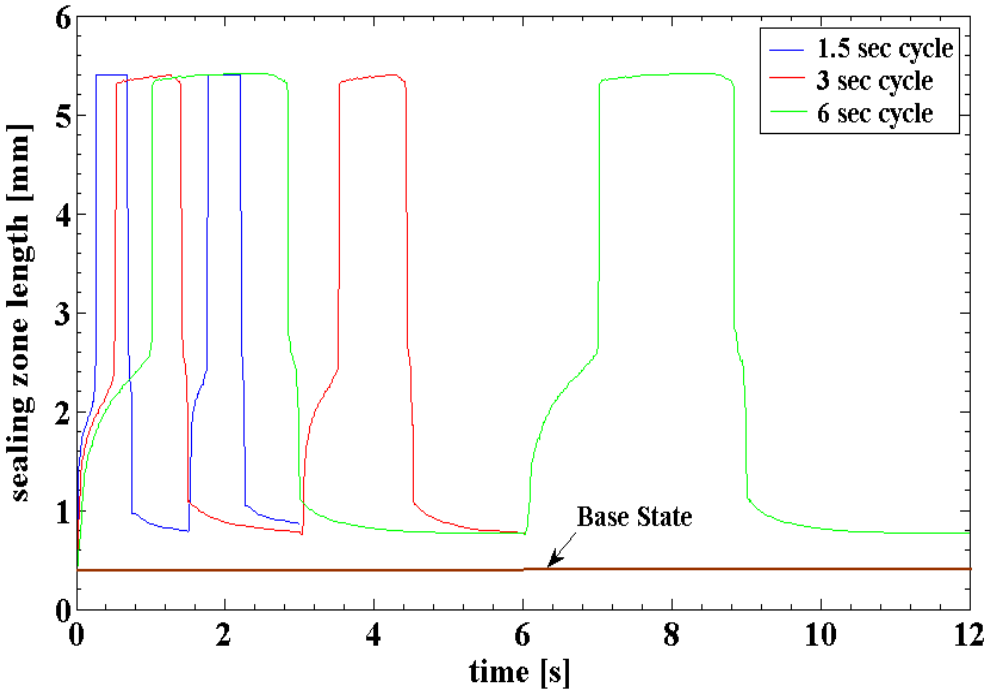

Figure 8.21: Sealing zone lengths obtained for 1.5 sec, 3 sec and 6 sec cycles.

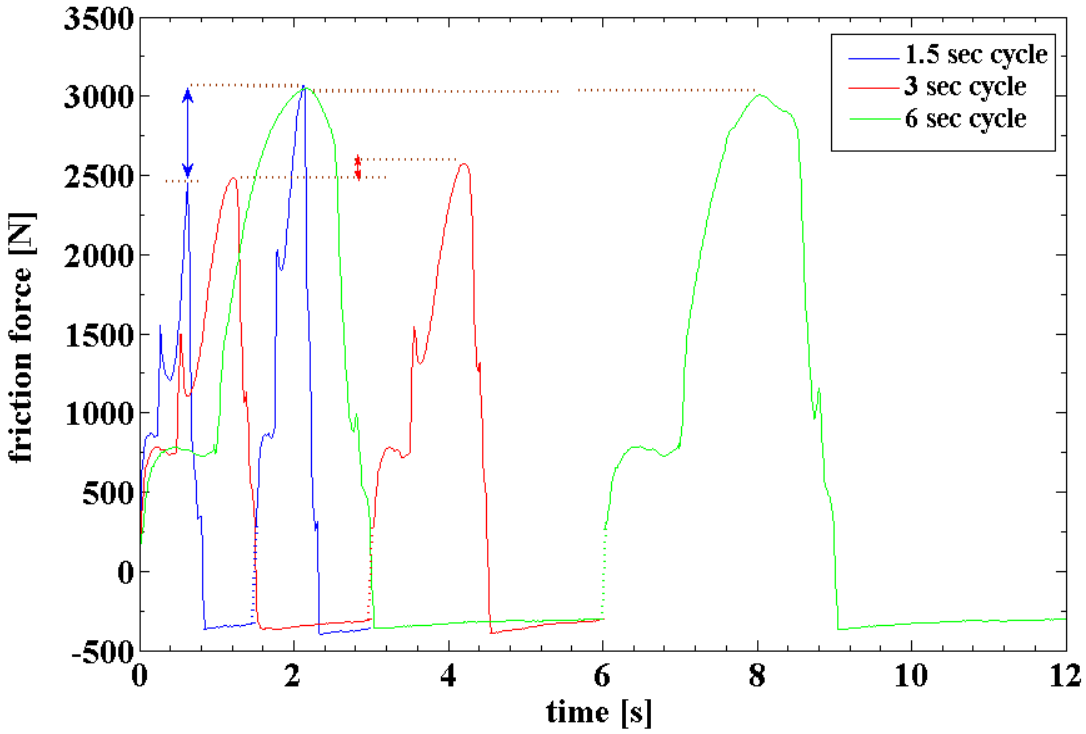

Figure 8.22: Friction force comparison for 1.5 sec, 3 sec and 6 sec cycles.

Figure 8.22 shows the comparison of friction force history obtained with the three different cycles. The behavior seen in Poiseuille flow plots is again seen in friction plots, with the difference between consecutive cycles reducing with the reduction in frequency of cycle, as the polymer chain structure gets more and more time to reach internal equilibrium. It is also important to note that for the 1.5 sec cycle and 3 sec cycle, although the sealing length is same from one cycle to the next, the friction force for the second cycle is respectively 20 % and 4 % larger than that for the first one. This means that all the increase in friction is only coming from the increase in the shear of contacting asperities. This difference becomes negligible for the 6 sec cycles and hence the cycles with this frequency can be considered repetitive at least in terms of friction behavior.

8.3 Effect of Temperature and Polymer's Relaxation Time Scales on the High Pressure High Frequency Sealing Dynamics

It was discussed in chapter 7 that the viscoelastic response of a polymer is a function of temperature. Increasing the temperature pushes the seal material into a more "rubbery" state where the instantaneous relaxation moduli are lowered, while lowering the temperature pushes it towards a "glassy" state which increases the instantaneous moduli of the polymer response. Now, an increase in the instantaneous relaxation modulus can be considered to be equivalent to raising the time constant for a given elastic modulus from the Prony series. Hence, a change in operating temperature of a polymeric seal affects the relaxation time scales associated with the seal's polymeric chain network, the lower the temperature, the higher the relaxation time constant (at least within the range of typical operating temperatures). This in turn affects the visco-elasto-hydrodynamic response of the seal, especially during high pressure, high frequency sealing. Using our MSMP framework, several numerical experiments were performed to study the effect of such a change in relaxation time scales on the dynamic sealing characteristics. Using the time-temperature superposition model and the constrained optimization algorithm discussed in chapter 7, a combination of instantaneous moduli and relaxation time constants were found corresponding to different temperatures in the operating range. These viscoelastic parameters were then used in the MSMP framework to perform the calculations for various operating pressures and cycle frequencies.

As the relaxation time scales varied, significant differences were observed in the key sealing performance characteristics. A factor of 10 rise in the first relaxation time constant produced a much sluggish response of the seal and gave much smaller sealing

zones even at high operating pressures of 21 MPa. For example, the seals that had produced secondary contacts and jumps in sealing zones with $\tau = 0.3$ sec showed no such secondary contacts and produced much smaller sealing zones with $\tau = 3.0$ sec. This in turn critically changed the contact pressures, fluid pressure and hence leakage and friction characteristics of the seals. Also, the differences between consecutive cycles were observed to be much more pronounced for mid-frequency range than for the low-frequency or high-frequency cycles, as this range corresponds to the "transition range" between primary and secondary contact conditions for higher relaxation time constants.

A sample plot from such a study is shown in Figure 8.23 to demonstrate the effect of viscoelastic relaxation scales on high frequency sealing dynamics. It shows the sealing zone lengths obtained for two consecutive cycles of 1.5 sec , 3 sec and 6 sec cycle duration for a seal with $E_i = [\ 90\ ;\ 15;\ 11;\ 7\ ;\ 0.9\ ]$ and $\tau_i = [\ 3\ ;\ 20;\ 60;\ 300\ ;\ 1000\ ]$. Hence this seal has 10 times larger first relaxation time constant than the seal discussed in section 8.1 and 8.2, which corresponds to a lower temperature. Comparing Figure 8.23 with Figure 8.21, it can be seen that the 1.5 sec cycle now shows no sign of secondary contact and the maximum sealing zone length is restricted to 2.5 mm as compared to 5.5 mm in previous seal. This indicates that with much higher primary relaxation constant, the seal's polymer chain network does not yield as much to the applied stress as the previous one and shows significant latency during the high frequency operation.

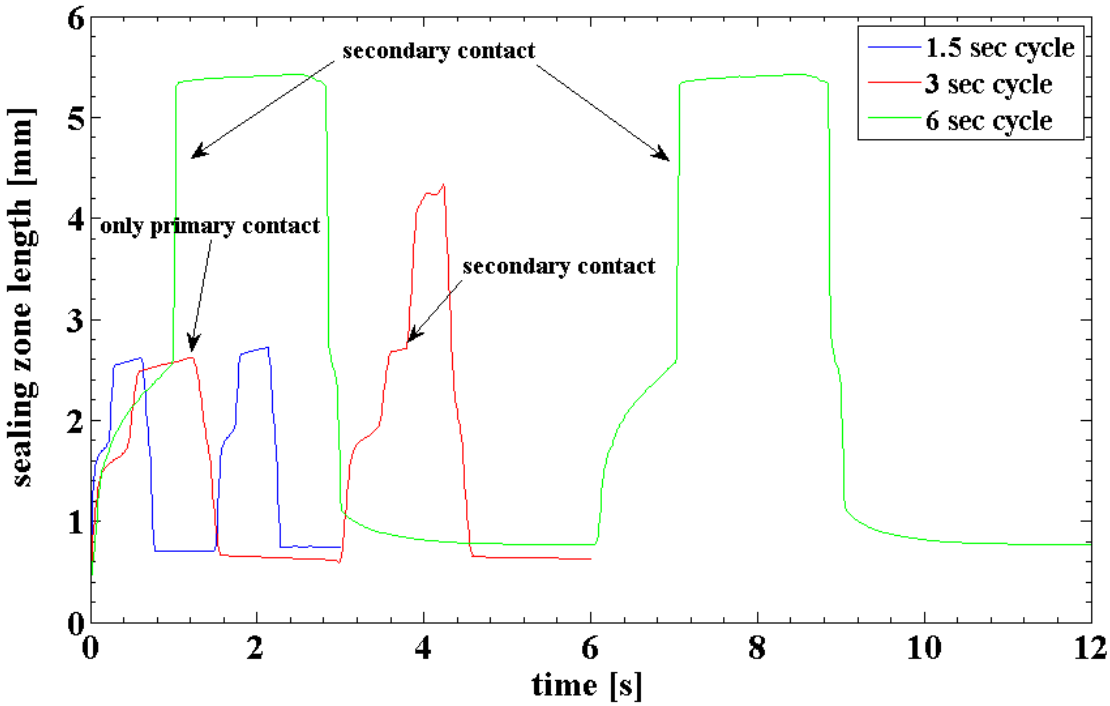

Figure 8.23: Sealing zone lengths obtained for 1.5 sec, 3 sec and 6 sec cycles for a seal with $\tau_1 = 3.0$ sec as the primary time constant.

During the first instroke of 3 sec cycle, the seal does not produce secondary contact and sealing zone length is much smaller than the one with lower relaxation constant. During the second instroke, again, the seal shows no sign of secondary contact initially; however, due to accumulated creep from the first cycle, at midway during the instroke, it suddenly jumps to the secondary contact and produces a 68 % larger sealing zone during rest of the high pressure time. It can also be noted from the blue and red curves that at constant high pressure, now the seal shows the signs of creep (as the sealing zone length increases at constant stress). This was not observed in the previous seal with lower primary time constant (Figure 8.21), which stayed at a constant maximum sealing length.

Green curves show the sealing zone lengths during 6 sec duration cycles. It is observed that for this low –frequency longer-duration cycle, even the large relaxation constant seal jumps to secondary contact during both, the first and the second instroke and interestingly, at exact same time instances as the seal with lower relaxation constant. Also, after reaching the maximum sealing length of 5.5 mm, it is no longer capable of producing any creep. This shows that the 6 sec cycle gives the seal with larger time constant enough time to respond to the applied stress history so as to behave same as the seal with 10 times lower time constant. Hence, during such a low frequency cycle even this new seal's behavior can be considered to be "repetitive" for the consecutive cycles.

Above discussion demonstrates that there exists a "critical frequency" of operation below which the seal at a given temperature (and hence a relaxation time constant) will exhibit the secondary contact and the contact pressure distributions will change significantly as was seen in Figure 8.3 (a) and Figure 8.6. Also, the friction and leakage characteristics of the seal will be significantly different for frequencies lower than the "critical frequency" than the ones above it. It can also be inferred that for a given cycle frequency, there is a "critical temperature" above which the secondary contact will occur, the sealing characteristics will vary from cycle to cycle and the consecutive cycles may not be considered repetitive. With the MSMP framework developed, it was possible to study such seal performance characteristics for seals with various relaxation scales for operational frequencies above and below the "critical frequency".

CHAPTER 9. CONCLUSIONS

The behavior of a hydraulic rod seal is governed by multi-physics interactions taking place at several different length and time scales spanning a broad spectrum. Most of the previous theoretical studies and numerical models developed for analyzing seal's performance neglected surface roughness and assumed full film lubrication, both of which are shown to be unrealistic through experiments and have produced erroneous results. Also, almost none of these models have taken into consideration the transient effects, the dynamic operation of seal or the viscoelastic effects arising from polymer's time dependent response.

In the present work, in pursuit of a realistic seal model, a multi-scale multi-physics (MSMP) seal model is developed. The model takes into account surface roughness, mixed lubrication, cavitation and two phase flow, transient squeeze film effects, dynamic operation with temporally varying sealed pressure and rod velocity as well as the effect of macro/micro/nano scale viscoelasticity of the seal. A new analytical model for viscoelastic contact of rough surfaces is also developed and is incorporated in the MSMP model.

A hybrid finite element-finite volume-statistical computational framework is developed to solve the highly coupled multi-physics interactions of the MSMP model efficiently. An augmented Lagrangian method is implemented with an adaptive penalty factor to handle the viscoelastic contact between soft polymer boundary and the stiff rod boundary. To tackle the problem of large mesh deformations caused by large changes in the seal geometry, an Arbitrary-Lagrangian-Eulerian (ALE) framework with a physics

based moving mesh algorithm is implemented. To solve the problem of time changing micro-scale computational domain, a Dynamic Domain Mapping (DDM) method is developed, which ensures an appropriate transfer of information at the fluid-solid interface. The comprehensive MSMP model and the hybrid computational framework developed here successfully solves the multi-scale multi-physics sealing interactions in a strongly coupled manner and predicts key seal performance characteristics as a function of time.

To extract the surface parameters needed for MSMP model, surface characterization experiments are performed. These experiments also revealed some new seal surface characteristics like directionality and allowed decomposition of surface features into low frequency (waviness) and high frequency (roughness) components. These experiments helped in detecting micro-scale surface imperfections that caused anomalies in the experimentally observed seal leakage characteristics. During optical profilometry, it was observed that the optical and system interference created large artificial noise peaks in the surface data that seriously affected the parameter values. To remedy this problem, a wavelet transform based adaptive surface extraction algorithm is developed which removes high frequency noise without removing the high frequency surface features. This algorithm facilitated accurate estimation of surface parameters needed for the MSMP model. The method developed has a great potential in several applications, where the problems of noise coupled with high frequency signal are prevalent.

To extract the macro-scale viscoelastic parameters needed for the MSMP model, dynamic mechanical analysis (DMA) experiments are performed over polyurethane and

PTFE seal samples. To extract the Prony coefficients from DMA data, the unconstrained and the constrained optimization algorithms are implemented. The constrained algorithm produces only positive Prony coefficients which have physical significance and hence are used in reconstructing the relaxation modulus. The DMA experiments also revealed the strong temperature and frequency dependence of storage and loss moduli of polyurethane and PTFE seals. The storage modulus for polyurethane decreased by as much as 58 % in going from 30^{o}C to 120^{o}C. The increase in storage modulus with frequency is more substantial (46 % rise from 0.1 Hz to 200 Hz) at low temperatures (30^{o}C) than at high temperatures (14 % rise at 120^{o}C). It was also found that PTFE is much stiffer over the given frequency range (0.1 Hz to 200 Hz) and temperature range (30^{o}C to 120^{o}C) with the modulus as high as 40 times to that of polyurethane at room temperature. Also, unlike polyurethane, PTFE was found to have a significant increase in loss modulus with frequency at high temperatures (120^{o}C). The experiments indicated that the seal material model should account for significant temperature variation of material properties. This was done using time-temperature-superposition method.

To investigate the micro/nano scale viscoelastic response of surface asperities, atomic force microscopy (AFM) experiments were conducted on polyurethane seal samples. The topography images were obtained to a spatial resolution as low as $10\,nm$ and a vertical resolution as low as $1nm$. The images obtained provided a validation of the "protuberance-on-protuberance" theory indicating various levels of surface roughness. The time averaged elastic properties of each individual asperity were mapped using tapping mode AFM. The micro/nano scale elastic moduli for polyurethane produced a surprising finding showing several local moduli to be varying within 2 orders

of magnitude (as high as 3000 MPa) higher than the bulk of the polymer (43 MPa). Also the phase plots of these micro-scale regions revealed the surface properties that were not expected from the surface topographies. They showed significant differences in local material properties like stiffness and adhesion and also revealed some underlying much harder filler materials.

To extract the viscoelastic response of the individual asperities, TRIF measurements were performed. Hertzian and DMT models were fitted to these interaction force curves and the temporally varying elastic moduli were obtained from which viscoelastic parameters for individual asperities can be extracted. Significant differences in both, the magnitude of the moduli and the relaxation time scales, of individual asperities were observed. Some asperities were found to be much stiffer than the others in their response to nano-scale pressures. It was concluded that the relaxation spectrum of individual asperities is very different from each other. Understanding the nano-scale elastic and viscoelastic properties of seal asperities and variations in their response to applied pressures is believed to be a valuable addition to the fundamental understanding of multi-scale sealing dynamics.

Finally, with the comprehensive MSMP model developed, key seal performance characteristics were analyzed. The results of the transient study (constant sealed pressure) confirmed that the rod seal operates with mixed lubrication in the sealing zone, and seal roughness plays an important role in determining its behavior. Critical seal roughness, above which the seal leaks, was found for the transient operation. During instroke, fluid films were found to be thicker than during the outstroke. This promotes non-leaking. Cavitation was shown to take place during outstroke which also helps in reducing

leakage. Model with linear elastic seal material showed only Couette flow to be dominant during the flow. The Poiseuille flow was found to be negligible. Also, when the sealed pressure is constant, during the outstroke, the film thickness decreases with increasing rod velocity, while it increases with increasing velocity during the instroke. Under such conditions, during the outstroke (diverging flow) the fluid pressures decrease with increasing rod speed, while during the instroke (converging flow) they increase with increasing rod speed. It was also found that the shear stress on the rod is primarily due to contacting asperities and since contact pressures reduce with increasing rod velocity during instroke, the shear stress was found to drop in magnitude during instroke with increasing rod velocity and the friction force was seen to follow a similar behavior as the sealing zone length is constant for constant sealed pressure.

With time changing sealed pressure, it was seen that the time variations in fluid pressure distributions are governed by a complex dual dependence on changes due to time varying sealed pressure boundary condition and those due to hydrodynamic effects produced by time varying rod velocity. The contact pressure distributions, shear stress and friction force are largely affected by changes in sealed pressure.

The inclusion of viscoelastic effects at macro and micro scale was a significant step forward in the pursuit of a realistic seal model. From the results of visco-elasto-hydrodynamic MSMP model, viscoelasticity is seen to affect the leakage and friction characteristics through its effects on the fluid pressure and contact pressure distributions. It critically affects the interplay between the transient sealed pressure effects and the hydrodynamic effects. Viscoelasticity is seen to increase the fluid pressure and the contact pressure significantly in the sealing region closest to the sealed end. It also shifts

the fluid pressure peaks away from the sealed end during instroke and enhances cavitation during the outstroke. It produces thicker fluid films during both, the outstroke and the instroke, and produces a significant increase in the Poiseuille component of the flow during the instroke, which was not seen by perfectly elastic seal models. Through its effects on mean shear stress and sealing zone length, viscoelasticity significantly alters the friction force behavior. Importantly, it is found that ignoring viscoelasticity leads to under prediction of the time required to reach the zero leakage state during a cycle.

Comprehensive viscoelastic MSMP model was also used to analyze high pressure - high frequency sealing applications. With high pressures of up to 21 MPa, and a high cycle frequency (low cycle time of 1.5 sec) a new phenomenon of “secondary” contact was observed in the rod seals. This secondary contact produces significant increase in contact pressures and hence in friction forces on the rod. A surprising finding of increase in the dry contact pressures in the secondary contact with time at a constant operating pressure was observed. This increase is attributed to the viscoelastic creep induced pressures in the seal body surrounding sealing edge. The fluid pressure, contact pressure and film thickness characteristics obtained for such high pressure-high frequency sealing were significantly different than those observed previously. Also, viscoelasticity induced significant differences in these variables in going from one cycle to the next. Especially, the Poiseuille flow decreased substantially from one cycle to the next. The Couette flow showed a similar reduction but kept the total flow constant from cycle to cycle. A large increase in friction force was observed from first cycle to the second, with peak friction increasing by as much as 26 %.

The effect of cycle frequency was investigate in high pressure-high frequency sealing dynamics. It was found that with reduction in cycle frequency, the differences in fluid flow and contact variables from cycle to cycle are reduced. This is because, with reduction in frequency, the viscoelastic seal gets more time to relax and come to internal equilibrium before it begins its next cycle. Importantly, the leakage characteristics were found to be very different for the same seal if it is operated in an application with different cycle frequency. The seal analyzed, if operated in a 1.5 sec cycle was non-leaking, but if operated in 3 sec or 6 sec cycle produced significant leakage. This was an important finding and shows that seals need to be designed by taking the relaxation time scales of the seal's polymer and cycle frequencies of application into consideration.

The study also showed that reducing temperature or increasing the relaxation time constant of the polymer, would reduce the tendency of secondary contact for a given frequency of operation. It revealed that for a given frequency, there is a "critical temperature" above which secondary contact will occur, the sealing characteristics will vary from cycle to cycle and the consecutive cycles may not be considered repetitive. Similarly, for a given operating temperature, there exists a "critical frequency" of operation below which the seal will exhibit secondary contact and the contact pressure distributions will change significantly. The friction and leakage characteristics of the seal will be significantly different for frequencies lower than the "critical frequency" than the ones above it. These are important findings and show that the seals performance can be manipulated by controlling its temperature or relaxation time constants. With this, the new seal designs where local temperature control is achieved by embedding resistive heating circuits can then be envisioned for controlling the seal response.

In conclusion, the comprehensive MSMP framework developed here can be used as an effective seal analysis and design tool. Using this framework, the realistic seal performance under varying dynamic and temperature conditions can be predicted and improved seal designs can be proposed before building any expensive test-rigs. Due to object-oriented nature of the MSMP framework, a variety of multi-physics phenomena can be added to the existing framework and new seal designs like, seals with embedded shape memory alloys, seals with micro/nano surface pattern or the seals with piezoelectric elements to micro-control the sealing edge deformations, can be proposed and analyzed. With this in mind, the MSMP computational framework developed here has a great potential to be used as a stand-alone seal design and analysis software in academic and industrial research.

CHAPTER 10. FUTURE WORK

As discussed earlier, the MSMP computational framework developed in this work has a strong potential to be used as a stand-alone seal design and analysis software. The object-oriented nature of code allows adding/ removing different physical phenomena into/from the existing multi-physics coupling. This particular feature of MSMP is expected to be of great value in analyzing more complex seal behaviors in the future, which would involve non-linear viscoelasticity, wear, fatigue, vibrations, gas diffusion and thermal transport. The multi-physics capability of MSMP will also be used for designing and manufacturing novel seals like the seals with micro/nano surface pattern, temperature controlled seals with embedded shape memory alloys or the active seal lip control by embedding piezo-electric elements in the polymeric seals. It should be noted that the MSMP computational framework developed is not limited to analysis / design of seals but has a potential to be used for analyzing a variety of engineering problems involving multi-physics interactions like fluid-structure, fluid-thermal, dynamics, contact, vibrations, two-phase flow and piezo-electro-mechanical couplings. The efforts will be directed in future in making the MSMP code more flexible and user-friendly so that it can readily be used by academic and industrial researchers for solving complex multi-scale multi-physics problems .

As a demonstration of the capability of the MSMP framework in producing novel seal designs, a variety of piezo- embedded polyurethane seals were designed and analyzed using MSMP. Some of these seal designs are shown in Figure 10.1 through Figure 10.3. The piezo-electric element used was Lead-Zirconate-Titanate (PZT 5-H). It

was embedded into the seal in various configurations, such as, single lip- single element (Figure 10.1 (a)), single lip-dual element (Figure 10.1 (e)), dual lip – dual element (Figure 10.2) and local micro-control array (Figure 10.3). General form of piezo-electro-mechanical coupling equations for this multi-physics system is given below.

$$\{\sigma\} = [c_E]\{\varepsilon\} - [e^T]\{E\}$$
$$\{D\} = [e]\{\varepsilon\} + [\varepsilon_s]\{E\}$$

Where σ is the stress tensor, ε is the strain tensor, E is the electric field strength and D is the electric charge density displacement. These equations are solved along with structural mechanics equilibrium equations and electrostatics equations in a coupled manner. The stiffness matrix c_E, coupling coefficient matrix e and permittivity matrix ε_s which serve as input to the model are shown below:

$$c_E = \begin{bmatrix} 127.2 & 80.2 & 84.7 & 0 & 0 & 0 \\ 80.2 & 127.2 & 84.7 & 0 & 0 & 0 \\ 84.7 & 84.7 & 117.4 & 0 & 0 & 0 \\ 0 & 0 & 0 & 23 & 0 & 0 \\ 0 & 0 & 0 & 0 & 23 & 0 \\ 0 & 0 & 0 & 0 & 0 & 23.5 \end{bmatrix} \; GPa$$

$$e = \begin{bmatrix} 0 & 0 & 0 & 0 & 17 & 0 \\ 0 & 0 & 0 & 17 & 0 & 0 \\ -6.6 & -6.6 & 23.2 & 0 & 0 & 0 \end{bmatrix} C/m^2 \qquad \varepsilon_s = \begin{bmatrix} 1.5 & 0 & 0 \\ 0 & 1.5 & 0 \\ 0 & 0 & 1.3 \end{bmatrix} \cdot 10^{-8} \; F/m .$$

The active control of the lip was obtained by passing the time varying voltage signal through the appropriate face (as indicated in the figures) of the piezo element. Voltage applied between the two faces of the piezo element induces deformations of the piezo element which in turn deform the seal lip. By precisely controlling the voltage input to the piezo, fine control over the seal lip deformations can be obtained.

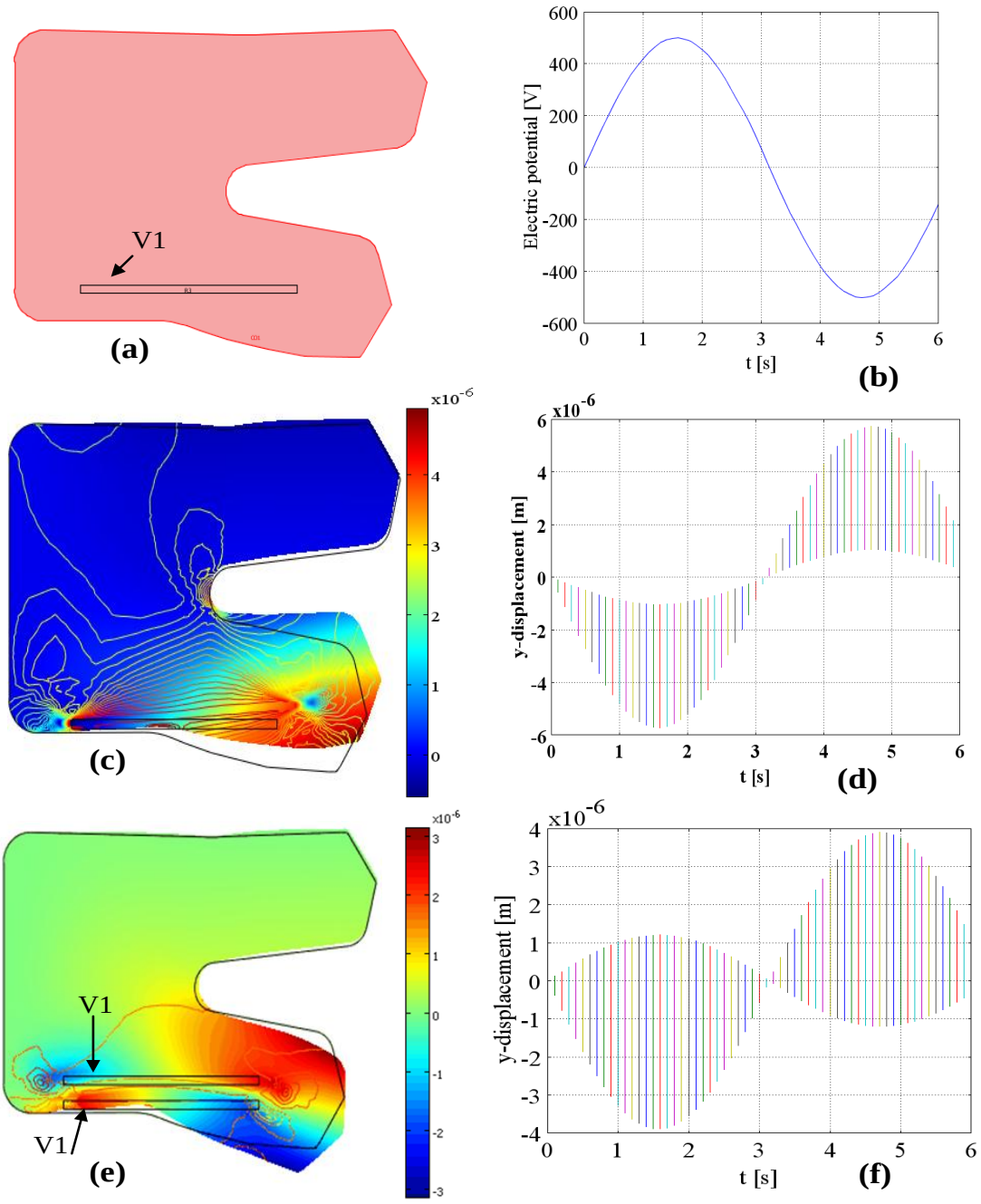

Figure 10.1: **(a) Polyurethane seal with single lip-single piezo element configuration. (b) Time varying voltage signal. (c) Displacement field and strain contours in the seal body. (d) Radial displacements of the sealing edge. (e) Displacement field in the seal with single lip–dual element piezo configuration. (f) Radial displacements of the sealing edge of the seal in part (e).**

Figure 10.1 (a) shows a polyurethane seal with single lip- single piezo embedded configuration. The thin strip black strip shown is the piezo element. A time varying voltage signal V1 with peak amplitude of 500 V is applied on the top face of the piezo element. This voltage signal is shown in part (b). Applied bias voltage causes the deformations of the piezo element which in turn deform the entire seal, mainly the lip region. The displacement field (surface plot) and axial strain contours in the seal body at a certain time instant are shown in the part (c). Although, the magnitude of these deformations as seen from the color scale is correct, the deformed shape of the seal shown is highly exaggerated for the visualization purpose. The displacement vs time plot shown in part (d) gives the time varying radial deformations of the lower edge of the bottom seal lip due to piezo actuation. The vertical line at each time instant indicates the range of these deformations going from the left to the right end of the lip edge. It can be seen that the magnitude of these sealing edge deformations is in the micrometer range. The micro-scale seal deformations can be seen to follow the sinusoidal pattern of the applied voltage. Also, it can be seen that the deformations along the sealing edge follow sinusoids of progressively varying amplitudes (0.5 - 6 micrometer) indicating that fine control over local deformations of spatially varying material points is possible.

Figure 10.1 (e) shows a seal with single lip – dual piezo element embedded configuration and its displacement and strain field obtained from piezo actuation. In this configuration, the time varying voltage signal, same as that in figure (b), was applied to the bottom face of the lower piezo and the top face of the upper piezo, while the other two faces were electrically grounded. Corresponding radial displacements of the lower edge of the bottom lip are shown in part (f) of the figure. It can be seen that the radial

displacement of the sealing edge now shows a different pattern than that observed in part (d). Although, sinusoidal, its range now extends from 1 micron in the positive direction to 4 micron in the negative direction. With the sinusoidally varying voltage, the piezo elements arc upward or downward depending on the sign of the voltage. This parabolic deformed shape of the piezos, in turn causes some points along the sealing edge to move up and some to move down from their original location, hence producing the displacement field as seen in part (f). Comparison of magnitudes between plot (d) and plot (f) also indicates that the 2 piezo configuration with voltage applied to the opposing faces actually produces a damping effect on sealing edge deformations. This effect can be used to our advantage for having a finer control over the amplitude of local micro-deformations in the sealing zone.

Figure 10.2 shows the dual lip-dual piezo seal configuration, where the two piezo strips are embedded in each of the lip regions. In this configuration the local micro-deformations of the two lips can be individually controlled by applying different voltage signals to the piezos in the two lips as shown in the figure. Part (a) shows the lip deformations (at a certain time instant) when the two signals V_{in1} and V_{in2} are exactly the same in amplitude and phase. The displacements of the two lips can be seen to be in phase. Part (b) shows the lip deformations when V_{in2} is 180^o out of phase with V_{in1}. The resulting piezo - induced displacements for the two lips can be seen to be almost of the same magnitude but in the opposite directions. Similarly, part (c) shows the resulting lip deformations when V_{in2} is 90^o out of phase with V_{in1}. The displacements for the bottom lip can be seen to be in the opposite direction and of much lower magnitude than that of

the upper lip, as the piezo deformations in the bottom lip peak at a later time instant than that in the upper lip (due to 90^o phase difference between the voltages).

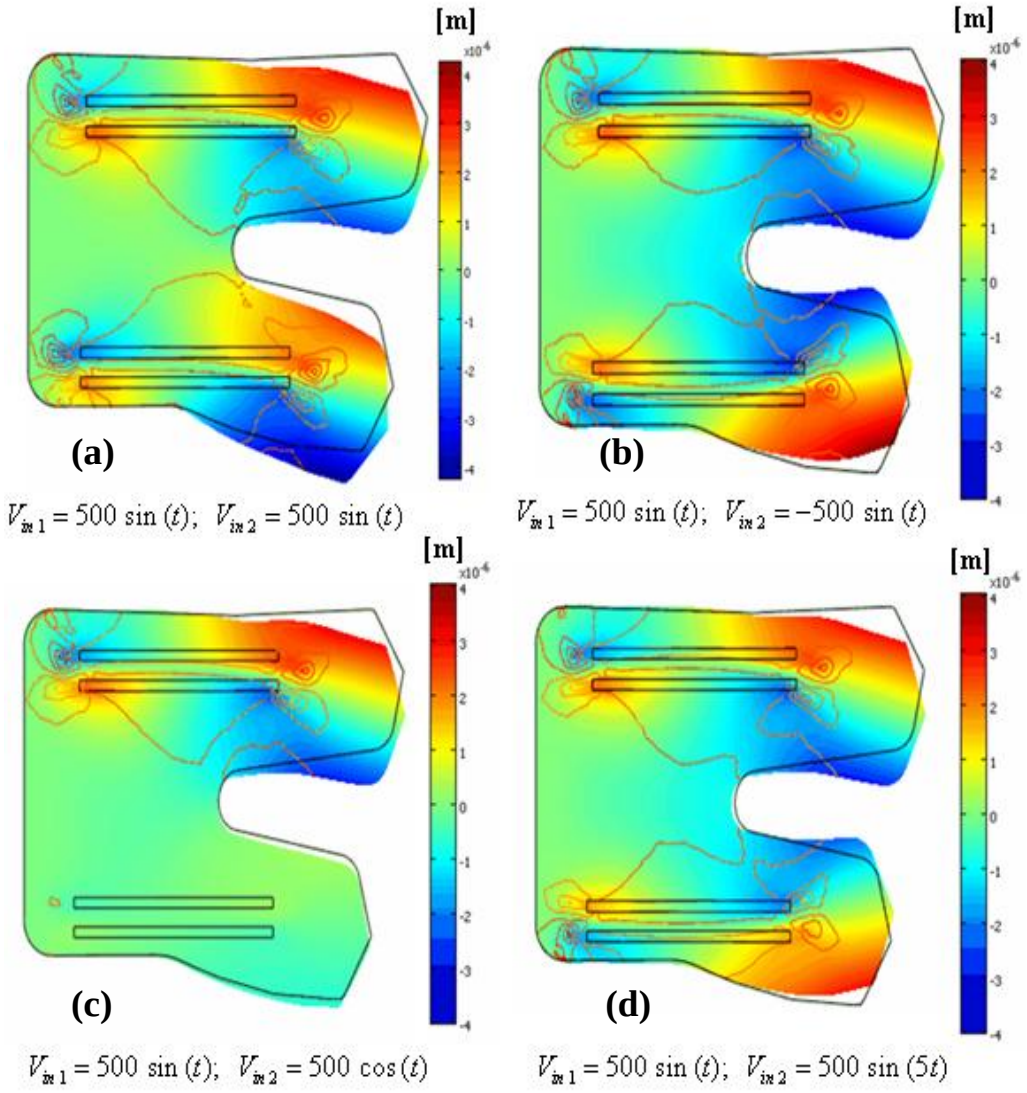

Figure 10.2: Dual lip-dual piezo seal configuration with different types of piezo actuation signals.

Part (d) of the figure shows deformations of the two lips (at a certain time instant) when the frequency of V_{in2} is five times faster that of V_{in1}. With these faster voltage oscillations

applied to the piezos in the bottom lip, lower lip oscillates five times quicker than the upper lip. Hence we can have much faster control of contact pressure, fluid pressure and film thickness in the contact region of the bottom lip with the rod while still maintaining slowly varying contact pressures in the housing side contact region (contact of upper lip), to suit certain high frequency sealing applications. Such dual lip- dual piezo embedded seal configurations indicated that it is possible to control the contact pressures and other sealing characteristics in the two different contact regions individually by passing voltage signals differing in amplitude and phase to the piezo sets embedded in the two lips of the seal..

Figure 10.3 shows the micro-control piezo arrays embedded in the two lips of the seal. The piezo array has large number of smaller piezo elements which can be individually controlled by passing individual voltage signal to each one of them With such a local control of these piezo elements, there will be a much finer control over the local micrometer scale deformations of the sealing edge with the resolution of local control defined by the pitch of the array. The amplitude and phase of the voltage signals supplied to individual piezo elements can be varied to accomplish desired film thickness and contact pressure distributions. This figure also shows the deformations of the two lips obtained by passing a voltage signal V_{in1} to the first three and the last three piezo elements of the lower array and passing signal V_{in2}, which is 180^o out of phase with V_{in1}, to the middle four piezo elements. The reverse is true for the upper piezo array. It can be seen that the deformations of the sealing edge portion underneath the middle piezos are out of phase with those underneath the first three and last three piezos as expected. The local deformations can again be seen to be in the micrometer range. This demonstrates

that with such micro-control piezo arrays embedded in the seal lips, local film thickness, contact pressure and fluid pressure distributions can be microscopically controlled as per the need of the application and hence the sealing performance characteristics like leakage and friction can be much fine tuned.

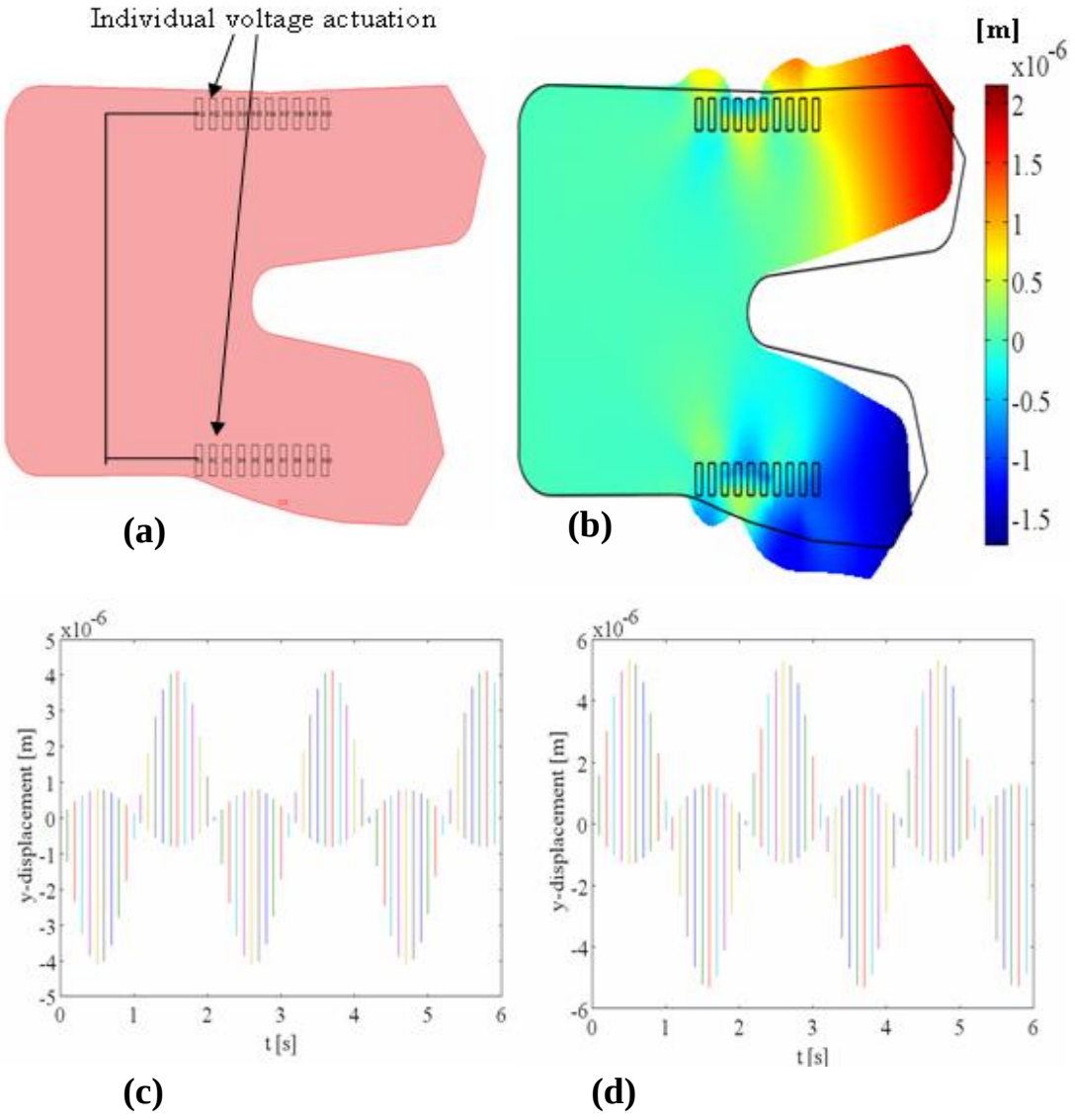

Figure 10.3: (a) Micro-control piezo array embedded seal. (b) Displacement field in the seal body at a certain time instant after piezo actuation. (c) Radial displacements of bottom edge (d) Radial displacements of top edge.

Above discussion shows that there exists a large potential for improving seal performance in a wide variety of applications by developing novel seal designs like the ones shown in this chapter. With significant advances in micro-electro-mechanical systems (MEMS) and micro/ nano fabrication techniques, it is possible to prototype and manufacture seals with active control. Local active control of sealing element can be obtained embedding piezo-electric ceramics or MEMS elements into the polymeric seals. Temperature control of seal performance can be achieved by embedding shape memory materials like Ni-Ti based alloys into the polymer matrix. Some other new seal designs like micro/ nano patterned seal surfaces, seals with nano-scale coatings etc. can also be envisioned. With the understanding of the fundamental multi-scale physics of polymeric seals under dynamic conditions gained from this research, the future steps are to design such novel seals using the MSMP framework developed here, analyze them under variety of operating conditions, modify the designs to suit appropriate applications and prototype the promising designs to be used for real industrial applications.

The variety of multi-physics coupling capabilities of the MSMP code demonstrated in the current and the previous chapters show that the MSMP framework developed in this work is not limited to analysis / design of seals but has a strong potential to be used for analyzing a large variety of engineering problems involving multi-physics interactions. In the future, this MSMP framework will be made more flexible and user friendly so that the researchers from industry and academia can readily add / remove appropriate physical phenomena from the framework for solving complex multi-scale multi-physics problems at hand.

REFERENCES

[1] R. G. Claus, "Development of a High Performance, Heavy Duty Piston Seal," *Proc. 49th National Conference on Fluid Power, NFPA* pp. 383-389, 2002.

[2] S. Peng, Sun, S. and Albertson, K., "FEA-Assisted Design of Low-Friction U-Cup as Spool Valve Seals," *Proc. 47th National Conference on Fluid Power, NFPA*, pp. 175-182, 1996.

[3] A. Naderi, Albertson, K. and Peng, S., "Finite Element Analysis of a Hydraulic Seal: BS U-Cup," *Proc. 46th National Conference on Fluid Power, NFPA*, pp. 99-105, 1994.

[4] H. Weiss, 1996, "New Generation of Hydraulic Seals Supports Progress for Hydraulic Cylinders," *Proc. 47th National Conference on Fluid Power, NFPA*, pp. 153-163, 1996.

[5] D. D. F. White C. M., "The sealing mechanism of flexible packings," *Scientific and Technical Memorandum 3/47,Ministry of Supply (reprinted 1972, BHRA Fluid Engineering, Cranfield, Bedfordshire*, 1947.

[6] A. F. C. Kanters, "On the calculation of leakage and friction of reciprocating elastomeric seals," *PhD Thesis, Eindhoven University of Technology, the Netherlands*, 1990.

[7] M. Visscher and A. F. C. Kanters, "Literature-Review and Discussion on Measurements of Leakage, Lubricant Film Thickness and Friction of Reciprocating Elastomeric Seals," *Lubrication Engineering*, vol. 46, pp. 785-791, Dec 1990.

[8] M. Visscher, "The measurement of the film thickness and roughness deformation of lubricated elastomers," *PhD Thesis, Eindhoven University of Technology, the Netherlands*, 1992.

[9] J. M. Lawrie, O'Donoghue, J. P., "The mechanism of lubrication in a reciprocating seal," *Proceedings of the 2nd International Conference on Fluid sealing*, vol. (BHRA), pp. 69-80, 1964.

[10] K. Gawrys, "The effect of operation conditions on the design of seals for reciprocating motion," *Proceedings of the 10th International Conference on Fluid sealing*, vol. (BHRA), pp. 285–294, 1984.

[11] R. F. Cnops, "The friction of elastomer seals," *Proceedings of the 2nd International Conference on Fluid sealing*, vol. (BHRA), pp. 81-91, 1964.

[12] H. K. Müller, "Leakage and friction of flexible packings at reciprocating motion with special consideration of hydrodynamic film formation," *Proceedings of the 2nd International Conference on Fluid sealing*, vol. (BHRA), pp. 13-28, 1964.

[13] M. W. Aston, Fletcher, W., and Morrell, S. H., "Sealing force of rubber seals and its measurement," *Proceedings of the 4th International Conference on Fluid sealing*, vol. (BHRA), pp. 64-75, 1969.

[14] P. G. Molari, "Stresses in O-ring gaskets," *Proceedings of the 6th International Conference on Fluid sealing*, vol. (BHRA), pp. 15–31, 1973.

[15] G. J. a. N. Field, B. S., "An experimental study of reciprocating rubber seals," *Proceedings of the IMechE Symposium on Elastohydrodynamic Lubrication, Leeds, UK*, pp. 29-36, 1972.

[16] R. M. Austin, Flitney, R. K., and Nau, B. S, "Contact stress, friction and the lubricant film of hydraulic cylinder seals," *In Proceedings of the 8th International Conference on Fluid sealing*, vol. (BHRA), pp. 11-20, 1978.

[17] Y. Kawahara, Ohtake, Y., and Hirabayashi, H, "Oil film formation of oil seals for reciprocating motion," *Proceedings of the 9th International Conference on Fluid sealing*, vol. (BHRA), pp. 73–85, 1981.

[18] D. a. S. Dowson, P. D, "The development of elastohydrodynamic conditions in a reciprocating seal," *Proceedings of the 4th International Conference on Fluid sealing*, vol. (BHRA), pp. 2–10, 1969.

[19] H. a. I. Kambayashi, H, "A study of oil seals for reciprocating motion " *Proceedings of the 2nd Inter-national Conference on Fluid sealing*, vol. (BHRA), pp. 29–40, 1964.

[20] A. S. Rana, "A tribological study of elastomeric reciprocating seals for hydraulic actuators," *PhD Thesis, Imperial College London, Mechanical Engineering Department*, 2005.

[21] A. Rana, Sayles, R. S., Nikas, G. K., and Jalisi, I, "An experimental technique for investigating the sealing principles of reciprocating elastomeric seals for use in linear hydraulic actuator assemblies," *Proceedings of the 2nd World Tribology Congress, Vienna, Austria*, 2001.

[22] B. Duhring and G. Iversen, "The application of plastics in dynamic seals," *Proceedings of the Institution of Mechanical Engineers Part J-Journal of Engineering Tribology*, vol. 213, pp. 227-237, 1999.

[23] R. W. Ogden, "Large Deformation Isotropic Elasticity - Correlation of Theory and Experiment for Incompressible Rubberlike Solids," *Proceedings of the Royal*

Society of London Series a-Mathematical and Physical Sciences, vol. 326, pp. 565-&, 1972.

[24] L. R. G. Treloar, "Mechanics of Rubber Elasticity," *Proceedings of the Royal Society of London Series a-Mathematical Physical and Engineering Sciences*, vol. 351, pp. 301-330, 1976.

[25] M. Mooney, "A theory of large elastic deformation," *Journal of Applied Physics*, vol. 11, pp. 582-592, Sep 1940.

[26] R. S. Rivlin, "Large Elastic Deformations of Isotropic Materials .4. Further Developments of the General Theory," *Philosophical Transactions of the Royal Society of London Series a-Mathematical and Physical Sciences*, vol. 241, pp. 379-397, 1948.

[27] H. F. Brinson, Brinson, L. C., *Polymer Engineering Science and Viscoelasticity: An Introduction*. New York: Springer, 2008.

[28] W. Flugge, *Viscoelasticity*, 2nd rev. ed. Berlin: Springer-Verlag, 1975.

[29] J. D. Ferry, *Viscoelastic properties of polymers*. New York: Wiley, 1961.

[30] R. S. Lakes, *Viscoelastic solids*. Boca Raton: CRC Press, 1999.

[31] H. K. Muller, Nau, B. S., *Fluid sealing technology: principles and applications*. New York: Marcel Dekker, 1998.

[32] A. F. C. Kanters, *et al.*, "On Reciprocating Elastomeric Seals - Calculation of Film Thicknesses Using the Inverse Hydrodynamic Lubrication Theory," *Tribology Transactions*, vol. 33, pp. 301-306, Jul 1990.

[33] G. K. Nikas and R. S. Sayles, "Study of leakage and friction of flexible seals for steady motion via a numerical approximation method," *Tribology International*, vol. 39, pp. 921-936, Sep 2006.

[34] D. Dowson, Swales, P. D., "An elastohydrodynamic approach to the problem of the reciprocating seal," in *3rd International Conference on Fluid sealing*, 1967, pp. 33 - 44.

[35] F. H. Theyse, "The inverse hydrodynamic theory and its application in the design of controlled leakage seals between moving parts," in *3rd International Conference on Fluid sealing*, 1967, pp. 17-32.

[36] H. Blok, "Inverse problems in hydrodynamic lubrication and design directives for lubricated flexible surfaces," in *International Symposium on Lubrication and Wear*, Houston, Texas, USA., 1963, pp. 7-79.

[37] L. E. C. Ruskell, "A Rapidly Converging Theoretical Solution of the Elastohydrodynamic Problem for Rectangular Rubber Seals," *Journal of Mechanical Engineering Science,* vol. 22, pp. 9-16, 1980.

[38] G. J. a. N. Field, B. S., "Film thickness and friction measurements during reciprocation of a rectangular section rubber seal ring," *Proceedings of the 6th International Conference on Fluid sealing,* vol. (BHRA), pp. 45-56, 1973.

[39] A. F. C. Kanters, Visscher, M., "Lubrication of Reciprocating Seals: Experiments on the Influence of Surface Roughness on Friction and Leakage," in *15th Leeds-Lyon Symposium on Tribology*, 1988, pp. 69-77.

[40] G. K. Nikas, "Elastohydrodynamics and mechanics of rectangular elastomeric seals for reciprocating piston rods," *Journal of Tribology-Transactions of the Asme,* vol. 125, pp. 60-69, Jan 2003.

[41] G. K. Nikas, "Transient elastohydrodynamic lubrication of rectangular elastomeric seals for linear hydraulic actuators," *Proceedings of the Institution of Mechanical Engineers Part J-Journal of Engineering Tribology,* vol. 217, pp. 461-473, 2003.

[42] G. K. Nikas and R. S. Sayles, "Nonlinear elasticity of rectangular elastomeric seals and its effect on elastohydrodynamic numerical analysis," *Tribology International,* vol. 37, pp. 651-660, Aug 2004.

[43] B. Yang and R. F. Salant, "Soft EHL Simulations of U-Cup and Step Hydraulic Rod Seals," *Journal of Tribology-Transactions of the Asme,* vol. 131, pp. -, Apr 2009.

[44] R. F. Salant, *et al.*, "Numerical model of a reciprocating hydraulic rod seal," *Journal of Tribology-Transactions of the Asme,* vol. 129, pp. 91-97, Jan 2007.

[45] B. Yang and R. F. Salant, "A numerical model of a reciprocating rod seal with a secondary lip," *Tribology Transactions,* vol. 51, pp. 119-127, 2008.

[46] B. Yang and R. F. Salant, "Numerical model of a tandem reciprocating hydraulic rod seal," *Journal of Tribology-Transactions of the Asme,* vol. 130, pp. 032201:1-032201:7, Jul 2008.

[47] Y. Ongun, *et al.*, "An axisymmetric hydrodynamic interface element for finite-element computations of mixed lubrication in rubber seals," *Proceedings of the Institution of Mechanical Engineers Part J-Journal of Engineering Tribology,* vol. 222, pp. 471-481, May 2008.

[48] S. Stupkiewicz and A. Marciniszyn, "Elastohydrodynamic lubrication and finite configuration changes in reciprocating elastomeric seals," *Tribology International,* vol. 42, pp. 615-627, May 2009.

[49] T. Schmidt, *et al.*, "A transient 2D-finite-element approach for the simulation of mixed lubrication effects of reciprocating hydraulic rod seals," *Tribology International,* vol. 43, pp. 1775-1785, Oct 2010.

[50] G. K. Nikas, "Eighty years of research on hydraulic reciprocating seals: review of tribological studies and related topics since the 1930s," *Proceedings of the Institution of Mechanical Engineers Part J-Journal of Engineering Tribology,* vol. 224, pp. 1-23, 2010.

[51] Greenwoo.Ja and Williams.Jb, "Contact of Nominally Flat Surfaces," *Proceedings of the Royal Society of London Series a-Mathematical and Physical Sciences,* vol. 295, pp. 300-&, 1966.

[52] S. Timoshenko, *Theory of elasticity,* 2d ed. New York: McGraw-Hill, 1951.

[53] J. I. Mccool, "Comparison of Models for the Contact of Rough Surfaces," *Wear,* vol. 107, pp. 37-60, Jan 1 1986.

[54] A. W. Bush, *et al.*, "Elastic Contact of a Rough Surface," *Wear,* vol. 35, pp. 87-111, 1975.

[55] A. W. Bush, *et al.*, "Strongly Anisotropic Rough Surfaces," *Mechanical Engineering,* vol. 101, pp. 95-95, 1979.

[56] C. Yang, *et al.*, "A multiscale molecular dynamics approach to contact mechanics," *European Physical Journal E,* vol. 19, pp. 47-58, Jan 2006.

[57] A. Majumdar and B. Bhushan, "Role of Fractal Geometry in Roughness Characterization and Contact Mechanics of Surfaces," *Journal of Tribology-Transactions of the Asme,* vol. 112, pp. 205-216, Apr 1990.

[58] R. L. Jackson and J. L. Streator, "A multi-scale model for contact between rough surfaces," *Wear,* vol. 261, pp. 1337-1347, Dec 20 2006.

[59] N. Patir and H. S. Cheng, "Average Flow Model for Determining Effects of 3-Dimensional Roughness on Partial Hydrodynamic Lubrication," *Journal of Lubrication Technology-Transactions of the Asme,* vol. 100, pp. 12-17, 1978.

[60] N. Patir and H. S. Cheng, "Application of Average Flow Model to Lubrication between Rough Sliding Surfaces," *Journal of Lubrication Technology-Transactions of the Asme,* vol. 101, pp. 220-230, 1979.

[61] L. Floberg, *Cavitation in Lubricating Oil Films*. Amsterdam: Elsevier, 1964.

[62] H. G. Elrod, "A Cavitation Algorithm," *Journal of Lubrication Technology-Transactions of the Asme,* vol. 103, pp. 350-354, 1981.

[63] P. Payvar and R. F. Salant, "A Computational Method for Cavitation in a Wavy Mechanical Seal," *Journal of Tribology-Transactions of the Asme,* vol. 114, pp. 199-204, Jan 1992.

[64] S. R. Harp and R. F. Salant, "An average flow model of rough surface lubrication with inter-asperity cavitation," *Journal of Tribology-Transactions of the Asme,* vol. 123, pp. 134-143, Jan 2001.

[65] S. R. Harp and R. F. Salant, "Inter-asperity cavitation and global cavitation in seals: An average flow analysis," *Tribology International,* vol. 35, pp. 113-121, Feb 2002.

[66] I. Daubechies, "Ten lectures on wavelets," in *Regional Conference series in Applied Mathematics,* Philadelphia, PA, 1992.

[67] D. Van de Ville, *et al.*, "Surfing the brain - An overview of wavelet-based techniques for fMRI data analysis," *Ieee Engineering in Medicine and Biology Magazine,* vol. 25, pp. 65-78, Mar-Apr 2006.

[68] F. K. Hansen, *et al.*, "Foreground subtraction of cosmic microwave background maps using WI-FIT (wavelet-based high-resolution fitting of internal templates)," *Astrophysical Journal,* vol. 648, pp. 784-796, Sep 10 2006.

[69] L. Tenorio, *et al.*, "Applications of wavelets to the analysis of cosmic microwave background maps," *Monthly Notices of the Royal Astronomical Society,* vol. 310, pp. 823-834, Dec 11 1999.

[70] S. G. Mallat, "A Theory for Multiresolution Signal Decomposition - the Wavelet Representation," *Ieee Transactions on Pattern Analysis and Machine Intelligence,* vol. 11, pp. 674-693, Jul 1989.

[71] S. G. Mallat, "Multiresolution Approximations and Wavelet Orthonormal Bases of L2(R)," *Transactions of the American Mathematical Society,* vol. 315, pp. 69-87, Sep 1989.

[72] D. L. Donoho and I. M. Johnstone, "Adapting to unknown smoothness via wavelet shrinkage," *Journal of the American Statistical Association,* vol. 90, pp. 1200-1224, Dec 1995.

[73] D. L. Donoho and I. M. Johnstone, "Minimax estimation via wavelet shrinkage," *Annals of Statistics,* vol. 26, pp. 879-921, Jun 1998.

[74] D. L. Donoho, *et al.*, "Wavelet Shrinkage - Asymptopia," *Journal of the Royal Statistical Society Series B-Methodological,* vol. 57, pp. 301-337, 1995.

[75] C. S. Burrus, Gopinath, R. A., Haito G., *Introduction to wavelets and wavelet transforms: a primer*. Upper Saddle River, N.J.: Prentice Hall, 1998.

[76] G. Binnig, *et al.*, "Atomic Force Microscope," *Physical Review Letters,* vol. 56, pp. 930-933, Mar 3 1986.

[77] N. A. Burnham and R. J. Colton, "Measuring the Nanomechanical Properties and Surface Forces of Materials Using an Atomic Force Microscope," *Journal of Vacuum Science & Technology a-Vacuum Surfaces and Films,* vol. 7, pp. 2906-2913, Jul-Aug 1989.

[78] H. J. Butt, *et al.*, "Force measurements with the atomic force microscope: Technique, interpretation and applications," *Surface Science Reports,* vol. 59, pp. 1-152, Oct 2005.

[79] U. Rabe, *et al.*, "Vibrations of free and surface-coupled atomic force microscope cantilevers: Theory and experiment," *Review of Scientific Instruments,* vol. 67, pp. 3281-3293, Sep 1996.

[80] K. Yamanaka and S. Nakano, "Ultrasonic atomic force microscope with overtone excitation of cantilever," *Japanese Journal of Applied Physics Part 1-Regular Papers Short Notes & Review Papers,* vol. 35, pp. 3787-3792, Jun 1996.

[81] A. RosaZeiser, *et al.*, "The simultaneous measurement of elastic, electrostatic and adhesive properties by scanning force microscopy: pulsed-force mode operation," *Measurement Science & Technology,* vol. 8, pp. 1333-1338, Nov 1997.

[82] Q. Zhong, *et al.*, "Fractured Polymer Silica Fiber Surface Studied by Tapping Mode Atomic-Force Microscopy," *Surface Science,* vol. 290, pp. L688-L692, Jun 10 1993.

[83] A. G. Onaran, *et al.*, "A new atomic force microscope probe with force sensing integrated readout and active tip," *Review of Scientific Instruments,* vol. 77, pp. -, Feb 2006.

[84] Z. Parlak, *et al.*, "Controlling tip-sample interaction forces during a single tap for improved topography and mechanical property imaging of soft materials by AFM," *Ultramicroscopy,* vol. 109, pp. 1121-1125, Aug 2009.

[85] A. F. Bower, *Applied Mechanics of Solids*. Boca Raton: CRC Press, 2010.

[86] Comsol, "Structural Mechanics Module : User's Guide," ed, 2008.

[87] N. Kikuchi, Oden, J. T.,, "Contact problems in elasticity: a study of variational inqualities and finite elements method," in *SIAM*, Philadelphia, 1988.

[88] J. C. Simo and T. A. Laursen, "An Augmented Lagrangian Treatment of Contact Problems Involving Friction," *Computers & Structures,* vol. 42, pp. 97-116, Jan 1992.

[89] A. Faraji, *Elastic And Elastoplastic Contact Analysis: Using Boundary Elements And Mathematical Programming* UK: WIT Press, 2005.

[90] Comsol, "Comsol Multiphysics : Reference Guide," ed, 2008, p. 533.

[91] S. V. Patankar, *Numerical heat transfer and fluid flow*. Washington: Hemisphere Pub. Corp., 1980.

[92] X. Huo, "Wavelets," *Lecture Notes: ISYE 6416, Georgia Institute of Technology,* 2009.

[93] D. L. Donoho, "De-noising by soft-thresholding," *Information Theory, IEEE Transactions on* vol. 41, pp. 613-627, 1995.

[94] C. M. Stein, "Estimation of the Mean of a Multivariate Normal-Distribution," *Annals of Statistics,* vol. 9, pp. 1135-1151, 1981.

[95] J. Donea, Huerta, A., Ponthot, J. P., Rodriguez-Ferran, A., "Arbitrary Lagrangian-Eulerian methods," in *Encyclopedia of Computational Mechanics* vol. Chapter 14, E. Stein, de Borst, R., Hughes. T. J. R., Ed., ed. New York: John Wiley & Sons, Ltd., 2004.

[96] M. Sakai, "Time-dependent viscoelastic relation between load and penetration for an axisymmetric indenter," *Philosophical Magazine a-Physics of Condensed Matter Structure Defects and Mechanical Properties,* vol. 82, pp. 1841-1849, Jul 10 2002.

[97] C. Y. Hui, *et al.*, "The mechanics of tack: Viscoelastic contact on a rough surface," *Journal of Polymer Science Part B-Polymer Physics,* vol. 38, pp. 1485-1495, Jun 1 2000.

[98] R. D. Bradshaw, Brinson, L. C, "A sign control method for fitting and interconverting material functions for linearly viscoelastic materials," *Mechanics of Time-Dependent Materials* vol. 1, pp. 85-108, 1997.

[99] J. C. Lagarias, *et al.*, "Convergence properties of the Nelder-Mead simplex method in low dimensions," *Siam Journal on Optimization,* vol. 9, pp. 112-147, Dec 21 1998.

[100] Y. Q. Wang, *et al.*, "Dynamic mechanical analysis and dynamic infrared linear dichroism study of the frequency-dependent viscoelastic behavior of a poly(ester urethane)," *Vibrational Spectroscopy*, vol. 42, pp. 74-77, Oct 18 2006.

[101] L. E. Nielsen, Landel, R. F., *Mechanical properties of polymers and composites*, 2nd ed. New York: M. Dekker, 1994.

[102] M. L. Williams, Landel, R. F., Ferry, J. D., "The temperature dependence of relaxation mechanisms in amorphous polymers and other glass-forming liquids," *Journal of the American Chemical Society*, vol. 77, pp. 3701–3706, 1955.

[103] M. Balantekin, *et al.*, "Quantitative mechanical characterization of materials at the nanoscale through direct measurement of time-resolved tip-sample interaction forces," *Nanotechnology*, vol. 19, pp. -, Feb 27 2008.

[104] B. Bhushan, *Handbook of micro/nano tribology*, 2nd ed. Boca Raton: CRC Press, 1999.

[105] N. A. Burnham, Colton R. J., Pollock H. M. , "Interpretation of force curves in force microscopy," *Nanotechnology*, vol. 4, p. 64, 1993.

VITA

Azam Thatte

Azam Thatte was born in Pune, India in 1981. He received his Bachelor of Engineering degree in Mechanical Engineering (with "Distinction") from University of Pune, India in 2003. He received his MS degree in Mechanical Engineering from Pennsylvania State University, USA in 2005, where he conducted research in developing mathematical models and high performance computational algorithms for predicting flame propagation and gas dynamics during in-situ combustion of oil-spills. At Penn State he also worked on developing fluid-structure interaction models and intelligent image extraction algorithms for bio-mechanics applications.

Azam entered the Department of Mechanical Engineering at Georgia Tech in 2006 as a Ph.D student and worked with Prof. Richard Salant. His major research interests include multi scale- multi physics modeling, fluid-structure interaction, contact mechanics, surface characterization, nano-scale material property imaging and developing efficient computational algorithms. Besides these, Azam is also interested in developing intelligent signal processing algorithms for astrophysics applications.

During his research at Georgia Tech Azam has authored / co-authored 6 journal publications including one in "Nature" and several peer reviewed conference publications. He has also received several awards and honors including 2010 Young Tribologist award from STLE, an invited talk at World Tribology Congress, Japan in 2009 and awards at Georgia Tech Graduate Research Symposium in 2008 and 2009.